CRANFIELD UNIVERSITY

Almabrok Abushanaf Almabrok

Gas-Liquid Two-Phase Flow in Up and Down Vertical Pipes

School of Engineering
Department of Offshore, Process and Energy Engineering

PhD Thesis
Academic Year: 2009 - 2013

Supervisor: Prof. Hoi Yeung
October, 2013

CRANFIELD UNIVERSITY

School of Engineering
Department of Offshore, Process and Energy Engineering

PhD Thesis

Academic Year: 2009 - 2013

Almabrok Abushanaf Almabrok

Gas-Liquid Two-Phase Flow in Up and Down Vertical Pipes

Supervisor: Prof. Hoi Yeung
October 2013

This thesis is submitted in partial fulfilment of the requirements for the degree of Doctor of Philosophy

© Cranfield University 2013. All rights reserved. No part of this publication may be reproduced without the written permission of the copyright owner.

ABSTRACT

Multiphase flows occurring in pipelines with a serpentine configuration is an important phenomenon, which can be encountered in heat exchangers used in a variety of industrial processes. More specifically, in many industrial units such as a large cracking furnace in a refinery, the tubes are arranged in a serpentine manner and are relatively short. As flow negotiates round the 180^{o} bend at the ends of the tubes, the generated centrifugal force could cause flow maldistribution creating local dry spots, where no steady liquid film is formed on the adjacent straight sections of the pipe. As a result, events including coking, cracking and overheating of heat transfer surfaces may occur and lead to frequent shutdown of the facilities. Consequently, this could increase operating costs and reduce production revenue. Thus, it is desirable to know the effect that the bends exert on the flow in the straight part of the pipe. Apart from this, knowledge of the bend effects on the flows in the pipeline could also be important for the design of other pipelines for gas/liquid transport, e.g. offshore gas and oil pipelines.

Quite a large number of studies have been found in the literature. The majority of them were for two-phase flow with small diameter pipes (i.d. ≤ 50 mm). However, studies with large diameter pipes (i.d. ≥ 100 mm), have increasingly been considered in recent years as problems related to large diameter vertical pipes are being encountered more and more often in industrial situations.

This thesis studies the effect of 180^{o} bends on the characteristics and development of gas-liquid two-phase flows in large diameter downward and upward pipes. The study particularly focuses on the influence of serpentine configuration on flow structure, cross-sectional void distribution and circumferential liquid film profiles and their development along the downward and upward sections.

It was found that both the top and bottom bends have considerable impacts on flow behaviour, although to varying degrees. These impacts were highly dependent on the air and water flow rates. For sufficient flow rates, the bends

were observed to create flow maldistribution in the adjacent straight section, due to the effects of centrifugal force. The air moved towards the inner zone of the bend and the water towards the outer zone, while a lesser quantity of water was identified on the other surfaces of the pipe.

Investigation of the film thickness development in the downward and upward sections showed that, the liquid film behaviour close to the bends was significantly different from those located further away. This can be attributed to the centrifugal force of the bends.

Examination of the power spectral density (PSD) along the downward and upward sections showed that, the shape of PSD located in the adjacent section to the bends, was substantially different from those located further away.

Furthermore, several flow regime maps were generated which showed that, in addition to bubbly, intermittent and annular flows, unstable flows existed along the upward section, particularly for low gas and water flow rates. In this study it was found that, the lower bend was periodically blocked by the liquid and then blown through by the accumulated air.

The data obtained from this study were compared with different theoretical correlations found in the existing literature. Some discrepancy between the results of the current study and those of previous published materials was noted. Updated correlations were presented which provided well results when they applied for the data obtained from the current study and previous studies.

Keywords: Serpentine configuration, downward, upward, bends, liquid film thickness, void fraction distribution, PSD, flow regime maps

DEDICATION

I dedicate this work to my late father and mother. May Allah grant them Jannat Alfirdaus.

ACKNOWLEDGEMENT

First and foremost, I thank the Almighty Allah for his boundless mercies, blessings and favour, without whom nothing exists or flourishes. He has been a constant source of strength during my doctorate studies.

Secondly, I extend my profound gratitude to the Libyan Government who provided the scholarship for the PhD. The skills I have learnt at Cranfield University will now be transferred for the betterment of my mother country.

I sincerely thank my supervisor Professor Hoi Yeung for his mentoring, support, and patience throughout the duration of this study. His guidance has been profoundly valuable.

I would also like to thank Dr Liyun Lao for his time and patience during the experimental planning, and explaining complex laboratory instrumentation.

I also acknowledge the support of my family: my wife for her constant support and care during my study, without which it would have been impossible to carry on; my wonderful daughters who despite enduring many hours without me, have been a constant source of happiness; and also my two sisters. I am lucky indeed.

Special thanks to Mrs Sam Skears for her help and support during my PhD study, and the technicians in the PSE Lab of the Department of Offshore, Process and Energy Engineering. I really appreciate the efforts of the Lab Manager Stan Collins, and technicians Dave and Kelvin. I am truly grateful.

Last but not least I thank my colleagues and fellow students at the Process Systems Engineering Group for the good times we had, the discussions and insights. I will forever have very fond recollections of my time with you all at Cranfield.

TABLE OF CONTENTS

LIST OF FIGURES

LIST OF TABLES

LIST OF ABBREVIATIONS

Symbol	*Description, Units*
A	Area, m^2
D	Pipe diameter, m
i.d.	Internal pipe diameter, m
k	mass transfer coefficient
E	Liquid entrainment rate
g	Gravitational acceleration, m/s^2
Usg	Gas superficial velocity, m/s
Usl	Liquid superficial velocity, m/s
Ust	Transition gas velocity, m/s
V_m	Mixture velocity, m/s
x	Gas quality
L	Length, m
P	Pressure, bar
ΔP	Differential pressure, bar
F	Frequency, Hz
Q_L	Liquid volume flow rate per wetted perimeter length, m^2/s
U_f	Measured liquid film velocity, m/s
α	Measured void fraction
δ	Measured liquid film thickness, mm
$\delta+$	Dimensionless liquid film thickness
T	Liquid film mass flux, kg/m s
μ_G	Dynamic gas viscosity, Pa-s
μ_L	Dynamic liquid viscosity, Pa-s
ν_G	Kinematic gas viscosity, m^2/s
ν_L	Kinematic liquid viscosity, m^2/s
ρ_G	Gas density, kg/m^3
ρ_L	Liquid density, kg/m^3
$\Delta\rho$	Density difference between the two-phase, kg/m^3

σ	Surface tension, N/m
C_w	Wall fraction factor= 0.008
L/D	Length to diameter ratio
Z/D	Distance to diameter ratio
Fr_G	Froude number of gas
Fr_L	Froude number of liquid
Bo	Bond number
Re_G	Reynolds number of gas
Re_L	Reynolds number of liquid
Re_{Lf}	Reynolds number of liquid film
Ku_G	Kutateladze number of gas
Ku_L	Kutateladze number of liquid
PDF	Probability density function
∩-bend	Top bend
U-bend	Bottom bend
DAQ	Data acquisition system
WMS	Wire mesh sensor
CapWMS	Capacitance wire mesh sensor
CondWMS	Conductive wire mesh sensor

1 Introduction

1.1 Motivations for this study

Upward and downward vertical pipes connected together by 180^o bends are common in heat transfer equipment and furnaces. Typically the flow in such equipment can be single phase (liquid or gas) flow or liquid-gas two-phase flow, depending on the fluid properties and operational conditions of the facilities. Among these flows, it is the gas liquid two-phase flow that imposes the most challenging problems related to the design and operation of engineering facilities.

Some parameters, including cross-sectional gas void fraction, pressure drops and liquid film thickness, are vital for identifying the flow behaviour in such facilities. Accurate measurement and/or prediction of these parameters could lead to enhanced design and productivity. However, although quite a large number of studies have been found in literature, the majority are for upward flow with diameter pipes less than 50 mm. Conversely, investigations on the bend effects on either upward or downward annular flow development in pipes with diameters over 100 mm have been found to be particularly scarce. To date, the studies of both upward and downward flows in a serpentine configuration and those of concurrent downward gas-liquid annular flows are limited or none at all.

Thus, it is desirable to know the effect of the bends' exertion on the flow in the straight part of the pipe. Apart from this, the knowledge of the bend effects on the flows in the pipeline could also be important for the design of other pipelines for gas/liquid transport, e.g. offshore gas and oil pipelines. The current work intends to study the effect of 180^o bends on gas-liquid two-phase flow characteristics in up and down orientations with a large diameter pipe – as widely used in heat exchanger application.

1.2 Background

Gas liquid two-phase flows are extremely complicated because of the deformable gas-liquid interfacial structures and the compressibility of the gas phase.

To deal with the gas-liquid two-phase flow issues, it is essential to identify the flow regimes (also known as flow patterns). A flow regime can be defined as the physical spatial distribution of two or more fluids along a pipe, which represents the flow structure and its patterns. Factors including the operational conditions (temperature and pressure), fluid properties (density, viscosity and surface tension), gas and liquid flow rates, gas void fraction, pipe orientation and its diameter, all contribute highly to the flow regime formation.

Flow regimes can be formed in both the horizontal and vertical pipes. They may occur, for instance, due to the co-production of oil and gas, water vaporisation, and a combination of two fluids together in a pipeline. To identify the two-phase flow regimes, a high-speed camera and/or visual observation or analysis of the probability density functions (PDFs) of averaged void fraction can be used (Dong et al., 2001).

It is widely accepted that vertical gas-liquid flows can be categorised into the following types – also illustrated in Figure 1-1:

- Bubbly flow

The gas phase is distributed in discrete bubbles within a liquid continuum. The size and shapes of the gas bubbles moving within the liquid are uniform, and occupy the pipe centre. This flow regime is known to occur at low flow rates of gas (Barnea, 1987; Taitel et al., 1980).

- Slug (or plug) flow

By increasing gas flow rates gradually, some large bubbles tend to collide and coalesce with the smaller ones to form larger bubbles, which occupy the greater part of the channel cross section, and move along in bullet-shaped bubbles. These bubbles are classified as Taylor bubbles (Nicholas, 2000).

- Churn flow

Increasing the flow rates of gas leads to further breakdown and distorts the Taylor bubbles immediately, to form an unstable flow regime known as churn flow. In churn flow, a thin liquid film that exists around the liquid that contains bubble will fall downward. The falling film will accumulate to form a bridge on the base of the pipe which is lifted again by the gas (Hewitt and Jayanti, 1993).

- Annular flow

In an annular flow regime, the liquid film flows along the pipe walls, while a stream of gas (gas/liquid droplet mixture) flows in the centre of the pipe. More detailed information is presented in a subsequent chapter.

- Wispy flow

When the liquid mass flux is high enough, the liquid droplets presented in the central zone of the pipe are agglomerated into large wisps, leading to wispy annular flow formation.

- Mist flow

This flow can only take place in a non-adiabatic system, where the liquid phase will be completely dispersed.

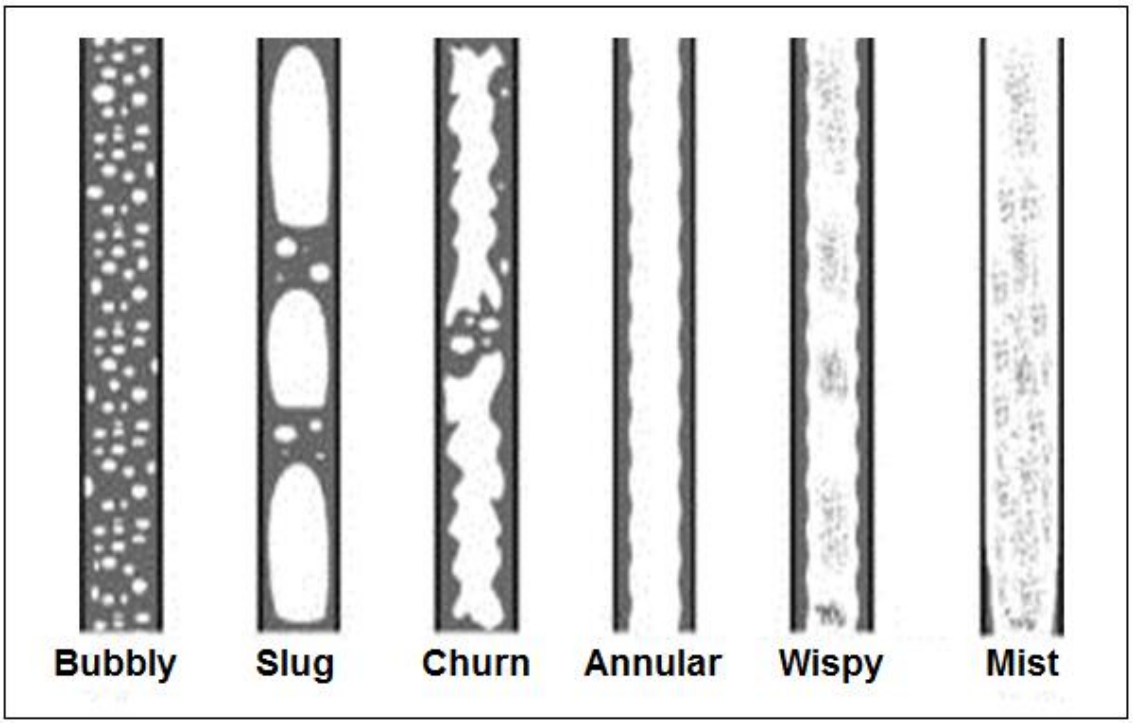

Figure 1-1 Gas-liquid flow regimes in vertical pipes, adapted from Cheng et al., (2008)

1.3 Scope of this study

The work presented in this thesis was carried out mainly to investigate the effects of 180^{o} bends on flow behaviour in up and down vertical pipes.

It was noted from the literature that the bends have considerable impacts on the gas-liquid flow characteristics. There have been many studies of vertical annular flow with upward gas flows. However, relatively few studies on the upward and downward flows in a serpentine configuration have been published. The majority of published works were mainly confined to small diameters (mostly less than 50 mm internal diameter pipes). Thus, there is still a need to carry out experiments for two-phase flows in large diameter pipes (i.d. > 100 mm), as a number of studies, for example, Kataoka and Ishii (1987), and Cheng et al. (1998), reported that the gas liquid flow behaviours in large diameter pipes are likely to be quite different from those in smaller sized pipes.

In this study, data including gas void fraction and liquid film thickness were collected by applying the wire mesh sensor (WMS) and film thickness probes

respectively. Upward and downward flows were interrogated at different positions along the pipe and over various conditions of gas and liquid velocities. The film thickness data were presented by using time trace, probability density function (PDF) and circumferential profile. Void fraction data measured by WMS were interpreted by corresponding time trace, PDF and local distributions. In addition, flow patterns were presented by analysing the above data. Flow patterns were confirmed by cross-sectional and longitudinal views of the void fraction and visual observations. Flow regime maps were created for both up and down orientations, in order to identify the dominant flow regimes in such configurations. Furthermore, the effects of gas and liquid velocities on film thickness development and void fraction distributions were also investigated. A comparative study of the flow before and after the U-bend was also performed by analysing the probability density function of the average void fractions. Further efforts were made to compare the collected data with the available models published in the literature.

1.4 Research aim and objectives

This thesis is aimed at gaining further understanding of gas-liquid two-phase flow behaviours in equipment with vertical serpentine configurations and thus improves their design capability. In particular, the study presented in this thesis highlights the effects of 180^{o} bends on the liquid film development and void fraction distributions. The aim of this study was achieved through the following objectives:

- Carry out a thorough literature review on two-phase flow in up and down vertical pipes with special attention to the effects of pipe diameter on flow regime transition, film thickness, film wave occurrence and liquid entrainment.

- Perform experimental work using the Serpent rig facility with the assistance of a wire mesh sensor, liquid film probes and pressure transducers to determine the gas void fraction distributions, flow regimes, film thickness,

film velocity and pressure drops at a number of locations along the flow path.

- Investigate the flow development along downward and upward sections of the test facility with operating conditions covering a wide range of gas and liquid flow rates.

- Produce flow regime maps at different locations of the test facility for a wide range of flow rates.

- Carry out simultaneous measurements to investigate the different between the flow behaviour before and after the bends.

- Compare the results obtained from this work with existing experimental and theoretical works.

- Conclude on the effects of the 180^{o} bends on gas liquid flow characteristics in serpentine geometries.

Based on the achieved results from this study, a set of recommendation for future work will be presented.

1.5 Thesis outline

The rest of this thesis is structured into six chapters, which are presented below.

Chapter 2 reviews the relevant literature about gas/liquid flows in vertical pipes in general and 180^{o} bends in particular. The chapter highlights the previous investigations of liquid film and gas void fraction distributions. The axial development of liquid film and flow regimes maps for downward and upward sections are also described. In addition, the effects of pipe diameter, and injector types on flow behaviour, are reviewed and summarised.

Chapter 3 describes with Figures, the experimental facility – the Serpent rig facility. A technical description of the flow loop, overview of the liquid film thickness, integrated probes of film thickness and velocity, wire mesh sensor

(WMS) is given. Furthermore, the flow diagram indicating the locations of the sensor spool sensors is also described.

Chapter 4 reviews and summarises the procedures that were used to commission and calibrate the instrumentation. The procedure tests for single and two-phase tests are also provided. In addition, measurement repeatability is presented to ensure the quality of the data obtained.

Chapter 5 discusses the experimental data of gas void fraction obtained from the wire mesh sensor technique placed at different locations throughout the test facility. The data are presented and summarised for various gas and liquid flow rates. Visual observation results, with the necessary photographs for the bends and both straight sections, are also provided for the selection of gas and liquid superficial velocities. The chapter also provides the experimental results and data analysis related to this work using pressure transducers, film thickness, integrated film thickness and film velocity probes. The results obtained from air-water two-phase flow tests are presented for a wide range of gas and liquid superficial velocities and at different positions along the downward and upward sections.

Chapter 6 presents comparisons between the experimental results achieved from this study and other published studies; it also evaluates some of the existing models against the experimental results of this study.

Chapter 7 summarises the main conclusions drawn from the research work, based on the analysis of the measured data, which are followed by recommendations for future work.

2 Literature review

2.1 General overview

The detailed literature review covering all aspects of two-phase flows in vertical pipes, though important, is beyond the objectives of the current investigation. The subsequent sections of this chapter concentrate on the topics pertinent to the aim of this study. These include the importance and applications of serpentine geometries in some engineering facilities, vertical annular flow regimes and their axial development. In addition, the effects of pipe diameter on the liquid film thickness behaviour are also presented.

2.2 Heat exchangers and two-phase flows

Most of the previous studies on multiphase flows were focused on straight pipes. However, in reality industrial plants rarely consist of straight pipes only. Typically, equipment can contain various fittings such as valves and bends. Contraction and enlargement sections connecting pipes of different diameter can also be present. The 180^o bend is one example of such widely occurring industrial fittings. In nuclear reactors, waste heat boilers, evaporators, steam generators, oil and gas pipelines, and heat exchangers, 180^o bends affect both efficient operation and plant safety. Multiphase flows in the vertical 180^o return bends tend to produce intricate flow phenomena, due to the combined effect of gravitational and centrifugal forces. Gravitational force pulls the liquid in the direction of the inner wall of the bend shifting the gas toward the outer wall in the ∩-bend, and vice versa in the case of the U-bend. Conversely, the centrifugal force, acting normally to the main flow, moves the gas towards the zone of lesser curvature radius and the liquid towards the outer zone. These forces affect the flow structure in the bend and might cause a phase separation (Usui et al., 1983).

The flow structure is also influenced by the existing flow pattern entering the bend. These patterns cause distinctive characteristics to the distribution of local liquid film thickness and local void fraction. In the case of annular flow with low fractions of entrained liquid before the bend, there is the likelihood of dryout

occurring on the inside of the bend. According to Abdulkadir et al. (2012), these observations were made from research that utilised pipes of small internal diameter (i.d.). As such, it is imperative that further experimental data be obtained to expand the current knowledge of flow regime mechanisms in large diameter pipes in general and 180^{o} returned bends in particular.

Flowing liquid usually enters heat transfer equipment sub-cooled. Vaporisation begins as the wall reaches a high enough temperature, although this can also occur at mean liquid temperatures below the saturation temperature at the operating pressure. Vapour fraction continues to increase as flow develops along the pipe into the churn and annular flow regimes. Given sufficiently high heat fluxes, the liquid film in the annular flow can dryout leaving the heat transfer surface covered with a boiling blanket of vapour film. This can occur even at low vapour qualities with the remaining liquid flowing as droplets and being well insulated from the pipe surface by the vapour, hence marking the start of a nucleate boiling heat transfer in the wetted region, and dryout can occur as a result. In summary, dryout appears at high vapour fraction, when there is insufficient liquid to fully wet the walls of the channel. At dryout, the wall temperature starts increasing due to the heat transfer deterioration. Hills (1973) noted that liquid distribution and wall shear stress have a substantial influence on heat transfer. They not only affect the heat transfer rate directly, they affect its mechanism of occurrence. Nucleate boiling, caused by the pipe wall temperature well exceeding the film saturation temperature, occurs as an extreme. Another extreme is the possibility of pipe wall dryout which causes catastrophic damage to equipment due to overheating. Some applications involving entrained solids may have deposition around the dry patch area, and coupled with alternate drying and wetting can cause corrosion.

Accurate prediction of dryout is important for optimal heat exchanger design. This guarantees a decent balance between safety, cost and efficiency of vital industrial heat transfer equipment such as bubble columns and reboliers. Carey and Mandrusiak (1986) measured local heat transfer data for annular film flow boiling of saturated liquids and developed an approximate analytical transport

model in the liquid film. Flow visualisation photographs they took indicated that virtually no nucleate boiling was present when the flow was in the film-flow regime. Carey and Mandrusiak (1986) observed dry patches formed at different locations of the heated surface, which increased in their size with growing distance from the inlet until the entire film vanished.

Maqbool et al. (2012) studied the effects of different parameters such as mass flux, saturation temperature, vapour quality and internal diameter on dryout in minichannels. Their results showed that heat flux increases with the increase in mass velocity, with the decrease of vapour quality and with the increase of internal diameter, and almost no effect of saturation temperature on dryout heat flux was observed. Researchers such as Abdulkadir et al. (2012) observed that, the dryout phenomenon could occur round the bend due to the impacts of both centrifugal and gravitational forces. They stated that the former tends to push the liquid into the bend outer curvature, while the latter moves the liquid into the bend inner curvature.

Rooyen et al. (2012) developed a method of visualising two-phase flow inside the pipe using a dummy tube with a tubular glass section for visual access with a high-speed digital video camera and a laser light photodiode. These were used to observe and characterise the two-phase flow structure to improve the understanding of the physical phenomena taking place. Particularly, a dryout line was objectively identified in a flow pattern map separating high- and low-performance heat transfer data measured locally on the bundle. The tests spanned low mass velocities applicable in flooded evaporators, and heat fluxes include adiabatic and diabatic tests of 7-25 kW/m^2. They proposed a new prediction method for the onset of dryout on smooth pipe.

In the nuclear industry, Smith et al. (2012) noted that nuclear boiling water reactors are susceptible to the slightest of changes as regards two-phase flow. In such cases where dryout is likely to occur, lack of fundamental knowledge in this area can have significant ramifications for nuclear safety.

2.3 Bend effects on gas/liquid flows

Studies of the bend's effect on flow behaviour can at least date back to Eustice (1910, 1911), who investigated the streamlines in water flows within a variety of bends. Later on, Dean (1927, 1928) examined the motion of the flow in curved tubes and proposed a dimensionless Dean number, to evaluate the curve's effect on the flow. There are a number of published studies concerning the effects of upstream bends on the gas/liquid flow behaviour in bends and pipes. The majority of these studies were mainly on pipes of 1" or similar sizes. For example, Alves (1954), Hills (1973), and Anderson & Hills (1974) presented studies on liquid film behaviours in 180^o bends of 1" diameter pipe for different orientations. Oshinowo & Charles (1974) measured the effect of a return bend on the void fraction in a 1" pipe. They applied the balance between centrifugal and gravitational forces acting on the phases in the bend to explain the phase distributions. Usui et al. (1980, 1983) used a modified Froude number as a criterion to decide the liquid phase distribution tendency towards outside or inside of the bend and to explain the film behaviours in the bend. An experimental study on the behaviour of air-water flows and characteristics of dryout and pressure drops was carried out by Takemura et al. (1986). They conducted their work using returned and inverted 180^o bends with diameter of 18 mm. From the data obtained they noted that the two-phase flow behaviours in two configurations were extremely different. The gas was observed to flow on the inner surface of the U-bend for all flow conditions tested, while it moved on the outer surface of the ∩-bend at $120\text{-}150^o$ when applied to low gas and liquid flow rates. They also observed that the possibility of the dryout phenomenon is higher in the case of the U-bend than for the ∩-bend. Poulson (1991) studied the mass transfer at return bends and concluded that the mass transfer at the bends relative to the straight sections increases at high gas superficial velocities and is constant at low liquid superficial velocities. Azzi and Friedel (2005) modelled a pressure loss over 90^o bends in terms of a two-phase flow multiplier. Their results were based on experimental pressure loss data during air-water flow in vertical 90^o bends with 30 mm diameter and curvature radii of 120, 180, 240 and 300 mm.

Studies on bend effects on two-phase flows were also extended, to much smaller or larger sized pipelines. Hoang and Davis (1984) reported their experimental results of void fraction in froth flow in a 2" diameter U-bend by utilising needle probes. Wang et al. (2003, 2004, 2008), investigated the two-phase flow in small pipes. The pipe sizes of their work were down to 3 mm, where the surface tension played a much more significant role than in larger sized pipes. Chong et al. (2005) calculated liquid film in 150 mm i.d. of 180^{o} bends which were used to join vertical straight pipes to form a serpentine pipeline.

Reported literature on two-phase air-water flow in 180^{o} bends in large diameter pipes (> 100 mm) is scarce. Recently, Abdulkadir et al. (2012) carried out an experimental investigation on two-phase air-water flow through vertical 180^{o} bends with 127 mm internal diameter pipe. They reported that the flow characteristics around the bend were affected due to the existence of centrifugal and gravitational forces. They also carried out an experimental study into the churn-annular flow behaviour to measure mean film fraction of air-water mixture through a vertical 180^{o} return bend using electrical conductance tomography sensors. The study was distinctive in that it is probably the first major study in open literature on 180^{o} bends utilising a large, 127 mm i.d. They measured film fraction using conductance ring probes positioned before, within the bend (at different angles) and after the bend. They noted the average film fraction to be higher in the straight pipes than in the bends and that at low liquid/higher gas flow rates, film break up occurs at a 45^{o} angle due to gravity drainage. The conditions for which the liquid goes inside or outside the bend were identified based on a modified Froude number derived by Hills (1973).

2.4 Vertical flow regime

Two-phase flow is complex phenomenon. This can partly be attributed to the existence of different flow regimes (or flow patterns). The flow regime may vary depending on the respective distribution of the gas and liquid phases in the pipe. A considerable number of experimental campaigns were carried out by various investigators over the last 50 years. Most of them used air and water as

the working fluids; however others used different fluids such as gas-oil, gas-glycerine, gas-naphtha, and gas-kerosene mixtures. Consequently, these investigators have employed different nomenclatures to describe the observed flow regimes. This is because flow regimes can be very chaotic and objectively identifying them can be difficult. This section of the thesis discusses various efforts made by researchers over the years on flow regime identification. This will be followed by a discussion on the reported flow regime maps.

Nichols (1965) observed bubbly, bubbly-slug, slug, falling film and annular flows while studying vertical two-phase flow in 54 mm i.d. pipe. Falling film flow was observed to occur at low gas and liquid flow rates. He established that the annular flow is the most obvious and prevailing flow regime in vertical downward flow but did not observe any froth flow.

Golan (1968) reported results of bubbly, slug, oscillatory and annular flow regimes based on experimental work conducted in 38 mm diameter pipe with an air-water mixture. The flow regime map he produced was annular flow dominated. He noted that the unstable oscillatory flow occurred as the bubble velocity equalled the downward liquid velocity and could be attributed to the presence of U-bends. However, Golan remarked that it was unusual for this kind of flow regime to occur in downward vertical flow in the absence of U-bends and that bubbly-slug flow exists only if the downward water velocity exceeds the velocity of the bubble.

Oshinowo (1971) noted bubbly, slug, falling film, froth and annular-mist flow regimes, in a vertical upward and downward pipe with diameter of 25 mm. The term “coring-bubbly” was used because of the predisposition of the bubbles to travel towards the centre of the tube. He found that the radius of the core and size of the bubbles increased as the flow rates were increased and that the observed slug had no tiny bubbles in their wake. The front edge was frothy which was attributed to liquid draining from the side of the gas slug. As the gas flow rate increased further, this led to deformation of the slug, so that the edges moved towards the pipe wall. On the other hand, at low gas and liquid flow rates, the liquid phase slipped easily over the tube surface surrounding the

inner gas core containing little or no liquid entrainment inside. He classified this flow regime as “falling-film flow”. Also noted was a flow pattern where the liquid film was thicker with some entrained gas bubbles. This flow type was named the “falling bubbly film flow” regime.

The work of Yamazaki and Yamaguchi (1979) employed visual observation and photographic images to study air-water two-phase flow in a 25 mm diameter pipe. From their experiments carried out for downward orientation, they observed slug, falling film, annular and wispy annular flow regimes. An annular-like flow was observed with some entrainment at low water and moderate air rates. This they termed “wetted-wall flow”. This flow was also labelled falling-film by other researchers.

A 19.5 mm tube was used by Paras (1982) to experimentally study downward two-phase flow with air-water as the flowing mixture. He observed slug flow with continuous Taylor bubbles and intermittent water slugs. The bubbly flow observed had a “coring” tendency. Paras’ flow regime map contained large regions of churn flow whereby the bubbles surrounded an irregular void region. This flow regime has similarities to slug flow in that it fluctuates. The observations for annular flow in these conditions were those of a falling film on the pipe edges.

Crawford (1983) experimentally investigated two-phase flow using refrigerant R-113 and its vapour in a pipe with 38 mm internal diameter pipe. The observed flows were core bubbly, slug, churn, falling film and annular flows. He realised that, the smaller fast-moving bubbles were likely to coalesce towards the pipe centre, while those with larger size migrated to the pipe wall. Large air slugs, almost the size of the tube, were also present. Typical Taylor bubbles occurred only at relatively low pressures and these became distorted when the pressure increased. The falling film and annular flow observed in Crawford’s work were similar to those of other investigators such as Nguyen (1975) whose work was an extensive study on flow regimes in vertical upward and downward pipes. He observed seven flow regimes in the 45.5 mm pipe utilised. These were termed: bubble, slug, slug-froth, annular-slug, annular, annular-roll wave and annular-

droplet even though detailed descriptions of these regimes were absent in the paper. The annular-slug flow pattern observed was similar to the churn or semi-annular flow described in other investigations.

Usui and Sato (1989) using a 16 mm diameter pipe at atmospheric pressure investigated air-water flows and were able to observe four distinct flow regimes: bubbly, slug, falling film and annular flow. The bubbles in the bubbly flow regime had coring ability as a result of a lift force acting on the bubbles that formed when the phase velocity decreased gradually. They also noted that in slug flow, the majority of the slugs did not possess the classical Taylor bubble bullet shape. Buoyancy forces acting in opposition to the flow were responsible for distorting the bubbles so that near the pipe wall, they were wedge-shaped. Usui and Sato (1989) observed that transition to annular flow occurred as the fluid flow rates were increased.

Yijun and Rezkallah (1993) carried out an experimental campaign with a 9.5 mm diameter pipe in the vertical downward direction using air-water as working fluids. They reported bubbly, slug, froth, annular and falling film flow. For low gas flow rates and high liquid flow rates, bubbly flow was observed.

Abdullah and Al-Khatab (1994) examined air-water flow data obtained in a 38 mm diameter downward pipe. They produced a flow regime map determined by using visual observations and distinctly identified bubbly, slug and annular flow regimes. They reported that at low air flow rates, tiny air bubbles move randomly downwards and move away from the pipe axis. This is in contrast to what was reported by other investigators with regard to bubbly flow. Bubble coalescence occurred at higher flow rates. Slugs occurred at even higher air flow rates, and these moved towards the centre of the pipe and in spite of the flow being in the downward direction, the slugs were bullet-shaped. Further increase in the air flow rate produced annular flow such that the liquid film thickness decreased markedly.

From the foregoing, it is clear that flow regime identification is subjective, with no consistent quantitative methods employed in determining distinct flow patterns. However, it can be stated that flow regimes are dependent on the pipe

geometry, orientation, fluid combination and physical properties. Bubbly, slug, falling film and annular flow regimes highlight that the majority of research has been carried out in downward two-phase flow. The majority of the flow regimes were conducted in small diameter pipes. Limited flow regime was investigated for large pipe diameters, particularly for downward flows. Thus, there is a need to expand the investigation of vertical flow regimes to include large diameter pipes. Thus, flow regimes and corresponding maps are reported with pictorial evidences in chapter 5 of this thesis.

2.5 Flow regime map

A flow pattern map is a graphical illustration of the different flow patterns that occur in a pipe when the flow rates of the respective phases are varied. The type of flow pattern map depends on the properties plotted on the axes. Several flow regime maps have appeared in the literature with not only the superficial velocities plotted but also mass flow rates, mass fluxes, or dimensionless numbers such as liquid Reynolds number and Froude number. As such, flow regime maps are tools that categorise the existence of a specific flow pattern, given the aforementioned flow parameters. One problem with flow regime identification is that flow regime transitions are not sharply defined but gradual.

It is instructive to note that since flow pattern definition, and hence identification, depends on individual perception, universal flow pattern maps do not exist. Literature contains several flow pattern maps put forward by many investigators. These were plotted using different physical parameters on the axes. The map presented by Oshinowo (1971) was plotted for a 25 mm diameter pipe with the fluids' (air-water) mass flow rates on the respective coordinates (Figure 2-1). He observed that bubbly flow occurs at high water mass flow rates and low air mass flow with the falling film flow regime classified into the falling film and bubbly falling film flow. His flow pattern map was without a definite line showing flow regime transition with annular flow occupying a dominant portion of the map.

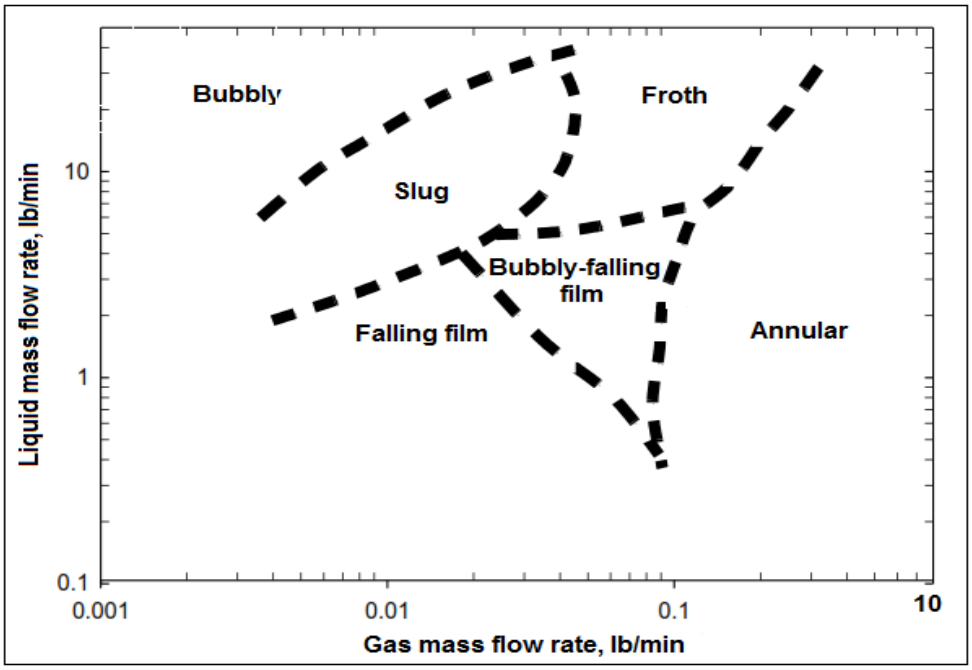

Figure 2-1 Vertical downward flow regime map (Oshinowo, 1971)

Yamazaki and Yamaguchi (1979) reported a flow pattern map (Figure 2-2) in terms of the phase mass fluxes, which was in fact the only flow pattern map reported in terms of the mass fluxes in kg/m^{2}s. Bubbly flow was not reported to occur in their experiments.

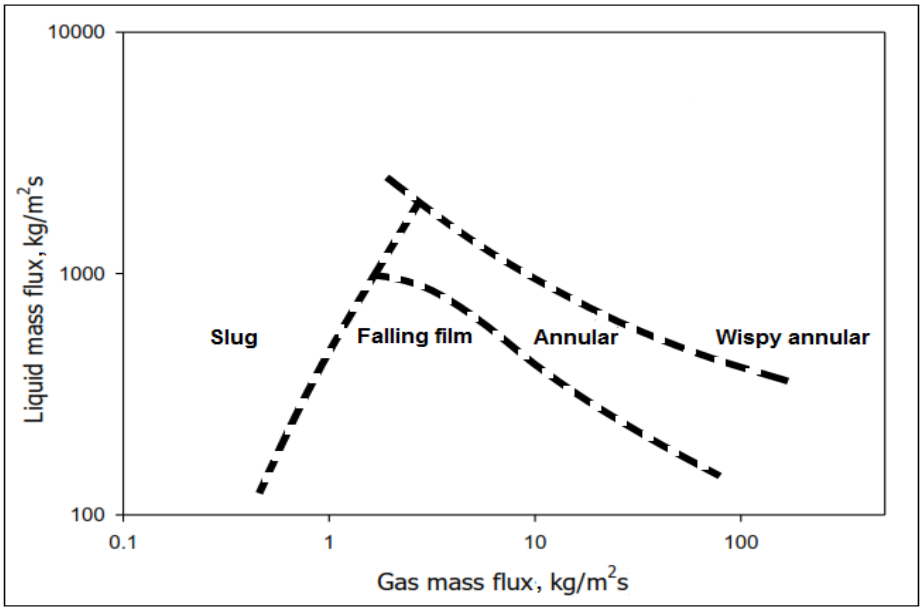

Figure 2-2 Vertical flow regime map (Yamazaki and Yamaguchi, 1979)

Figure 2-3 shows the map produced by Paras (1982). As can be seen, the boundaries around churn flow are not well established.

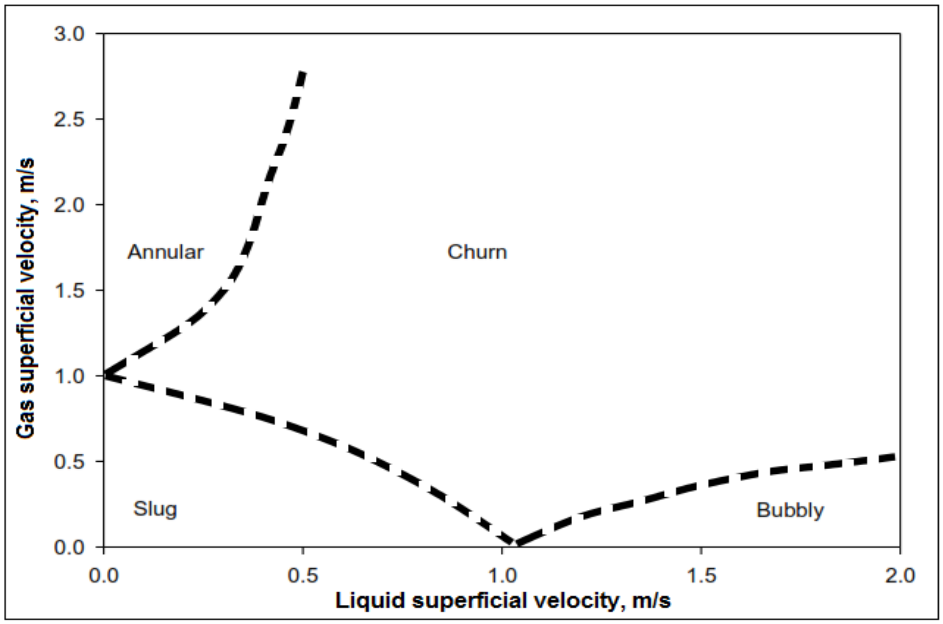

Figure 2-3 Vertical flow regime map (Paras, 1982)

Yijun and Rezkallah's (1993) flow regime map was in terms of the liquid and gas superficial velocities, as illustrated in Figure 2-4. This shows the high dependence of flow patterns on pipe diameter and fluid combination.

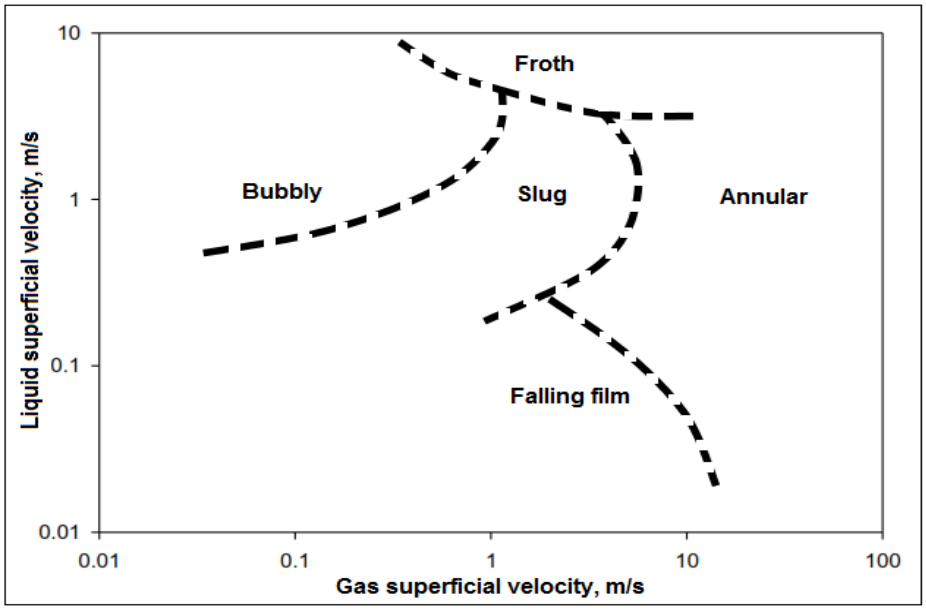

Figure 2-4 Vertical flow regime map (Yijun and Rezkallah, 1993)

2.6 Vertical annular flow

As stated in the previous chapter, in annular flows most of gas phase is occupied in the pipe centre, while the liquid phase is flowing along the inner pipe wall, as shown in Figure 2-5.

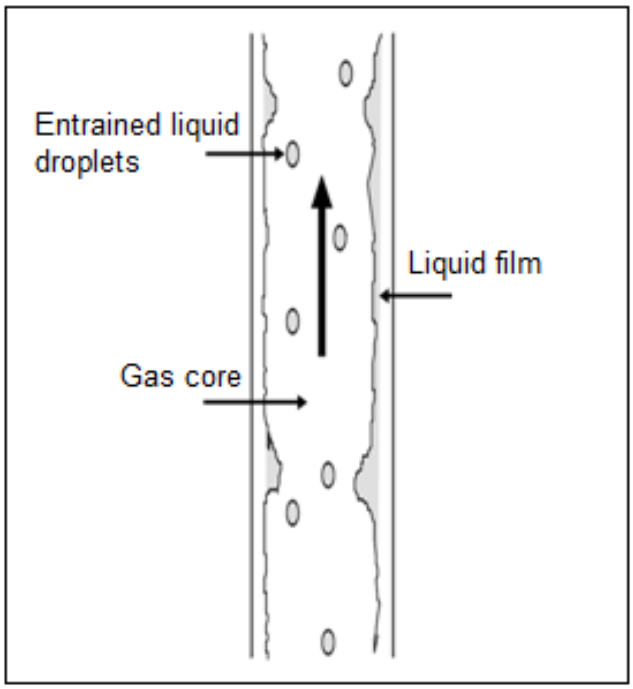

Figure 2-5 Vertical annular flow regime (Geraci, 2007)

Annular flow can be grouped based on the fluid flow directions to concurrent upward annular flow: both gas and liquid are flowing in an upward direction (Figure 2-6 (a)), concurrent with downward annular flow: both gas and liquid flow are flowing downward (Figure 2-6 (b)), and a counter current upward annular flow: gas flow is moving upward and liquid is flowing downward (Figure 2-6 (c)). Obviously, for a given liquid flow rate, counter current annular flow can only take place for a limited range of the gas flow rates. Outside of the range, the flow regime becomes either a concurrent upward flow or a concurrent downward flow, as illustrated in Figure 2-7. For a vertical pipe with a liquid film at a fixed liquid flow rate, increasing the gas upward flow rate gradually will change the flow regime from counter current annular flow to concurrent upward annular flow. The transition from downward to upward film flow is known as flooding. In upward concurrent annular flow, the reduction of gas flow rate will

lead to a counter current annular flow. The transition to downward liquid film flow is known as flow reversal. The transition between the counter current upward flow and concurrent downward flow is much simpler due to the gas direction reversing.

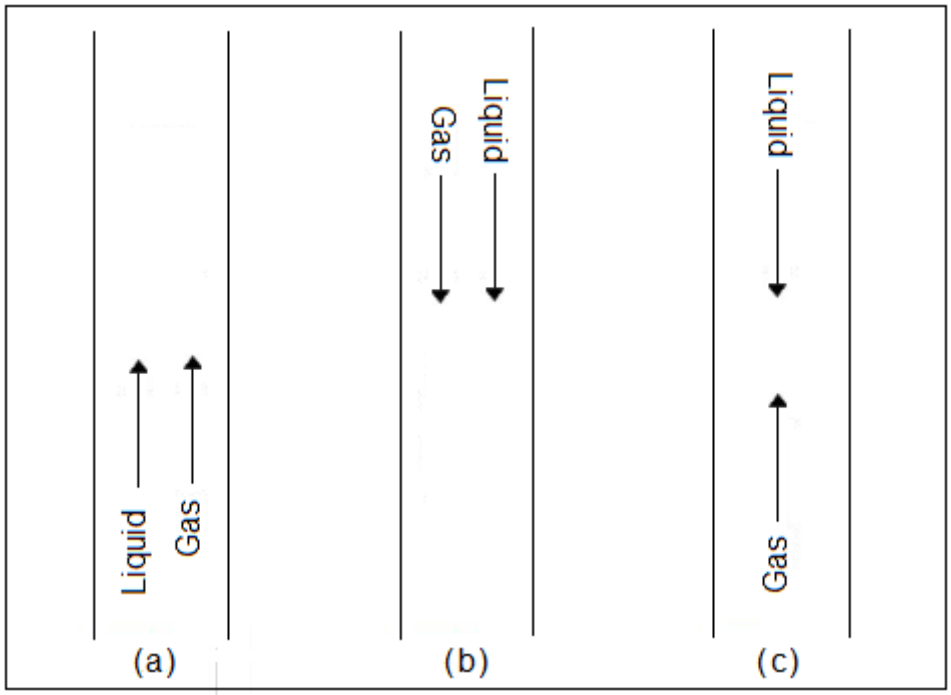

Figure 2-6 Annular flow types based on flow directions

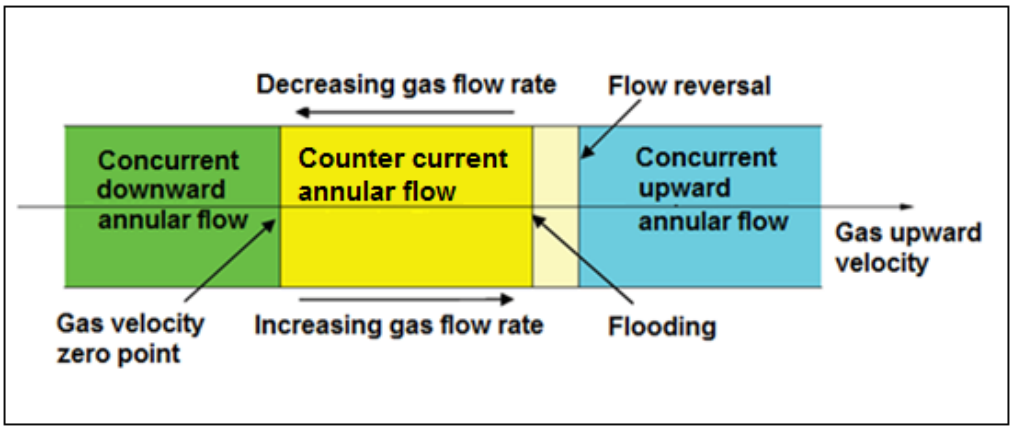

Figure 2-7 Transitions between the three types of annular flow

2.6.1 Annular flow development

Investigation of flow development is important in two-phase flow. Experimental work carried out by Omebere-Iyari et al. (2008), revealed that to reach a fully developed flow, the devices used to detect the flow behaviour need to be installed at (or greater than) 40 pipe diameters from the inlet point of liquid.

The behaviours of the two-phase flow in serpentine pipelines are changing when flowing through the bends. It is noteworthy that, the flow will still be developing after the bend (i.e. when entering a straight section of the pipe). This is due to the effect of the bend on the fluids that exist in the adjacent section. Hence the knowledge of two-phase flow development is essential in order to understand the phase distribution in the pipeline with serpentine geometry. As a major concern for the heat exchange facility operation, is closely related to the liquid film distribution on the pipe wall surface, thus the knowledge of the development related to annular flow regime is particularly important.

The development of gas/liquid annular flows has long been noted by a number of researchers, but so far most of them were on the upward flows. Gill et al. (1963) and Gill & Hewitt (1966) measured a film thickness and entrained droplets flow rate at different axial positions which ranged from 5-160 pipe diameters, downstream of gas-liquid injector, in a 31.8 mm pipe diameter. They also compared the results from different liquid injectors, namely porous sinter and axial jet injectors, and found that the liquid film thickness development in vertical annular flow largely depends on the inlet geometry when a low liquid mass flux is applied. Brown et al. (1975) extended the investigations above and conducted measurements of the pressure gradient and the entrainment rate obtained at distances up to 560 pipe diameters from the inlet. Similarly they also used porous sinter and centre jet devices. They found that, the differences between the two inlet devices persisted even at 550 pipe diameters indicating that, the flow was not yet fully developed. Hawkes et al. (2000) reported on experiments to study the development of wispy annular flow, with air and water mass fluxes of 70-210 kg/m^{2}s and 120-1030 kg/m^{2}s respectively. They observed that, the frequency of the wisps present in the gas core was ranged

from 5 to 8 Hz, and moved at a similar velocity of the gas phase. Wolf et al. (2001) reported on a study on the development of an air-water upward annular flow, giving local values of the pressure gradient, film thickness, wall shear stress, film flow rate, disturbance wave velocity and frequency. Lao et al. (2004) extended the flow conditions up to a liquid mass flux of 1200 kg/m^{2}s, using different liquid inlet devices. It was concluded that, at a high liquid mass flux, the effect of injecting on the film thickness of the wall was less significant than that at low liquid mass flux. More recently, Hazuku et al. (2008) reported the measurements of the interfacial wave structure development of upward annular two-phase flow in a vertical pipe using a laser focus displacement (LFD) technique. Experiments were conducted using a 3 m long, 11 mm diameter pipe, with Reynolds numbers ranging from 31,800 to 98,300 for the gas phase and 1,050 to 9,430 for the liquid phase. They found that the flow development persisted until the end of the pipe. Abdulkadir et al. (2012) experimentally studied the annular flow development, from a riser towards a downstream return bend and from the bend towards a downstream downcomer. They noted that, the average film thickness both in the downcomer and riser was different from that in the bend. As such it showed that, the two-phase flow develops both in and after the bend.

2.6.2 Interfacial waves behaviours

There are two types of interfaces in annular flows that have been reported in the literature. One exists between the moving fluids and the inner wall surface of the pipe, the other between the liquid and gas phases. In most cases of annular flows, the former was classified as a liquid film/pipe wall surface interface, i.e. liquid/solid interface; however, in a mist flow it can be a gas/solid interface. This section is about the gas/liquid interface.

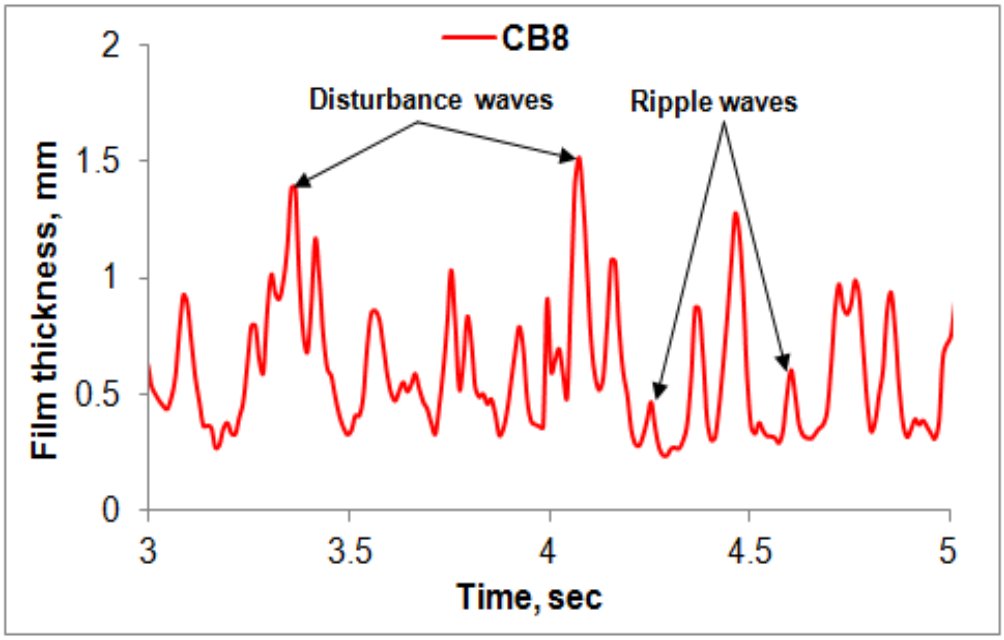

Figure 2-8 Interfacial waves in liquid film obtained from this study

The gas/liquid interfaces in annular flow can also be presented as one of the following two types or both: the interface between liquid film and gas, and interface between liquid droplets and gas, depending on whether liquid entrainment occurs or not.

The liquid film/gas interface is a fundamental problem in vertical annular flows. The interface is mainly attributed to the surface of the liquid film covered by waves. The waves are widely varied in their frequency and amplitudes, thus the wave pattern could be very complex. Generally, these waves are known as ripple waves, characterised by small wavelength and amplitude, and roll waves characterised by large wavelength and amplitude (Figure 2-8). A number of researchers such as Arnold and Hewitt (1967), Cousins and Hewitt (1968), Woodmansee and Hanratty (1969), and Azzopardi and Whalley (1980), have suggested that the roll waves are responsible for the occurrence of the majority of liquid entrainment in annular flows. Other types of waves were also observed, for example, a wave with a larger wavelength and amplitude, classed as a huge wave. This wave type was identified by Sekoguchi and Takeishi (1989). The occurrence of waves with large amplitude and small wavelength, in vertical annular upward flows in 31.8 mm diameter pipe was noted by Wolf (1995).

Bursts of waves with an even larger ratio of amplitude to wavelength in liquid film were observed by Badie et al. (2001).

It is worth noting that, in the liquid film, there may be the existence of another type of gas/liquid interface which is formed by gas bubbles that are moved in it. The gas bubbles may be entrained into the film from the gas phase moving in the central zone of the pipe (Hanratty and Woodmansee, 1965), or produced by evaporation due to heating on the pipe wall (Hewitt et al., 1965). This type of liquid/gas interface is of a particular importance in heat transfer processes.

However, in comparison with a considerable amount of investigation into the heat transfer characteristics of liquid film containing evaporation-produced bubbles, a relatively rare amount of work has been undertaken for the heat transfer characteristics of liquid film with entrained bubbles. The gas/liquid interfaces, or the gas/liquid structures in the central zone of the annular flows, are largely dependent on the liquid loading. For low liquid loading, the liquid phase in the core is presented as a gas/droplets mixture that is moved along the pipe. In general, there are two processes: some liquid droplets are entrained from the liquid film into the gas core, and are then deposited in the liquid film.

A number of variables, e.g. the liquid holdup, velocity profile and distribution of the droplets, are used to describe the core structures. Once the liquid loading is high enough, a substantial change in the core structure could occur. The liquid phase then appears as liquid lumps (termed “liquid wisps”) rather than as droplets, due to the agglomeration and break up processes in the liquid phase. These are accompanied by a very large instability in the core structures. This in turn leads to large fluctuations in the related variables, such as pressure gradient, liquid holdup and, inevitably, the heat transfer characteristics. The structure of wisps was observed for the first time by Bennett et al. (1965), by using an X-ray radiography technique (Figure 2-9 (a)). Lao et al. (2004) observed the waves caused by droplets hitting on and pinching off from the liquid film, by using a flash photo taken through a viewing section in an annular flow regime, as shown in Figure 2-9 (b).

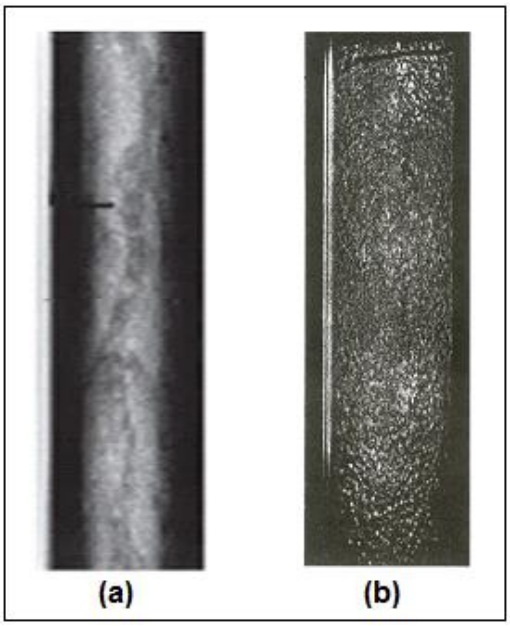

Figure 2-9 Structure of annular flow regime (a) core structure of wispy-annular regime (Bennett et al., 1965) and (b) waves on the liquid film caused droplet hitting and pinching off (Lao et al., 2004)

2.6.3 Liquid entrainment and deposition

In annular flows, part of the liquid flows in the form of film on the tube wall while the other part flows as entrained liquid droplets in the gas core. The liquid droplets in the core structure, are produced by entrainment (or atomisation) while being deposited back into the liquid film, thus leading to a continuous exchange of mass, momentum, and energy between the liquid film and the core structure. The ratio of the liquid mass flow rate existing in the gas core in droplet form, to the total liquid mass flow rate, is defined as the liquid entrainment fraction (also termed liquid entrained fraction). There are three types of mechanisms by which the liquid film is entrained into the gas core in a vertical annular flow:

(a) Entrainment by roll wave (or disturbance wave): this entrainment is caused by the breakdown of waves. There are two mechanisms of breakdown of the wave: undercutting and rolling, as shown in Figure 2-10 (a) and (b) respectively.

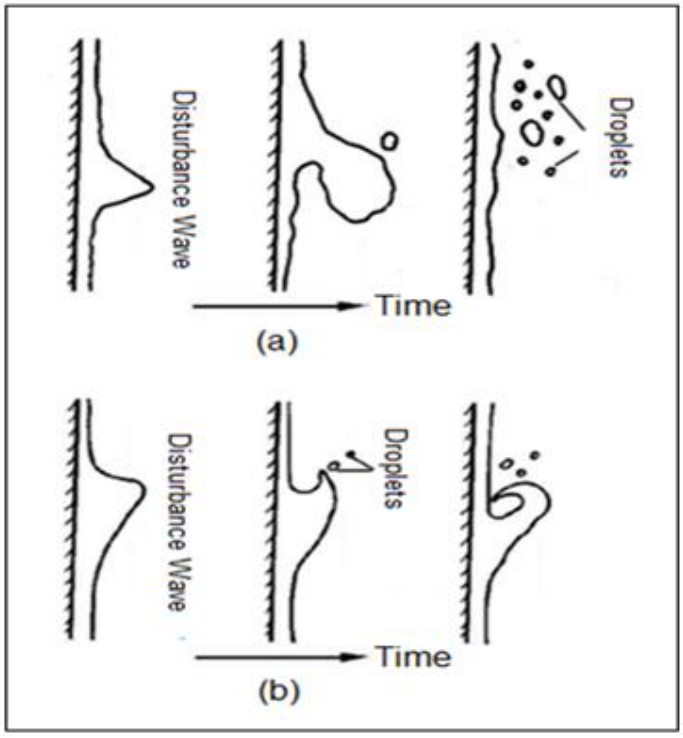

Figure 2-10 Mechanisms of entrainment by (a) wave undercutting and (b) wave rolling (Hewitt and Hall-Taylor, 1970)

(b) Entrainment by bubble release: The bubble bursts on the surface of the liquid film leading it to produce and transfer the droplets into the pipe centre. The mean size of these droplets is usually very small, in the order of 1 mm (Newitt et al., 1954).

(c) Entrainment by droplet impingement: This entrainment type was identified by Woodmansee and Hanratty (1969), who proposed that the ripples riding on top of the disturbance waves are removed by the incoming gas stream causing entrainment. Their study was based on using a high-speed photographic camera.

It is widely accepted that, the disturbance wave entrainment is the most dominant liquid entrainment mechanism, while other two types are generally neglected. This fact was supported by the experimental work conducted by Azzopardi and Whalley (1980). They produced artificial disturbance waves and observed the flow at the top position of the pipe, by means of a high speed cine camera used in conjunction with a special axial viewing device. They noted that,

the droplets were not able to form when the waves were not present. The droplets were only identified after the injection. The number of these droplets was increased as the waves approached the end of the pipe. Once the waves passed out, no droplets were observed. For a fully developed annular flow it is reasonable to assume that the entrained fraction is constant, due to a dynamic equilibrium between entrainment and deposition of the droplets.

The interchange of droplets between the liquid film and core structure, is significantly important both for the fundamental and practical aspects of annular flow studies. Cousins and Hewitt (1968) proposed that the deposition rate (D) of the annular flow can be expressed as:

$$D = kc \qquad \textbf{(2-1)}$$

Where k is the mass transfer coefficient and c is the droplets concentration in the core structure. Further studies, e.g. Namie and Ueda (1973), and Govan (1990), showed that k is dependent on concentration c.

2.6.4 Effect of pipe diameter on vertical flow

2.6.4.1 Introduction

A considerable number of researchers have reported that, the behaviours of two-phase flow in vertical pipe and the flow's characteristics very much depend on the pipe diameter. The detailed literature review covering the major effects of this parameter on such a flow was one of the main objectives of this study.

Wallis (1969) assumed that pipe diameter has a significant impact on a two-phase vertical flow. The following equations were used in the assumption:

$$Re = \frac{\rho U D}{\mu} \qquad \textbf{(2-2)}$$

$$\mathrm{Fr} = \left[\frac{\rho \mathrm{U}^2}{\mathrm{D}g(\Delta\rho)}\right]^{\frac{1}{2}} \qquad \textbf{(2-3)}$$

$$\mathrm{Bo} = \frac{\mathrm{D}^2 g\,(\Delta\rho)}{\sigma} \qquad \textbf{(2-4)}$$

Where Re, Fr and Bo are the Reynolds, Froude and Bond numbers respectively, ρ, U and μ are fluid density, velocity and viscosity respectively, $\Delta\rho$ is the density deference between gas and liquid, D is the pipe diameter, g is the gravitational acceleration and σ is the surface tension.

The above dimensionless parameters are related to the diameter of the pipe (D). From the experimental perspective, the flow regimes were observed to significantly vary with pipe diameter. Experiments on gas-liquid two-phase flows in mini scale pipe showed that, the pipe inclination has little effect on the flow regime formation and there was no stratified flow present, even in a horizontal tube, thus the flow regime map could be based on pipe diameter, rather than being tube orientation dependent (Serizawa and Feng, 2002). On the other hand, with large diameter vertical pipe, studies showed the dissipation of conventional slugs in upward gas-liquid flows, e.g. Omebere-Iyari et al. (2007), and Ali and Yeung (2008). Cheng et al. (1998) also noted that, instead of the traditional slug flow in the 150 mm i.d. column, there is a very gradual transition to a type of churn flow as the gas rate is increased.

2.6.4.2 Effects of pipe diameter on annular flow formation

Gas flow rate associated with flow flooding or reversing is significantly influenced by the transition between churn and annular flows. The transition occurs either by decreasing or increasing the gas velocity. The transition gas velocity, pipe diameter and flow conditions need to be well defined. However, it was also found that the accurate value of the transition gas flow rate is dependent on how liquid can be introduced into the system, because the transition corresponds to zero wall shear stress (Hewitt and Hall-Taylor, 1970).

Table 2-1 presents a number of results related to the effect of pipe diameter on the transition between churn and annular vertical flows. Some of these results were also represented by plotting the transition gas velocity against the pipe diameter, as illustrated in Figure 2-11 (a) and (b).

Source	i.d., mm	Ust, m/s	Method
Nicklin and Davidson (1962)	31.8	9.5	Flow reserving
Bashforth et al. (1963)	31.8	9.5	Flooding
Pushkina and Sorokin (1969)	6.2	14.5	Flooding and flow reserving
	8.8	14.5	
	9	15	
	13	15	
	13	16	
	30.2	15.5	
Wallis (1969)	22.2	11	Flooding
Wallis and Makkenchery (1974)	19	7	Flow reserving
	38	10.3	
	51	11.5	
	64	10.9	
	76	10.2	
	89	10.7	
	100	9.4	
	140	6.5	
Hewitt (1977)	31.8	9.4	Flooding
	31.8	11.8	
Imura et al. (1977)	11.2	9	Flooding
	16	9.5	
	21	9.5	
Suzuki and Ueda (1977)	10	11	Flooding and flow reserving
	18	11	
	28.8	12	
Taitel et al. (1980)	51	15	Flooding
Richter (1981)	25.4	8.3	Flow reserving
	50.8	11.8	
	152	14.2	
	254	15.1	
Barnea et al. (1982)	4	15	Flooding
Govan et al. (1991)	31.8	11.3	Flooding
Vijayan et al. (2001)	25	2~4.3	Flooding
	67	9~13	

Table 2-1 Data collected from literature related to the effect of pipe diameter on the transition of churn/annular vertical flows. Fluids are air and water

The transition velocity of gas was measured by flow reversing and flooding methods, as shown in Figure 2-11 (a) and (b) respectively. It is important to mention that, there were a few discrepancies about the pipe diameter effects on the transition velocity.

Pushkina and Sorokin (1969), who applied the reversing method, observed that the pipe diameter represented only a very moderate effect on the transition velocity. Wallis and Makkenchery (1974) obtained a maximum gas superficial velocity of 11.5 m/s using 51 mm diameter pipe. They identified that, the transition velocity is decreased to 6.5 m/s, when the pipe diameter increased to 140 mm. Richter (1981) who also used a flow reversing method, stated that there is a positive correlation between the transition velocity and pipe diameter (D), as presented in Figure 2-11 (a). For a particular diameter, when the flooding method was used, the transition velocity scattered over quite a wide range, as shown in Figure 2-11 (b). An extreme case was that reported by Vijayan et al. (2001) who used 25 mm diameter pipe; they observed the lowest transition velocity, which was at 3 m/s. On the other hand, Wallis (1969) noted that the transition velocity could reaches 11 m/s for the same pipe diameter namely, 25 mm. However, if neglecting this exceptional case, the data from the flooding method present an appreciable tendency for the transition velocity to increase with an increase in pipe diameter. Nevertheless, it seems that the flow regime transition boundaries obtained by a number of researchers were considerably different. Hewitt and Hall-Taylor (1970) pointed out this phenomenon could occur as a result of film instabilities from different liquid injection methods. They suggested that, the minimum pressure gradient method would give more definitive results for the transition gas velocity. It is widely accepted that, the transition velocity maybe slightly affected by the liquid flow rate. However, investigations such as those of Karimi and Kawaji (2000), Vijayan et al. (2001), and this study, found that there is an appreciable effect of liquid loading on the flow regime transition. Ignoring the effect of liquid flow rate may be attributed to the discrepancies between the previous studies.

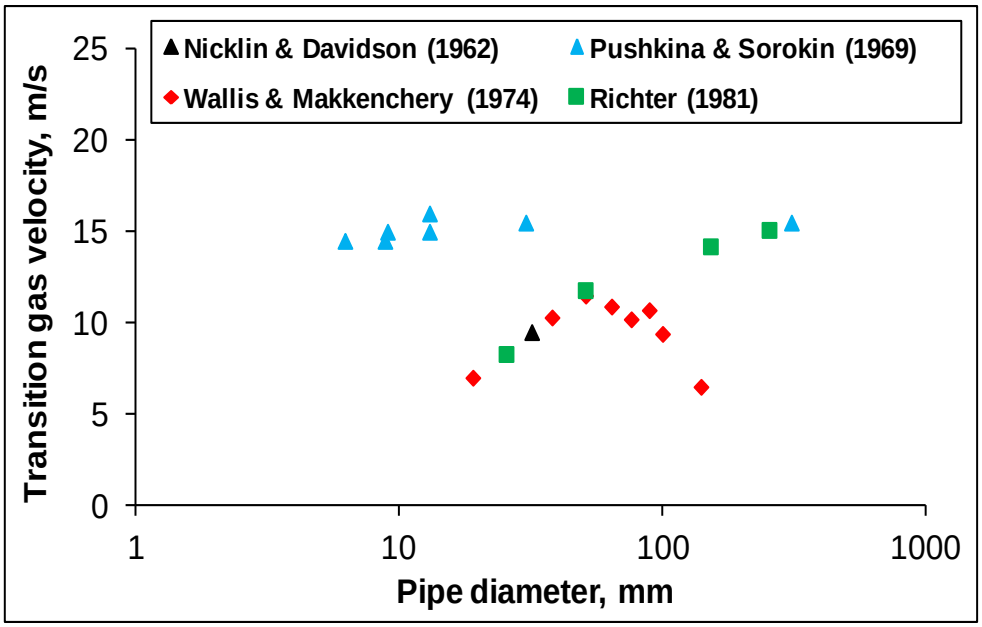

(a)

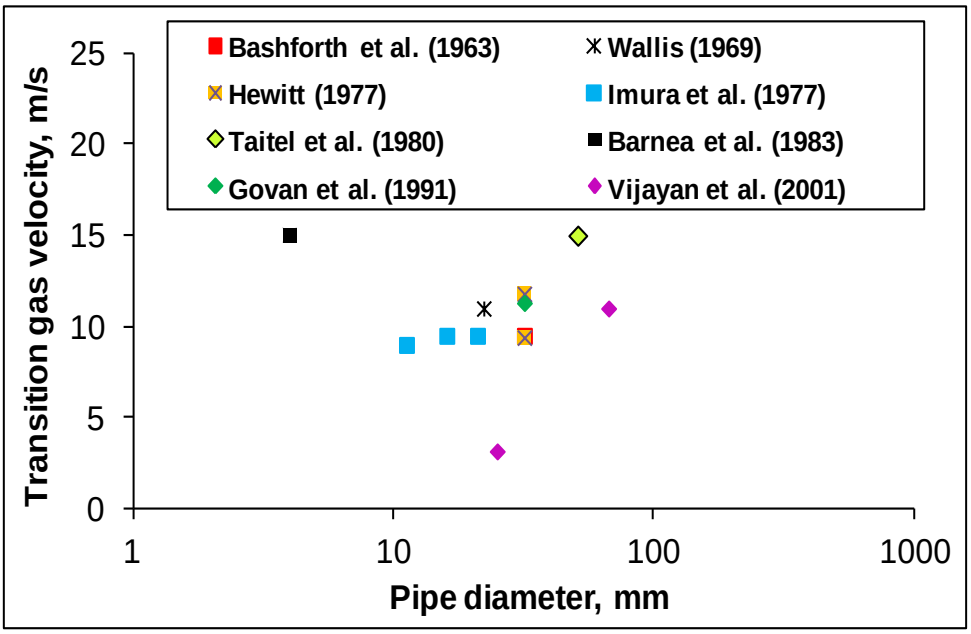

(b)

Figure 2-11 Effect of pipe diameter on the transition gas velocity, (a) reversing method and (b) flooding method. (Fluids are air and water)

The arguments mentioned above are also reflected in the correlations reported by many researchers to predict the flow regime transition. A number of correlations are available in the literature to predict the transition gas velocity, at which flow regime transition may occur for a certain flow conditions. Wallis

(1961), and Hewitt and Wallis (1963) developed a correlation based on modified Froude numbers of gas and liquid, which takes the following form:

$$\mathrm{Fr}_{\mathrm{G}}^{0.5} + C_1 \mathrm{Fr}_{\mathrm{L}}^{0.5} = C_o \quad \textbf{(2-5)}$$

Where Fr_{G} and Fr_{L} are the modified Froude numbers of gas and liquid, respectively, which can be obtained using the superficial velocities and densities of gas and liquid. C_0 and C_1 are constants which are in the order of unity.

Taitel et al. (1980) considered the onset of liquid droplets entrainment in the gas core based on a modified Kutateladze number, and derived an equation to predict the minimum gas velocity required to suspend a droplet. The equation was based on a balance between gravity and drag forces on a liquid drop. Their study led to the definition of the following criterion for predicting the transition gas velocity.

$$\mathrm{Ku}_{\mathrm{G}} = 3.1 \quad \textbf{(2-6)}$$

Where the Kutateladze number $(\mathrm{Ku}_{\mathrm{G}})$ can be expressed as:

$$\mathrm{Ku}_{\mathrm{G}} = \frac{\mathrm{U}_{\mathrm{G}} \rho_{\mathrm{G}}^{0.5}}{(\sigma g \Delta\rho)^{0.25}} \quad \textbf{(2-7)}$$

Sun (1979) had already used modified Kutateladze numbers to develop the following correlation:

$$\mathrm{Ku}_{\mathrm{G}}^{0.25} + m_1 \mathrm{Ku}_{\mathrm{L}}^{0.25} = m_0 \quad \textbf{(2-8)}$$

Where m_1 and m_0 are constants and Ku_{L} is the Kutateladze number for the liquid which can be calculated using the following correlation:

$$\mathrm{Ku}_{\mathrm{L}} = \frac{\mathrm{U}_{\mathrm{L}} \rho_{\mathrm{L}}^{0.5}}{(\sigma g \Delta\rho)^{0.25}} \quad \textbf{(2-9)}$$

Bi and Grace (1996) suggested that, the transition gas velocity can be simply estimated by letting $Fr_L = 0$. It can be concluded that, the equation is mainly concerned with the buoyancy/inertia balance for the occurrence of flow regime transition, by using the Froude number. However, at a high liquid flow rate the $C_1 Fr_L$ in equation (2-5) becomes large. As a result, the correlation needs to be modified. Otherwise Fr_G becomes very small or even negative, which is incorrect.

On the other hand, equations (2-7) and (2-9) take into account the drag and gravity balance, that is related to the droplets as the principal mechanism of the transition between churn and annular flows. But they neglected the buoyancy in the flow system due to the pipe diameter. Many efforts were made to combine both mechanisms into one correlation, in order to predict the flow regime transition. For instance, Richter (1981) and Jayanti et al. (1996) noted from different arguments that, the Froude number-based correlation can work well for small diameter pipes, while the Kutateladze number was recommended for a large diameter pipe. An alternative equation was proposed by Richter (1981), which includes the effects of both column diameter and surface tension. This was expressed as follows:

$$\mathrm{Ku}_{\mathrm{G}}^{2} = -75\,[1 - (1 + D^{*2}/75/\ C_w)^{\frac{1}{2}}]/D^{*} \qquad \textbf{(2-10)}$$

Where the Bond number (D^{*}) can be defined as: $D\,(\frac{g\Delta\rho}{\sigma})^{\frac{1}{2}}$ and C_w is the wall friction factor which is approximately equal to 0.008. It is important to mention that, this correlation did not include the effect of liquid flow rate on the flow regime transition.

McQuillan and Whalley (1985) compared the performance of several empirical and semi-empirical correlations with a data set compiled from the literature. They commented that among the empirical correlations, that of Alekseev et al. (1972) performs the best. The correlation takes the following form:

$$\mathrm{Ku}_{\mathrm{G}} = \ C_t \mathrm{Fr}^{-0.22} \mathrm{Bo}^{0.26} \qquad \textbf{(2-11)}$$

Where C_t is a constant, Fr and Bo are the modified Froude and Bond numbers respectively. The modified Froude number was expressed as:

$$\mathrm{Fr} = \frac{Q_L g^{0.25} \Delta\rho^{0.75}}{\sigma^{0.75}} \quad \textbf{(2-12)}$$

Where Q_L is the liquid volume flow rate per wetted perimeter length, m^2/s and the Bond number can be calculated using equation (2-4) above. It can be seen that this correlation also considered the effect of liquid flow rate, in addition to the pipe diameter and liquid surface tension. Therefore this correlation can be used to calculate the transition gas velocity.

2.6.5 Liquid film development

2.6.5.1 Introduction

In many industrial operations concerning annular flow, determining the flow characteristics is essential for improving system performance or ensuring safety. For instance, in a large cracking furnace in a refinery, good knowledge of the liquid film behaviour is important in avoiding catastrophic burnout in heated furnace tubes. Therefore, a considerable number of researches have been undertaken to gain a better understanding of liquid film behaviour. From the previous literature survey, there has been several measurement techniques for liquid film thickness and these have been classified as film average, localised, and point methods.

For the current study, conductance film thickness probes were used and they fall under the localised methods category. Geraci (2007) reported that, conductance probes are the most common devices to be used in measuring the time varying film thickness, and are particularly good for fluids of highly differing conductivities, e.g. air and water. Basically, a circuit containing a pre-determined electrode configuration is used to measure the conductance, and then the output device is used to amplify and display the readings. A calibrated linear relationship can be established between the two parameters, within the range of measurements in order to obtain the film thickness data.

2.6.5.2 Effect of injection devices on liquid film development

Previous experiments showed that the behaviours of liquid film, e.g. the mean film thickness and the wave structure were changed significantly during flow development. In addition the behaviours appear to be related to the method of introducing the flow.

Gill and Hewitt (1966) reported the axial development of the mean film thickness in a 31.8 mm pipe, with the mass fluxes of water and air of 160 kg/m^{2}s and 80 kg/m^{2}s respectively. Figure 2-12 (a) and (b) illustrates the centre jet and porous sinter injectors respectively. With the centre jet, all the liquid was introduced into the pipe centre. The film thickness was about 0.04 mm at the axial position of 5 pipe diameters from the injection point and reached 0.2 mm, at the axial position of 30 pipe diameters. With the porous sinter injector, all liquid was introduced in the form of a liquid film. The film thickness was about 0.41 mm at the axial position of 8 pipe diameters from the injection point, and reached 0.32 mm at the axial position of 60 pipe diameters. Considerable difference of film thickness was observed even after 160 pipe diameters, in the results of the two injectors. This suggests that, the flow was not developed on reaching this axial position. This conclusion was also confirmed by Brown et al. (1975).

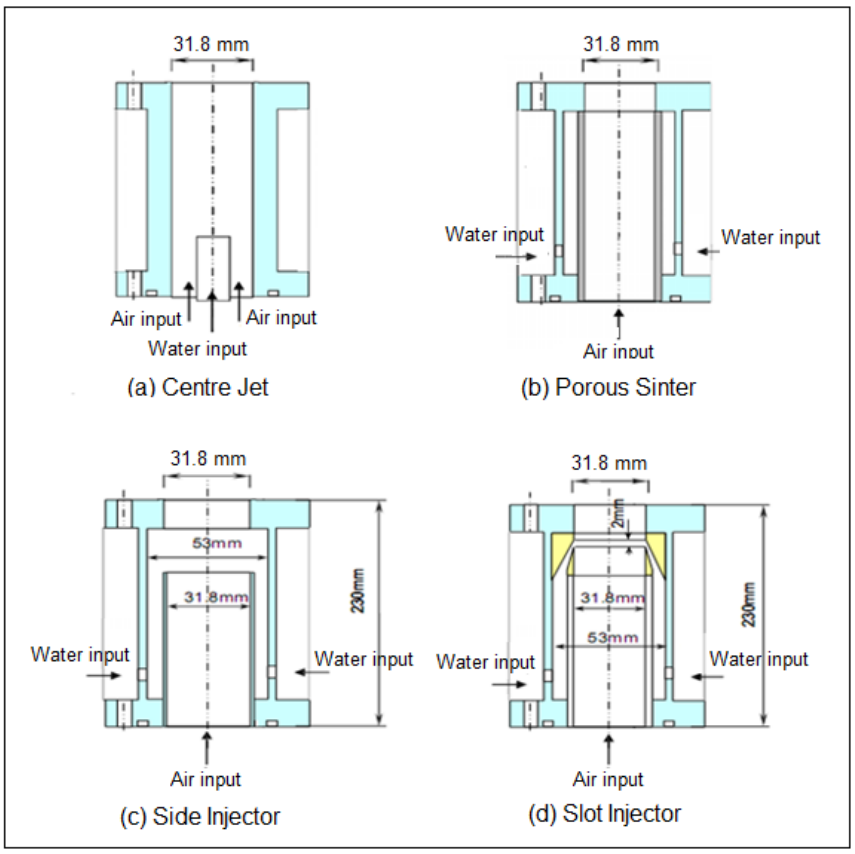

Figure 2-12 Geometries of injectors (a) and (b) for Gill and Hewitt (1966) and (c) and (d) for Lao et al. (2004)

However, the flow development at higher mass fluxes seems less sensitive to the injection device. Lao et al. (2004) reported experimental results using three different injection devices. In addition to porous sinter (Figure 2-12 (b)), they also used side and slot injectors, as shown in Figure 2-12 (c) and (d) respectively. The results for the variation of liquid film thicknesses, with air mass flux at the height of 3.51 m (axial distance of 110 pipe diameters from the inlet) are illustrated in Figure 2-13. Different curves in each panel of the Figure 2-13 correspond to different inlet geometries. The increase of air mass flux and/or water mass flux, led to a considerable reduction in the differences between the curves that were obtained by using different liquid injection devices.

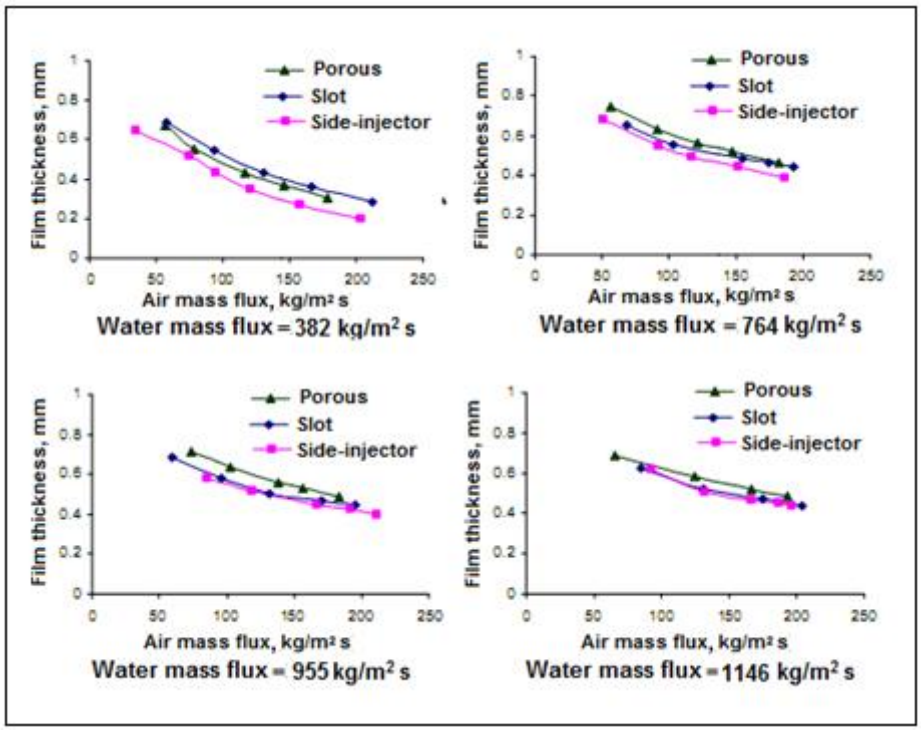

Figure 2-13 Variations of the liquid film against the air mass flux for water mass fluxes of 382, 764, 955 and 1146 kg/m^{2}s respectively (Lao et al., 2004)

2.6.6 Wave structure of liquid film

Wave structure has been studied by a number of researchers. Among them were Wolf et al. (2001) who noted that, the mean film thickness varies over a wider range than the other parameters. They found that the disturbance waves were not formed at the inlet, but took a finite distance to develop. Power spectra of the film thickness measured at various distances from the inlet (Figure 2-14) show that, the maximum intensity of wave component at 1.6 pipe diameters is only about a fifth of that at other distances. Disturbance waves were formed after 10 pipe diameters from the inlet, and the intensity decays from a distance of 120 pipe diameters. This was confirmed by Lao et al. (2004) who obtained their results using different injectors, as mentioned above.

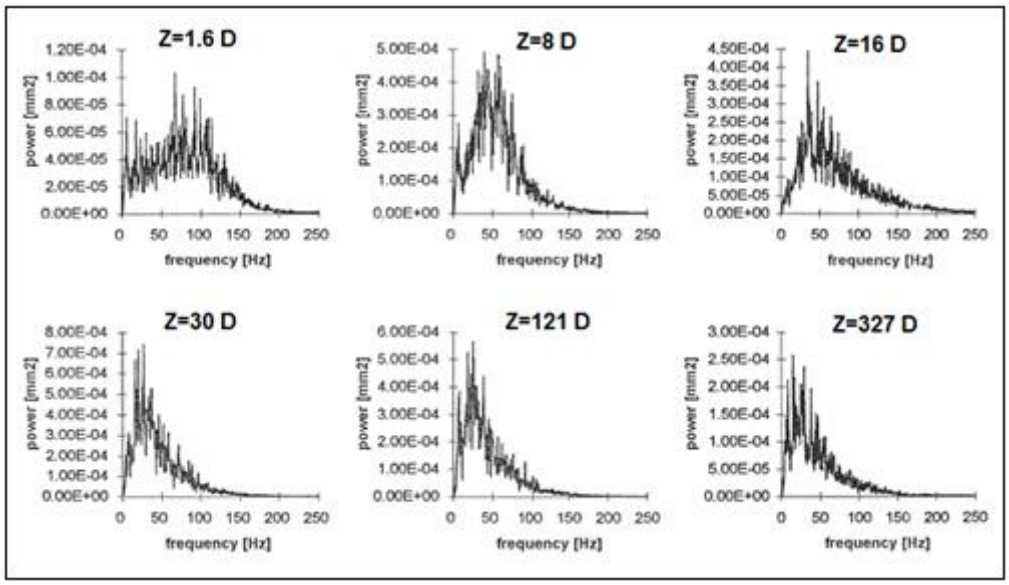

Figure 2-14 Power spectra of film thickness variation carried out by Wolf et al. (2001) for air flow rate of 71 kg/m^{2}s and water flow rate of 20 kg/m^{2}s at axial distances of 1.6, 8, 16, 30, 121 and 327 pipe diameters from the water inlet

The probability density functions (PDFs) of film thickness corresponding to the above cases are given in Figure 2-15. At a distance of 1.6 pipe diameters from the water inlet, the liquid film did not show large fluctuations. When the flow reached 8 pipe diameters from the water inlet, the height of the liquid film increased significantly. As a result, large waves (classified as disturbance waves) were formed, and the probability density function began to exhibit a well-defined peak corresponding to the thickness of the substrate between two successive disturbance waves (Jayanti and Hewitt, 1992). It was observed from the plots that, the probability values of the peak and the disturbance waves were increased with the growing distance from the water inlet. Thus, the interfacial structure takes a fairly short distance, of the order of 50-100 pipe diameters, to develop completely. The pattern will stay fairly stable once the wave structures are developed.

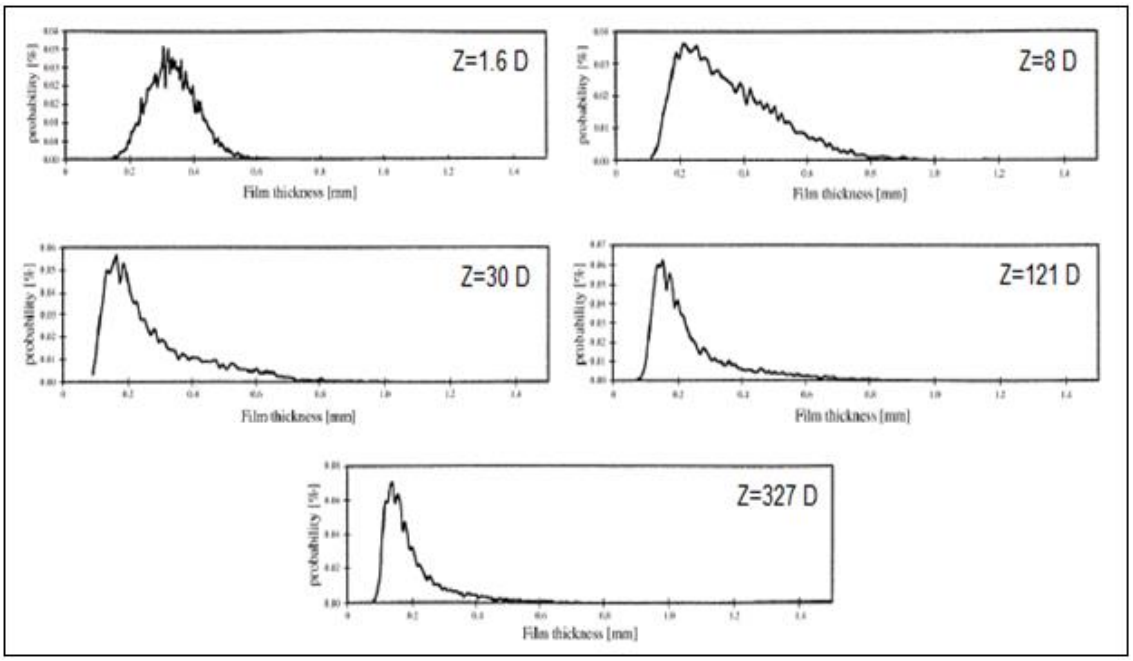

Figure 2-15 Probability density functions (PDFs) of the film thickness for the cases presented in Figure 2-13 (Wolf et al., 2001)

Precise measurements of the liquid film thickness revealed that, the minimum level of thickness signals with different flow conditions, remains quite stable even at a fairly small distance from the liquid injection point. The variation of the maximum, mean and minimum of film thickness along the axial position of the pipe reported by Hazuku et al. (2008) is illustrated in Figure 2-16. They used a laser focus displacement (LFD) technique, in order to measure the interfacial wave of the liquid film. The uncertainty of the measurement was claimed as less than 1%. The experiments were conducted using a 3 m long, 11 mm diameter pipe. They noted that, in contrast to the considerable decrease in maximum thickness with the increase of axial distance from the injection point, the minimum thickness remains almost constant. This behaviour may suggest that, the minimum film thickness in vertical upward annular flows is not dominated by flow conditions when low liquid loading is used.

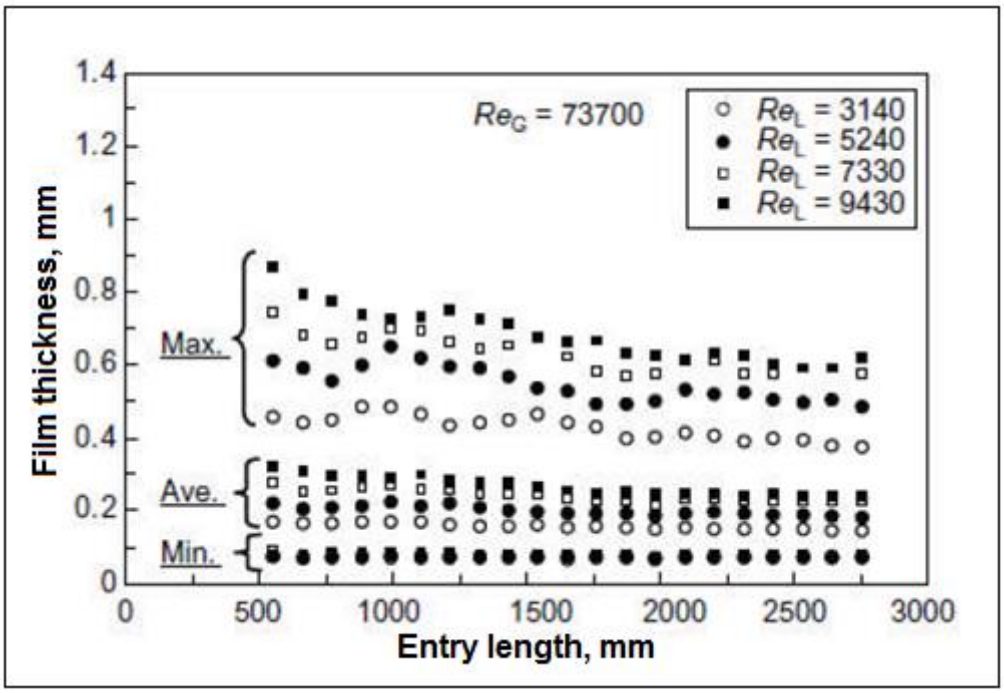

Figure 2-16 Axial development of maximum, mean and minimum film thickness (Hazuku et al., 2008)

2.6.7 Entrainment development of liquid droplets

A few directly measured entrained droplet flow rate data related to flow development were available. Amongst them are Gill et al. (1963), Gill and Hewitt (1966), and Wolf et al. (2001). All of them measured the liquid film flow rate by a sucking method, using a porous sinter section, and derived the entrained droplet flow rate by deducting the film flow rate from the known total liquid flow rate. This method is widely accepted as a reliable and accurate one for annular flows with low liquid flow rate. The development of entrainment is closely interrelated with the development of liquid film thickness. Gill and co-workers' results show that, the amount of liquid flowing as an entrained droplet flow rate is very sensitive to the method of liquid injection. They found that even after 160 tube diameters, the entrained droplet flow rate with porous sinter injector was still only 60% of that with a centre jet injector.

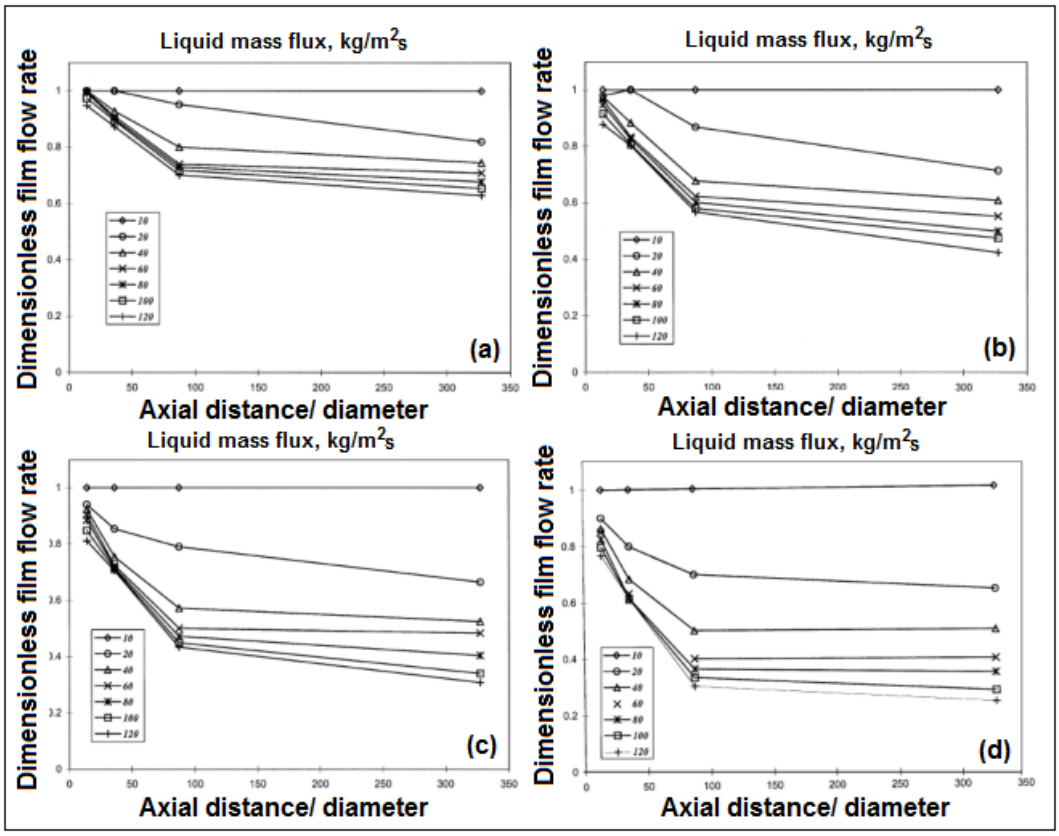

Figure 2-17 Axial development of film flow rate for air mass flux (a) 71, (b) 97, (c) 124 and (d) 154 kg/m^{2}s and for different liquid mass fluxes (Wolf et al., 2001)

Wolf et al. (2001) reported the effect of the flow rates of gas and liquid on the development of vertical annular flow, as illustrated in Figure 2-17. The film flow rate was used to symbolise liquid entrainment. It was as expected that for the lowest water mass flux of 10 kg/m^{2}s, there was no entrainment and hence the dimensionless film flow rate remains constant in all the plots. For other flow rates, it decreases rapidly with Z/D – the decrease being more rapid as the water/air flow rate increases further. The dimensionless film flow rate shows much less variation between 100 and 300 pipe diameters. This means that, hydrodynamic equilibrium of the film flow (deposition rate equals entrainment rate) was nearly established within the first 100 pipe diameters at the highest air flow rate. At lower air fluxes significant differences in the film flow rate persist between 100 and 300 pipe diameters, thus indicating that the flow was not yet fully developed. This was consistent with the results of Gill et al. (1963) who used air and water fluxes of 80 and 160 kg/m^{2}s.

2.7 Local void fraction distributions

Studies on local gas void fraction distribution have been considered over the last 50 years. Figure 2-18 shows an experimental work conducted by Malnes (1966), for local distribution of void fraction at lower and higher positions along the pipe. The measurements were carried out for a bubbly flow regime. He observed that, the void fraction varies over the gas superficial velocity range. Higher void fraction was observed close to the pipe wall than at the pipe centre, for lower and upper measuring points. However, a centre peak was observed for the upper measuring point when the gas velocity increased to 0.5 m/s.

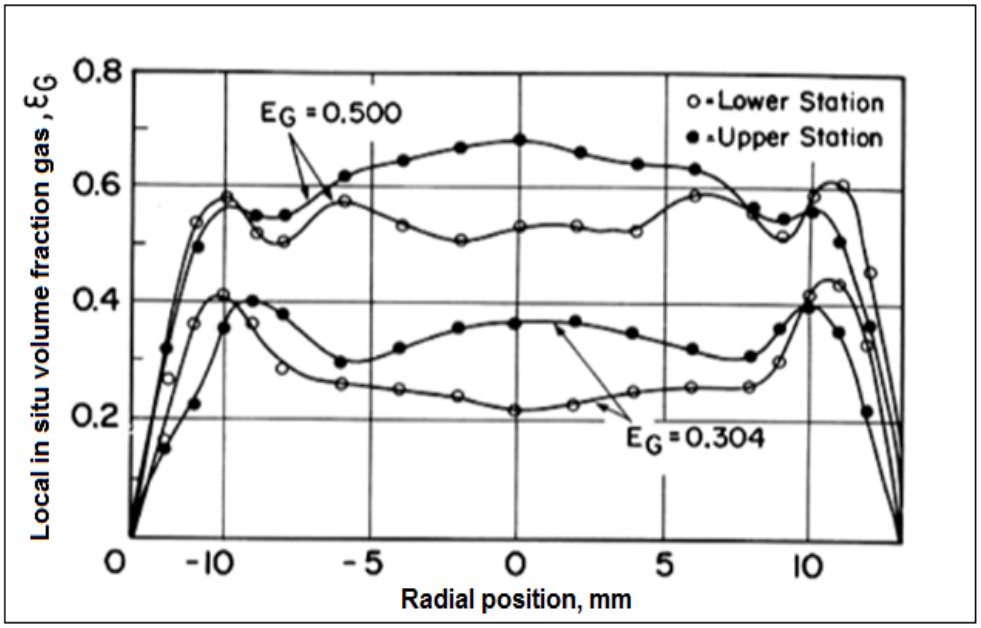

Figure 2-18 Gas volume fraction distributions in bubbly flow (Malnes, 1966)

Observations by Wang et al. (1987) showed that, wall peak occurred for the fluid flows in an upward orientation, while a core peak was observed in the case of downward orientation. Similarly, Serizawa and Katoaka (1988) experimentally studied the distribution of local void fraction in the region of bubbly flow (Figure 2-19). They reported that, the air distribution shows different profiles for different gas and liquid flow rates, which was in tandem with the observations of both Malnes (1966) and Wang et al. (1987). In addition, Serizawa and Katoaka (1988) observed that, the void fraction values on the pipe wall became higher

(wall peak) than at the other part of the pipe's cross section, when a higher gas velocity shifted towards the pipe wall. Intermittent and slug peaks were formed when increasing the gas flow rate gradually. Further increases in the gas flow rate led to high void fraction in the pipe centre (classified as centre peak). Experimental work carried out by Liu and Bankoff (1993) shows that the gas void fraction distribution is partial, depending on the shape and size of bubble, particularly for low liquid velocities. The observed wall peak was attributed to the influence of bubbles that moved close to the pipe's wall.

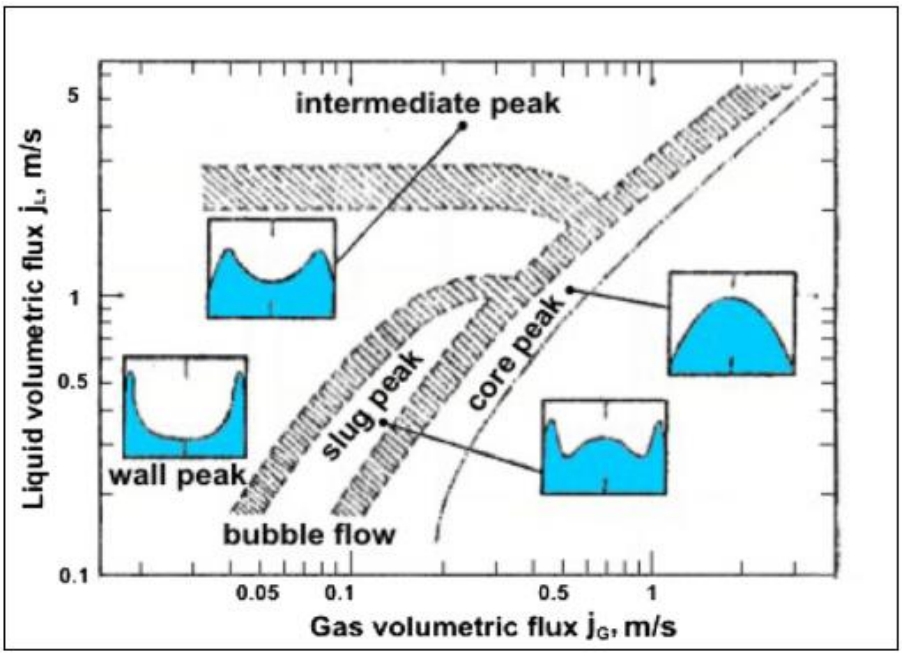

Figure 2-19 Patterns of void fraction distributions (Serizawa and Katoaka, 1988)

More recently, Olerni et al. (2013) made a comparison in terms of gas void fraction distribution between their work and those presented above using a 16 × 16 wire mesh sensor (WMS), as illustrated in Figure 2-20. The comparison was made for a wide range of gas superficial velocity, and for constant liquid superficial velocity of 1.039 m/s. They found that their work was consistent with the corresponding previous studies. However, they noted that the void fraction profile observed was not in complete agreement with the other investigators' work. This was attributed to dissimilarity of the WMS's sampling resolution and pipe diameter between both studies.

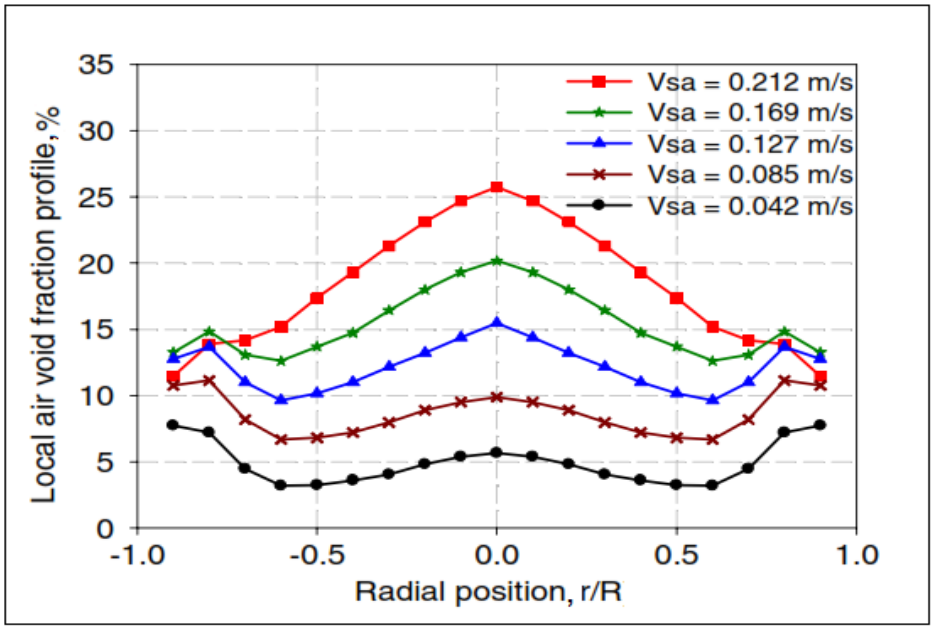

Figure 2-20 Local distributions of gas void fraction obtained from WMS for liquid superficial velocity of 1.039 m/s (Olerni et al., 2013)

Olerni et al. (2013) also observed that, the void fraction profile shifted from wall peak to centre peak as the gas velocity increased to higher values. Further comparison was made using the electrical resistance tomography (ERT) technique, as illustrated in Figure 2-21. They found that, the ERT did not show clear details in respect of the void fraction distribution near the pipe wall. Also, they identified that, the void fraction profile was different in both studies for low gas superficial velocity, which they attributed to the limitations in the back-projection algorithm employed to generate the images.

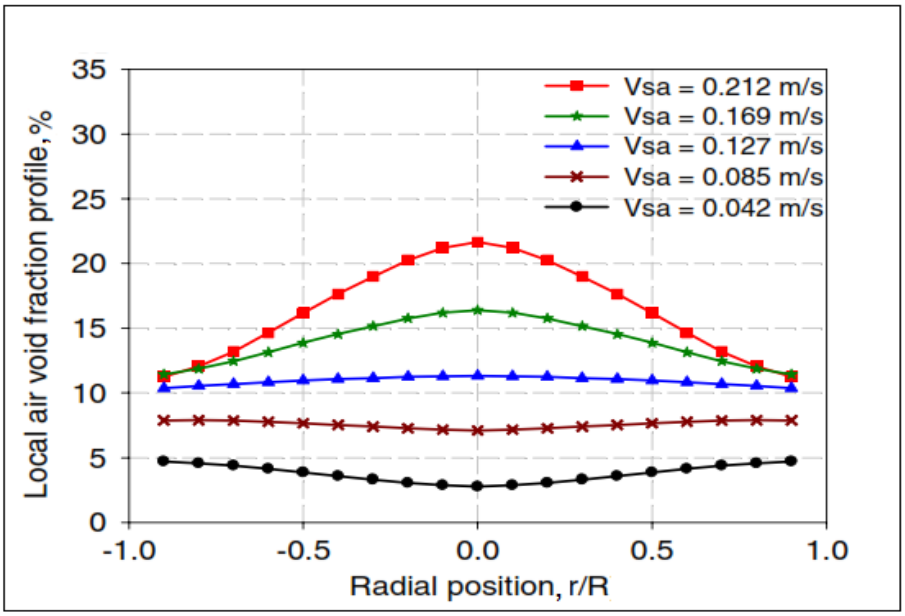

Figure 2-21 Local distributions of gas void fraction obtained from ERT for liquid superficial velocity of 1.039 m/s (Olerni et al., 2013)

2.8 Conclusions

From the above, the following conclusions were drawn:

- The axial development of vertical annular flow, is largely dependent on the inlet geometry (liquid injector) when low mass fluxes of liquid and gas are used. Most of the previous studies on the annular flow development, were concerned with upward concurrent flows and liquid injection methods. Increase of both the liquid and gas fluxes will dampen the effect of inlet geometry on flow development.
- The interfacial wave structure showed only a small variation between Z/D of 100 and 300. For a gas mass flux higher than 150 kg/m^{2}s, there was little variation after 100 pipe diameters.
- Entrained droplet flow rate development was very much dependent on the air mass flow rate.
- It is worth noting that, as far as the author aware, very few, if any at all, investigations on the bend effects on either upward or downward annular flow development, in pipes with a diameter over 100 mm have been publicly

reported. Therefore, the current study has been conducted to clarify the impacts of the bend on the flow behaviour in vertical pipes with serpentine configurations.

3 Test facility and instrumentation

3.1 Description of the Serpent rig

A purpose-built rig, the Serpent test facility, is designed and set up in the Flow Laboratory at Cranfield University. The rig (schematically shown in Figure 3-1), is comprised of the fluid supply and metering section, the test section and the fluid separation section.

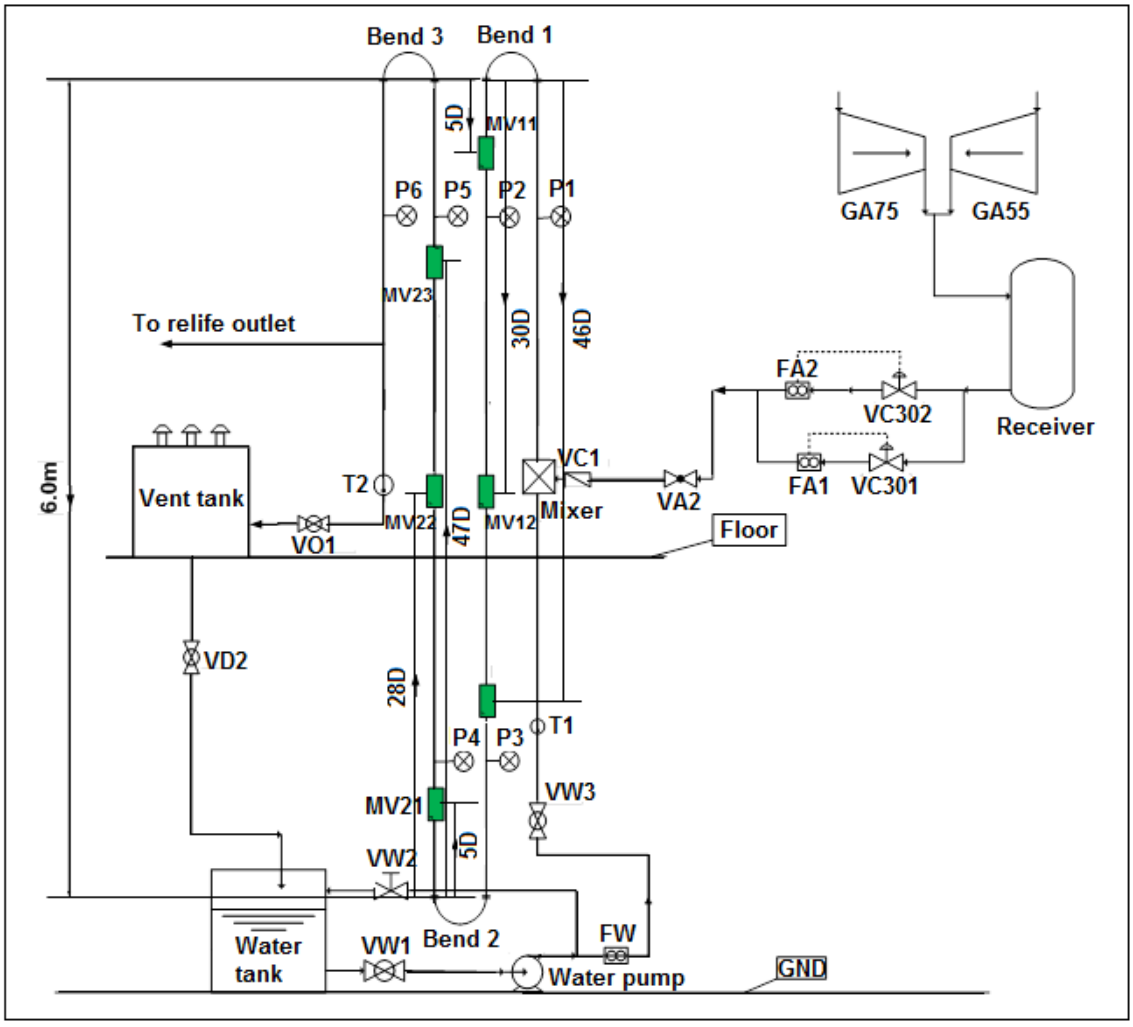

Figure 3-1 Schematic of the Serpent rig

3.1.1 Test section of the Serpent rig

The test section consists of a flow loop of about 20 m long in total, 101.6 mm diameter pipe which includes four vertical sections connected by three 180° bends (bends 1, 2 and 3), as illustrated in Figure 3-2. Each bend, with a radius of 203 mm, is made of cast Perspex, as shown in Figure 3-3. It was first machined using a CNC milling technique in two halves, inner surface polished and then glued together. The wall roughness of the bends was estimated at around 5×10^{-6} m. The middle two vertical sections, one downward and one upward, each have a 6 m length of straight pipe where the raw data were collected. In each section, three measurement and visual observation (MV) stations are installed at different locations along the pipe. Each of these stations comprises a liquid film sensor spool which was used to measure water film thickness at four different circumferential locations, and a clear section for the visual observation of the flow. All straight sections in the test facility were made from ABS plastic. The test facility was rated to 10 barg at the ambient temperature.

A wire mesh sensor (WMS) spool can be added into the observation station if the void fraction cross-sectional distribution at the location needs to be measured. This spool is placed at the downstream of the liquid film sensor spool, in order not to disturb the measurement of liquid film thickness. More details about the liquid film sensor and WMS spools are described in section 3.2. Six GE PMP4070 pressure transducers, P1-P6, were also installed to measure the pressure along the downward and upward sections. In addition two PT100 temperature sensors, PT1 and PT2, were used to measure the water and air/water mixture temperatures respectively. The locations of the measurement and visual observation stations, pressure sensors and temperature sensors along the test section are presented in Table 3-1.

(a) Top (b) Middle (c) Bottom

Figure 3-2 Main parts of the Serpent rig

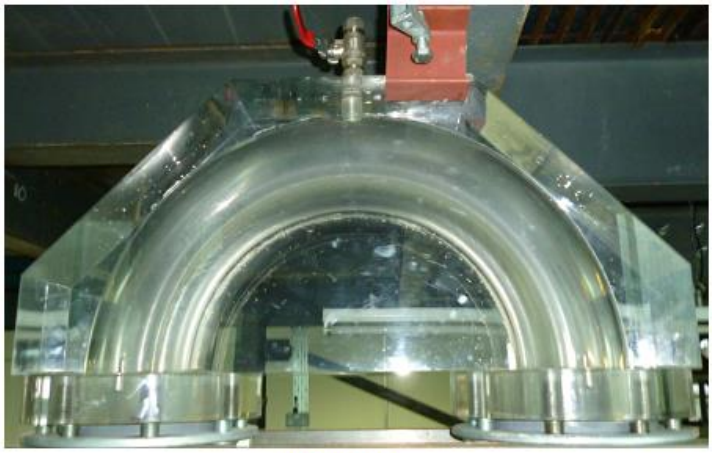

(a) Top bend

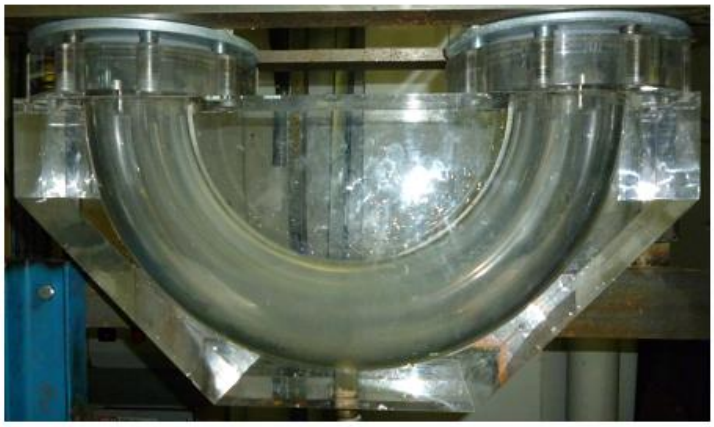

(b) Bottom bend

Figure 3-3 Return bends installed on the Serpent rig

Items	**Locations** (pipe diameter: 101.6mm)	**Note**
MV11	5 pipe diameters from the end of bend 1	Downward section, downstream of bend 1
MV12	30 pipe diameters from the end of bend 1	
MV13	46 pipe diameters from the end of bend 1	
MV21	5 pipe diameters from the end of bend 2	Upward section, downstream of bend 2
MV22	28 pipe diameters from the end of bend 2	
MV23	47 pipe diameters from the end of bend 2	
P1	10 pipe diameters upstream of the beginning of bend 1	
P2	10 pipe diameters downstream of the end of bend 1	Downward section, downstream of bend 1
P3	50 pipe diameters downstream of the end of bend 1	
P4	10 pipe diameters downstream of the end of bend 2	Upward section, downstream of bend 2
P5	50 pipe diameters downstream of the end of bend 2	
P6	10 pipe diameters downstream of the end of bend 3	
T1	In the water line before the mixer	For water temperature measurement
T2	At the exit of the test section	For water/air mixture temperature measurement

Table 3-1 Locations of the sensors and observation stations along the test section

3.1.2 Fluid supply and metering section

Air was supplied from a bank of two compressors, GA75 and GA55, connected in parallel; one of those compressors is shown in Figure 3-4 (a). A maximum air flow rate of 1200 Sm^3/h can be supplied. In addition to compressor GA75 and GA55, a small compressor was also used (Figure 3-4 (b)). The air from the compressors was accumulated in an air receiver with a capacity of 8 m^3 to reduce the pressure fluctuation from the compressor, as shown in Figure 3-4 (c). The air from the receiver passes through a bank of three filters and then through an air cooler (Figure 3-4 (d)), where debris and moisture were stripped from the air before it was metered. The flow rate of the air was regulated by two automated valves (i.e. VC301 and VC302) and measured by one of the two banks of Rosemount Mass Probar flow meters (i.e. FA1 and FA2) depending on the air flow rate range. FA1 was used to measure an air flow rate from 0 to150 Sm^3/h, and FA2 for an air flow rate of 150 Sm^3/h or higher.

Figure 3-4 Air supply equipment

Water was supplied from a 1.2 m^3 capacity water tank, as shown in Figure 3-5 (a). Water was pumped into the flow loop by a Grundfos CRE3-26 speed variable pump which has a maximum duty of 10 l/s at 6 barg, as illustrated in Figure 3-5 (b). The flow rate of water can be regulated by adjusting the pump speed, and/or one of two manual valves VW2 (bypass valve) and VW3. VW2 is located between the pump outlet and water tank (Figure 3-5 (a)), while VW3 is located in the lower part of the first upward section (Figure 3-5 (c)).

The water flow rate was metered by a 100 mm ABB electro-magnetic flow meter MMSG-Special (Figure 3-5 (d)). The air and water were mixed using a Tee-shaped junction before entering the test section, as illustrated in Figure 3-5 (e).

Figure 3-5 Water supply metering and control equipment

3.1.3 Phase separation section

The air and water mixture were separated in a ventilation tank which was covered by a lid with outlets (Figure 3-6). Air was vented into the atmosphere via the outlets after separation, while the water driven by gravity flows back into the water tank via a 6” pipe.

Figure 3-6 Ventilation tank used to separate air and water

The outlets have filters installed in order to reduce the amount of mist discharging into the atmosphere. There is a 4” outlet manual ball valve between the test section and the ventilation tank. This valve was used for leakage checks, pressure tests of the test section or to adjust the pressure in the test section if necessary.

3.2 Instruments

In this study, WMS and liquid film sensors were used to obtain the cross-sectional phase distribution and circumferential liquid film profile at different locations of the pipeline, respectively. Some of the key specifications of the instrumentation in the Serpent rig are listed in the following Table.

Instrument	Name	Manufacture & Model	Uncertainty	Range
Air flow meter 1	FA1	Rosemount Mass Probar ½''	0.5%	0-150 Sm^3/h
Air flow meter 2	FA2	Rosemount Mass Probar 1''	0.5%	150-4250 Sm^3/h
Water flow meter	FW	ABB MMSG-Special	0.1%	0.06-16 l/s
Pressure sensors	P1 to P6	GE Sensing PMP4070	0.08%	0-100 psig
Temperature sensors	T1-T2	Pt 100	0.5%	0°-100°C
Wire mesh sensor	-	Helmholtz-Zentrum Dresden-Rossendorf (HZDR), CAP200	-	Void fraction 0-100%
Liquid film thickness probes	FT1-FT2	Designed and manufactured by PSE group, Cranfield	0.1 mm	0-3 mm

Table 3-2 Summary of instruments installed on the serpent rig

3.2.1 Capacitance WMS (CapWMS)

A 32×32 WMS, as shown in Figure 3-7, was used for air-water void sectional distribution measurement at different locations along the pipeline. The sensor, associated electronics and data processing software were supplied by Helmholtz-Zentrum Dresden-Rossendorf, Germany. The method of phase fraction distribution measurement in air/water flows using similar WMS systems has been validated by a number of studies, for example Prasser et al. (2007), and Da Silva et al. (2010). In the sensor spool, wire electrodes were stretched across the flow cross-sectional area with the two sets of wire electrodes being perpendicular to each other. One set acts as a sender, the other as a receiver. The wire mesh sensor electronics measure the local permittivity of the fluid in the gaps of each crossing point, by successively applying an excitation voltage to each one of the sender electrodes, while keeping all other sender electrodes at ground potential, and measuring the AC electrical current flow to all receiver electrodes synchronously. Based on these measurements, the cross-sectional fluid distribution across the pipe sensor was able to be estimated. More details about WMS can be found in Da Silva et al. (2007). For the sensor used in this study, the separation between the sender and receiver planes of wires was 2.5 mm. The spacing between the two wires in parallel was 3.2 mm. A sampling rate of 1,000 frames of cross-sectional images per second was used for the measurement.

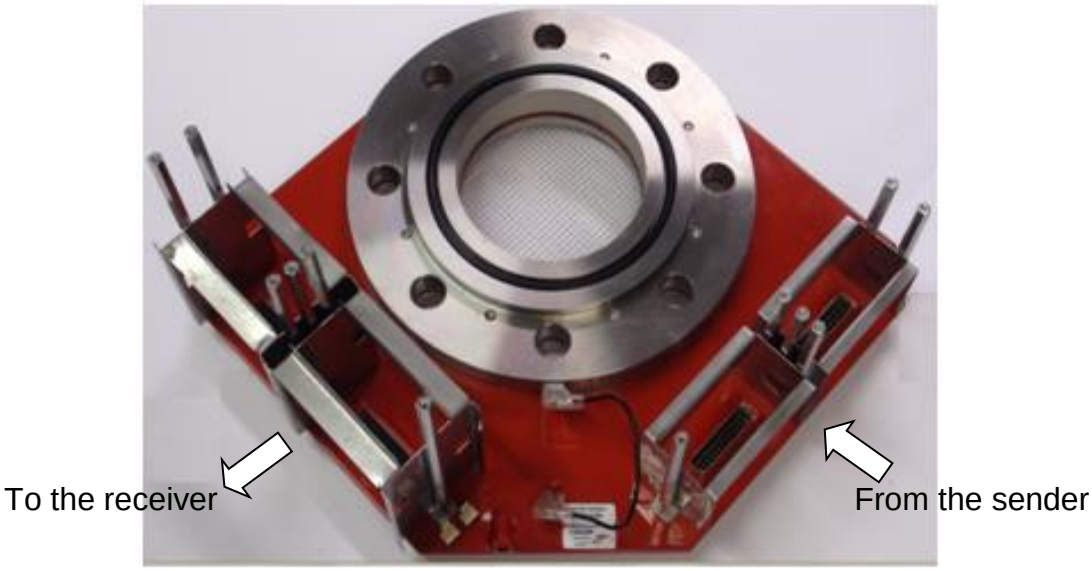

Figure 3-7 A 32×32 WMS spool used in this study

Figure 3-8 shows that, the sender wires are in the 0^o-180^o direction and the receiver wires are in the 90^o-270^o direction. With this arrangement the local distribution of the void fraction along both the 0^o-180^o and 90^o-270^o directions, can be conveniently obtained from the cross section distribution of the void fraction, which was used to assess the extent of the phase distribution asymmetry over a cross section at the measuring position of the pipe. Thus the influence of the upstream bend on the phase distribution at each axial position along the pipe can be judged.

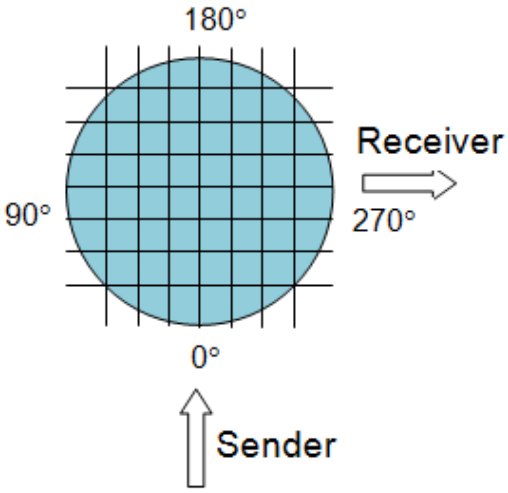

Figure 3-8 Cross section of the wire mesh sensor

3.2.2 Film thickness probe

The film thickness probe spool is shown in Figure 3-9 (a). The spool consists of four film conductivity sensors, which are evenly distributed circumferentially to measure the circumference distribution of the liquid film thickness, at the location where the spool is installed. As shown in Figure 3-9 (b), the sensing part of the conductivity film thickness probe, comprises a 10 mm diameter stainless steel rod and a stainless steel sleeve (18 mm outer diameter by 2 mm wall) arranged concentrically. Between them is a 2 mm thick insulation layer. The end of the sensor is flushed with the inner surface of the spool. Each conductor is electrically in contact with the liquid film, when the liquid film flows over them, so a conductive bridge is formed. The conductivity between the two conductors is expected to change with the thickness of the water film.

For precise measurements, calibration of the film thickness sensors was carried out by using acrylic blocks of different diameters, inserted into the probe spool coaxially to form a liquid layer of known thickness. The temperature variations against the voltage output, were also identified and considered to perform accurate film measurements. The correction of temperature was applied for a range of 10°-26^{o}C, which covers the range of fluid temperature in which the tests are performed. Tests on the repeatability of these liquid film sensors, and pressure drop measurements were also carried out. The former showed that, an uncertainty of 0.1 mm can be achieved for measuring a film thickness up to 3 mm.

(a) **(b)**

Figure 3-9 Liquid film sensor spools and the sensor, (a) sensor spool and (b) film sensor installed in the spool

The positioning of the film sensors around a circumference are shown in Figure 3-10. The 90^o position corresponds to the outside curvature of the upstream bend, and 270^o to the inside of the upstream bend. The film sensors C1-C4 were used for downward flows and the sensors C5-C8 for upward flows. For the sake of the clarity, the circumferential arrangement of each sensor is listed in Table 3-3.

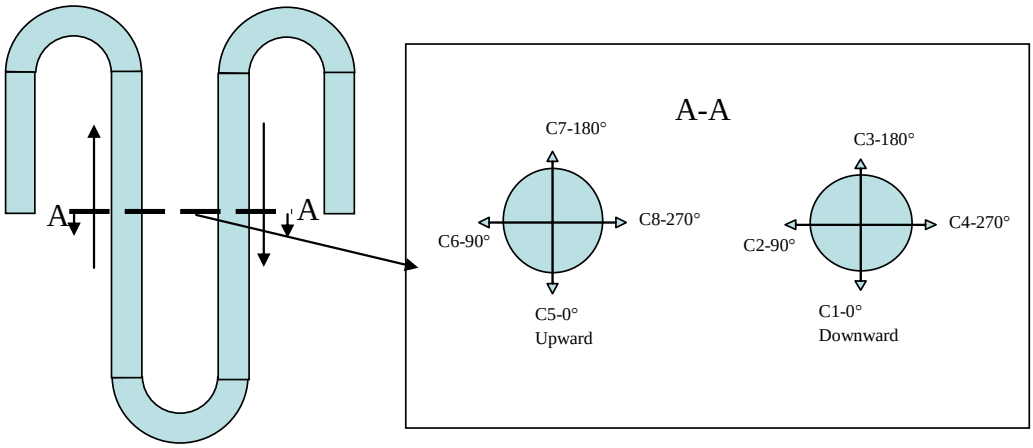

Figure 3-10 Positions of the liquid film sensors

Sensors	Downward section				Upward section			
Top spool	CT1	CT2	CT3	CT4	CT5	CT6	CT7	CT8
Middle spool	CM1	CM2	CM3	CM4	CM5	CM6	CM7	CM8
Bottom spool	CB1	CB2	CB3	CB4	CB5	CB6	CB7	CB8

Table 3-3 Circumferential arrangement of the liquid film sensors

3.2.3 Integrated liquid film velocity and thickness probe

The integrated liquid film velocity and thickness probe, was specially designed for the purposes of this investigation (its schematic is shown in Figure 3-11 (a)). The design combines the functions of film velocity and thickness measurement into one probe spool, which was assembled into the middle positions of the downward and upward sections using nuts and bolts.

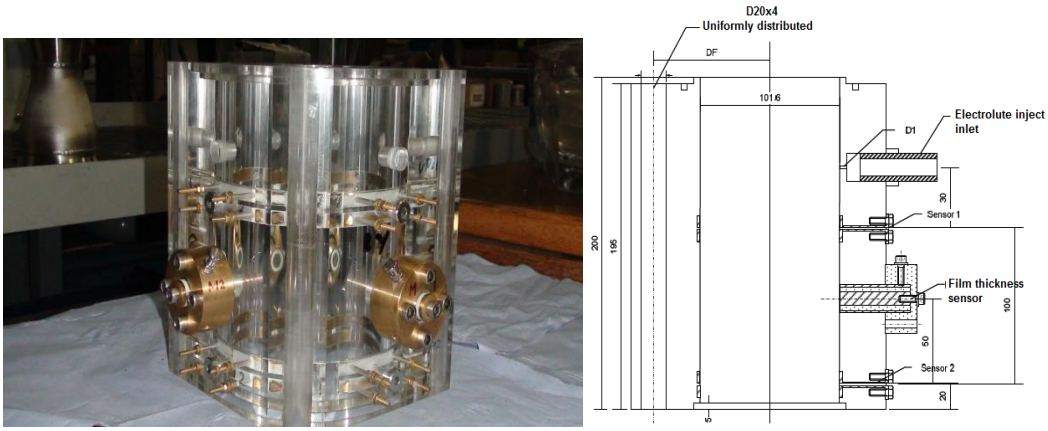

(a) Integrated film probe **(b) Drawing of integrated film probe**

Figure 3-11 Integrated film velocity and film thickness probe

Two identical sensors, sensors 1 and 2 (Figure 3-11 (b)), are arranged along the flow direction of liquid film. There are two metal rings structured in parallel and flush with the inner surface of the pipe. These are used to detect the conductance surges caused by the injected electrolyte. The transit time of the surges between the two sensors, can be determined by using a cross correlation method. The velocity thus can be calculated from the distance between the two sensors and the transition time obtained. The probe also has four film thickness sensors uniformly distributed around the probe. The design of liquid film thickness sensors in this spool, are similar to those installed at the

top and bottom positions of the downward and upward sections. The liquid film velocity measurements were based on the electrolyte injection method. The electrolyte was fed into the liquid film using an injection pump (Figure 3-12) through small holes in the probe.

Figure 3-12 Pump used to inject electrolyte

3.2.4 Data acquisition system (DAQ)

The data acquisition system consists of the DeltaV, Labview and WMS systems. The DeltaV system was used to record the fluid flow rates. Its sampling rate was fixed at 1 Hz. The Labview system was used to record the pressures, film thickness and fluid temperature at different locations in the test section of the Serpent rig, as illustrated in Figure 3-13. The sampling rate was 100Hz, which was fast enough to capture the fluctuation of those parameters in the test. The Labview system also provides an on-line view of the time traces of these parameters. This makes a real time display of the test parameters during the testing. The WMS data acquisition system was specifically for the WMS to measure phase distribution over the cross section of the pipe, as shown in Figure 3-14.

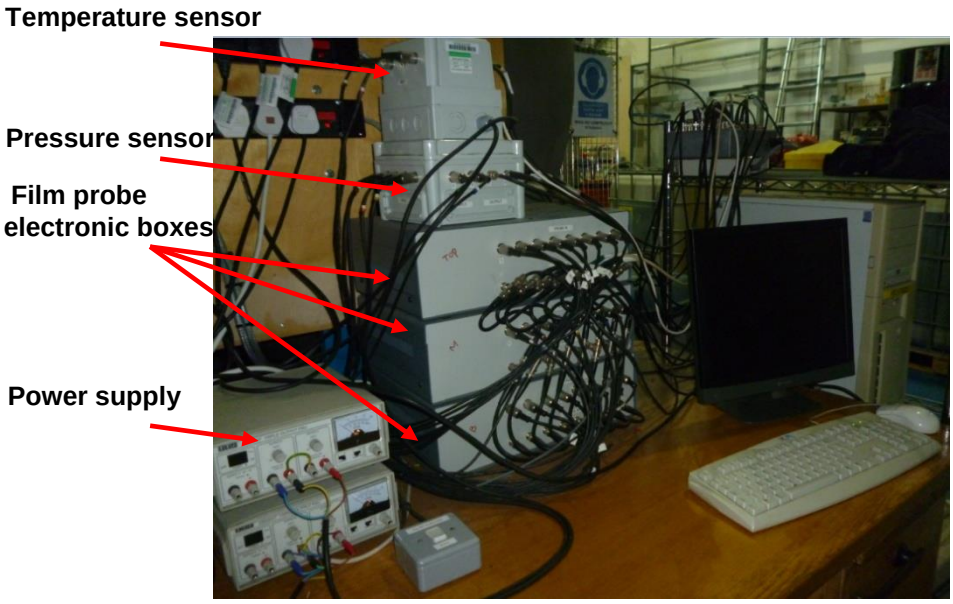

Figure 3-13 Data acquisition system used for film thickness

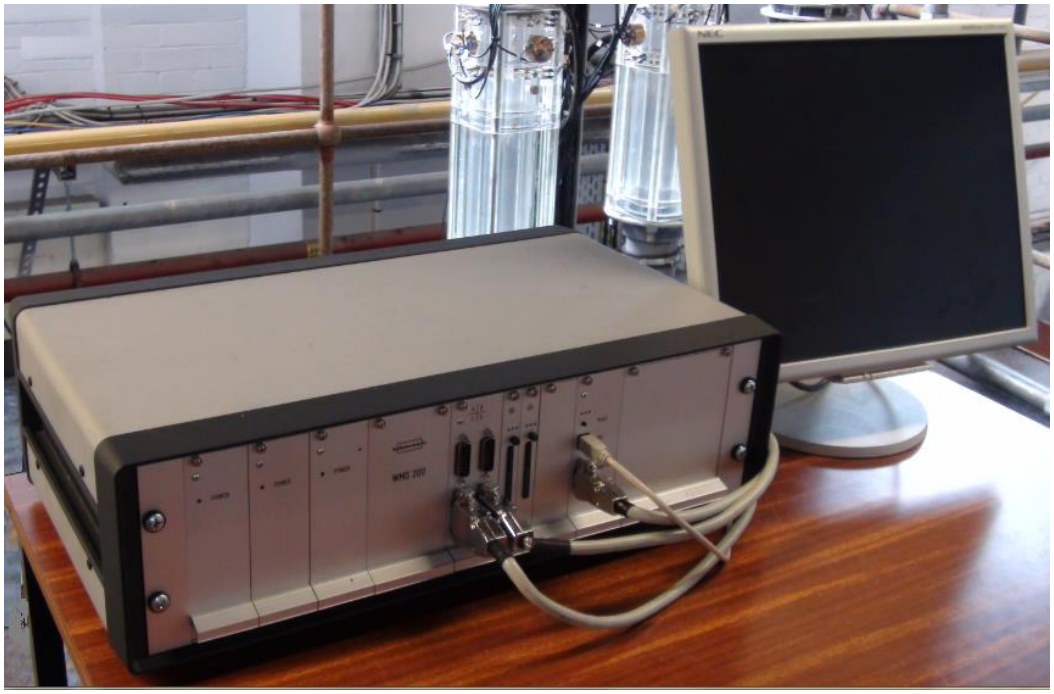

Figure 3-14 Data acquisition system used for capacitance WMS

4 Experimental work

4.1 Experiment procedure

The experimental procedure was divided into two parts: gas void fraction and liquid film thickness development tests, and liquid film velocity tests. These tests were carried out separately due to the fact that, the electrolyte used to detect the film velocity can significantly increase the conductivity of liquid. Thus, the film thickness values will increase accordingly. The film thickness probes were calibrated for precise film thickness measurements, as described in section 4.1.2 below.

4.1.1 Void fraction and liquid film thickness development tests

Prior to starting the experiments, the test section was first emptied and blown dry. The air flow was then stopped to record the zero points of the instrumentation. The Serpent rig was then filled with water to record the full scale output of liquid film probes and WMS, which were to be used for the normalisation of the outputs from the liquid film sensors and the WMS, respectively. During the experiments, for each test run the water flow rate was adjusted to a predetermined value before air was introduced to the test section. The water flow rate was monitored and adjusted to keep it at the predetermined value while the air flow was slowly increased to the desired value. The data were not logged until both the water and air flow rates became stable. The time traces data were checked regularly to ensure the flow stability. It was found from the time traces data that, the steady state condition was maintained for nine minutes before the air flow rate can be changed to another value. The water flow was monitored and adjusted accordingly. The recording period for each test run was three minutes for the liquid film and pressure sensors, and one minute for the WMS. In order to ensure the quality of the data, zero points of the instrumentation were checked regularly – at least twice a day during testing.

A Labview program was developed to record the pressures, film thickness and fluid temperature at different locations in the test section of the Serpent rig. The

sampling rate was 100 Hz, which was fast enough to capture the fluctuation of these parameters in the test. The Labview system also provides an on-line view of the time traces of these parameters. This makes a real time display of the test parameters during the measurements. The WMS system acquires data at a speed of 1,000 frames per second (fps). The test matrix and corresponding flow conditions are presented in the appendix of this thesis.

4.1.2 Calibration procedure of film thickness probes

The calibration film thickness probes were necessary for precise film thickness measurements. The calibration was carried out by using acrylic blocks of different diameters, inserted into the probe spool coaxially to form a liquid layer with known thickness, as shown in Figure 4-1.

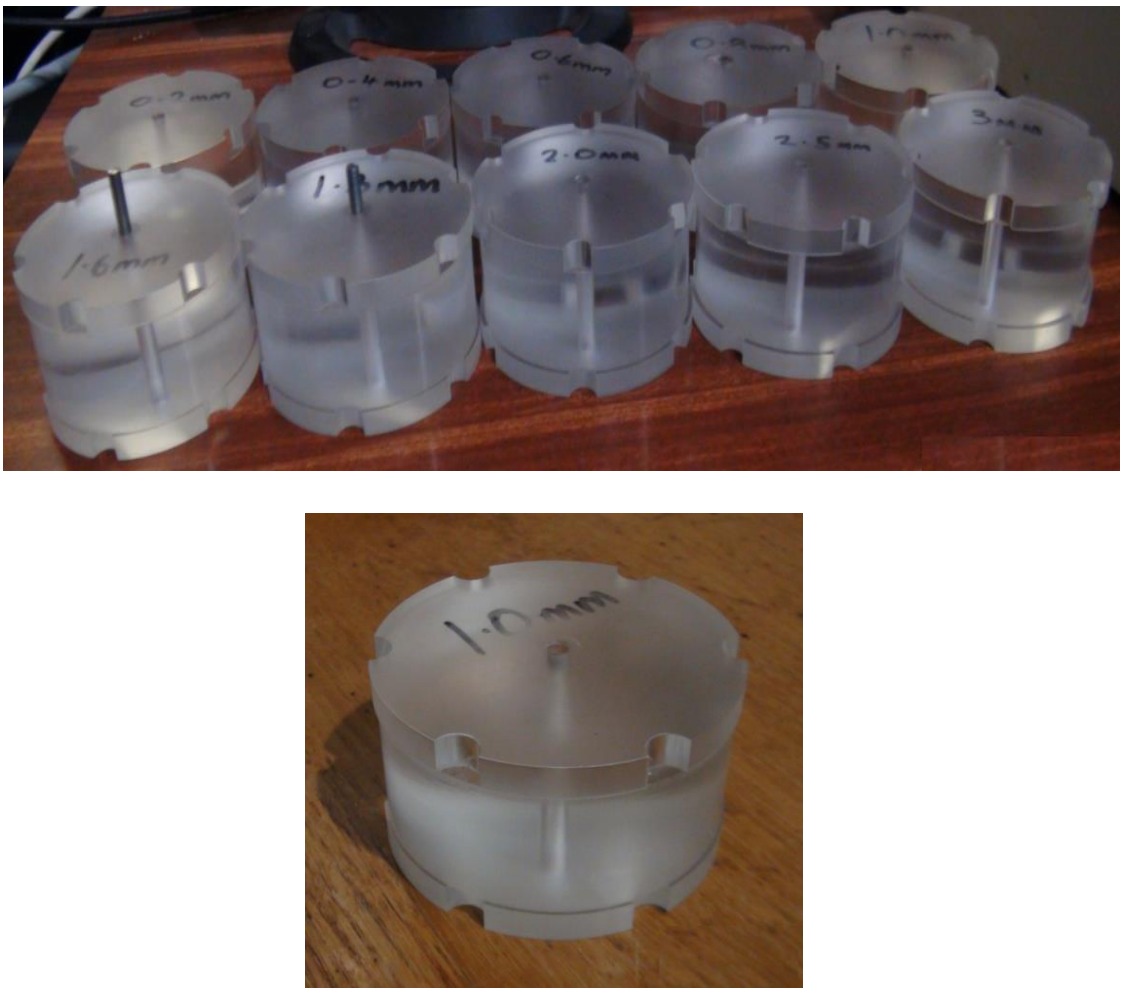

Figure 4-1 Blocks of different diameters used for the probes' calibration

The calibration blocks' diameters and corresponding film thicknesses are listed in Table 4-1.

Block diameter, mm	Film thickness, mm
101.6	0.0
100.8	0.2
100.4	0.4
100.0	0.6
99.6	0.8
99.2	1.0
98.6	1.3
98.0	1.6
97.2	2.0
96.2	2.5
95.2	3.0
89.2	6.0

Table 4-1 Blocks of different diameters inserted into the probes

Considering that the probes' measurement properties are stable when the conductivity of the probe is non-dimensional, it was reasonable to normalise the output voltage (ratio of output to full scale voltage output). The full scale output corresponding to a film thickness of 6 mm, was very close to the output voltage when the probe was full of water. Twenty four normalised calibration curves were obtained during the static experiments. It was found that, the obtained curves for sensors in one probe were almost identical. Therefore, one

normalised curve was used for the sensors in the same probe spool. Figure 4-2 (a-c) correspond to the normalised calibration curves obtained at the top, middle and bottom positions of the downward section, while those in Figure 4-3 correspond to the probes placed at the top, middle and bottom positions of the upward sections.

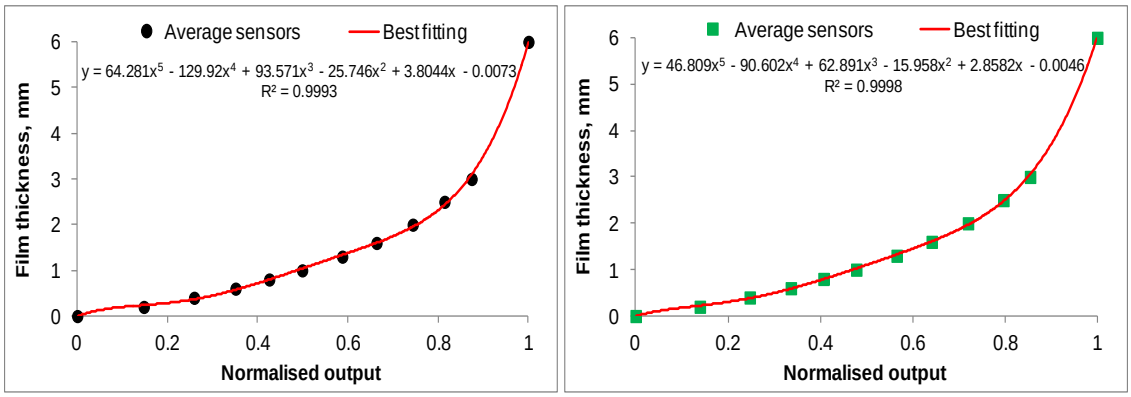

(a) Top position **(b) Middle position**

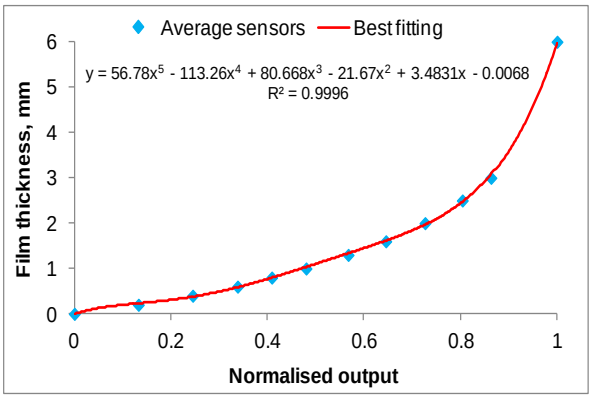

(c) Bottom position

Figure 4-2 Calibration curves of liquid film probes at downward section

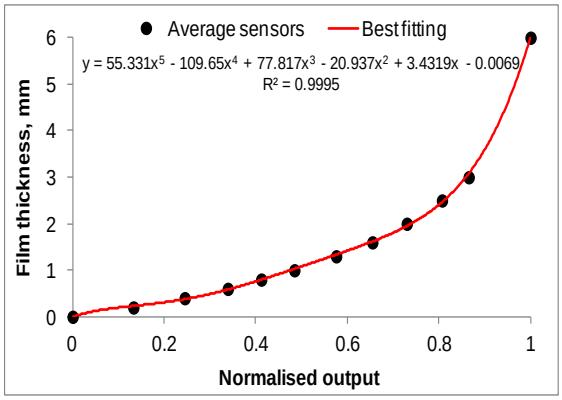

(a) Top position

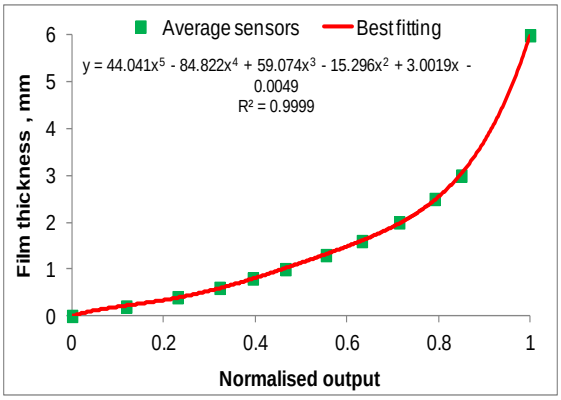

(b) Middle position

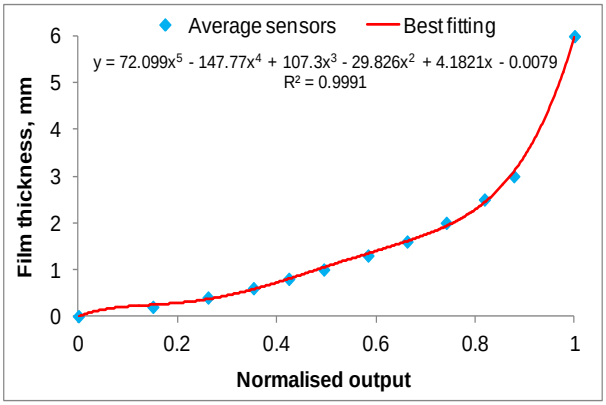

(c) Bottom position

Figure 4-3 Calibration curves of liquid film probes at upward section

4.1.3 Measurement repeatability of the liquid film probes and pressure sensors

In order to check the repeatability of the liquid film thickness probes and pressure sensors, it was necessary to perform several runs over a long period. Three runs were carried out for gas superficial velocities of 1.44, 3.02, 4.60, 6.20, 9.38, 12.47, 18.39, 23.66 and 28.87 m/s, with a constant liquid superficial velocity of 0.1 m/s.

Figures 4-4 and 4-5 illustrate the results achieved from the film probes and pressure sensors respectively. The plots presented in Figure 4-4 (a) and (b), represent the measurement repeatability of the film thickness for downward and upward sections respectively. Figure 4-4 (a) and (b) shows that, the discrepancy is below or about 0.1 mm for the downward and upward flows over

all gas velocities. The data of pressure drops (DP23) were collected from pressure transducers P2 and P3, placed at the higher and lower positions of the downward section respectively, as shown in Figure 4-5 (a). The pressure drops (DP45) data, were collected from sensors P4 and P5 placed at the lower and higher positions of the upward section respectively, as presented in Figure 4-5 (b). It can be seen from Figure 4-5 (a) and (b) that, the tendency of the three runs (i.e. run 1, 2 and 3) are the same for all gas superficial velocities.

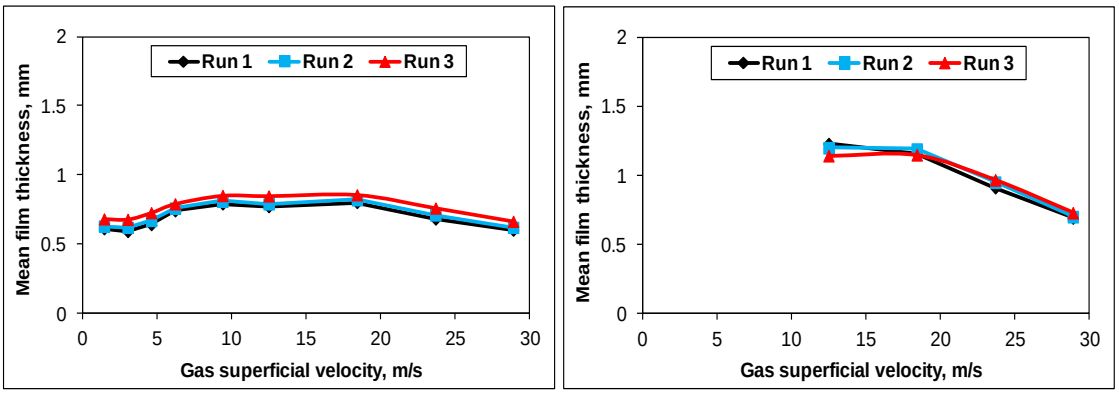

(a) (b)

Figure 4-4 Repeatability of liquid film measurements for (a) downward section and (b) upward section at water superficial velocity of 0.1 m/s

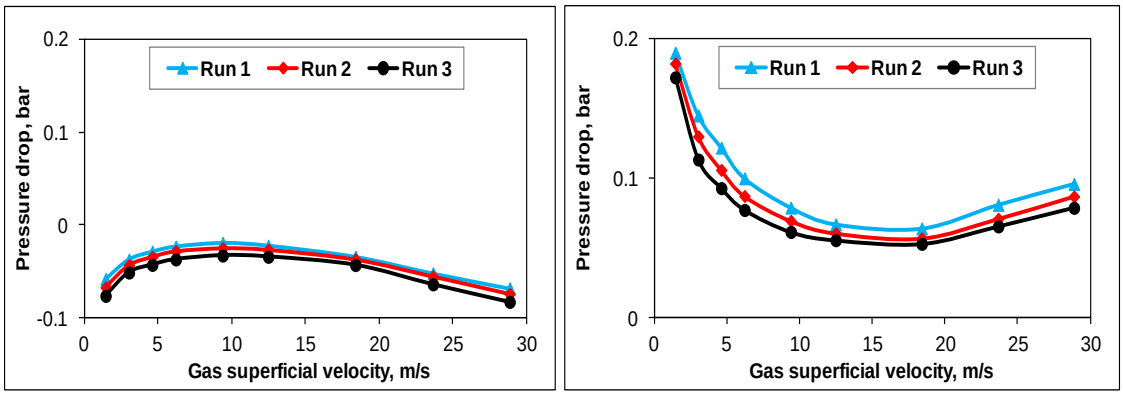

(a) (b)

Figure 4-5 Repeatability of pressure drop measurements for (a) downward section and (b) upward section at water superficial velocity of 0.1 m/s

4.1.4 Temperature effect on liquid film thickness variations

For a precise film thickness measurement, it was necessary to consider the effects of temperature on the conductivity of the water. Figure 4-6 illustrates the measurement results for the voltage output signal against the temperature. These measurements were carried out for the film probes CB1-CB4 located in the bottom position of the downward section. Figure 4-6 shows that the full scale output corresponded to a film thickness of 6 mm, which was very close to the output voltage when the probes were full of water. This was achieved by using acrylic blocks, inserted into the probe spool coaxially to form a liquid layer with the mentioned film thickness. The investigated range of the temperature was obtained at temperatures ranging from 10-26^{o}C. It can be seen from Figure 4-6 that, the voltage was increased with increasing fluid temperature.

Therefore, dynamic measurements were performed on the voltage when the pipe was full of water at the beginning, the middle and the end of the experiments. Later on temperature compensation was implemented in order to obtain film thickness values corresponding to each temperature.

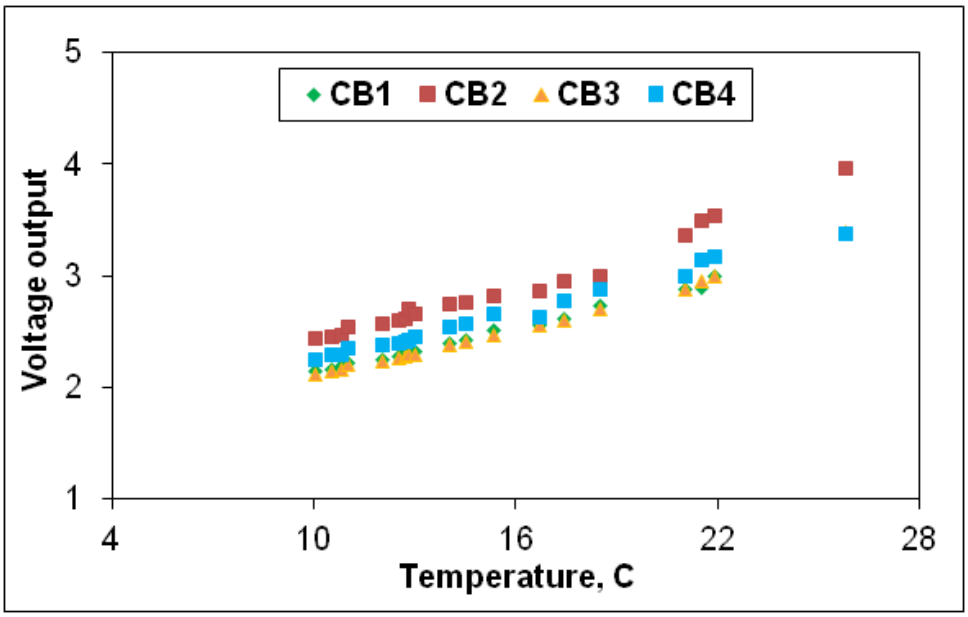

Figure 4-6 Static measurements when the probes were full of water to identify the effects of temperature on liquid film thickness variations

4.1.5 Liquid film velocity tests

Heat transfer to and from the liquid film is an important feature of many industrial furnace applications. The heat transfer rate is closely related the velocity of liquid film on the tube wall. Indeed, the average liquid film velocity can be estimated from the measured liquid film thickness and liquid flow rate if the liquid entrainment is insignificant. However, this assumption is difficult to justify. It is therefore, very valuable to obtain average liquid film velocity under several flow conditions.

The measurement of liquid film velocity was based on the electrolyte injection method (presented in section 3.2.3). During the film velocity tests, a similar procedure was used to that for the liquid film development measurement, in order to achieve a steady state of flow for predetermined values of air and water flow rates. When the steady state condition was achieved, the electrolyte (saturated NaCl solution) was fed into the liquid film by a pulsed pump through the injection hole (1mm i.d.) at a flow rate of 1.2 ml/s. The disturbance caused by this flow rate on the liquid film was only 0.15 % of the lowest liquid flow rate tested, which was negligible. The pulse period of the pump was set at approximately 2 seconds, with 1 second on and 1 second off. The signals from the conductivity probes were recorded for 30 second, at a sampling frequency of 1,000 Hz.

5 Experimental results and discussion

5.1 Flow regime identification in downward and upward flows

For this work, flow patterns were identified based on visual observations, videos, images obtained from wire mesh sensors and the average time trace of PDF. As a further corroboration, all observed flow regimes were plotted in flow regime maps generated at the top, middle and bottom positions of the downward and upward sections of the Serpent rig. The maps were produced by using gas and liquid superficial velocities.

5.1.1 Visual observation

The flow behaviour in the serpentine configuration was identified by using videoing and visual observation through five transparent sections. The transparent sections include two top bends, two straight sections (one in the middle of the downward and the other in the middle of the upward straight section) and a bottom bend. Information observed at each transparent observation station is presented in the following subsections.

It is noteworthy that, the pictures presented below demonstrate the flow behaviour in the Serpent rig facility over particular gas and liquid superficial velocities. More detailed information of the flow regimes, were presented by generating flow regime maps at different locations along the straight pipes of the test facility for a wider range of flow rates.

5.1.1.1 Downward and upward straight sections

The pictures below depict the flow regime observed in the Serpent rig over a range of gas and liquid superficial velocities. It can be seen that the annular flow was dominant in the downward section flow. No substantial changes were found even when the gas velocity increased further. On the other hand, the flow regime at the upward section was observed to vary from intermittent to annular flow. However, intermittent flow was present for the most flow conditions (as can be noted from the flow regime maps presented later). For instance for a gas velocity of 1.42 m/s and liquid velocity of 0.2 m/s, a typical intermittent flow was

identified, as presented in the pictures of Figure 5-1. At these flow conditions (gas superficial velocity of 1.42 m/s with liquid superficial velocity of 0.2 m/s), the liquid was periodically oscillated in upward and downward directions. Also it was noted that, incoherent waves existed and the liquid was falling down in some circumferential positions, while pushing up in other positions. This phenomenon of falling film was significantly reduced as the gas velocity increased to 12.08 m/s. However, the liquid film still pushed upward periodically with incoherent waves on its surface. For the highest gas velocity value of 26.61 m/s, the circumferential liquid film was distributed more evenly with some fluctuation. The annular flow regime was still present. Liquid film formed can be seen as a translucent, white layer inside the pipe wall. This was attributed to the liquid entrainment occurring at high gas flow rates. As a result, the waves that may be present on the liquid film surface were difficult to identify by direct observation. It is suggested that, the flow in the upward section is more sensitive to the flow rate changes.

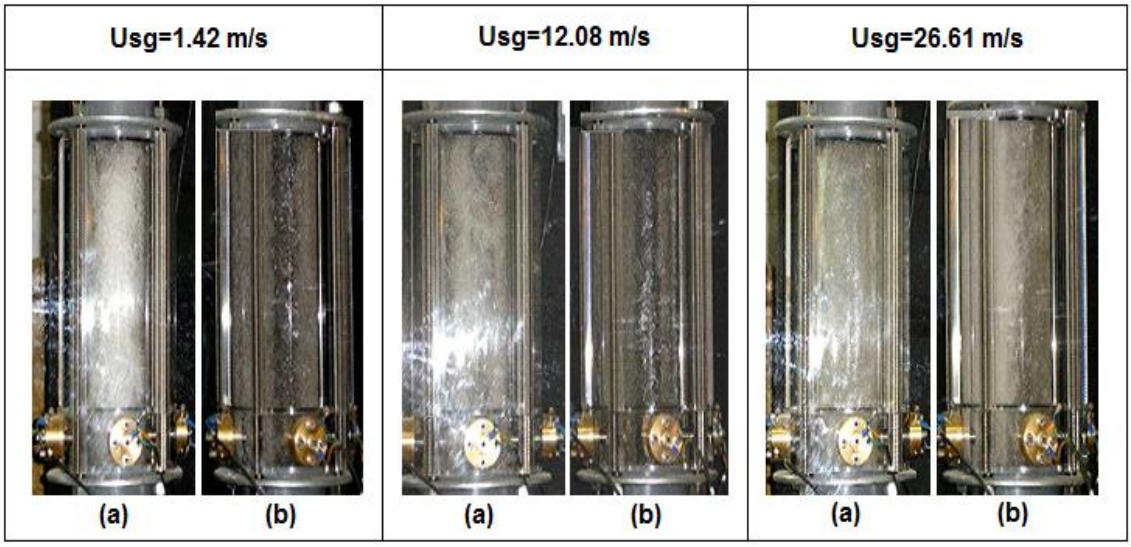

Figure 5-1 Flow regimes observed at the middle positions of (a) upward section and (b) downward section for gas superficial velocities of 1.42, 12.08 and 26.61 m/s, while liquid superficial velocity was kept constant at 0.2 m/s

For the sake of the clarity, the flow regimes are discussed at the downward and upward sections for a higher liquid superficial velocity of 1 m/s, with gas velocities of 1.32, 9.65 and 18.56 m/s, as shown in Figure 5-2. The film observed at the downward section, was found to be very thick (thicker than that at a liquid velocity of 0.2 m/s) for the gas velocity of 1.32 m/s. For a gas superficial velocity of 9.65 m/s, a large number of bubbles were observed entrained in the liquid film. For a gas velocity of 18.56 m/s, while liquid superficial velocity was constant at 1 m/s, the liquid was circumferentially distributed. At the upward flow, an intermittent flow with incoherent waves and a large number of small bubbles were observed for a gas velocity of 1.32 m/s. The annular flow was observed as the gas velocity increased to 18.56 m/s.

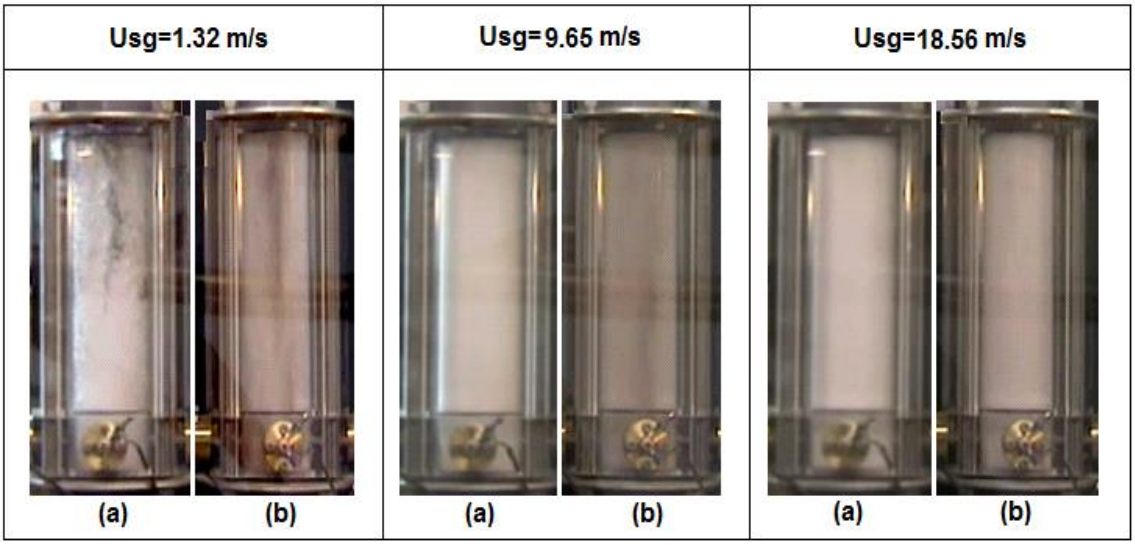

Figure 5-2 Flow regimes obtained at the middle positions of (a) upward section and (b) downward section for gas superficial velocities of 1.32, 9.65 and 18.56 m/s, while liquid superficial velocity was kept constant at 1 m/s

5.1.1.2 Flow behaviour in the top and bottom bends

Flow behaviour in the Serpent rig was also observed in the two inverted U-bends (i.e. top bends) and the U-bend (i.e. bottom bend). Striking similarity was observed for the flow behaviour in the two top bends, over the range of gas and liquid flow rates, although the first bend was placed closer to the mixing section than the second one. Figure 5-3 shows a comparison between the flow behaviour in the first top bend, and that in the bottom bend for three gas superficial velocities and

for liquid superficial velocity of 0.2 m/s. In the top bend, it was observed that the gas was trying to push the liquid periodically into the top bend, when the gas superficial velocity was 1.42 m/s. Small amounts of liquid existed on the outer (top) surface of the bend, due to the domination of gravitational force. The liquid phase was noted to flow mainly along the inner surface of the bend, with a large number of small bubbles present in the liquid body. By increasing the gas velocity to 12.08 m/s, the liquid film was observed to cover all parts of the outer surface of the bend, due to centrifugal force domination. The force acts to push the liquid into the bend's outer surface. Consequently, the liquid film present on the inner (bottom) surface of the bend was notably thinner than that on the bend's outer surface. Secondary flow was observed to occur in the bend, due to the combined effects of centrifugal force, gravitational force, interfacial shear stress and surface tension. When the gas velocity increased to 26.61 m/s, both the gas and liquid were noted to enter the bend at high speed, and hit the outer surface of the bend continuously, while part of the liquid phase was progressed along the outer surface of the bend. This led to create dry patches at the straight sections that located in the same direction of the bend's inner surface.

In the bottom bend, the flow was mainly progressed on the bend's outer (bottom) surface for gas and liquid superficial velocities of 1.42 and 0.2 m/s respectively. Comparatively, a less amount of the liquid phase was observed on the inner (top) surface of the bend, due to the impact of centrifugal and gravitational forces. For these flow conditions, the liquid phase present in the outlet section of the bend was accompanied by a large number of small bubbles. The gas and liquid was observed to oscillate up and down in the second half of the bend (i.e. close to the outlet part of the bend, where the flow was being initiated into the straight upward orientation). For the higher velocity of gas, which was 12.08 m/s, the film appears thicker and covered most parts of the bend's outer surface. This was due partly to the domination of centrifugal and gravitational forces, existing in the bottom bend. An interesting observation was that the inner surface of the bend was also covered by a huge amount of liquid phase. This can be attributed to the deposition of liquid droplets. Similar to that observed at the top bend, secondary flow was also observed at the bottom bend. The observation of the flow behaviour in the bottom

bend was similar to that observed in the top bend for a gas velocity of 26.61 m/s. However, the fluctuation of the flow in the bottom bend was found to be significantly less than that in the top bend.

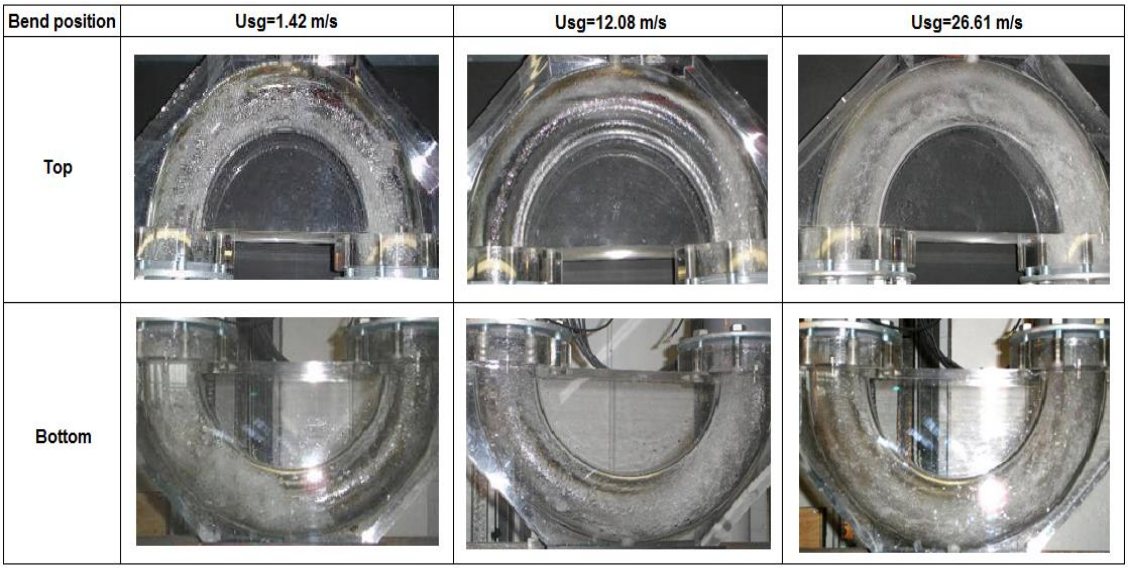

Figure 5-3 Flow behaviour in top and bottom bends for gas superficial velocities of 1.42, 12.08 and 26.61 m/s, while liquid superficial velocity was kept constant at 0.2 m/s

5.1.2 Reconstructed images as depicted by WMS

The flow regimes and their development along the serpentine pipe, were investigated by examining the data of cross-sectional phase distributions collected using WMS at the top, middle and bottom positions of the downward and upward sections.

5.1.2.1 Reconstructed images in the downward section

Figure 5-4 shows axial slice images (X and Y) and cross section images (Z) phase distribution, at different axial positions and under different flow conditions in the downward section. The data used for Figure 5-4 were obtained for different gas superficial velocities, while the liquid superficial velocity was kept constant at 1 m/s. The images were reconstructed from the WMS data. Image X is obtained by stacking cross section images, and then axially slicing in a 0^o-180^o direction, likewise for image Y along the 90^o-270^o direction, as shown in Figure 3-8. In order to give near reality geometries of phase structures in the

pipe, the number of the cross section images *N* was used to reconstruct the axial slice images which is given by $N = {f_s L_p}/{U_m}$, where f_s is the WMS system frame rate, i.e. 1,000 fps; L_p is the pipe section length represented by the axial sliced images, i.e. 1,000 mm in this study; and U_m is the mixture velocity at the respective flow conditions. In the images, the colour varies from blue to red representing the void fraction changing from 0 (i.e. air) to 100 (i.e. water). As can be seen from Figure 5-4, for a gas superficial velocity of 0.17 m/s, the flow is aerated; however, there is a significant amount of water in the form of wisps entrained into the flow at the top position. These wisps are like objects with long tails and occupied some parts of the pipe. The cross section images clearly show that, the liquid phase has a tendency towards the circumferential position of 90^o, corresponding to the outside curvature of the upstream top bend (bend 1). However, the flow at the middle position becomes liquid phase dominated and the gas phase is no longer continuous; the cross section images show that, the cross-sectional phase distribution at the middle position is less asymmetric with respect to the pipe axis, when compared with its top position counterpart. At the bottom position the axial slice images show that the large bubbles break down into small bubbles, and are evenly distributed at various places of the cross section of the pipe, resulting in a bubbly flow formation; meanwhile the cross section image shows that the cross-sectional phase distribution is fairly homogeneous.

At the top position, as the gas superficial velocity increases, the wisps disappear and the flow regime becomes a typical annular flow. For all gas flow rates in Figure 5-4, the liquid phase fractions at the circumferential position of 90^o, corresponding to the outside curvature of the upstream top bend (bend 1), are much larger than the other positions (i.e. 0^o,180^o and 270^o). This phenomenon should be mainly due to the centrifugal force in the upstream bend.

At the middle position, the images show that the flow regimes are significantly different from those at the top position, when the gas superficial velocities are low. For all gas superficial velocities, the cross section images show that the cross-sectional phase distributions, are much less asymmetric with respect to the pipe axis in comparison with their top position counterparts. This is particularly obvious for the gas superficial velocity of 18.56 m/s.

At the bottom position, when the gas superficial velocity increases from 0.17 to 0.52 m/s, large bubbles are formed as a consequence of the coalescence of small bubbles which fill most of the pipe cross section. At higher gas superficial velocities of 1.02 and 2.67 m/s, it is observed that an intermittent flow regime is created. The flow regime observed for a higher gas superficial velocity of 18.56 m/s was an annular flow. The cross-sectional phase distribution is fairly symmetric, with respect to the pipe axis in comparison with their counterparts at the top and middle positions.

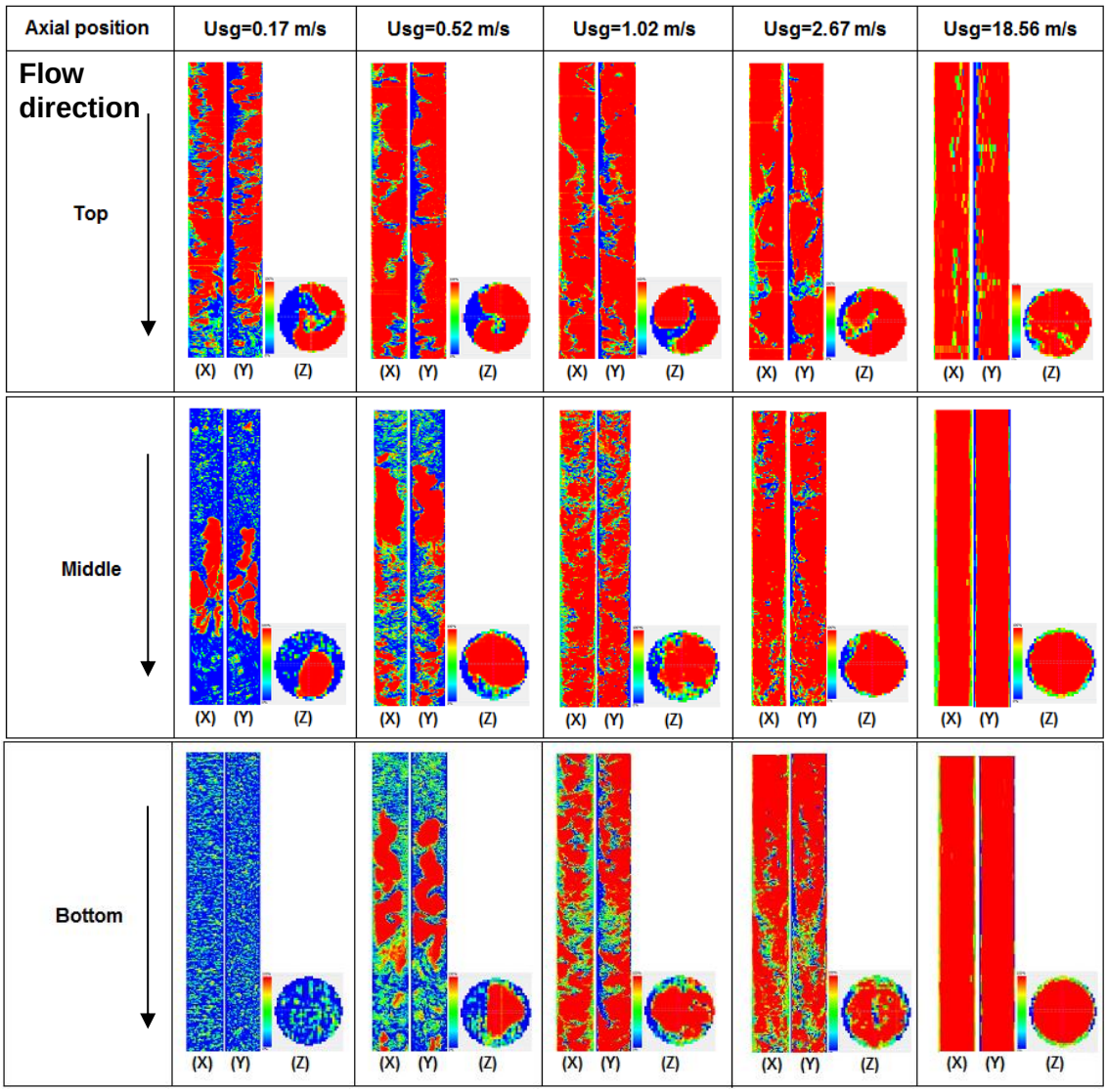

Figure 5-4 Axial slice images (X and Y) and cross section images (Z) phase distribution obtained from WMS, at different axial positions of the downward section, for different gas superficial velocity with liquid superficial velocity of 1 m/s. For all images, red colour is air and blue is water

5.1.2.2 Reconstructed images in upward section

Figure 5-5 illustrates the axial slice images (X and Y) and cross section images (Z) of the air-water mixture distribution at the bottom, middle and top positions of the upward section. These images were reconstructed from the WMS data at different ranges of gas superficial velocities, and for a fixed liquid superficial velocity of 1 m/s. Similar to the case of the downward section, in each panel image X is obtained by axially slicing along the 0^o-180^o direction and image Y

along the 90^{o}-270^{o} direction, both representing a 1,000 mm long pipe section. In Figure 5-5, blue and red colours represent the water and air respectively. The axial slice images were reconstructed to give geometries similar to the real phase structures, as stated in section 5.1.2.1.

It can be noted from the plots that, a bubbly flow regime dominates for the gas and liquid superficial velocities of 0.17 and 1 m/s respectively. This is characterised by dispersed large bubbles evenly distributed across the pipe centre. These bubbles are classified as spherical cap bubbles, the sizes of which are much smaller than the pipe diameter. Transition from bubbly to intermittent flow occurs at a higher gas superficial velocity of 0.52 m/s. As the gas velocity increases to 1.02 m/s, these bubbles coalesce and intermittent flow is observed. By increasing the gas superficial velocity further to 2.67 m/s, an intermittent flow is still present and the bubbles become larger and occupy most parts of the pipe centre. An annular flow regime is identified by increasing the gas velocity to 18.56 m/s. At this gas velocity it is noted that, at the bottom and middle positions, a large amount of liquid lumps and droplets are entrained in the pipe centre. However, these fractions of entrained liquid became much less when the flow reached the top position.

For a gas superficial velocity of 1.02 m/s, large gas bubbles very similar to Taylor bubbles, are well formed in the middle and top positions of the pipe. Arguably, the Taylor bubble is a signature of a slug flow regime which occurs in much smaller sizes of upward pipes. In the large diameter upward pipes (i.d. > 100 mm), there is increasing evidence that the transitions: bubbly/slug, slug/churn, do not exist. This is because the traditional bullet-shaped Taylor bubbles in slug flow are not present, probably due to the existence of a limit on the size of spherical cap bubbles. Schlegel et al. (2012) pointed out that, this limit is due to Raleigh-Taylor instability. Therefore, there is a direct transition from normal bubble flow to the so-called churn-turbulent flow. A number of authors, such as Peng et al. (2010), Smith et al. (2012), Lao et al. (2012) and Schlegel et al. (2012), have observed and documented this occurrence. It is worth mentioning that, the churn turbulent flow precedes the churn flow regime.

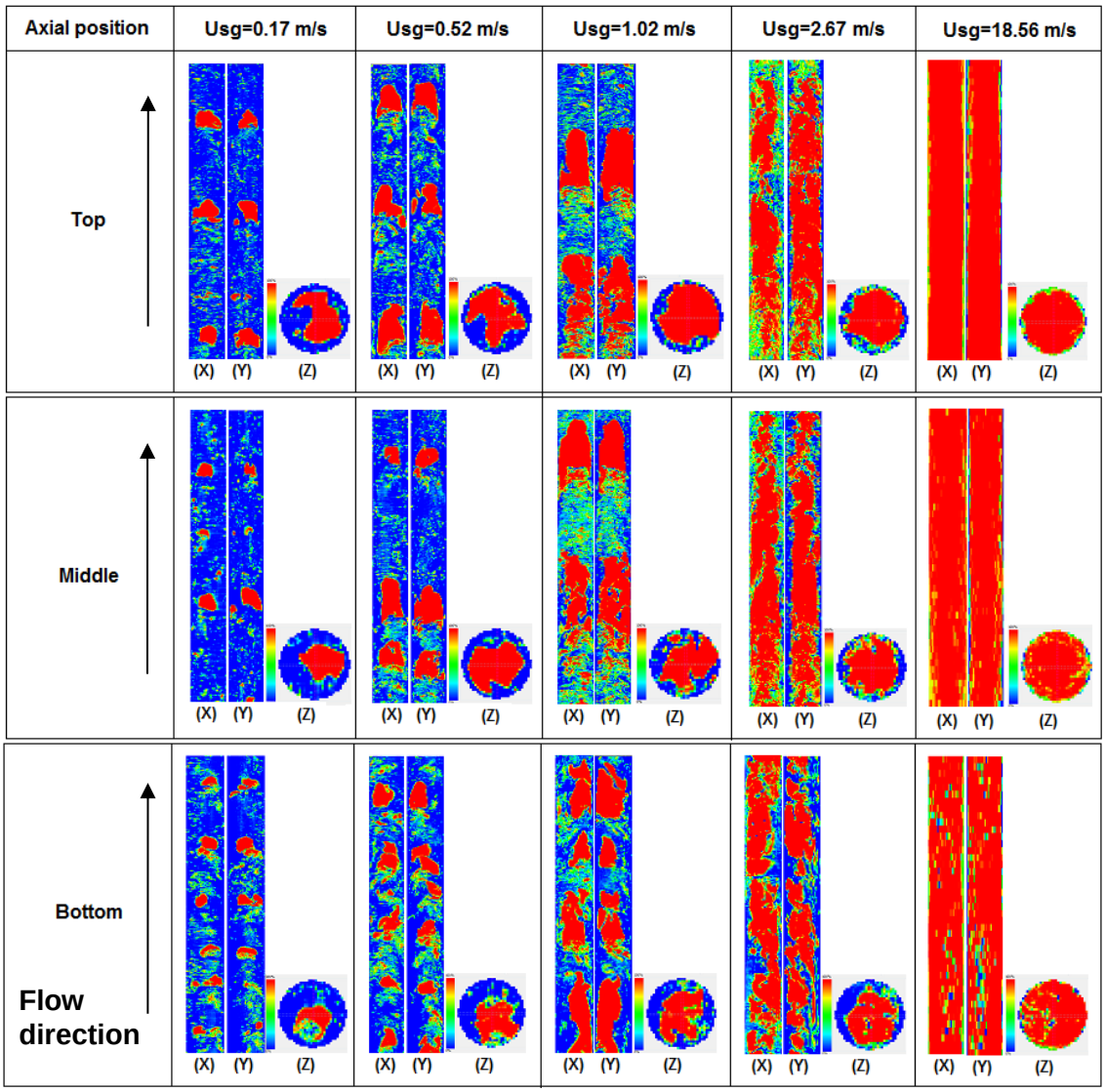

Figure 5-5 Axial slice images (X and Y) and cross section images (Z) phase distribution obtained from WMS, at different axial positions of the upward section, for different gas superficial velocity with liquid superficial velocity of 1 m/s. For all images, red colour is air and blue is water

5.1.2.3 Time traces and PDFs for downward section

Flow regimes and their developments and asymmetries of cross-sectional phase distribution in the downward section, were also confirmed by examining the void fraction time traces, and corresponding probability density functions (PDFs) obtained from the WMS data. The void fraction PDF method is a widely recognised method, which has been used by many researchers for decades, for example, Kelessidis and Dukler (1989), and more recently Omebere-Iyari et al. (2008). Figure 5-6 shows the time traces of the void fraction and the respective

PDFs of the average void fractions obtained at the top, middle and bottom positions of the downward section, for a fixed liquid superficial velocity of 1 m/s and for a gas superficial velocity ranging from 0.17 to 18.56 m/s. As can be seen, at gas velocity of 0.17 m/s, the time trace at the top position presents oscillations in a period of ~10 s, which is different from those obtained at the middle and bottom positions. The PDF of the time trace related to the top position has a feature of double peaks, which suggests the flow regime is an intermittent one. The PDFs related to the middle and bottom positions are single peak with a much lower mean value of the void fraction (about 0.1), suggesting the flow regime is similar to the dispersed bubbly flow. However, it is also noted that the bubbly flow regime is mixed with periodic large air pockets; hence the flow is still an oscillatory one. A visual observation of the flow behaviour inside the downstream bend 2 suggests that, the water periodically blocks this bend and then is being blown off. Each of the cycles is also about 10 seconds long. The coincidence of periods may suggest that, the above-mentioned flow regime is related to both the flow conditions and the pipeline's vertical serpentine geometry. The flow regime is similar to that which occurred in an inverted U-type pipeline reported by Golan & Stenning (1969). Figure 5-6 shows that, the oscillatory flow regime also occurs when the gas superficial velocity is increased to 0.52 and 1.02 m/s; however, both the amplitude and period of the oscillation decreases as the gas velocity increases. When the gas velocity increases to 2.67 m/s or higher, the oscillatory flow regime disappears and the PDFs of the void fraction time traces at the top, middle and bottom positions have only one peak. However, the peak width of the PDF is decreased from the top towards the bottom, which indicates the cross-sectional void fraction is less fluctuated.

Usg, m/s	Time trace	PDF
0.17	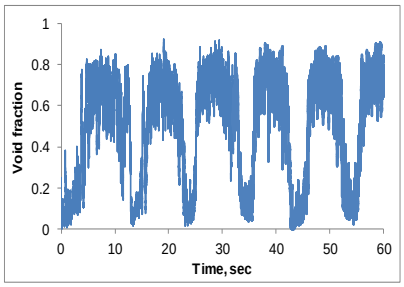	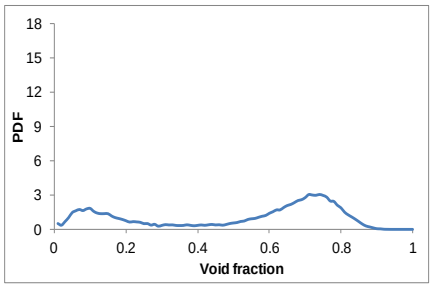
0.52	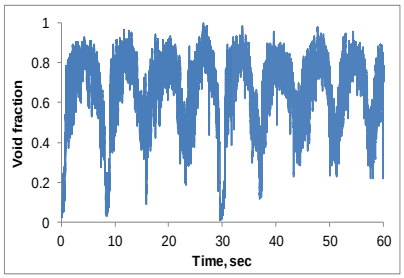	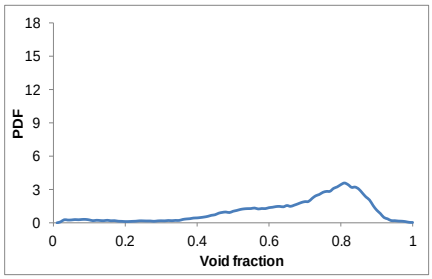
1.02	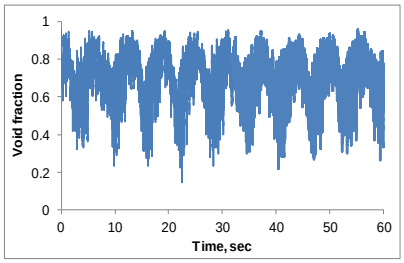	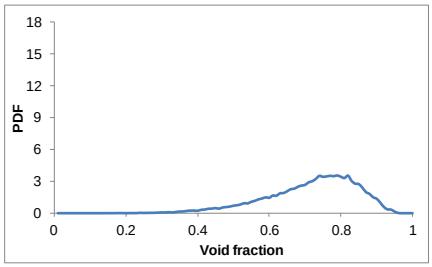
2.67	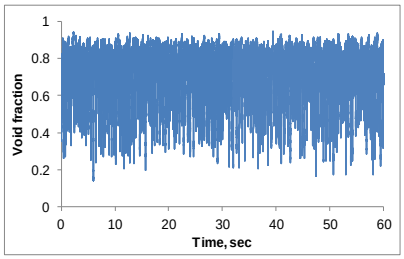	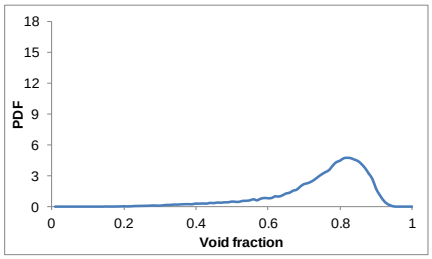
18.56	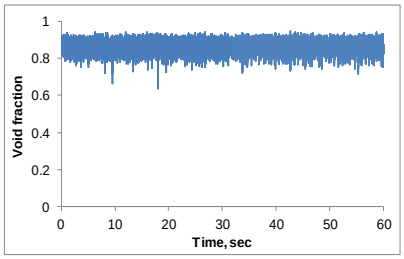	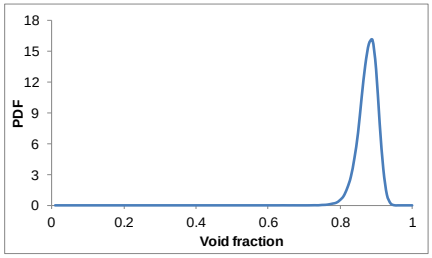

(a) Top position (downward)

Usg, m/s	Time trace	PDF
0.17	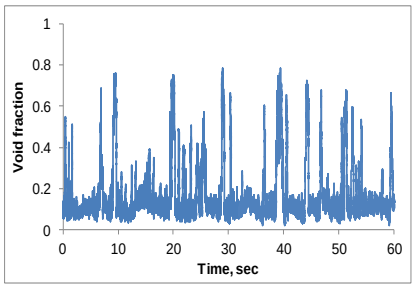	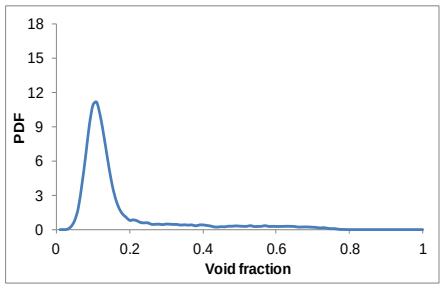
0.52	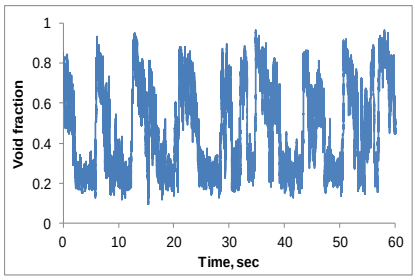	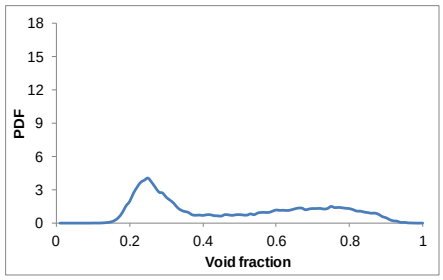
1.02	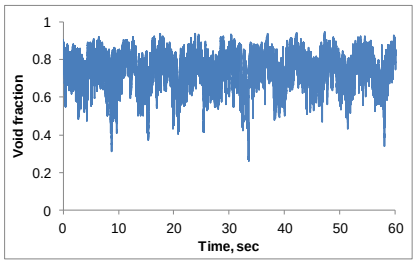	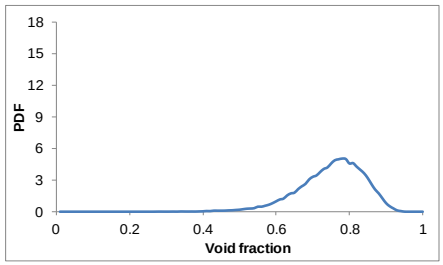
2.67	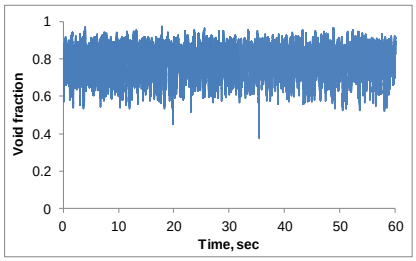	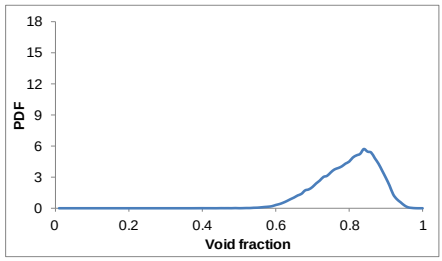
18.56	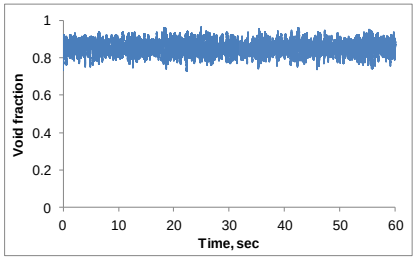	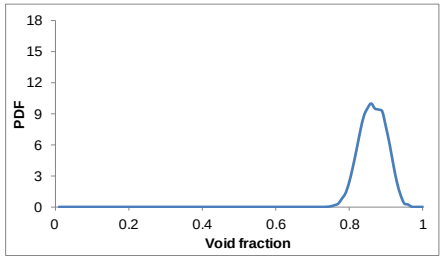

(b) Middle position (downward)

Usg, m/s	Time trace	PDF
0.17	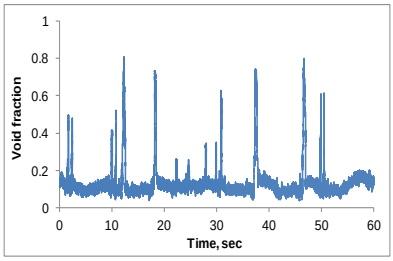	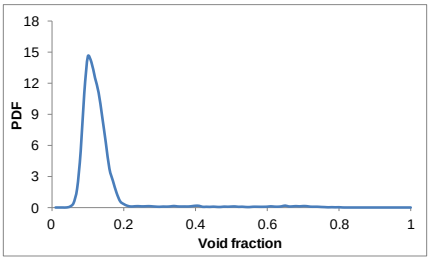
0.52	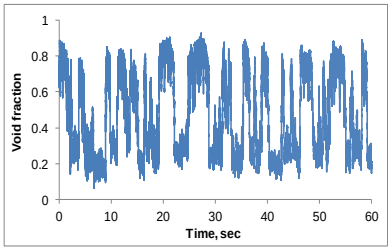	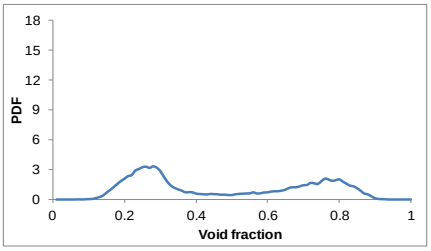
1.02	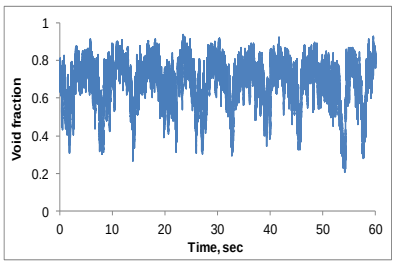	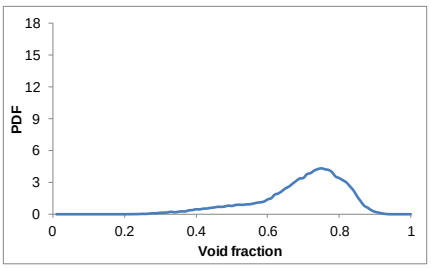
2.67	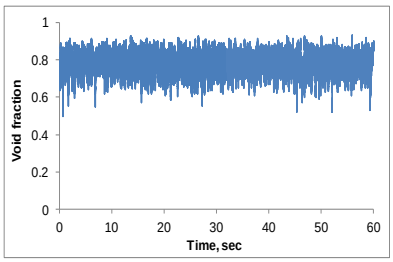	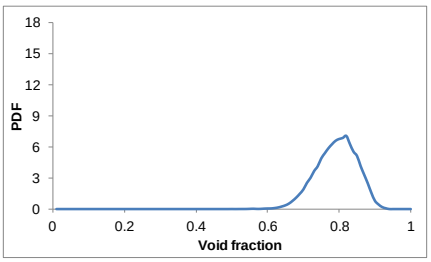
18.56	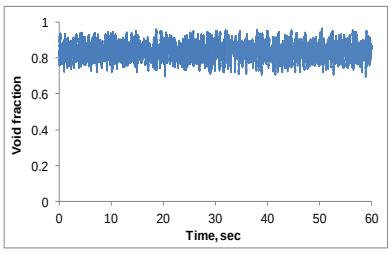	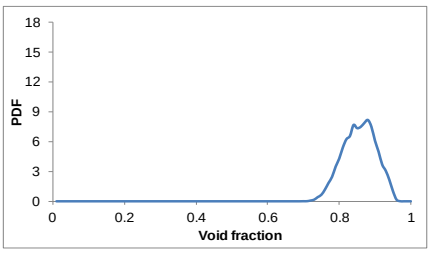

(c) Bottom position (downward)

Figure 5-6 Time traces of the void fraction and their PDFs, at the top, middle and bottom positions of the downward section for different gas superficial velocities and for a fixed liquid superficial velocity of 1 m/s

Investigation of flow regimes along the downward flow was extended further by analysing the PDFs' data, which are plotted against various velocities of air with water velocities of 0.48 and 0.7 m/s, as presented in Figure 5-7. Different shapes of PDF are observed for different flow conditions; consequently various flow regimes are formed. Examining PDFs at the top position did not show any discrepancies for water superficial velocities of 0.48 and 0.7 m/s. The plots showed that, the same flow regime varied from intermittent to annular flows. An intermittent flow is observed with the base spanning from 0.6 to 1. For water superficial velocity of 0.48 m/s, the maximum height of the PDF for each particular air flow rate is similar to that of water superficial velocity of 0.7 m/s. For the highest air velocity, the annular flow regime with a narrow peak at high PDF of the void fraction value is dominant for both velocities of water (i.e. 0.48 and 0.7 m/s). With water superficial velocity of 0.48 m/s, the observed flow regimes at the middle position are substantially different from those observed at the same position for water superficial velocity of 0.7 m/s. The dissimilarity is particularly identified when the flow is in the intermittent region (for example, at air superficial velocity of 0.25 m/s).

Analysis of PDFs' data at the bottom position for both velocities of 0.48 and 0.7 m/s shows that, there are considerable differences for the lowest flow rate, while they showed a similar tendency for the rest of the flow rates. However, maximum PDF values were observed to be higher for the water superficial velocity of 0.48 m/s.

Comparison of PDFs' data at the top, middle and bottom positions confirms that, the PDFs at all positions do not show any significant differences for the lower water superficial velocity of 0.48 m/s. It can be noted that, the intermittent flow was recognised by broadening the base values of void fraction. The PDF shape moved to a higher value of the void fraction for the highest air superficial velocity. On the other hand, for water superficial velocity of 0.7 m/s, a significant difference is observed between the three positions when the low flow rate is applied.

The dissimilarity between the PDF curves of the three positions is based on the fact that, the flow starts to develop on entering the middle position and reaches full development on entering the bottom position.

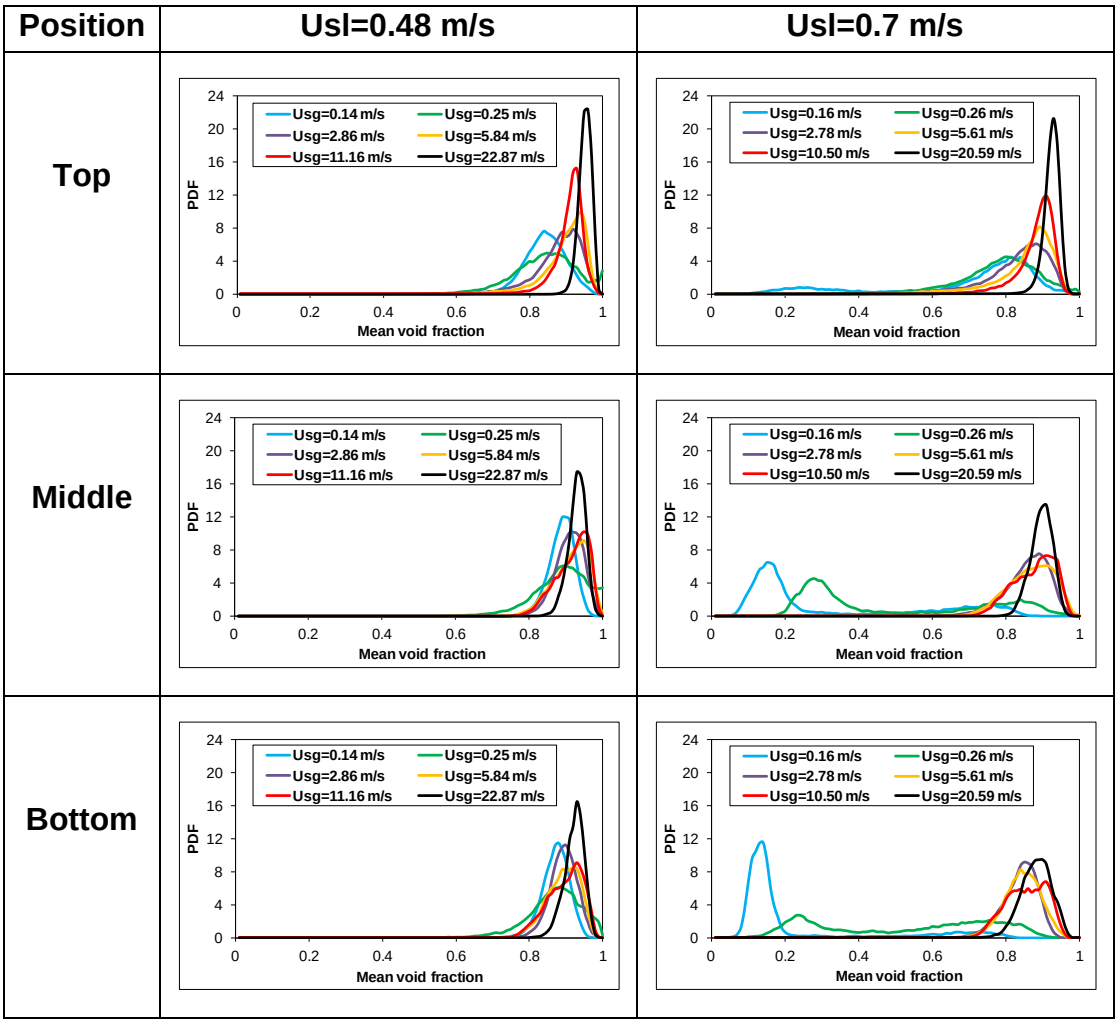

Figure 5-7 PDFs of the average void fraction at the top, middle and bottom positions of the downward section, for different air superficial velocities and for water superficial velocities of 0.48 and 0.7 m/s

5.1.2.4 Time traces and PDFs for the upward section

Figure 5-8 presents a comparison between the top, middle and bottom positions along the upward section for time trace and PDF of the void fraction, at different flow conditions. The time trace data for the three (top, middle and bottom) positions shows that, the flow regime is classified as bubbly flow accompanied by a huge number of high fluctuations on the interface between the air and water flows, for gas superficial velocity and liquid superficial velocity of 0.17 and

1 m/s respectively. This is due to the existence of spherical cap bubbles within a continuous liquid phase. The PDFs of the averaged void fraction values at these velocities also show that, the observed flow regime for the three positions can be classified as bubbly. It is clear from the plots that, the shape of PDFs is similar for all positions. However, the maximum void fraction of the PDF is noted to be a little higher at the top position than those at the middle and bottom positions, suggesting the cap bubble size increased, which is due to the reduced pressure as the bubble moves towards the top of the pipe.

When gas velocity is increased to 0.52 m/s, and liquid velocity is kept fixed at 1 m/s, the time traces of the void fraction are similar for all positions. However, it is clear from Figure 5-8 that, the peak height of the PDF at the bottom position is a little lower than those at the higher positions. The height of the former is about 4.5, and about 6 for the latter. The plots of the PDFs confirm that, a bubbly to intermittent flow transition is occurring at all positions. The flow regime observed at the bottom location, is accompanied by a wide base spanning from 0 to 0.6. The existence of large bubbles in a liquid phase contributes to the wide base of void fraction values.

At gas velocity of 1.02 m/s, the time traces data show that there is a good agreement between both the middle and top positions, where intermittent flow is identified. The time traces characteristics at the bottom position are identified by larger fluctuations. Examining the PDF data at the bottom position clearly shows a single peak with a broad base of void fraction values extending to 0.6. On the other hand, double peaks of PDF at void fractions of 0.22 and 0.47 are observed at the middle position. The characteristic of PDF at this position is indicating an intermittent flow. Similar flows are identified at the top position having double peaks with void fractions of 0.2 and 0.5 respectively. As mentioned above, the flow regime at the middle and top positions is likely to be an intermittent flow.

With increasing the gas superficial velocity further to 2.67 m/s, the time trace results show extreme similarity between all positions, where the variations of the void fraction signals are very large at all positions. It can be noted from the

shape of the PDF plots that, an intermittent flow regime still exists with a wide base spanning from 0.2 to 0.7 at the bottom position, and from 0.3 to 0.8 at both the middle and top positions.

For the highest gas velocity of 18.56 m/s with liquid velocity remaining constant at 1 m/s, analysing the time traces of the cross-sectional void fraction at the middle and top positions shows that, there is a great deal in terms of the signal characteristics, where the frequency appears to be very high in both cases. Larger oscillations of the void fraction signal are noted at the bottom position, due to the small effects of the bottom bend. The PDF plots show the same flow regime for all positions, which is annular with a narrow peak at the high void fraction values, although the peak height of the PDF is lower in the case of the bottom position than those at higher positions.

Usg, m/s	Time trace	PDF
0.17	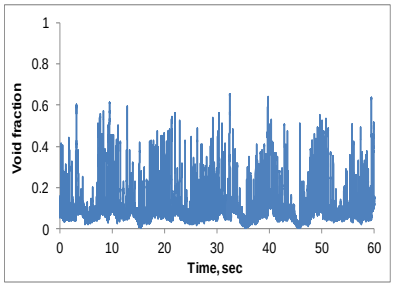	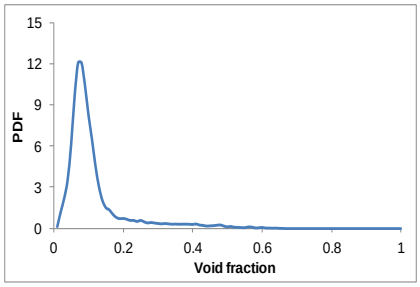
0.52	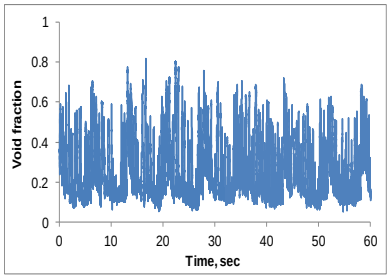	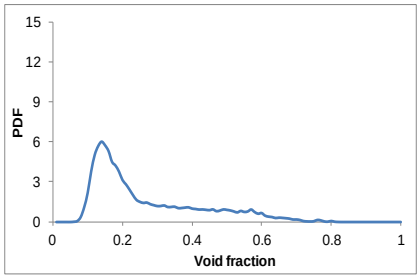
1.02	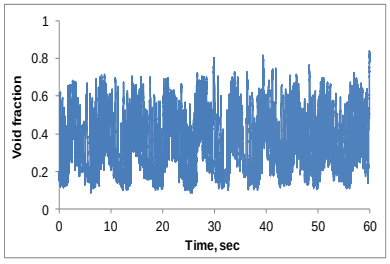	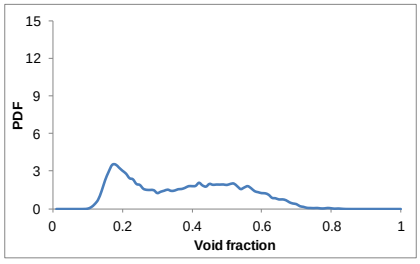
2.67	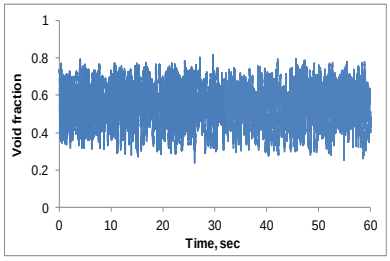	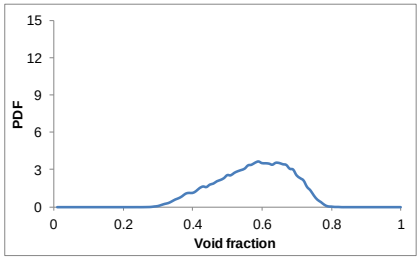
18.56	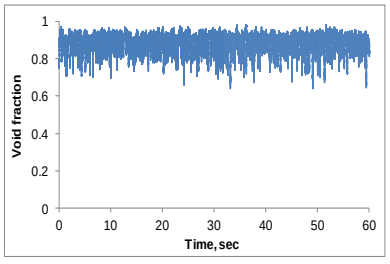	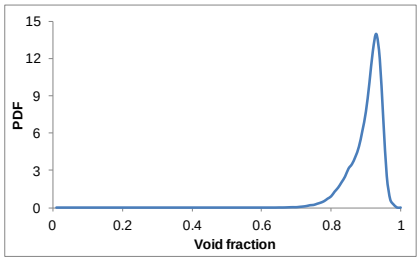

(a) Top position (upward)

Usg, m/s	Time trace	PDF
0.17	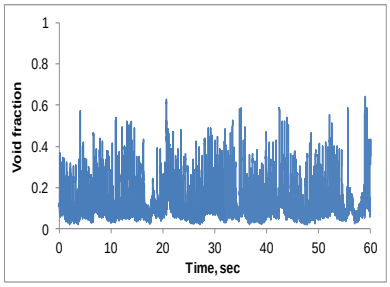	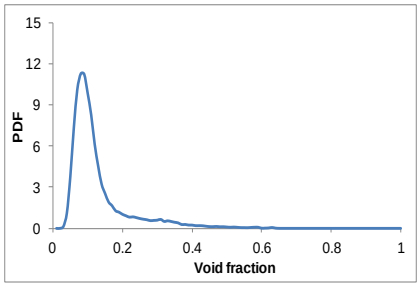
0.52	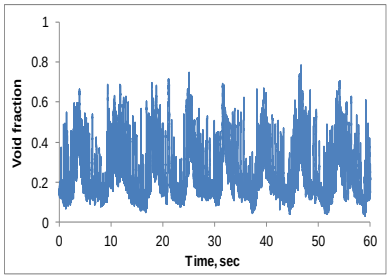	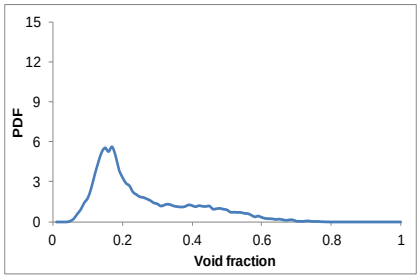
1.02	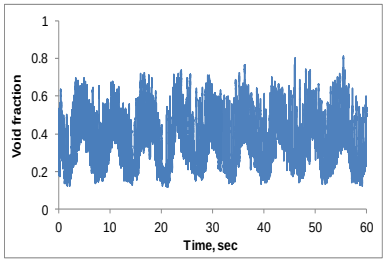	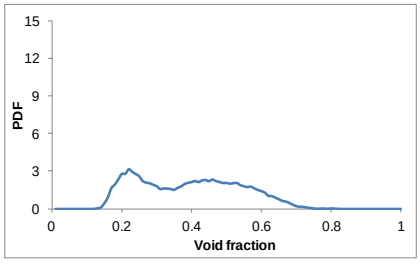
2.67	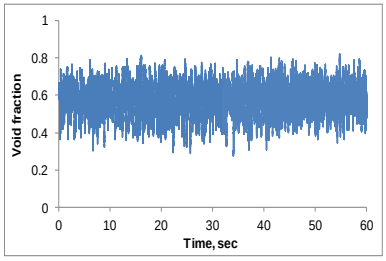	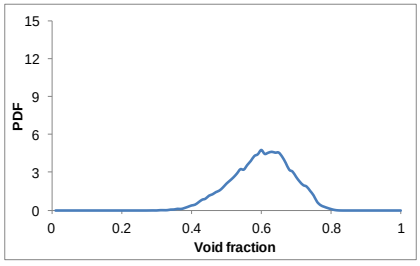
18.56	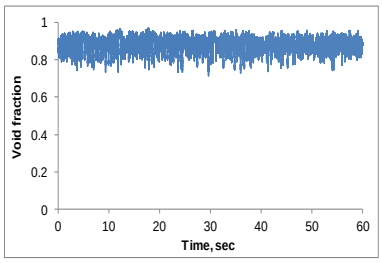	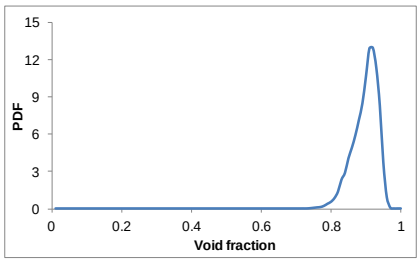

(b) Middle position (upward)

Usg, m/s	Time trace	PDF
0.17	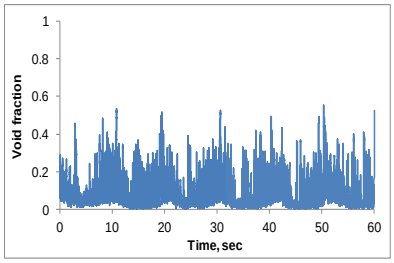	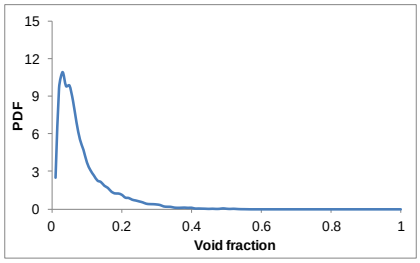
0.52	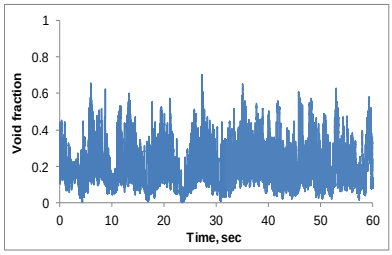	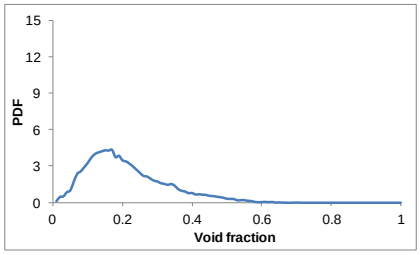
1.02	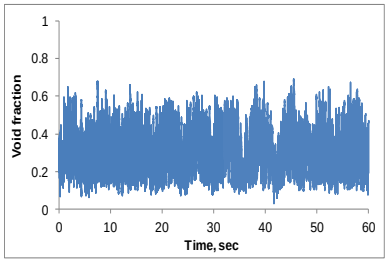	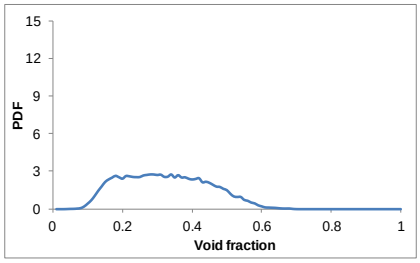
2.67	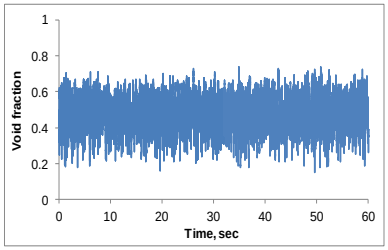	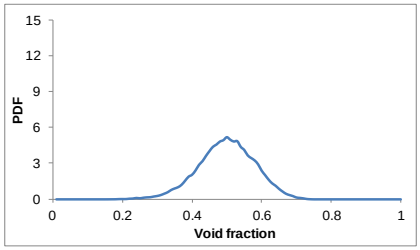
18.56	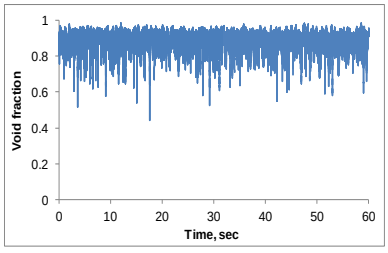	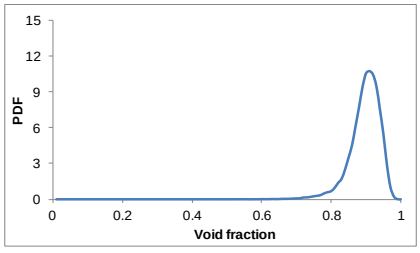

(c) Bottom position (upward)

Figure 5-8 Time traces of the void fraction and their PDFs respectively at the top, middle and bottom positions of the upward section for different gas superficial velocities and for a fixed liquid superficial velocity of 1 m/s

Figure 5-9 comprises PDFs' data obtained at the top, middle and bottom positions of the upward section for different air velocities, and for water superficial velocities of 0.48 and 0.7 m/s. It can be seen that, for the same flow rates, the PDFs are consistent with a striking similarity for all positions. Bubbly flow with a long tail extended to the high values of void fraction, was observed for air and water superficial velocities of 0.14 and 0.48 respectively. Examining the reconstructed images of this condition confirmed that, the bubbly flow regime was accompanied by a large number of spherical cap bubbles within a continuous liquid phase.

In general, the PDFs show similar shapes for all positions for water velocity of 0.48 m/s. The shape of the PDFs did not change even for higher water superficial velocity of 0.7 m/s. The extracted PDFs' data for water superficial velocity of 0.7 m/s showed that, the observed flow regime for the three positions is bubbly with air superficial velocity of 0.16 m/s. For higher air velocity of 0.26 m/s, the PDF at all positions presented a similar shape, indicating transition from bubbly to intermittent. For air superficial velocities of 2.78 and 5.61, an intermittent flow with a wide base is identified for both water superficial velocities of 0.48 and 0.7 m/s. The broad base of void fraction is due to continuous large bubbles present in the liquid body. For the highest flow rates, annular flow with a single peak at high void fractions is identified at the three positions.

Position	Usl=0.48 m/s	Usl=0.7 m/s
Top	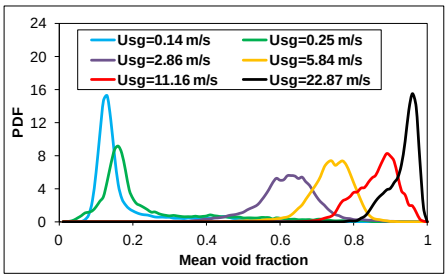	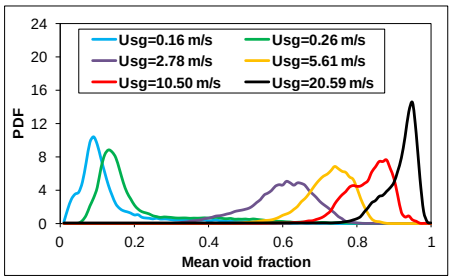
Middle	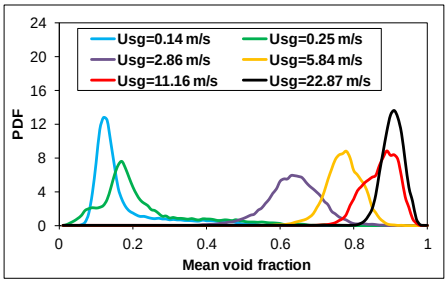	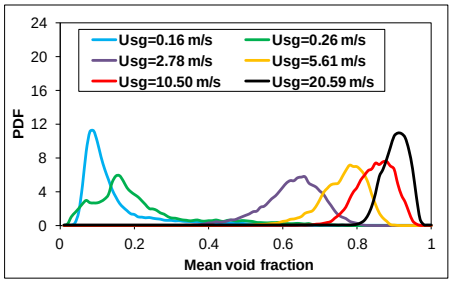
Bottom	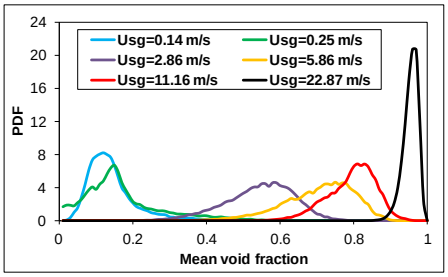	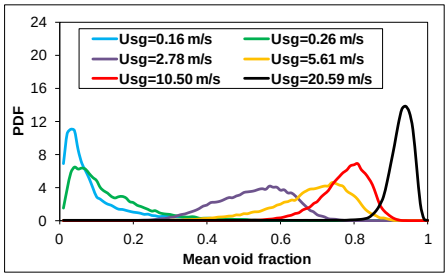

Figure 5-9 PDFs of the average void fraction at the top, middle and bottom positions of the upward section, for different air superficial velocities and for water superficial velocities of 0.48 and 0.7 m/s

5.1.2.5 Comparison of flow regimes before and after the U-bend

Figure 5-10 (a-d) presents a comparison of the PDFs of void fraction at 5 pipe diameters, before and after the U-bend (i.e. at the bottom positions of the downward and upward sections respectively). In all plots, the red colour indicates the flow behaviour at 5 pipe diameters before the U-bend (i.e. at the lower position of the downward section), and the light blue colour indicates the flow behaviour at 5 pipe diameters after the U-bend (i.e. at the lower position of upward section). The comparison was made for a number of gas superficial velocities while liquid superficial velocity was maintained constant at 1.2 m/s.

At air superficial velocity of 0.17 m/s and water superficial velocity of 1.2 m/s, as presented in Figure 5-10 (a), the identified flow regime before and after the U-bend is a bubbly. However, the PDF length for both positions is substantially different. The value of PDF after the U-bend is higher, reaching 18 with a quite narrow void fraction value spanning to a higher void fraction value of about 0.2. In contrast, the maximum height of the peak of PDF before the U-bend is 10 with void fraction values extending to 0.2. For both positions and under these conditions, there were elongated large bubbles separated by a continuous liquid phase. This is due to the void fraction variations along these sections. When the gas superficial velocity is increased to 0.53 m/s (Figure 5-10 (b)), the large bubbles coalesce together resulting in the intermittent flow having a "hill" shape in the bottom position of the upward section (just after the bottom bend). On the other hand, an intermittent flow with double peaks and a "hill" shape was formed at the same position of the downward section (just before the bottom bend). By increasing the gas superficial velocity to 1.05 m/s and maintaining the same superficial liquid velocity at 1.2 m/s, as presented in Figure 5-10 (c), double peaks at 2 and 3 values were identified on the PDF plots at the lower position before the U-bend, corresponding to an intermittent flow regime. At the same position after the U-bend and under the same conditions, the flow was also intermittent but exhibits a single peak with a maximum height of 4.

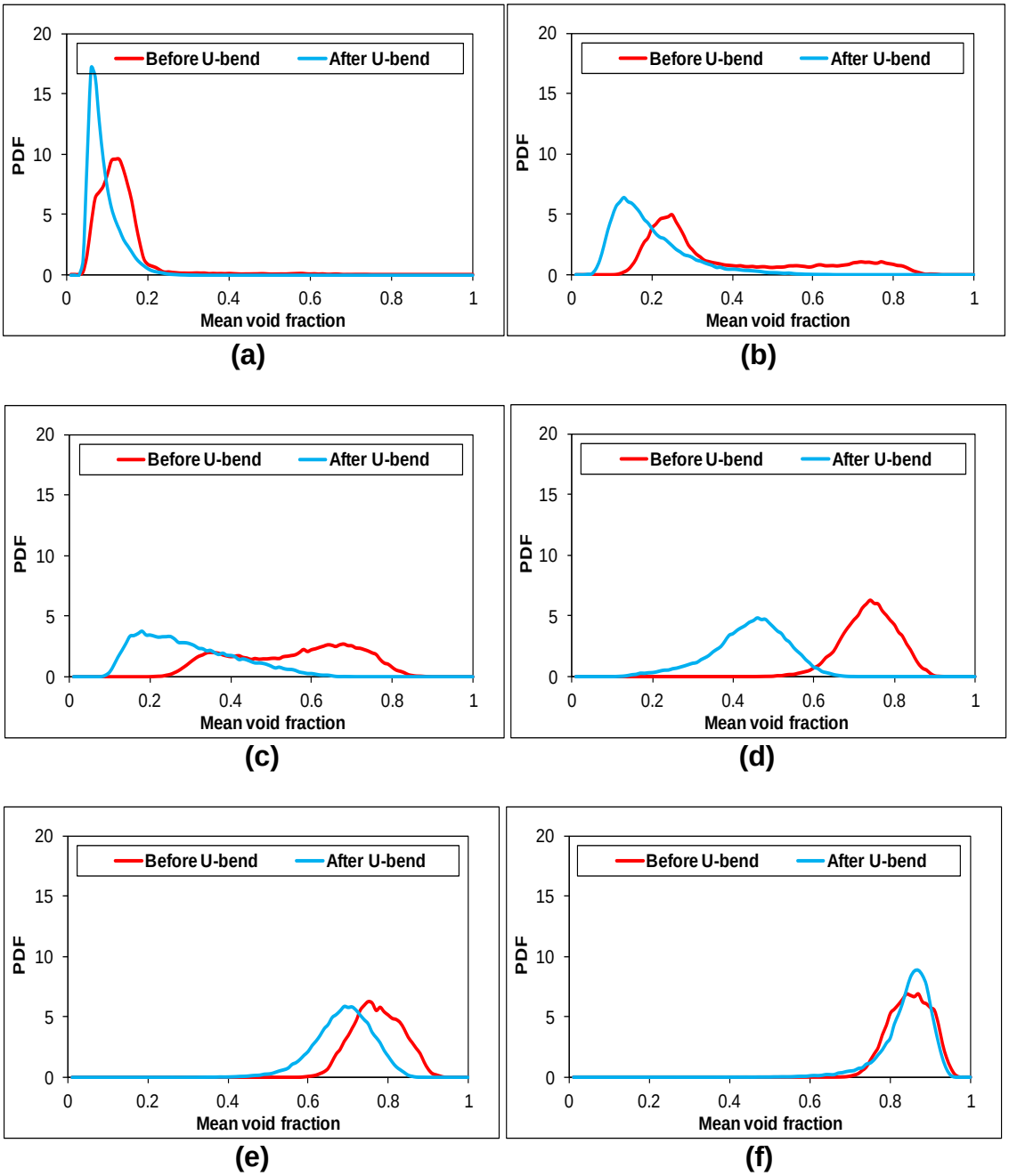

Figure 5-10 Time traces (a) and PDFs (b) of the void fraction before and after the U-bend for air superficial velocities of (a) 0.17, (b) 0.53 (c) 1.05, (d) 2.63 (e) 9.32 and (f) 17.55 m/s and water superficial velocity of 1.2 m/s

With increasing the gas superficial velocity to 2.63 m/s, while the liquid superficial velocity remains constant at 1.2 m/s, an intermittent flow regime is still present at both positions, as shown in Figure 5-10 (d). The PDF shape before the U-bend appears as a single peak with a broad base spanning from 0.55 to 0.9, while a single peak of PDF identified after the U-bend has a wide base range extending to 0.65. With an increase of the gas superficial velocity to

9.32 m/s (Figure 5-10 (e)), the flow regime before the U-bend is classified as an intermittent to annular flow transition. The flow regime observed after the U-bend was still an intermittent flow. One interesting observation is that, the PDF shape for both positions is following the same pattern. At gas and liquid superficial velocities of 17.55 and 1.2 m/s respectively, the annular flow regime is approached at both positions with a similar shape to the PDF, as illustrated in Figure 5-10 (f). This suggests that, the flow regime becomes the same over all the sections of the pipe when higher flow conditions are applied.

Figure 5-11 (a-d) illustrates a comparison of the PDFs at 5 pipe diameters before and after the U-bend, for lower liquid superficial velocity of 0.07 m/s and gas superficial velocities of 0.14, 3.05, 12.75 and 29.83 m/s. It can be seen that, the flow regime at 5 pipe diameters before the U-bend is different from that observed at 5 pipe diameters after it, particularly when the gas velocity is low. The plots of Figure 5-11 (a) confirm that the annular flow is formed before the U-bend, while the flow regime observed after the U-bend location is intermittent. When the gas superficial velocity increases to 3.05 m/s, and maintaining the velocity of liquid at 0.07 m/s, PDF demonstrates that the annular and intermittent flows still exist at the same position, before and after the bend respectively, as shown in Figure 5-11 (b). Again, annular and intermittent flows were still present before and after the U-bend, with the gas superficial velocity of 12.75 m/s (Figure 5-11 (c)). By increasing the gas superficial velocity further to 29.83 m/s, it was not surprising to observe an annular flow regime for both positions, as illustrated in Figure 5-11 (d). This was expected due to the fact that, the annular flow is well established at high gas flow rates.

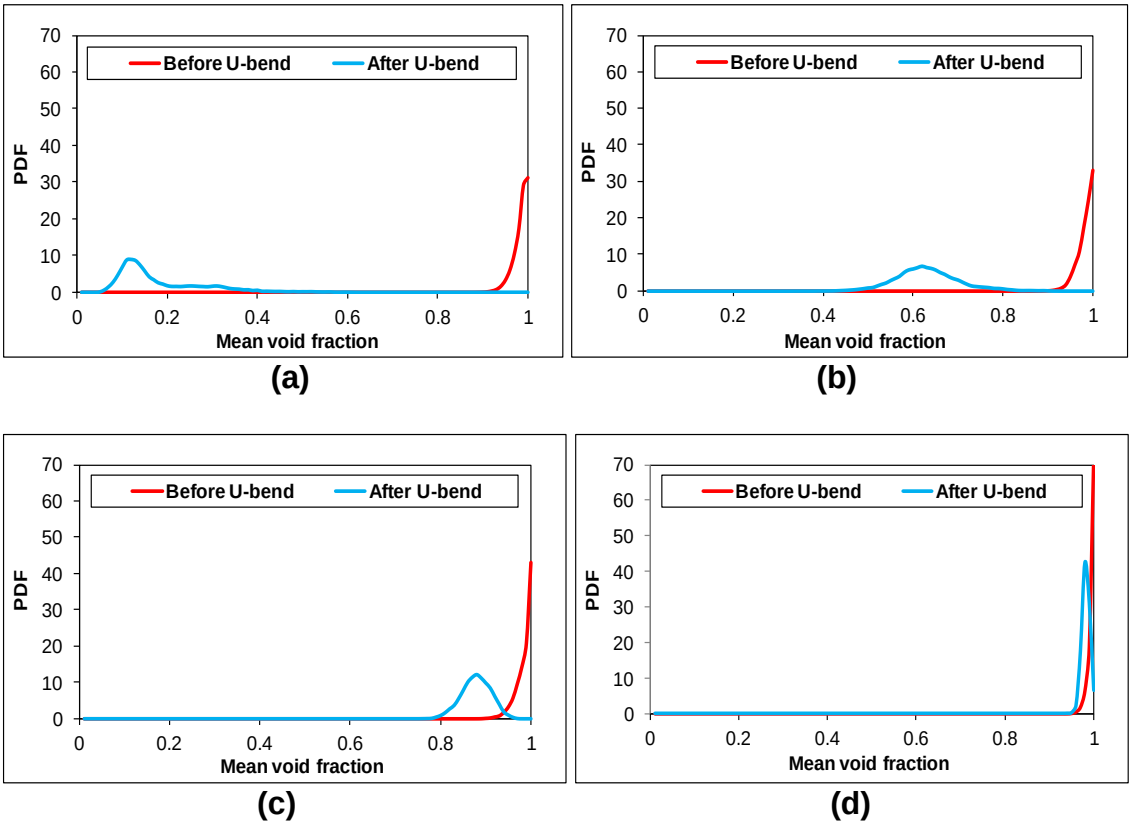

Figure 5-11 PDFs of the void fraction identified before and after the U-bend for air superficial velocity of (a) 0.14, (b) 3.05, (c) 12.75 and (d) 29.83 m/s and for fixed water superficial velocity of 0.07 m/s

5.1.3 Flow regime map for downward and upward flows

The simplest way to create a flow regime map is to determine the region of each flow regime in term of velocities of gas and liquid, and then make a relationship between them as X and Y axes. Various flow regime maps have been found in the literature; however, there were some discrepancies between most of them. This was due to the fact that they were extremely dependent on direct visualisation, operational conditions, pipe orientation and the diameter. All these factors could contribute to the creation of different flow regime maps. Therefore, such maps need to be established very carefully by estimating the actual range of the flow regime transition.

5.1.3.1 Flow regime maps for downward flow

The flow regime maps for the top, middle and bottom positions are presented in Figure 5-12 (a-c) for various air and water superficial velocities. It can be noted

from Figure 5-12 (a-c) that the bubbly, intermittent and annular flows are present for all three axial positions. The dominant flow regime in the downward section is annular. The boundary between the bubbly flow region and intermittent flow region in the flow regime map, for the top position corresponds to a higher liquid and lower gas velocity than that at the middle and bottom positions. However, the boundary between the intermittent flow region and the annular flow region in the flow regime maps related to all positions are similar. Overall, the flow maps for both middle and bottom positions are very similar. This suggests that, the 180º top bend has a major influence on the flow characteristics at the top position. The influence is much reduced when the flow reaches the middle and bottom positions.

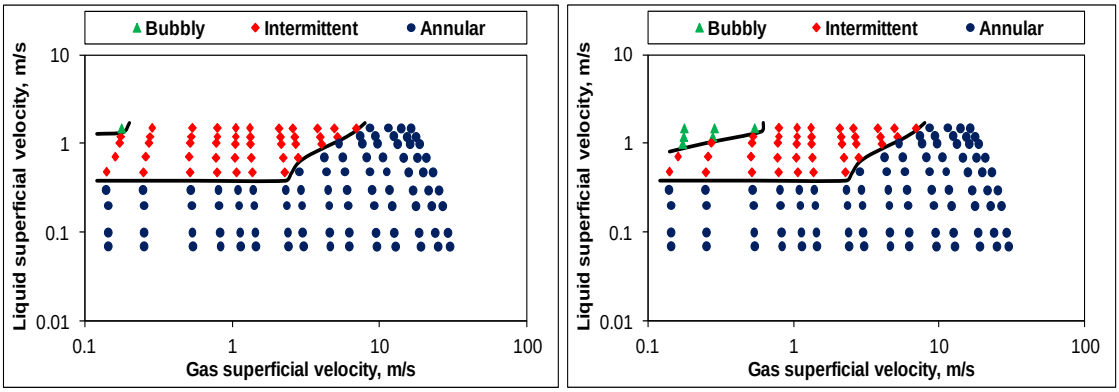

(a) Top position **(b) Middle position**

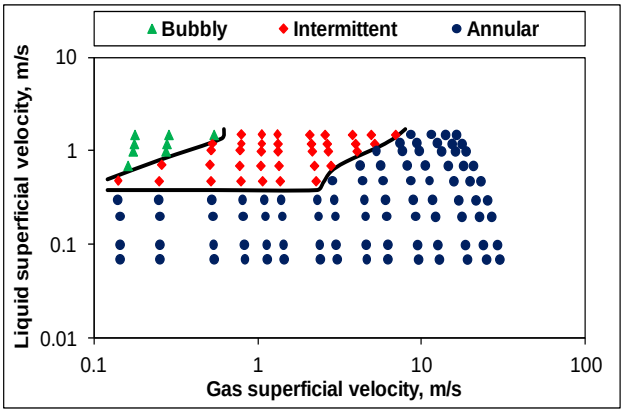

(c) Bottom position

Figure 5-12 Flow regime maps at (a) top, (b) middle and (c) bottom positions of the downward section

5.1.3.2 Comparison of the present study with that of Barnea et al.'s (1982) downward flow regime map

Barnea et al. (1982) attempted to predict the gas/liquid flow regimes in downward pipes. They argued that, the transition from bubbly to intermittent flow will occur when the bubble size is sufficiently large, so that bubble coalescence occurs. They proposed an equation to determine the flow condition of the transition by using pipe diameter and fluid properties. They also suggested that, the transition between intermittent flow and annular flow will happen when the liquid void fraction is higher than 0.65. The flow regime maps obtained from this study were compared with those predicted by Barnea et al. (1982). Figure 5-13 shows the comparison between the flow regime map at the middle position of the downward section and Barnea et al.'s (1982) prediction. It is noted that, the boundary between the bubbly flow region and intermittent flow region related to the flows at the middle position matches the predicted boundary fairly well, though is slightly overestimated in terms of the liquid velocity. However, for the boundary between the intermittent flow region and annular flow region, the predicted one significantly overestimates the liquid velocity at which the transition occurs. This perhaps suggests that, the criteria for flow regime transition need modifying when being applied to downward flows in large diameter pipes.

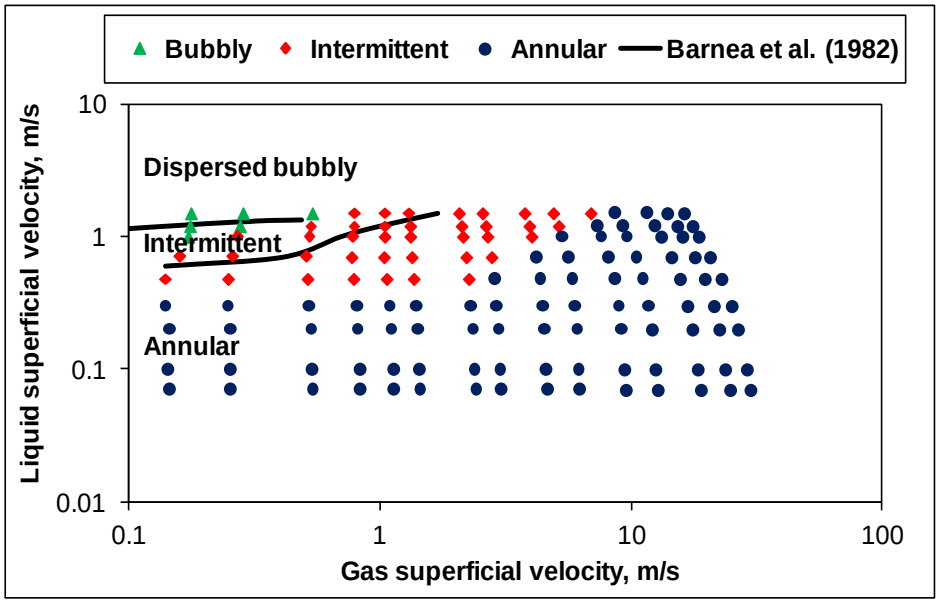

Figure 5-13 Comparison between the flow regime map at the middle position of the downward section obtained from this study and that reported by Barnea et al. (1982)

5.1.3.3 Flow regime maps for upward flow

The vertical upward flow regime maps presented in Figure 5-14 (a-c) represent the flow identified at the top, middle and bottom positions respectively. It can be concluded from these maps that, there is good agreement between the observed intermittent/annular flow regimes' transition boundaries at the three positions, while the bubbly/intermittent boundaries observed at the bottom position were different from those observed at the middle and top positions. It is very clear from the map obtained at the bottom section that, the bubbly/intermittent boundaries are extended to higher air and lower water velocities, as illustrated in Figure 5-14 (c). There is an unstable flow region in the maps with respect to the three positions, for water superficial velocities of 0.2 and 0.3 m/s with air superficial velocity in the range of 0.14-0.52 m/s. These conditions are considered to be particularly critical, as they yield dryout spots along the inner surface of the pipe. This is probably due to the vertical serpentine configuration of the pipeline, as observed by Golan and Stenning (1969). Alternatively, in this kind of pipeline, the lower bends can be periodically blocked by the liquid and then blown through by the accumulated air, which is certainly an undesirable flow regime in heat exchanger facilities.

It can be observed from the produced maps that unstable, bubbly, intermittent and annular flows are identified at different velocities. It can be seen from the generated maps that, an intermittent flow is dominant for all positions.

A similar observation was made by Azzopardi and Wren (2004) who stated that, the possibility of a churn flow formation in a large pipe diameter is much higher than in a small diameter pipe, particularly when the Taylor bubbles are not formed.

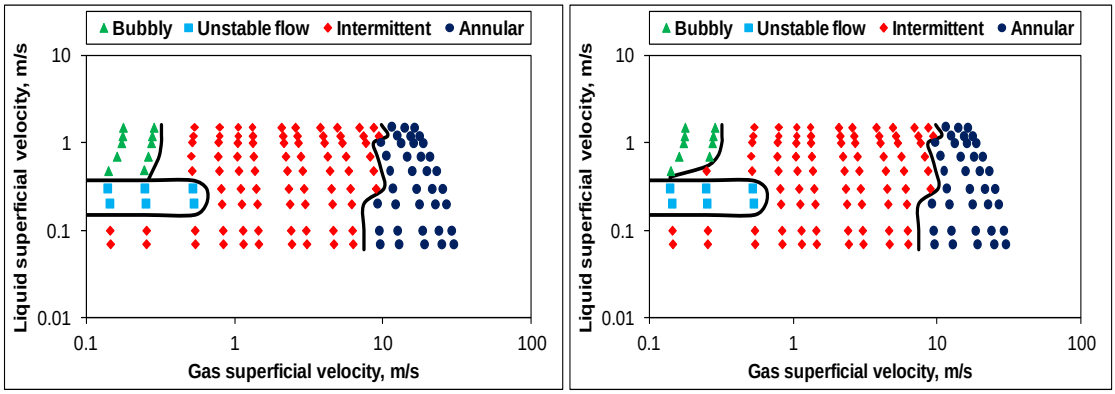

(a) Top position **(b) Middle position**

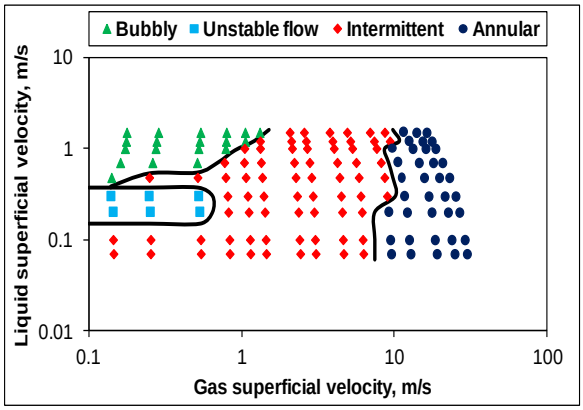

(c) Bottom position

Figure 5-14 Flow regime maps at (a) top, (b) middle and (c) bottom positions of the upward section

5.1.3.4 Comparison of the present study with that of Taitel et al.'s (1980) upward flow regime map

Figure 5-15 shows a comparison between the upward flow regime maps produced from the middle position of the Serpent rig (this study), and that proposed by Taitel et al. (1980) for a 51 mm diameter pipe. It can be noted from Figure 5-15 that, there is a good agreement in terms of the bubbly/intermittent flow regime boundary obtained from both studies; however, the pipe diameter used in the former study is double that used in the latter. The intermittent/annular flow transition boundaries obtained from this study, are somewhat different from those reported by Taitel et al. (1980). It is clear from the map that, the air superficial velocities required to establish annular flow in a 101.6 mm diameter pipe (current study) are lower than those required to establish the same flow regime in a 51 mm diameter pipe.

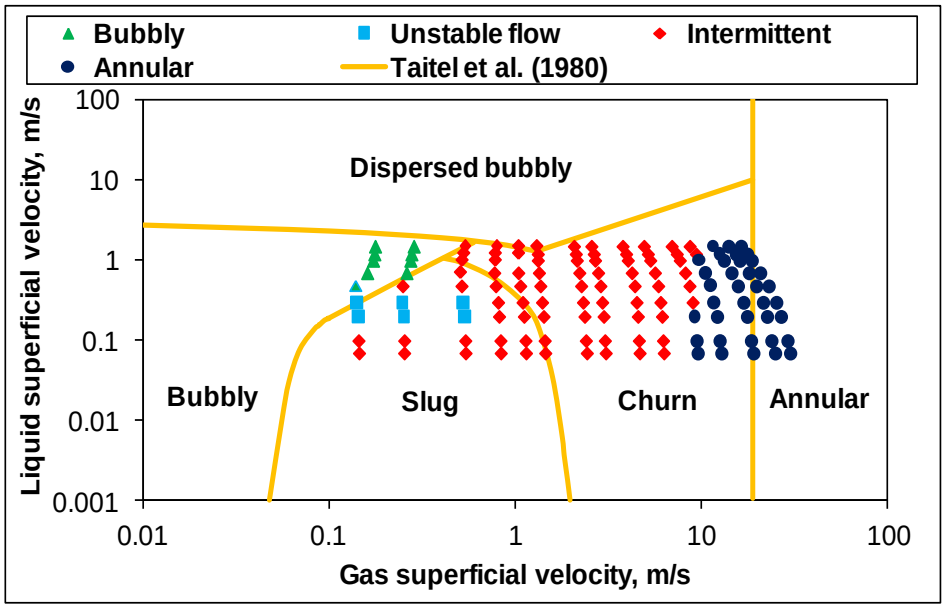

Figure 5-15 Comparison between the flow regime map at the middle position of the upward section obtained from this study and that reported by Taitel et al. (1980) for a 51 mm diameter pipe

5.2 Void fraction development in downward and upward flows

Efforts have been made to gain a deep understanding of the effects of 180^{o} bends on the void fraction development along the serpentine pipe geometry. The work presented in the subsections includes identification of the void fraction development along downward and upward flows.

5.2.1 Void fraction development in the downward flow

5.2.1.1 Effect of air and water superficial velocities on mean void fraction along the downward flow

Figure 5-16 (a-c) illustrates a relationship between air superficial velocity and mean void fraction. The comparison was made at the top, middle and bottom positions of the downward section for water superficial velocities of 0.07, 0.2, 0.48,1 and 1.5 m/s.

In all plots of Figure 5-16 (a-c), it is very clear that there is a similar tendency over all superficial velocities of air and water tested. At water superficial velocities of 1 and 1.5 m/s, as shown in Figure 5-16 (a), the mean void fraction values increase substantially when the air superficial velocities are between 0.17 and 2 m/s. Similar observations were made for middle and bottom positions, as presented in Figure 5-16 (b) and (c) respectively. It can be seen from the plots that, the mean void fraction values of the three positions are close to each other, when the water superficial velocities of 0.07, 0.2, 0.48 m/s. It could be suggested that, the mean void fraction variations are less sensitive at low liquid flow rates. It is worth mentioning that, the mean void fraction values at the top position were extremely different from those identified at the middle and bottom positions, when relative high liquid flow rates are applied. For instance, at water superficial velocities of 0.48, 1 and 1.5 m/s, and air superficial velocity was kept fixed at 0.17 m/s, the mean void fraction values are 0.84, 0.51 and 0.29 respectively, while the void fraction values at the middle position and for the same conditions are 0.88, 0.17 and 0.11 respectively. These values are close to those obtained at the bottom position. The discrepancies between the top position and the other two positions can be attributed to the fact that the top

position is located close to the top bend, where the bend effect is higher. This effect is reduced as the flow reaches the middle and bottom positions, and consequently the flow becomes more evenly distributed.

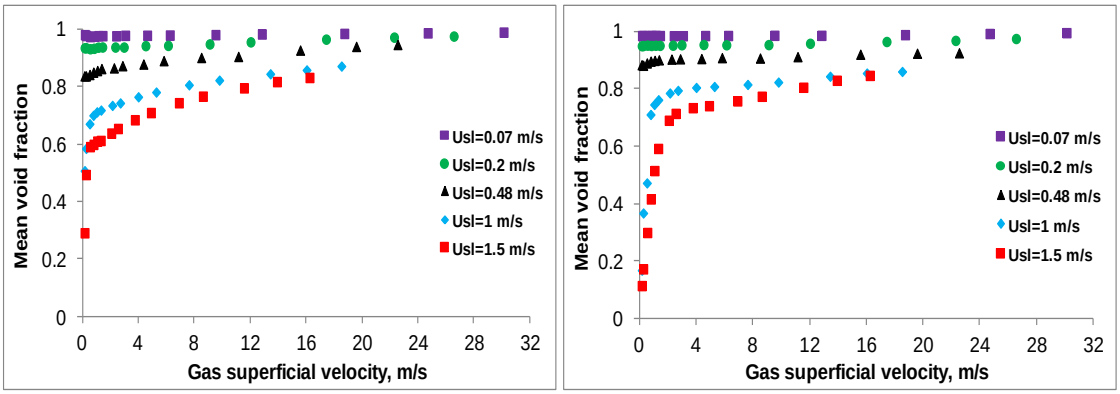

(a) Top position **(b) Middle position**

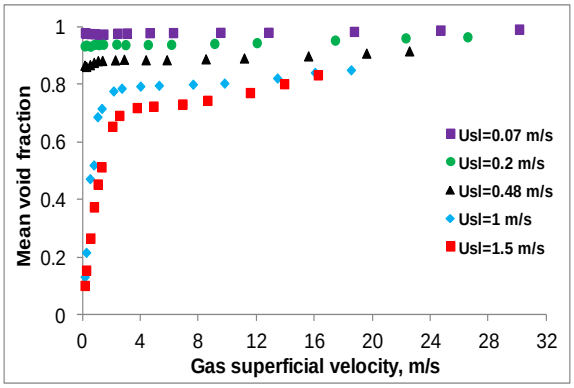

(c) Bottom position

Figure 5-16 Effects of the air and water superficial velocities on the void fraction development at the top, middle and bottom positions of the downward section

Effects of air and water superficial velocities on the void fraction development were investigated further, by plotting the mean void fraction against the gas superficial velocities for a given liquid superficial velocity. The comparison was made at the top, middle and bottom positions of the downward section, as illustrated in Figure 5-17 (a-f).

It can be seen from Figure 5-17 (a-f) that, the mean void fractions at the three positions present a similar tendency, in which they are increased with air superficial velocity. However, the mean void fraction values are increased moderately at the three positions for water superficial velocities of 0.07, 0.2 and 0.48 m/s. Also, it is observed that the mean void fraction values at the top, middle and bottom positions are very close to each other over all air velocities, and water superficial velocities of 0.07, 0.2 and 0.48 m/s, as presented in Figure 5-17 (a-c) respectively. This indicates that the annular flow is well established along the whole downward section, in which the liquid film and liquid entrainment are dominant.

For higher water superficial velocities of 0.7, 1 and 1.5 m/s, the mean void fraction values at the three positions are observed to increase substantially, particularly for low air superficial velocities (lower than 4 m/s), as shown in Figure 5-17 (d-f) respectively. It can be seen from the plots of Figure 5-17 (d-f) that, the values of the mean void fraction obtained at the middle and bottom positions are lower than those at the top position, when low air superficial velocities are used. This indicates that, the local air velocity becomes considerably higher as the fluids are moved towards the lower locations of the downward direction.

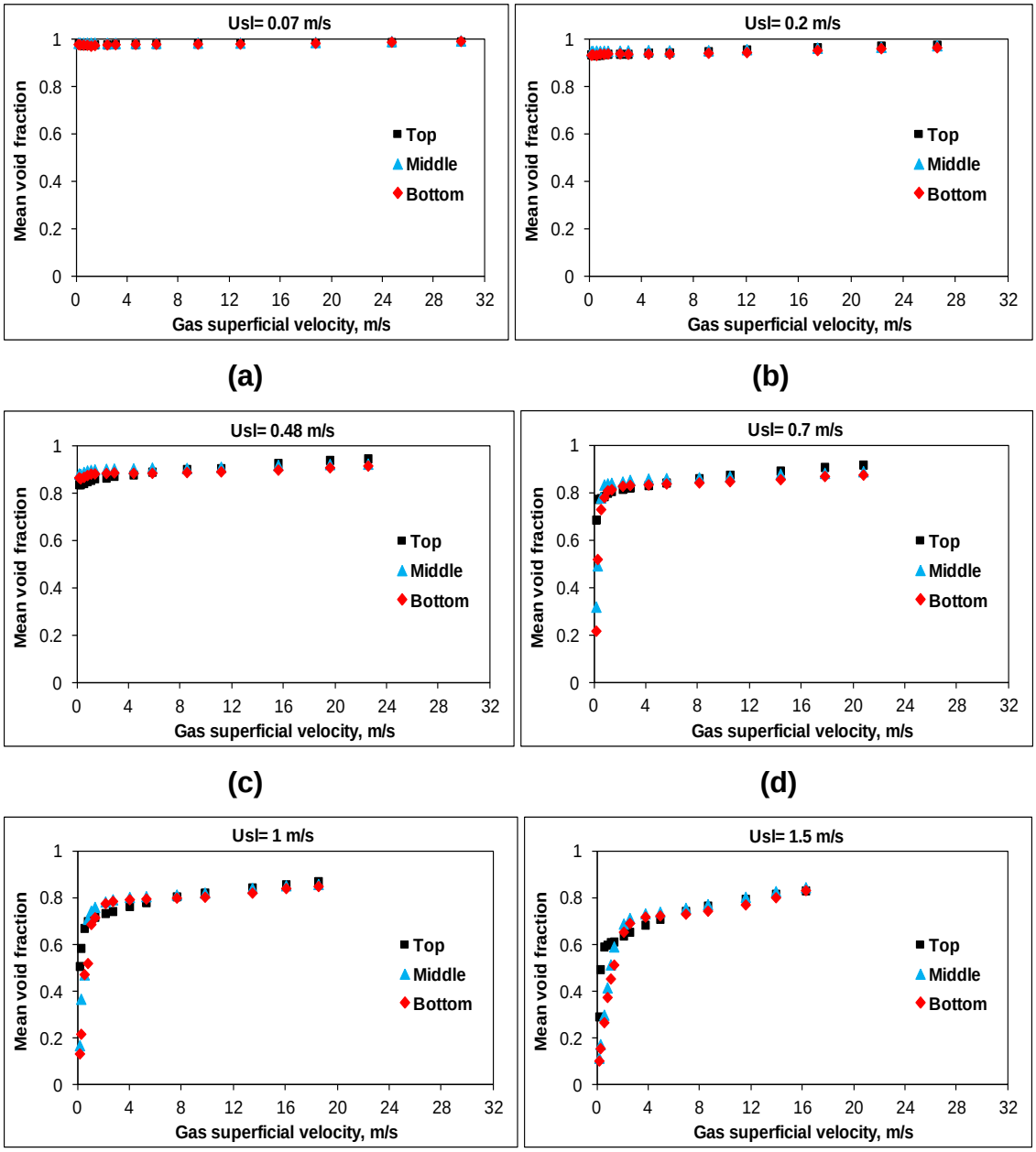

Figure 5-17 Mean void fraction development at the top, middle and bottom positions of the downward section, for different air superficial velocities and water superficial velocities of (a) 0.07, (b) 0.2, (c) 0.48, (d) 0.7, (e) 1 and (f) 1.5 m/s

5.2.1.2 Effect of an axial distance on mean void fraction along the downward flow

In order to address the void fraction development along the pipe, the data shown above was also presented as a void fraction ratio against axial distance (i.e. 5D, 30D and 46D after bend 1), as shown in Figure 5-18 (a-f). Here the void fraction ratio at an axial position, is defined as the ratio of the mean void fraction at that position to that of the bottom position, i.e. 46D after bend 1. From this, at any flow condition the void fraction ratio at the position of 46D is unity. It is observed in Figure 5-18 (a) that with water superficial velocity of 0.07 m/s, and at any air velocity tested the void fraction ratio of the three positions is close to unity. A similar feature can also be found in Figure 5-18 (b) and (c) for water superficial velocities of 0.2 and 0.48 m/s respectively, and some of the flow conditions presented in Figure 5-18 (d), (e) and (f) for water superficial velocities of 0.7, 1 and 1.5 m/s respectively. In these cases, the void fraction shows an insignificant variation against the axial position at lower water flow rates. Indeed at these flow conditions an annular flow regime is well formed in the whole downward pipe section, in which the flow development is manifested via liquid film and liquid entrainment rather than void fraction.

However, when flow regimes other than annular flow are involved, the void fraction decreases significantly when the fluids are flowing down, implying that the local air velocity is becoming significantly higher. In some flow conditions the void fraction development leads to a flow regime transition, e.g. in the case of water superficial velocity of 1 m/s and air superficial velocity of 0.17 m/s (Figure 5-18 (d)) where the flow regime is intermittent at the top position, but becomes bubbly flow occasionally with large bubbles at the middle position. In other cases, e.g. for water superficial velocity of 1.5 m/s and air superficial velocity of 1.05 m/s (Figure 5-18 (f)), the flow regime remains the same; however, due to the reduced void fraction the gas phase is significantly accelerated as it flows towards the bottom.

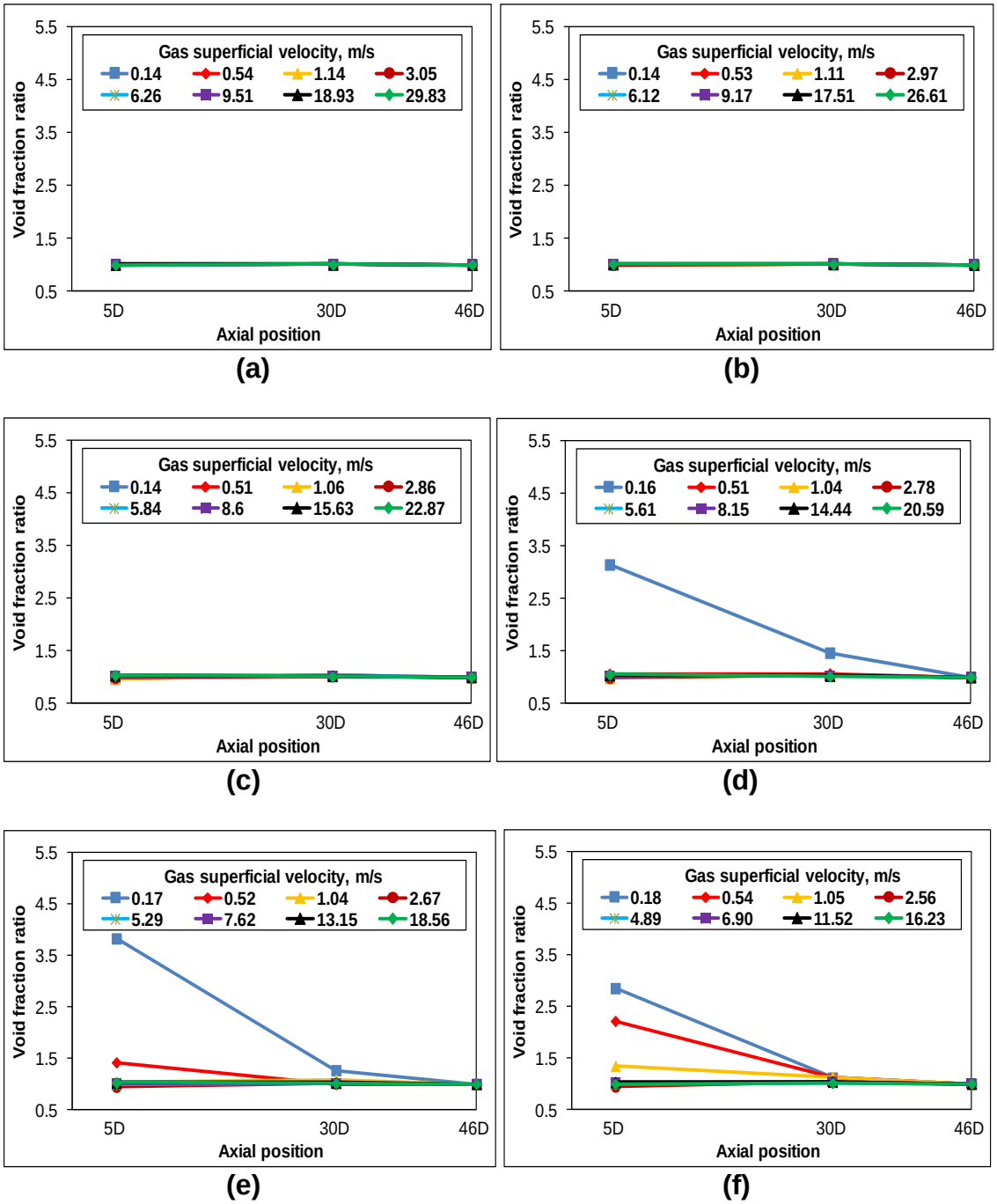

Figure 5-18 Void fraction development along the downward section, for water superficial velocities of (a) 0.07, (b) 0.2, (c) 0.48, (d) 0.7, (e) 1 and (f) 1.5 m/s

5.2.1.3 Local void fraction distribution along the downward flow

The cross-sectional void fraction distributions at different positions, also demonstrate the effect of the upstream top bend on the flow development in the downward section. Figures 5-19, 5-20 and 5-21 show the phase distributions at the top, middle and bottom positions of the downward section respectively, for three different air superficial velocities and at a fixed water superficial velocity of 1 m/s. In Figures 5-19, 5-20 and 5-21, the distributions of the local void fraction along two perpendicular chords are given in (a), and a contour plot of the void fraction distribution is given in (b). It can be seen from the plots of the Figures that, for all air superficial velocities, the void fraction on the 90^o side quarter of the pipe cross section is much less than that of its opposite quarter, i.e. the 270^o side quarter, while the void fraction is distributed fairly evenly along 0^o-180^o direction. As mentioned above, the 90^o position corresponds to the outside curvature of the upstream bend, and 270^o to the inside of the upstream bend, thus the asymmetry of the void fraction distribution over the cross section area of the pipe should be due to the centrifugal effect of the upstream bend. From the plots of the middle and bottom positions (Figures 5-20 and 5-21 respectively), it also can be seen that the void fraction distribution becomes quite symmetric over the cross section areas.

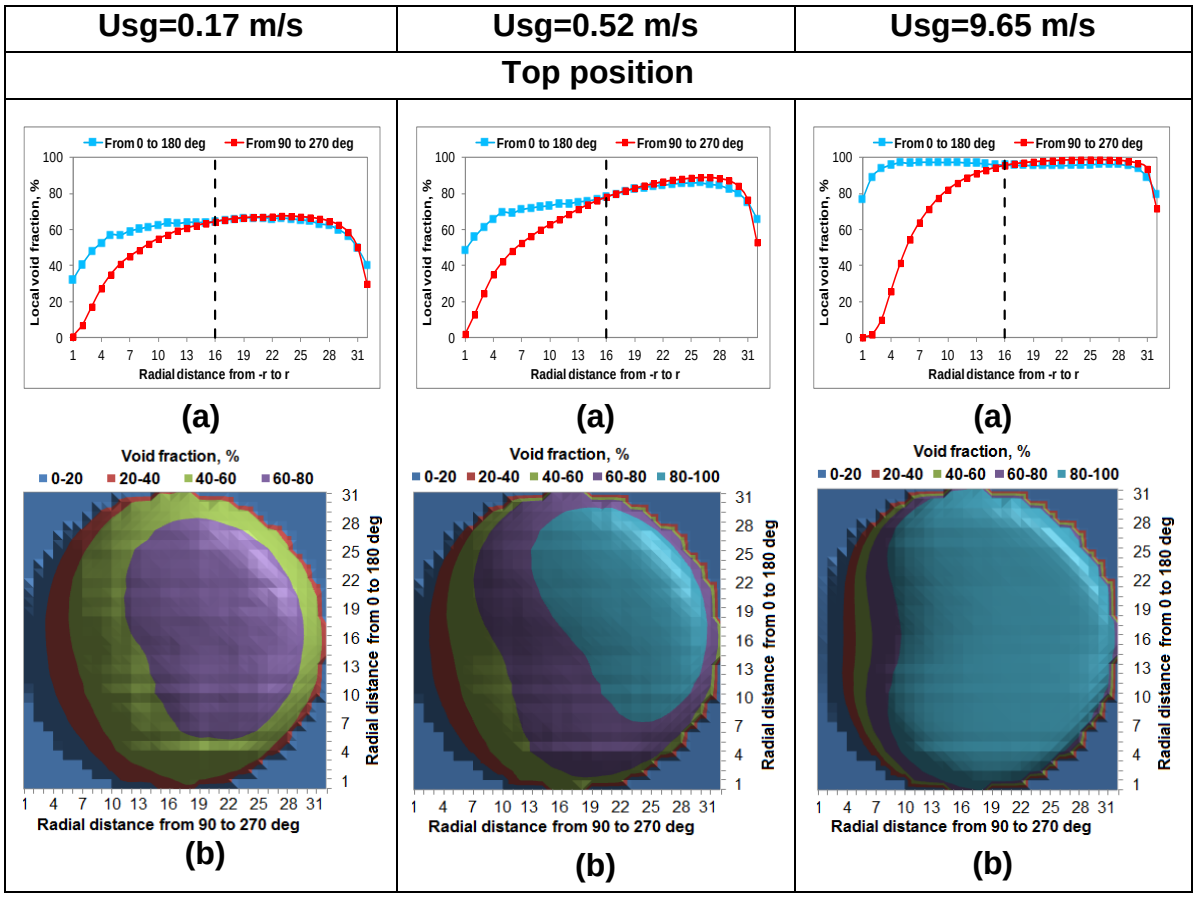

Figure 5-19 Local distributions (a) and contour plots (b) of the void fraction, at the top position of the downward section respectively, for different air superficial velocities and at fixed water superficial velocity of 1 m/s

Usg=0.17 m/s	Usg=0.52 m/s	Usg=9.65 m/s
Middle position		
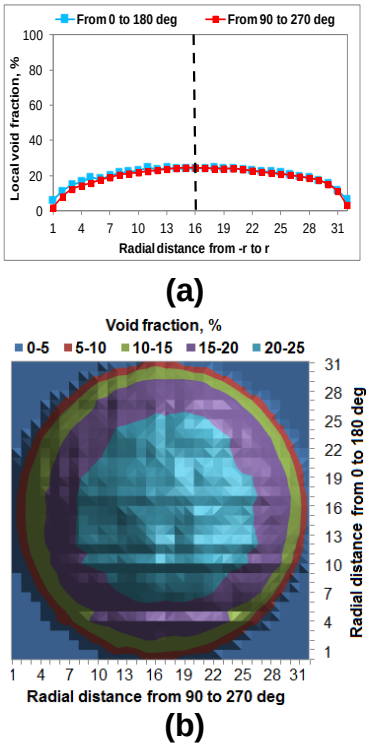	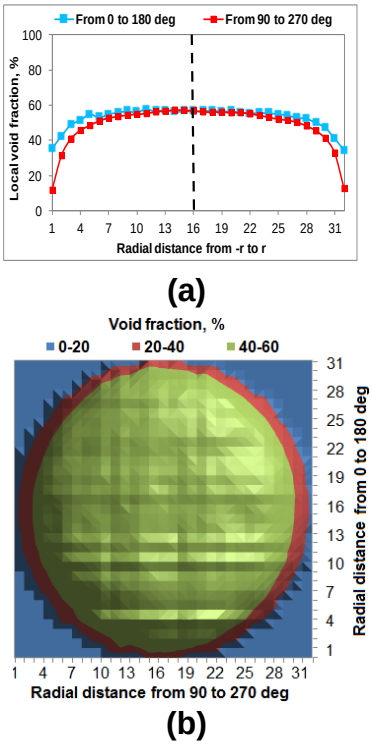	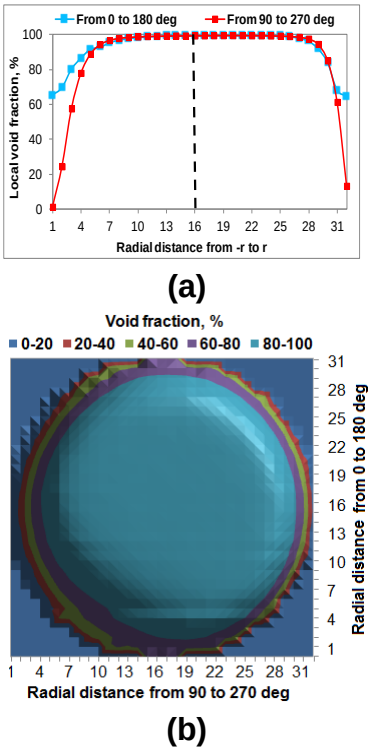

Figure 5-20 Local distributions (a) and contour plots (b) of the void fraction, at the middle position of the downward section respectively, for different air superficial velocities and at fixed water superficial velocity of 1 m/s

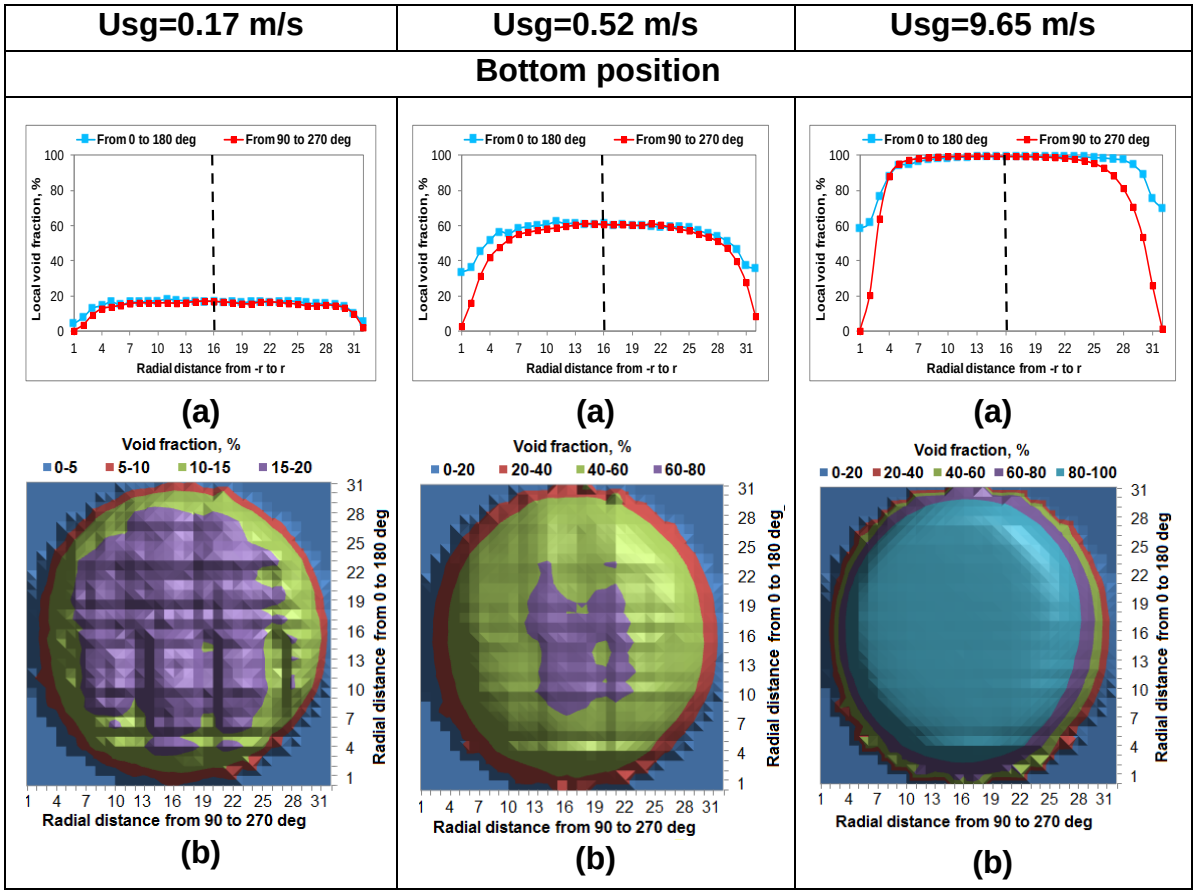

Figure 5-21 Local distributions (a) and contour plots (b) of the void fraction, at the bottom position of the downward section respectively, for different air superficial velocities and at fixed water superficial velocity of 1 m/s

Examining the local void fraction distribution in the downward section of the Serpent rig facility was also extended to include further flow conditions, as presented in Figures 5-22 and 5-23. It can be seen from the plots of the Figures that, there are different distributions of void fraction for different air velocities. Figures 5-22 and 5-23 show plots of local void fraction, against the wire positioned from the pipe wall towards the pipe centre and then from the pipe centre to the other side of the pipe. The data were obtained at the top, middle and bottom positions of the downward sections. The behaviour of the void fraction was obtained at eight gas superficial velocities, and at water superficial velocities of 0.48 and 0.7 m/s. In general, it was found that the void fraction gradually increases and varies as the gas flow rate increases to higher values. The plots of Figure 5-22 (a) and (b) depict the void fraction behaviour, from 90^o to 270^o positions, for water superficial velocities of 0.48 and 0.7 m/s respectively. Both the 90^o and 270^o positions are located inside the quarter of the pipe's cross section in the same direction as the outer and inner curvature of the top bend respectively. The plots of Figure 5-22 (a) show that, the void fraction observed at the middle position demonstrates evidence similar to that observed at the bottom position, however there is little difference. The profile of void fraction was symmetric at both positions (i.e. at the middle and bottom positions). On the other hand, an asymmetric profile of void fraction was identified at the top position. The void fraction profile at this position did not match those at the lower positions, due to impact of top bend on the 90^o side quarter of the top position. The bend impact was reduced when the flow reached the middle position.

For water superficial velocity of 0.7 m/s (Figure 5-22 (b)), the void fraction profile at the top position was also an asymmetric and different from those obtained at the middle and bottom positions. This was attributed to the bend effect observed at the top position. The void fraction profile at the lower (middle and bottom) positions was symmetric, implying that the bend effect was reduced when the flow reached the middle position of the downward section.

Position	Usl=0.48 m/s
Top	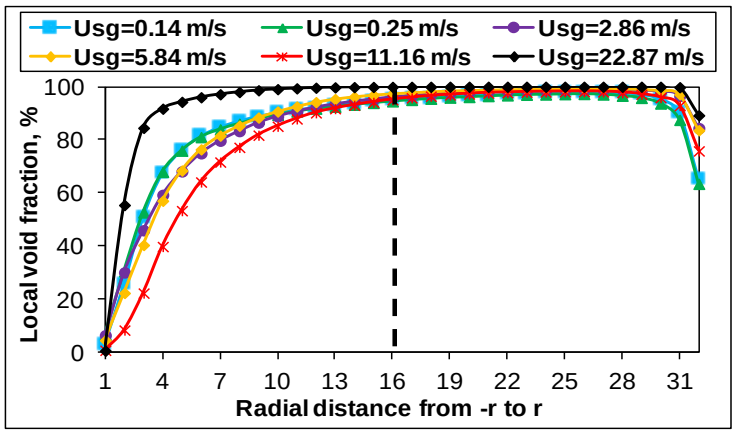
Middle	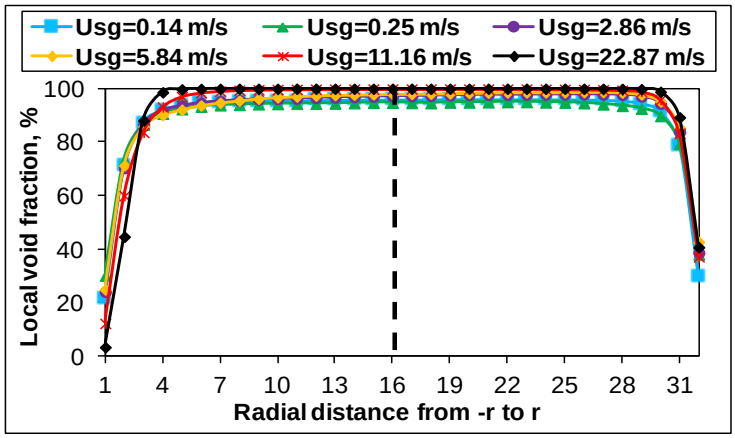
Bottom	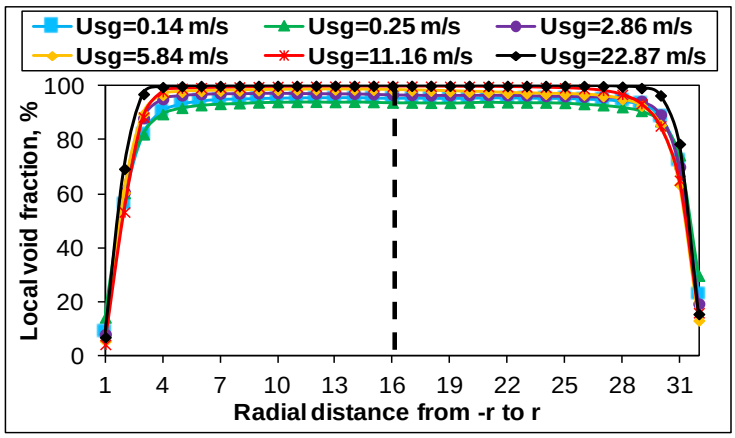

(a) Local void fraction distribution from 90^{o} to 270^{o} for Usl=0.48 m/s

Position	Usl= 0.7 m/s
Top	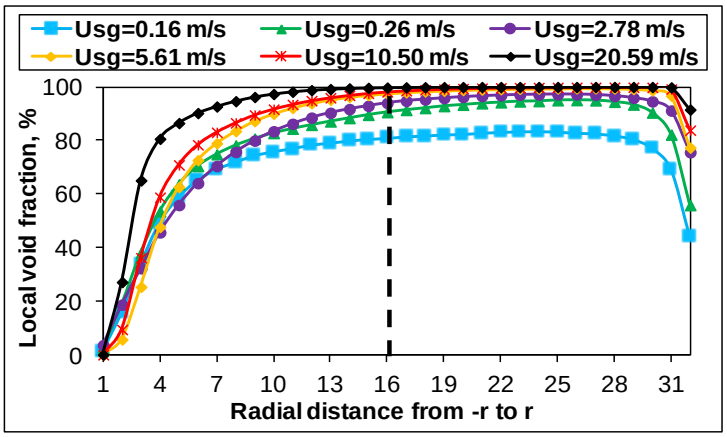
Middle	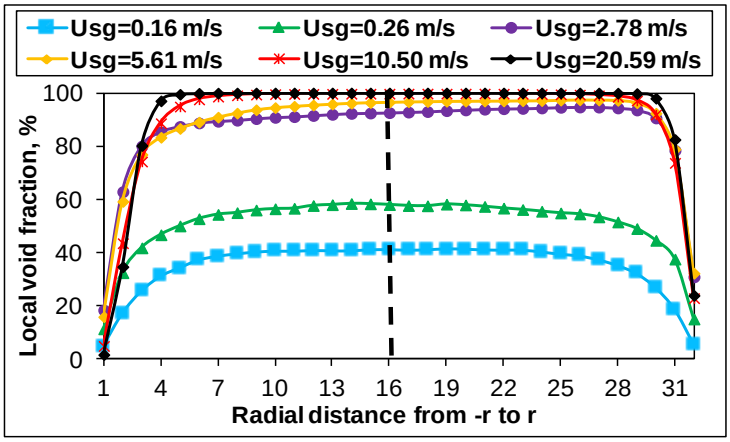
Bottom	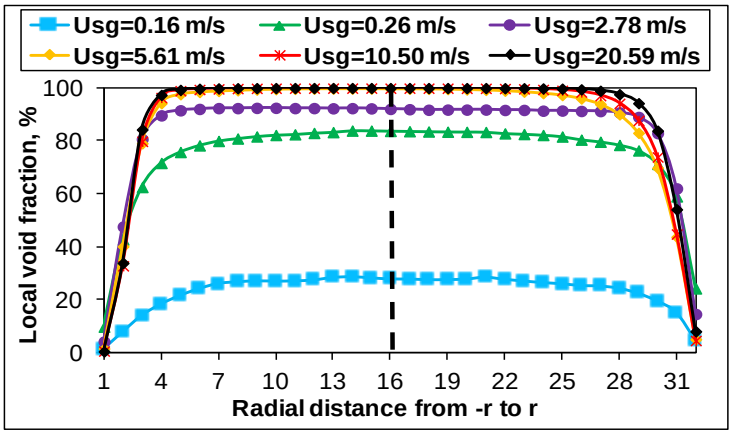

(b) Local void fraction distribution from 90° to 270° for Usl=0.7 m/s

Figure 5-22 Local void fraction distribution from 90° to 270° measured at the top, middle and bottom positions of the downward section, for different air superficial velocities with water superficial velocities of (a) 0.48 and (b) 0.7 m/s

Figure 5-23 (a) and (b) depicts the local void fraction distribution along the wires located from 0^o to 180^o, for water superficial velocities of 0.48 and 0.7 m/s respectively. Both the 0^o and 180^o positions are located in opposite quarters of the pipe's cross section (on the right and left sides of the 90^o position respectively). In general, it was observed that the peaks appeared in the centre of the pipe. The void fraction exhibited greater peaks at higher gas superficial velocities.

It can be noted from Figure 5-23 (a) that, the plots have similar tendencies at the top, middle and bottom positions, indicating that the bend has no obvious impact at these locations of the pipe. For water superficial velocity of 0.7 m/s, different void fraction distribution was noted at the top, middle and bottom positions, as illustrated in Figure 5-23 (b).

Position	Usl=0.48 m/s
Top	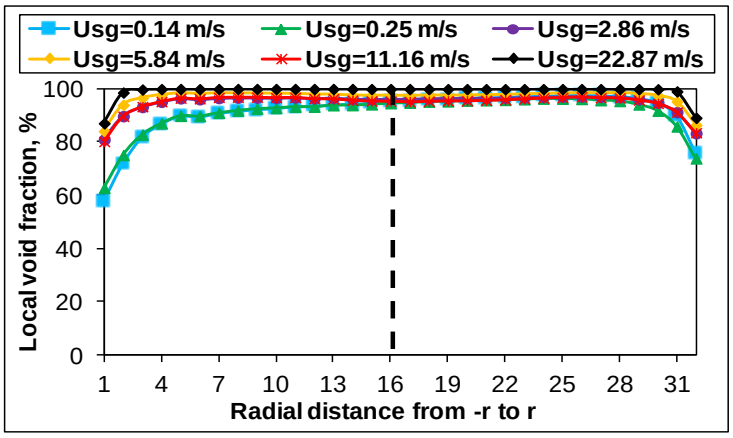
Middle	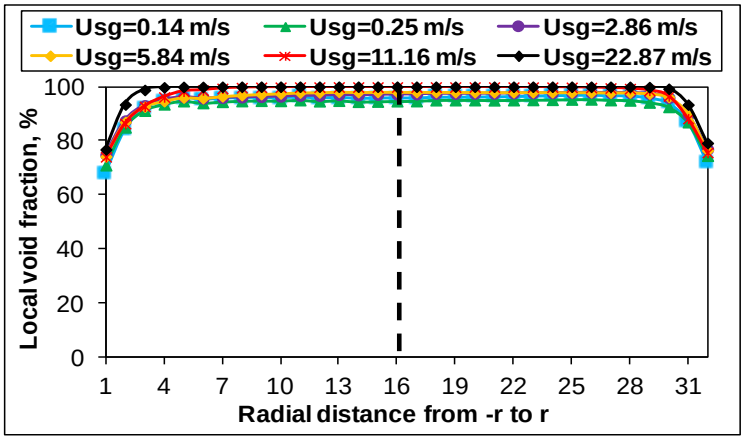
Bottom	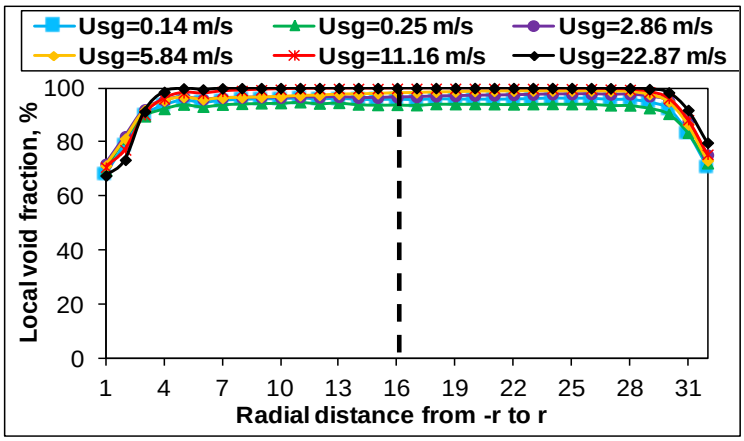

(a) Local void fraction distribution from 0° to 180° for Usl=0.48 m/s

Position	Usl= 0.7 m/s
Top	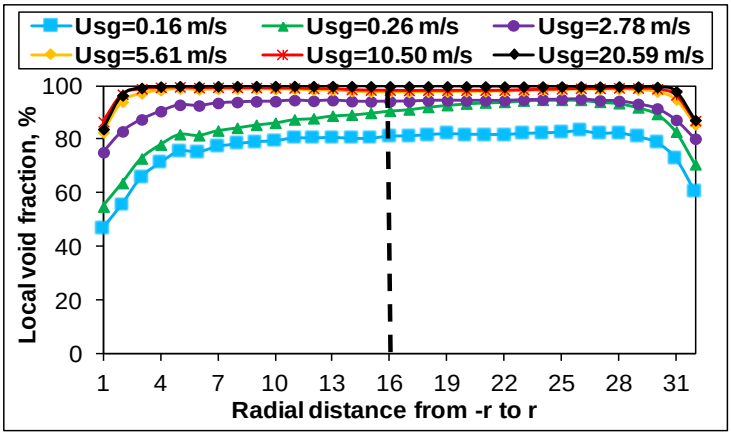
Middle	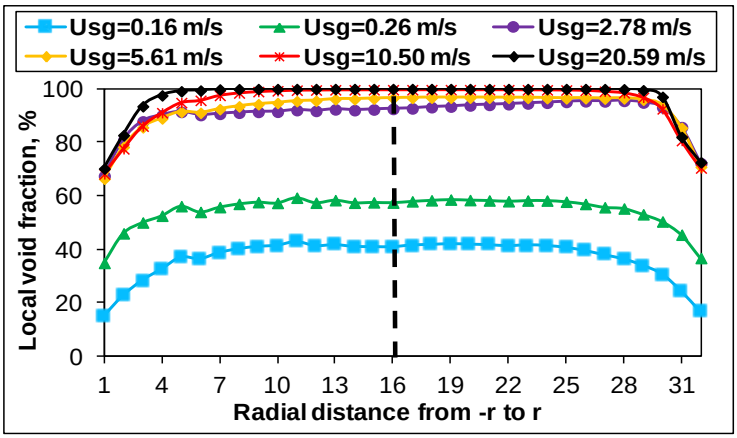
Bottom	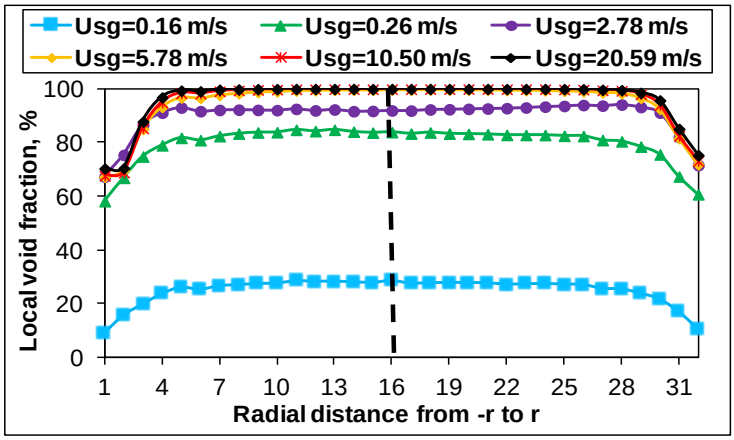

(b) Local void fraction distribution from 0° to 180° for Usl=0.7 m/s

Figure 5-23 Local void fraction distribution from 0° to 180° measured at the top, middle and bottom positions of the downward section, for different air superficial velocities with water superficial velocities of (a) 0.48 and (b) 0.7 m/s

5.2.2 Void fraction development in upward flow

5.2.2.1 Effect of air and water superficial velocities on the mean void fraction along the upward flow

Figure 5-24 (a-c) illustrates the mean void fraction plotted against air superficial velocity. The comparison is made for the top, middle and bottom positions of the upward section, for a wide range of air superficial velocities with water superficial velocities of 0.07, 0.2, 0.48,1 and 1.5 m/s. In all plots, it is very clear that there is a similar tendency over all superficial velocities tested. Figure 5-24 (a) shows that, the void fraction values at the top position increase as the air superficial velocity increases further, until it reaches higher values of void fraction, where the slope at the higher velocities of air is less than that at lower velocities. Similar behaviours are noted at the middle and bottom positions (Figure 5-24 (b) and (c) respectively). The same observation was made by Abdulkadir (2011), who claimed that the void fraction increases at lower gas superficial velocities more sharply than at higher gas superficial velocities. This confirmed that, the void fraction becomes less sensitive at higher air flow rates than at lower air flow rates. On the other hand, the void fraction values decrease as the water superficial velocity increases. From Figure 5-24 (a-c), it can be observed that both velocities of air and water have considerable effects on the void fraction values, although to varying degrees.

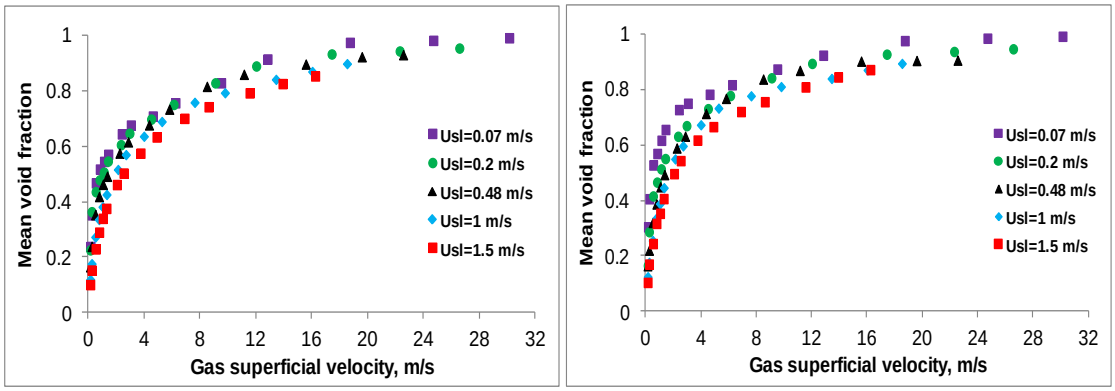

(a) Top position **(b) Middle position**

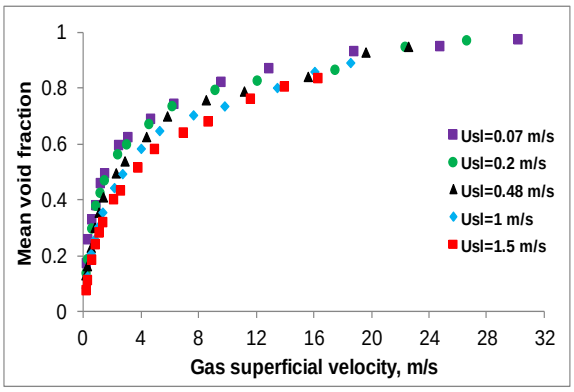

(c) Bottom position

Figure 5-24 Effects of the air and water superficial velocities on the void fraction development at the top, middle and bottom positions of the upward section

Figure 5-25 (a-f) illustrates a relationship between the mean void fraction and air superficial velocity, for water superficial velocities of 0.07, 0.2, 0.48, 1 and 1.5 m/s respectively. The comparison was made for the top, middle and bottom positions of the upward section, in order to clarify the behaviour of void fraction at different axial positions along the upward vertical pipe. It can be seen from Figure 5-25 (a-f) that, the mean void fraction behaviour at the top, middle and bottom positions follows similar tendency. The void fraction values are increased in a parabolic pattern with increasing the air superficial velocity. However, the void fraction at all positions increases sharply when the air superficial velocities are lower than 8 m/s. On the other hand, it increases moderately for higher air superficial velocities (i.e. higher than 8 m/s). This observation was made at all positions (namely at 5, 28 and 47 pipe diameters from the bottom bend), and over all water superficial velocities. The void fraction

becomes less sensitive at high air superficial velocities. While, increasing the water superficial velocity did not show any substantial changes in behaviour of the void fraction. It can be concluded that, the air superficial velocity has more important effect on the void fraction development than the water superficial velocity.

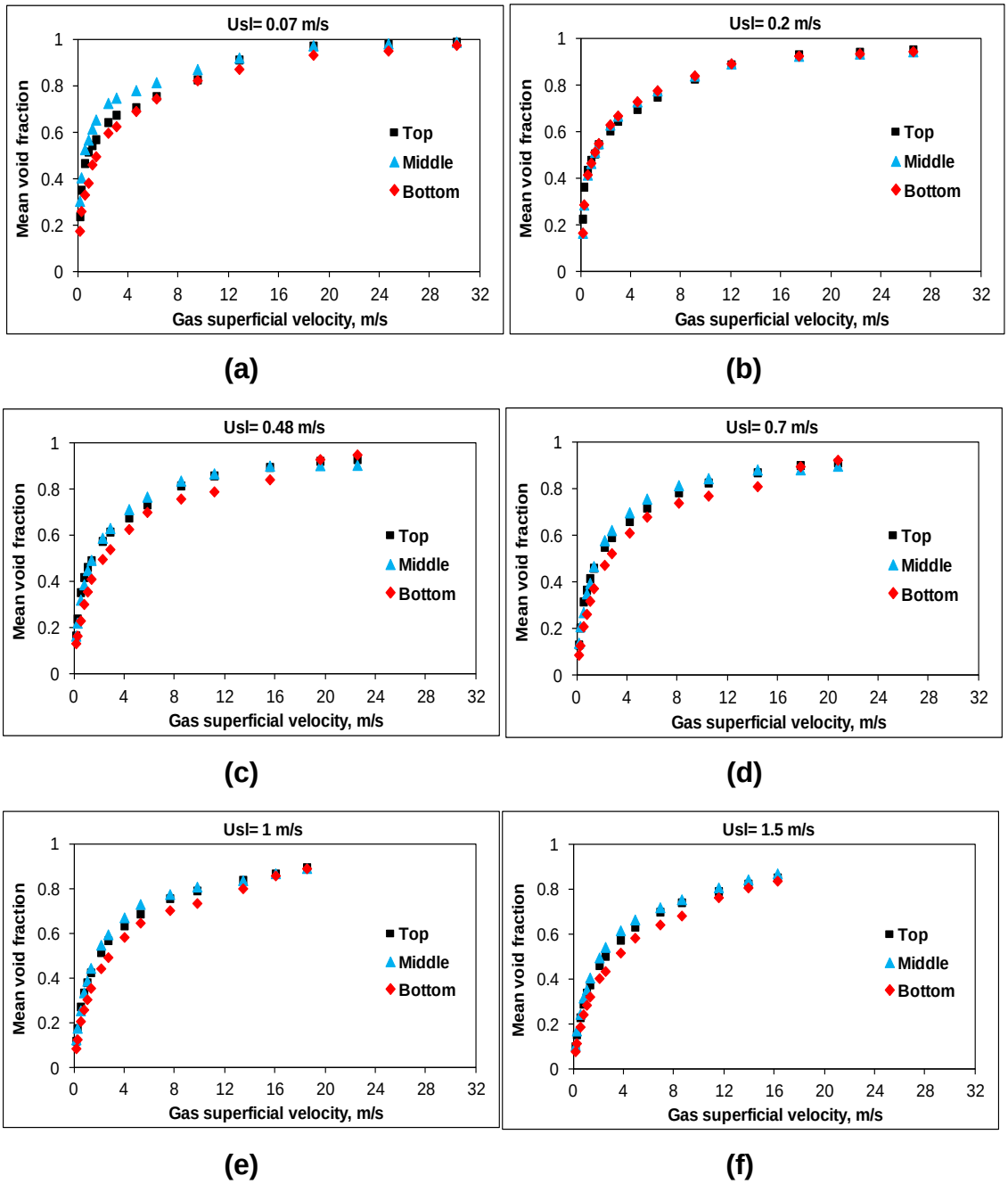

Figure 5-25 Mean void fraction development at the top, middle and bottom positions of the upward section, for different air superficial velocities and water superficial velocities of (a) 0.07, (b) 0.2, (c) 0.48, (d) 0.7, (e) 1 and (f) 1.5 m/s

5.2.2.2 Effect of an axial distance on mean void fraction along the upward flow

Figure 5-26 shows the void fraction ratio versus the axial distance along the upward section. The void fraction ratio is expressed by the ratio of the mean void fraction at any particular position to that at the top position (i.e. at 47 pipe diameters). As a result, the void fraction ratio at the top position becomes unity. It is clear from all plots of Figure 5-26 that, the void fraction variation against axial position is significantly different at lower air superficial velocities (for example, air superficial velocity of 0.14 m/s and water superficial velocity of 0.07 m/s) from that at higher air superficial velocities. The variation of void fraction is decreased by increasing the air superficial velocity. Consequently, the void fractions' behaviours at all axial positions (i.e. 5, 28 and 47 pipe diameters) become similar to each other and follow the same tendency (for instance, air and water superficial velocities of 16.23 and 1.5 m/s respectively). Based on this evidence, it can be concluded that void fraction can be easily developed when a higher velocity of air is applied. On the other hand, the void fraction behaviour does not show any significant changes when the water superficial velocity is changed. This indicates that, the air superficial velocity has more effect on the void fraction development than the water superficial velocity.

In addition, the void fractions are observed to have less variation on reaching 28 and 47 pipe diameters for all flow conditions except for low water and air flow rates (e.g. for water superficial velocities of 0.07 and 0.2 m/s with air superficial velocity of 0.14 m/s). These exceptional cases are mainly in the unstable flow region. These observations demonstrate that, the flow becomes less sensitive to the bend effect on entering the higher locations of the upward section. For high water flow rates, the void fraction varies much less against the axial position than that for low water flow rates. This could be due to the fact that, the higher the water flow rates the lower the void fraction values and hence the less the void fraction variations.

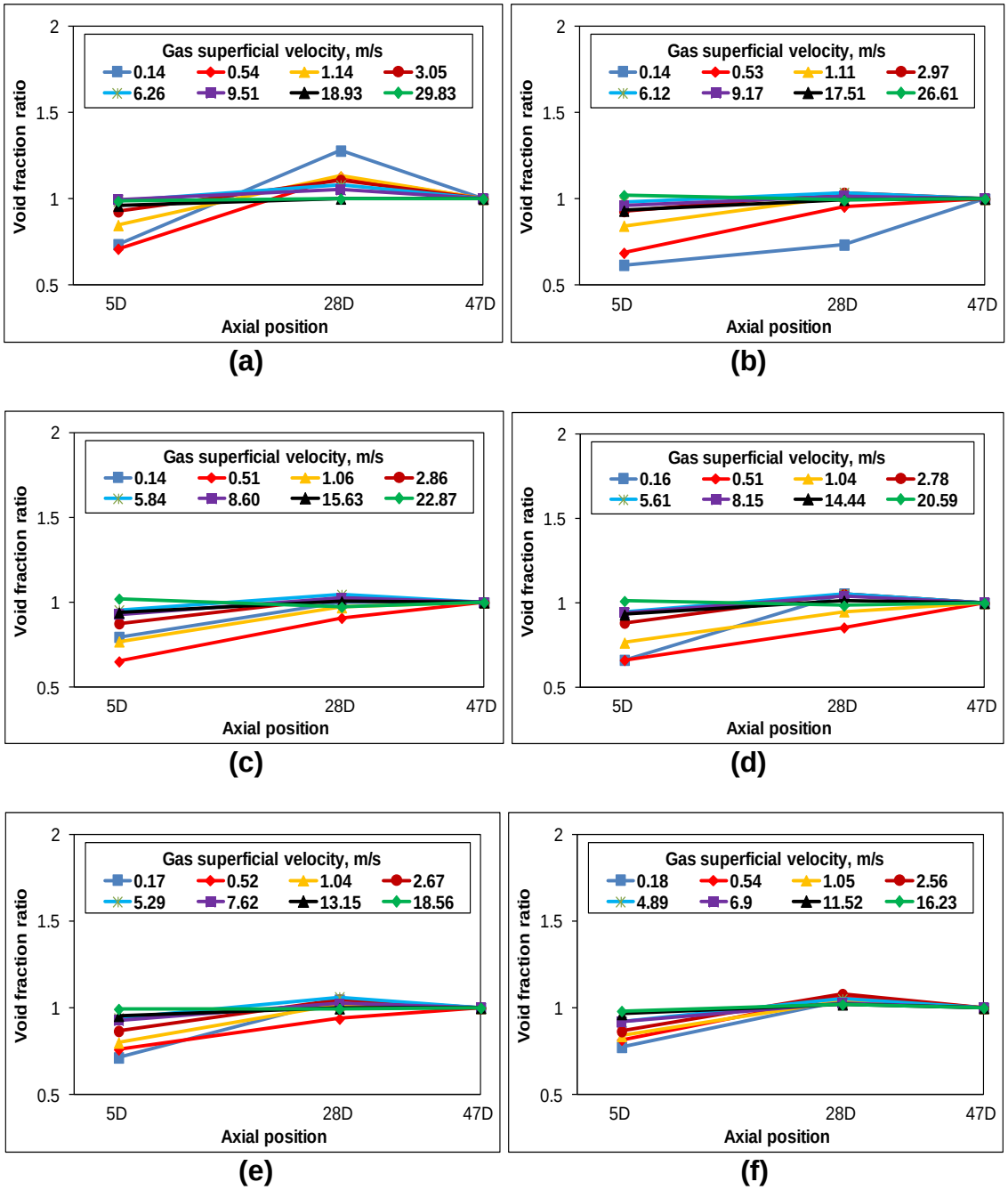

Figure 5-26 Void fraction development along the upward section, for water superficial velocities of (a) 0.07, (b) 0.2, (c) 0.48, (d) 0.7, (e) 1 and (f) 1.5 m/s

5.2.2.3 Local void fraction distribution along the upward flow

The cross-sectional void fraction distribution at different positions along the upward section, also demonstrates the effect of the upstream bottom bend on the flow development. Figures 5-27, 5-28 and 5-29 represent the phase distributions at the top, middle and bottom positions of the upward section respectively, for air superficial velocities of 0.17, 0.52, and 9.65 m/s, and a constant water superficial velocity of 1 m/s. In all plots of Figures 5-27, 5-28 and 5-29, the chordal distributions are named as (a), and the contour phase distributions are named as (b). The red colour indicates the wires numbered from 1 to 32 that are located at 90^{o} towards 270^{o}. The 90^{o} located in the outer pipe wall and 270^{o} are located in the inner pipe wall. Both the 90^{o} and 270^{o} respectively, are positioned on the upward straight section close to the outer and inner curvatures of the bottom bend. The blue colour indicates the wires numbered from 1 to 32 that are located at 0^{o} towards 180^{o}. Both 0^{o} and 180^{o} are located on the right and left positions of 90^{o} respectively.

From the local distribution plots of Figures 5-27, 5-28 and 5-29 it can be observed that, the minima of void fraction values are positioned on the pipe wall, for both the red and blue curves at all positions and over all flow rates. These values are gradually increased towards the pipe centre, which present maxima of the void fraction values (classified as core peak). By increasing the distance from the pipe centre towards another pipe wall, the void fraction values become lower again. It is interesting to note that, the flow behaviour at the bottom position is considerably different from those at the higher (top and middle) positions. The void fraction at the bottom position is unevenly distributed on the 90° side quarter of the pipe cross section. Conversely, this phenomenon is not distinguishable on other sides of the pipe, where the void fraction distribution becomes quite symmetric. This is because the bottom bend is observed to induce a flow of maldistribution along the same path of its outer curvature. The extent of the bend effects strongly depends on the flow conditions. In this study, the action of the bend is reduced with the growing distance from the bottom bend (namely, when the flow has reached the higher positions). The contour plots of the bottom position show that, the void fraction

is unevenly distributed along the 90^{o}- 270^{o} direction for air superficial velocity of 0.17 m/s. The void fraction at these flow rates (i.e. air and water superficial velocities of 0.17 and 1 m/s respectively), is showing lower void values on the 90^{o} side quarter of the pipe cross section than those of its opposite quarter (i.e. the 270^{o} side quarter). In contrast, distribution of the void fraction along the 0^{o}-180^{o} direction is fairly uniform. As mentioned earlier, this should be due to the action of the centrifugal force of the bottom bend that was observed to push the liquid into the outer curvature of the bend. The impact of the bend on the flow distribution is reduced as the flow approaches the higher positions. The bend action on the flow behaviour in the bottom position, becomes less as the air superficial velocity is increased further to 0.52 m/s. The flow at this condition is still unevenly distributed along the 90^{o}- 270^{o} direction, but it appears more even than that for air superficial velocity of 0.17 m/s. The bend effect is not distinguishable at the middle and top positions and the flow becomes evenly distributed. At air superficial velocity of 9.65 m/s, the flow distribution at the bottom position becomes more even along the 90^{o}- 270^{o} direction. This could suggest that, the centrifugal force generated by the bottom bend is becoming less when higher air flow rates are applied. Again, the 90^{o} and 270^{o} positions represent the outside and inside curvature of the bottom bend respectively.

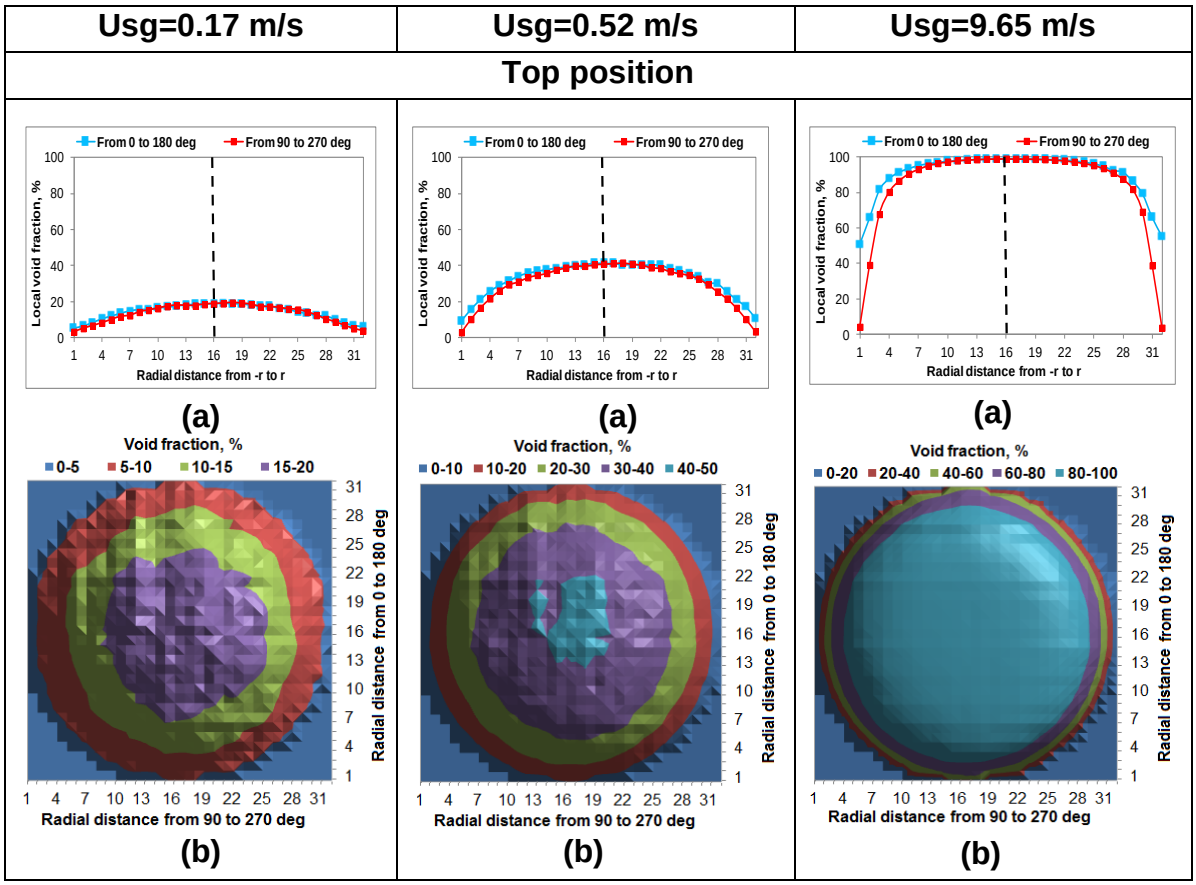

Figure 5-27 Local distributions (a) and contour plots (b) of the void fraction, at the top position of the upward section for different air superficial velocities with fixed water superficial velocity of 1 m/s

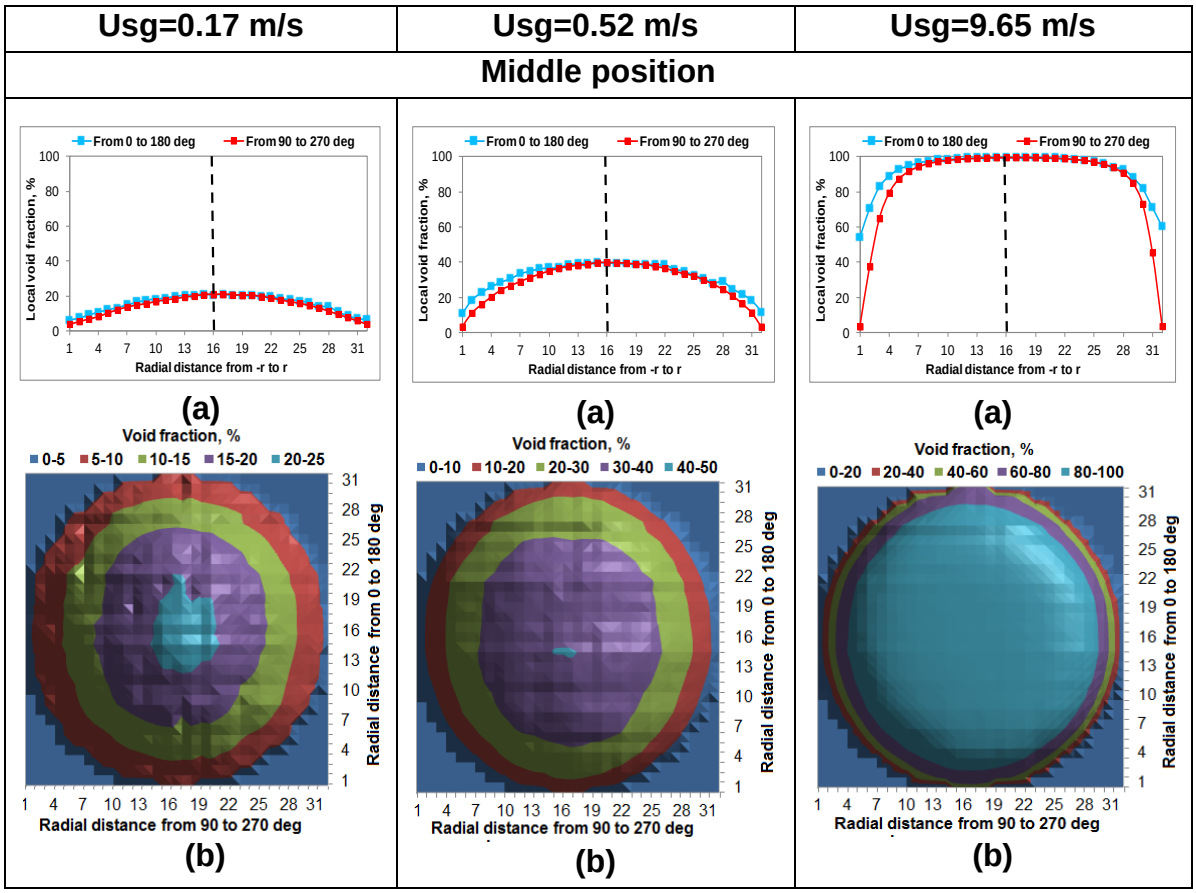

Figure 5-28 Local distributions (a) and contour plots (b) of the void fraction, at the middle position of the upward section for different air superficial velocities with fixed water superficial velocity of 1 m/s

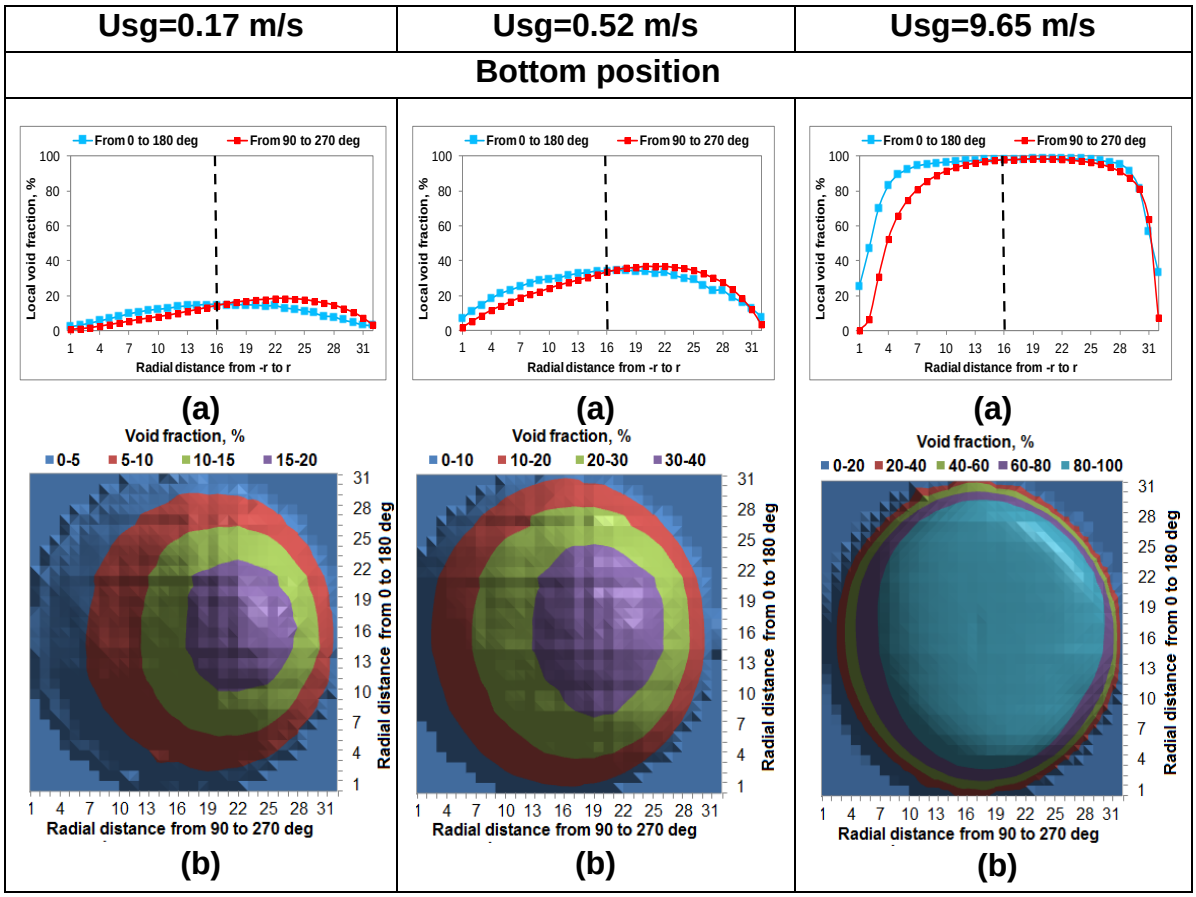

Figure 5-29 Local distributions (a) and contour plots (b) of the void fraction, at the bottom position of the upward section for different air superficial velocities with fixed water superficial velocity of 1 m/s

The local void fraction distributions at different positions of the upward section, were also analysed further for water superficial velocities of 0.48 and 0.7 m/s with a number of air superficial velocities. These summarised the effects of flow conditions on behaviour of void fraction in pipes with serpentine configurations. The local void fraction profile observed at the top, middle and bottom positions of the upward section is illustrated in Figures 5-30 and 5-31. Similar to the case of the downward flow, Figure 5-30 (a) and (b) represents the local void fraction distribution from 90^o to 270^o positions, for water superficial velocities of 0.48 and 0.7 m/s respectively. While, Figure 5-31 (a) and (b) illustrates the local void fraction distribution from 0^o to 180^o positions, for water superficial velocities of 0.48 and 0.7 m/s respectively. The measurements of local void fraction here, are carried out under the same flow conditions as those presented for the downward flow. Figures 5-30 and 5-31 show a symmetrical void fraction profile at all positions and over all flow conditions. It can be seen in all plots of Figures 5-30 and 5-31 that, the void fraction increases in a parabolic manner when the air superficial velocity ranged from 0.14 to 5.84 m/s (for water superficial velocity of 0.48 m/s), and also when the air superficial velocity ranged from 0.16 to 5.61 m/s (for water superficial velocity of 0.7 m/s). The void fraction values at these positions significantly increased towards the pipe centre, where the void fraction is at maxima. This then gradually decreased to exhibit minima in the pipe wall.

As the air superficial velocity increased further, the void fraction profile was still uniform with minima appearing on the pipe wall. However, the maxima of void fraction appeared along wire 5 towards wire 28 when highest air superficial velocity was applied. As a result, the void fraction profile exhibits a flat shape along all positions. It can be clearly noted that, each particular void fraction curve plotted in Figure 5-30 (a) is similar to that plotted in Figure 5-30 (b) for a given position. Also, a striking similarity can be seen between Figure 5-31 (a) and (b) for a given position. The similarity encountered is due to no bend effects being observed at all positions of the upward section, when the water superficial velocities of 0.48 and 0.7 m/s are applied.

Position	Usl=0.48 m/s
Top	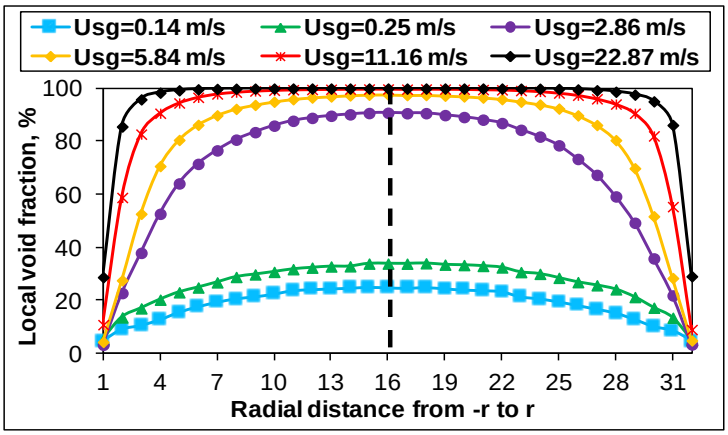
Middle	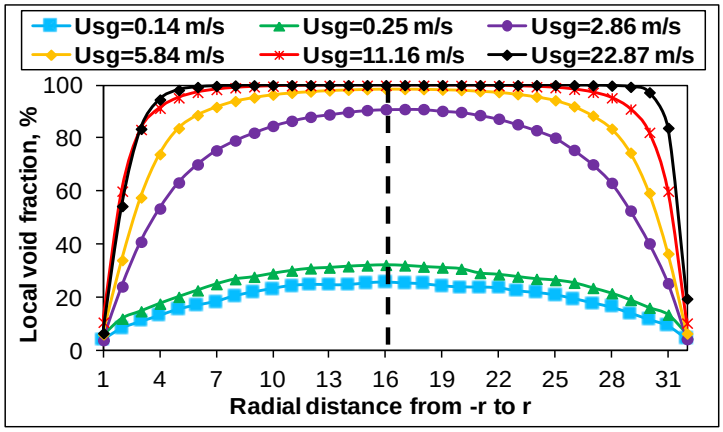
Bottom	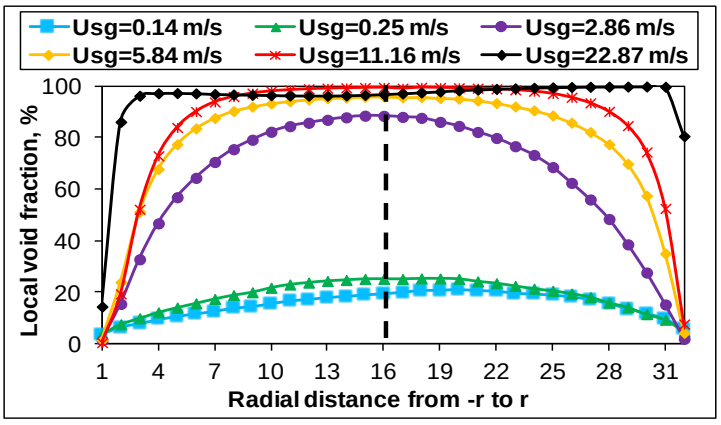

(a) Local void fraction distribution from 90^{o} to 270^{o} for Usl=0.48 m/s

Position	Usl=0.7 m/s
Top	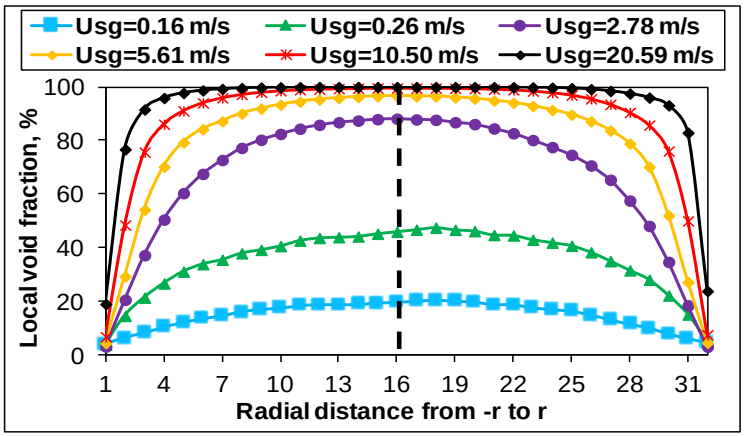
Middle	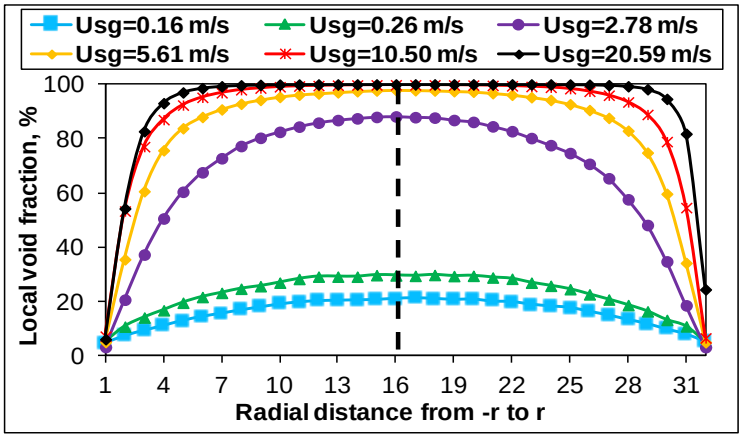
Bottom	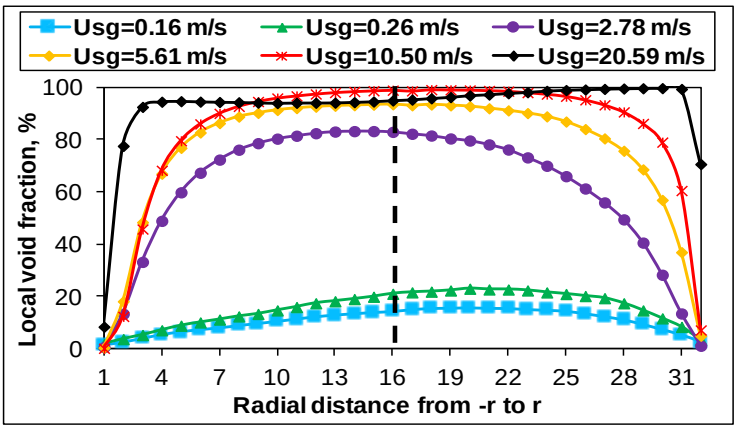

(b) Local void fraction distribution from 90^o to 270^o for Usl=0.7 m/s

Figure 5-30 Local void fraction distribution from 90^o to 270^o measured at the top, middle and bottom positions of the upward section, for different air superficial velocities with water superficial velocities of (a) 0.48 and (b) 0.7 m/s

Position	Usl=0.48 m/s
Top	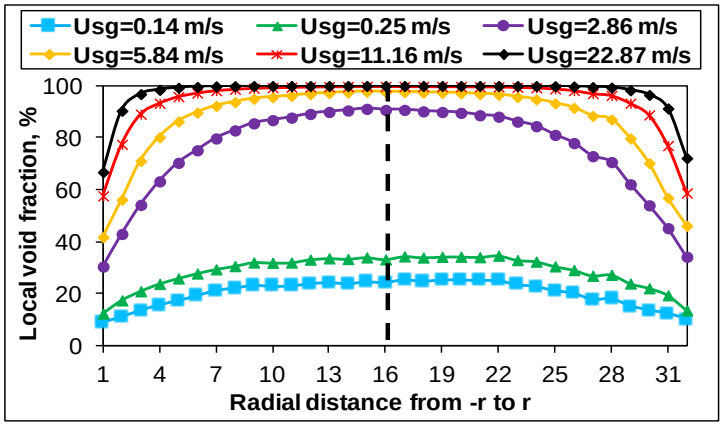
Middle	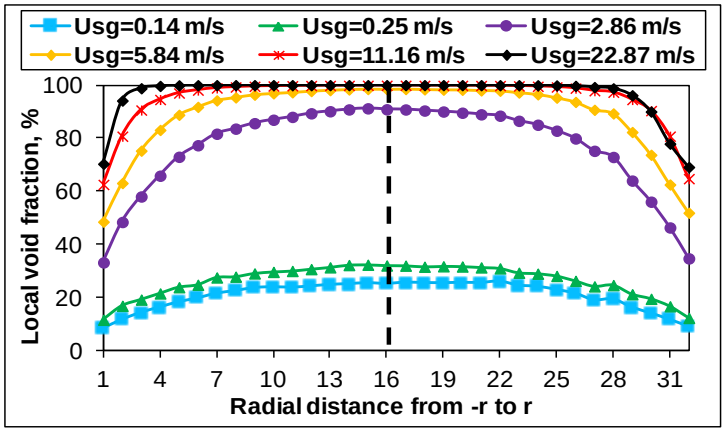
Bottom	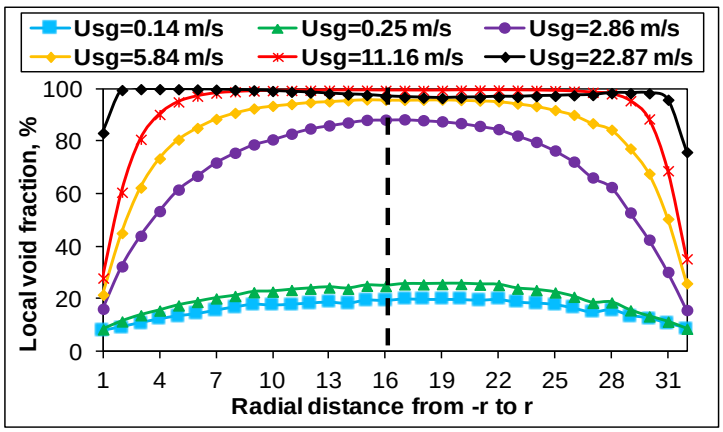

(a) Local void fraction distribution from 0^{o} to 180^{o} for Usl=0.48 m/s

Position	Usl=0.7 m/s
Top	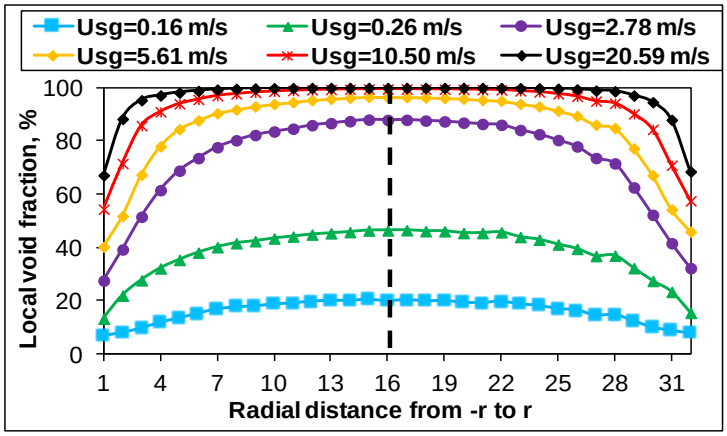
Middle	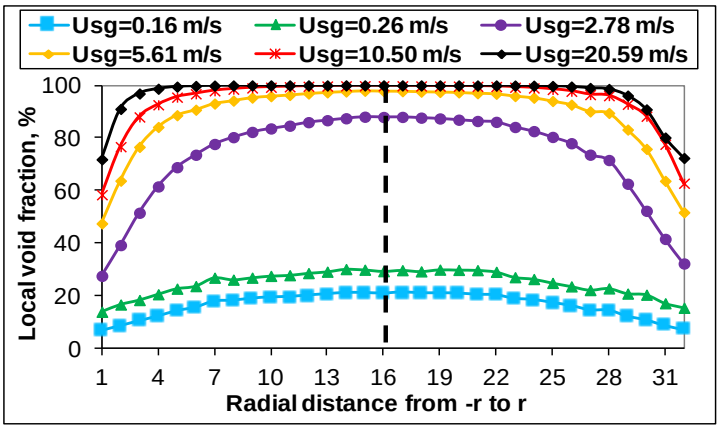
Bottom	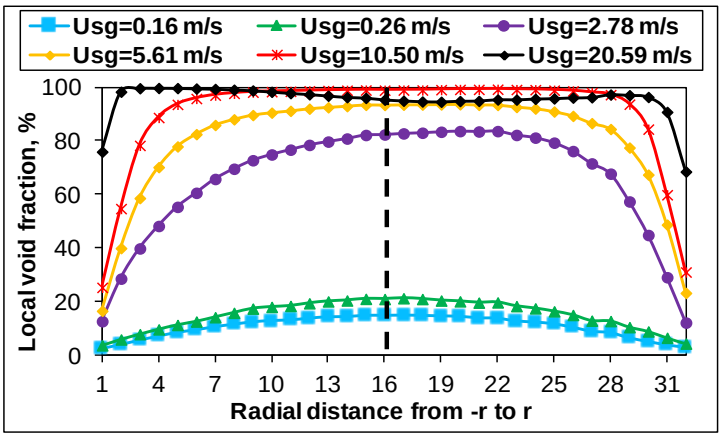

(b) Local void fraction distribution from 0° to 180° for Usl=0.7 m/s

Figure 5-31 Local void fraction distribution from 0° to 180° measured at the top, middle and bottom positions of the upward section, for different air superficial velocities with water superficial velocities of (a) 0.48 and (b) 0.7 m/s

5.3 Liquid film development and its circumferential distribution

As the liquid film only exists in annular flow, this section of the results is mainly based on the data from the flow conditions in which the annular regime can be established. Measurement results of liquid film thickness include time traces, average and statistical properties of film thickness at different positions for various flow conditions which were analysed and are discussed in the subsequent sections.

The mean film thickness at each axial position along both the downward and upward sections is obtained from the four film sensors distributed circumferentially in the film probe located at that position (refer to Figure 3-10). In this study, three film probes are installed in each section to explore the film thickness development along the flow path.

5.3.1 Liquid film thickness development along the downward flow

5.3.1.1 Effect of air and water superficial velocities on mean film thickness along the downward flow

Figure 5-32 (a-d) shows the mean liquid film thickness against the air superficial velocity, for three different water superficial velocities in the downward section of the Serpent rig.

From the plots of Figure 5-32 (a-d) it can be seen that, the mean liquid film thickness development in the downward flows is dependent not only on the air superficial velocity, but also the water superficial velocity.

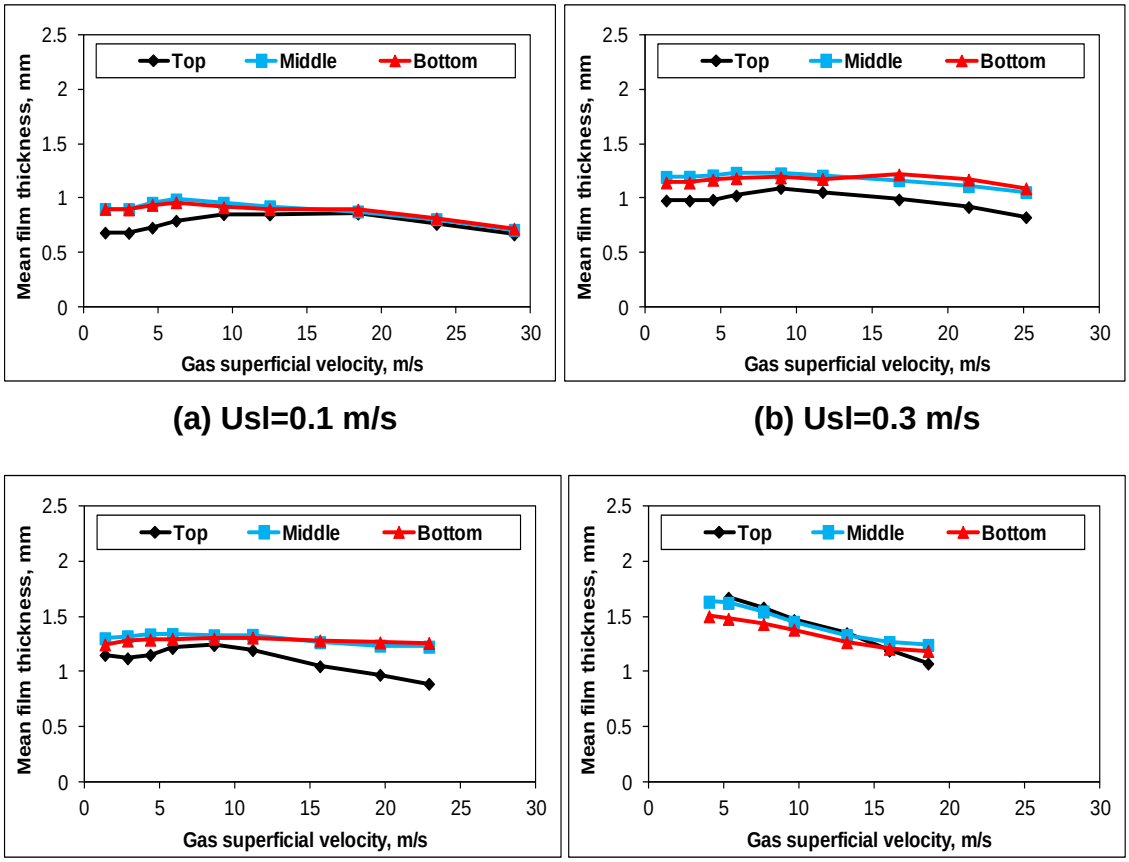

Figure 5-32 Mean film thickness development along the downward flow for different air velocities and water superficial velocities of (a) 0.1, (b) 0.3, (c) 0.48 and (d) 1 m/s

For water superficial velocity of 0.1 m/s (Figure 5-32 (a)), the average liquid film thicknesses at the middle and bottom positions are similar to each other over the whole range of the air flow rates tested. The liquid film at the top position is thinner than those at the lower positions when the air velocity is lower than 10 m/s. However, once the air superficial velocity becomes higher than 10 m/s, the film thickness at the top position approaches those at the middle and bottom positions.

For water superficial velocities of 0.3 and 0.48 m/s, the mean liquid film thickness at the middle and bottom positions are also close to each other over the whole range of the air flow rates tested, as illustrated in Figure 5-32 (b) and (c) respectively. The film at the top position is notably thinner than those in the lower positions for all of the air superficial velocity range.

At a higher water superficial velocity of 1 m/s, as shown in Figure 5-32 (d), it can be noted that the film thickness at all the positions against the air superficial velocity decreases more steeply than those at the lower water superficial velocities. Also, the film thickness at the top position shows a steeper decrease than those at the middle and bottom positions. This indicates that, the film thickness varied faster in the upper part than in the lower part of the section. When the air superficial velocity is higher than 14 m/s, the film thicknesses at the middle and bottom positions are converged to each other, while the film thickness at the top position becomes thinner and diverges towards lower values than those at the lower positions.

5.3.1.2 Effect of an axial distance on mean film thickness along the downward flow

The liquid film thickness ratios versus the axial distances (i.e. 5D, 30D and 46D after the top bend) at different flow conditions, are also presented to demonstrate the downward liquid film development (Figure 5-33 (a-f)). Similar to the method used for the void fraction ratio, the film thickness ratio at any particular axial position is defined as the ratio of the mean film thickness at this position to that at the position of 46D from the bend. Hence, the film thickness ratio for any velocity at the position of 46D is unity. In all plots of Figure 5-33, it can be noted that the film thickness ratio at the position of 5D shows significant variations under different flow conditions. More specifically, at low liquid flow rates, e.g. for water superficial velocity of 0.1 m/s (Figure 5-33 (a)), the liquid film thickness ratio at the top position is much less than that at lower positions when the air flow rate is relatively low, while it is fairly close to 1 when the air velocity is over 12 m/s. For water superficial velocity of 1 m/s, as shown in Figure 5-33 (f), the liquid film thickness ratio at the top position is close to that at the middle position when the air velocity is about 5.29 m/s, while it becomes lower than that at the middle position when the air flow rate is increased to 9.65 m/s or higher. However, the film thickness ratio at the position of 30D is close to or slightly higher than unity, regardless of the flow conditions. It can be inferred that, the liquid film ratio at the position of 5D from the upstream bend is more

sensitive to flow conditions, and this could be because of the bend effect. In contrast, the bend effect on film thickness becomes considerably lower as the flow reaches the 30D or is further away from the upstream bend.

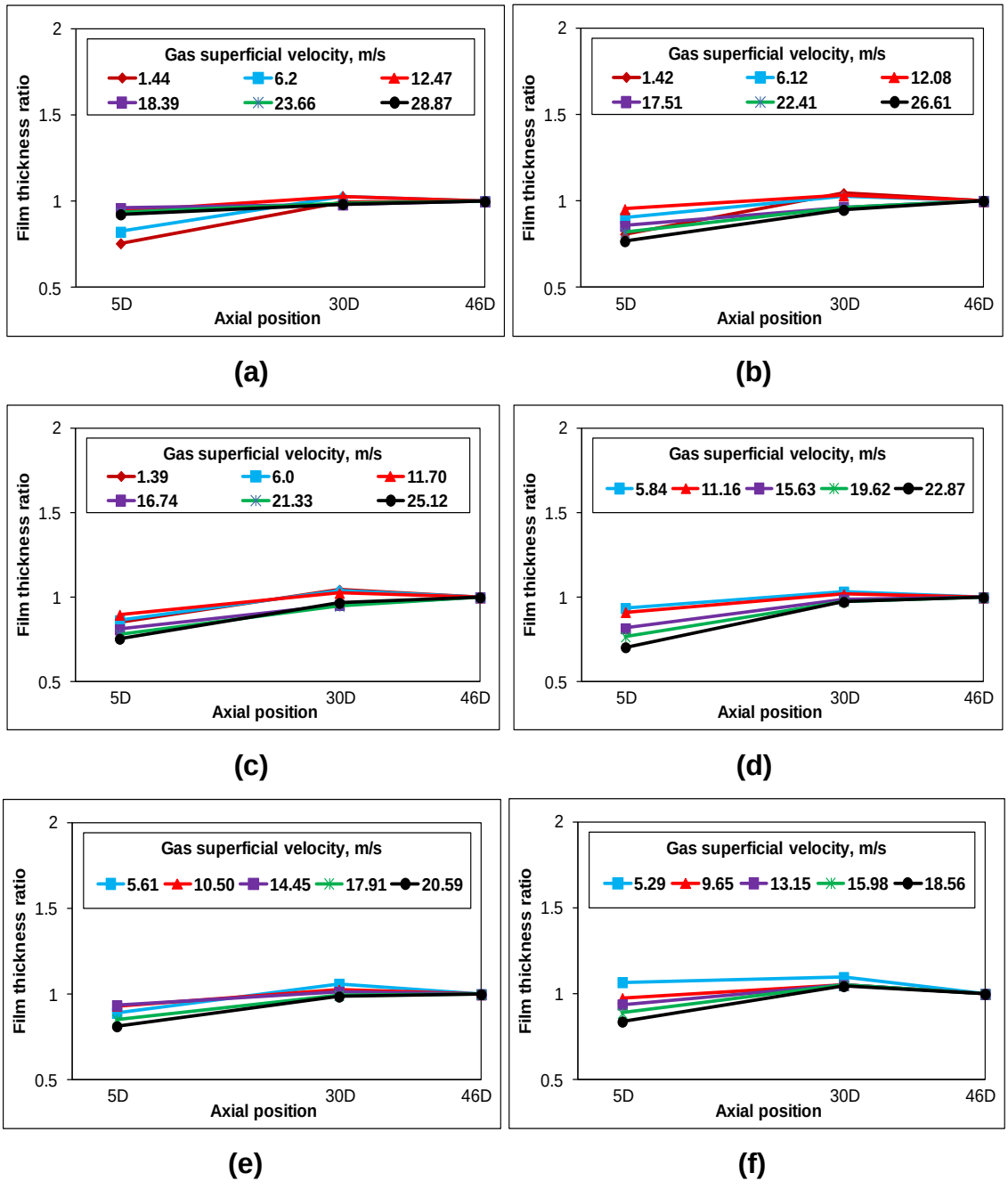

Figure 5-33 Variations of liquid film thickness along the axial distance from the inverted U-bend, for water superficial velocities of (a) 0.1, (b) 0.2, (c) 0.3, (d) 0.48, (e) 0.7 and (f) 1 m/s

5.3.2 Liquid film thickness development in the upward flow

5.3.2.1 Effect of air and water superficial velocities on mean film thickness along the upward flow

It is well accepted that, the overall tendency for the film thickness is to decrease with increasing gas velocity. This is due to the fact that, some liquid attached to the pipe wall is entrained into a gas core in the form of droplets, when increasing the gas flow rate. This was consistent with the experimental film thickness results reported in this study, as presented in Figure 5-34 (a-d). Fukano& Furukawa (1998) and MacGillivray & Gabriel (2003) reported that the mean film thickness in fact decreases asymptotically, not linearly, when increasing the gas mass flux, regardless of the liquid mass flux. According to Ariyadasa (2002), the asymptotic decrease can be partly attributed to the fact that the film becomes smoother as the gas superficial velocity increases further.

Figure 5-34 (a-d) illustrates the development of the mean liquid film thickness versus the air superficial velocities, with water superficial velocities of 0.1, 0.3, 0.48 and 1 m/s respectively. For all plots the liquid film thickness at the three axial positions namely, at 5, 28 and 47 pipe diameters is decreased as the air superficial velocity increased further. However, the liquid film at the bottom position (i.e. at 5 pipe diameters after the upstream bottom bend) shows different behaviours for water superficial velocities of 0.3, 0.48 and 1 m/s, due to the bend action. The bend is noted to yield more impacts over these water velocities. The higher the water flow rate the larger the film fluctuations in the straight sections, particularly those adjacent to the bend.

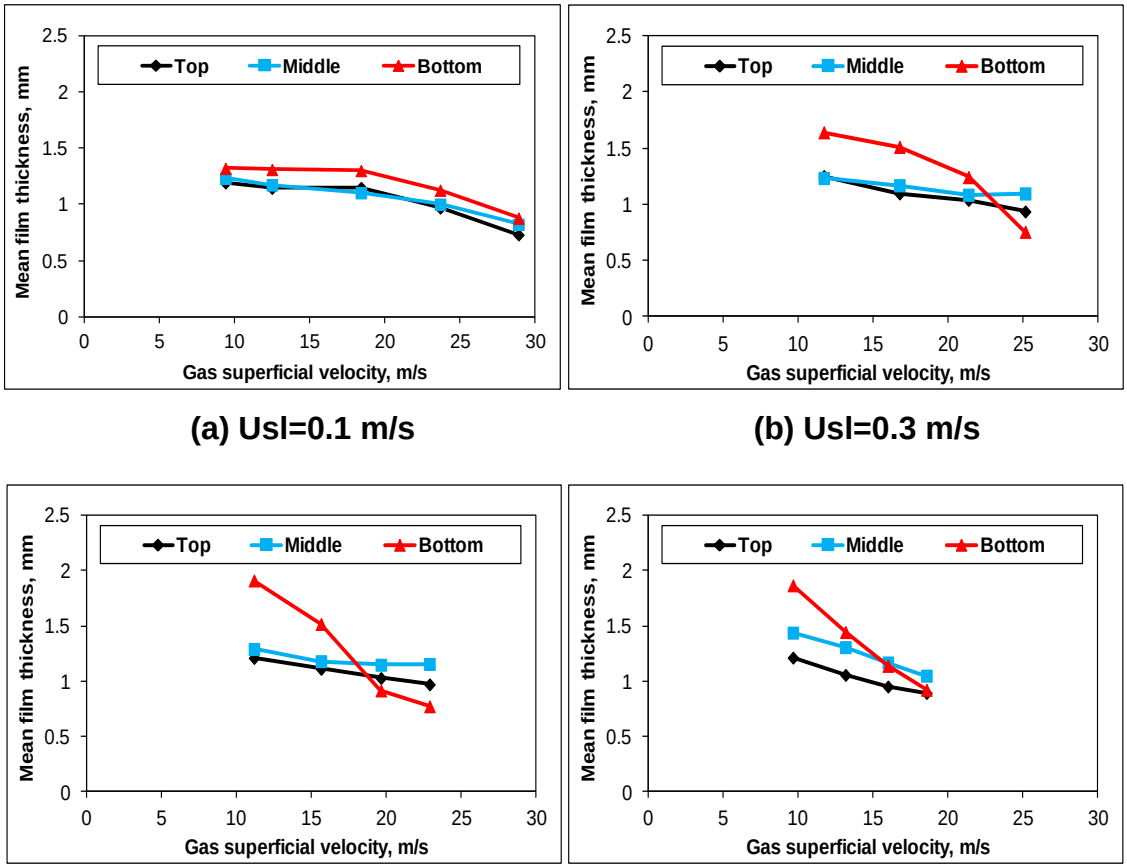

(a) Usl=0.1 m/s **(b) Usl=0.3 m/s**

(c) Usl=0.48 m/s **(d) Usl=1 m/s**

Figure 5-34 Mean film thickness development along the upward flow for different air velocities and water superficial velocities of (a) 0.1, (b) 0.3, (c) 0.48 and (d) 1 m/s

For water superficial velocity of 0.1 m/s (Figure 5-34 (a)), the average film thickness at all positions presented similar tendencies over the whole range of air superficial velocities. The values of liquid film at the middle and top positions are fairly close to each other for the most air superficial velocities. The film at the bottom position is notably thicker than those at the higher positions for the most air velocity tested. However, the liquid film at the bottom position converged with those at the middle position for the highest air velocity. At water superficial velocity ranging from 0.3 to 1 m/s (Figure 5-34 (b-d)), the film thickness profile at the bottom position is extremely different from those at the middle and top positions. This is because of the bottom bend effect that was observed to disturb the flow for these water flow rates. From the plots of Figure 5-34 (b), the liquid film at the bottom position is observed to be much thicker than those at the higher positions, for air velocity lower than 22 m/s. For air

velocities higher than 22 m/s, the liquid film at the bottom position becomes significantly thinner and diverges towards lower values than those at higher positions. This indicates that, the film thickness at the lower position varies faster than that in the upper positions of the upward section due to the action of the bottom bend, while the average liquid film thickness values at the middle and top positions are close to each other for the most air velocities tested. However, the film at the middle position is a bit thicker than that at the top position.

Figure 5-34 (c) represents the average film thickness for water superficial velocity of 0.48 m/s. Over the whole range of superficial air velocities tested, the tendencies of the liquid film at the middle and top positions are similar to each other. However, the film thickness at the middle position is notably thicker than that at the top position for all ranges of air superficial velocities. The liquid film thickness at the bottom position is substantially thicker than those at the higher positions when the air superficial velocity values are lower than 17 m/s. The liquid film at the bottom position presented a high variation with a much steeper slope of decrease than those at higher positions; this can cause the liquid film at the bottom and top positions to converge to the value of 1 mm, when the superficial air velocity increases to the highest value of air flow rate. The high variation of the liquid film observed at the bottom position indicates that, the liquid film becomes more sensitive at high flow conditions, due to the influence of the bottom bend on the flow behaviour in the bottom part of the upward section. A similar observation is made for water superficial velocity of 1 m/s, as illustrated in Figure 5-34 (d).

5.3.2.2 Effect of an axial distance on mean film thickness along the upward flow

The mean film thickness is plotted against the axial distances of 5, 28 and 47 pipe diameters along the upward flow in order to examine its development, as shown in Figure 5-35 (a-f). The plotted data are carried out for different values of air and water superficial velocities. It is important to mention that, the liquid film thickness ratio at each axial position is obtained by dividing the mean film

thickness at that particular position by that at the highest position (i.e. 47D) for the same flow condition. In this way, the film thickness data at 47 pipe diameters becomes a unity.

It can be observed from Figure 5-35 that, the film behaviour at 5 pipe diameters (i.e. at the bottom position) is inconsistent with those at 28 and 47 pipe diameters (i.e. the middle and top positions respectively) when the water superficial velocity is higher than 0.1 m/s. This can be attributed to the impact of centrifugal force of the upstream bottom bend on the adjacent locations. The impact of this force is noted to reduce at 28 and 47 pipe diameters. This contributes to the flow stability, when entering these locations. In Figure 5-35 (a), the ratio of film thickness values at 5 pipe diameters are almost the same for all air superficial velocities tested. The striking similarity of liquid film values for this water velocity (namely for Usl=0.1 m/s), is partly due to the less liquid entrainment observed at the lower position. Figure 5-35 (a) also shows that, the ratio of film values are decreased along the flow path (from 5 to 47 pipe diameters) even when the superficial air velocity is changed. This is because of the liquid entrainment that is identified to be higher when the flow approaches the higher positions. This observation is in good agreement with that made by Wolf et al. (2001), who noted that the film thickness at the pipe inlet increases for a finite distance, and decreases as the flow approaches the other positions (i.e. when it reached 15 pipe diameters). They attributed this behaviour to: first, the absence of disturbance waves close to the pipe inlet, while the disturbance waves were formed when the flow reached the higher axial locations. These waves were noted to be responsible for the liquid entrainment phenomenon and, as a result, the film thickness started to decrease. Second, the transition between laminar and turbulent flow was observed to occur close to the pipe inlet, this caused the film to be thicker.

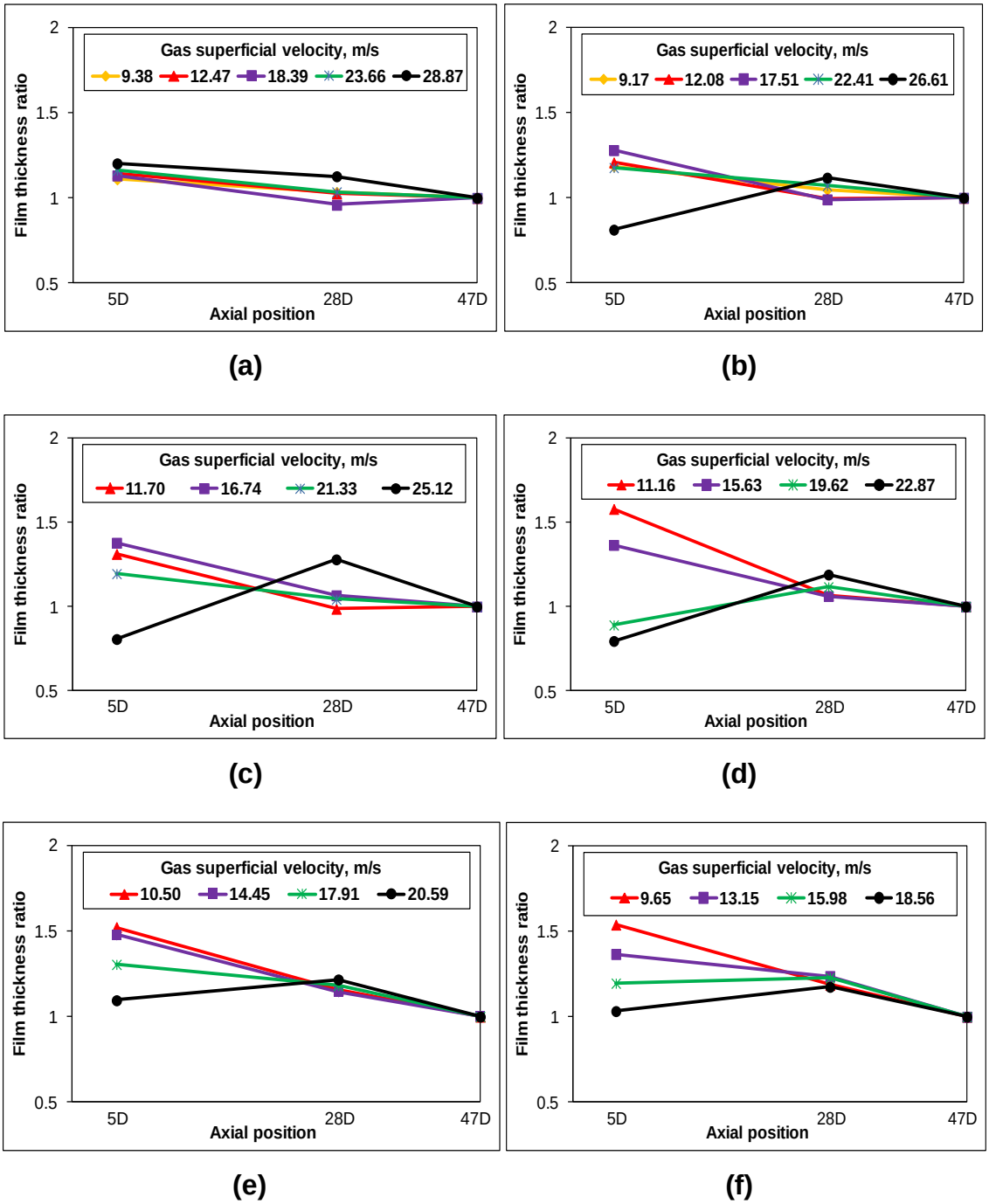

Figure 5-35 Variations of liquid film thickness along the axial distance from the U-bend, for water superficial velocities of (a) 0.1, (b) 0.2, (c) 0.3 (d) 0.48, (e) 0.7 and (f) 1 m/s

In this study, it is identified that the values of liquid film ratio are considerably changed when changing water superficial velocities (Figure 5-35 (b-f)), due to increasing the amount of the liquid entrainment into the pipe centre. It is also noted that, in most cases, the liquid film thickness ratio at 5 pipe diameters

presents lower values when applying the highest air superficial velocity. However, the film variation at this position (i.e. at 5 pipe diameters) shows a high fluctuation for the most air superficial velocities. This observation is also made even when the water superficial velocity increased. This can be explained by the film thickness variation along the pipe being significantly changed by changing the air flow rates. This was also confirmed by Wolf et al. (2001), who stated that the liquid film varied faster with the growing distance from the pipe inlet, especially when high air flow rates were used, as illustrated in Figure 5-36.

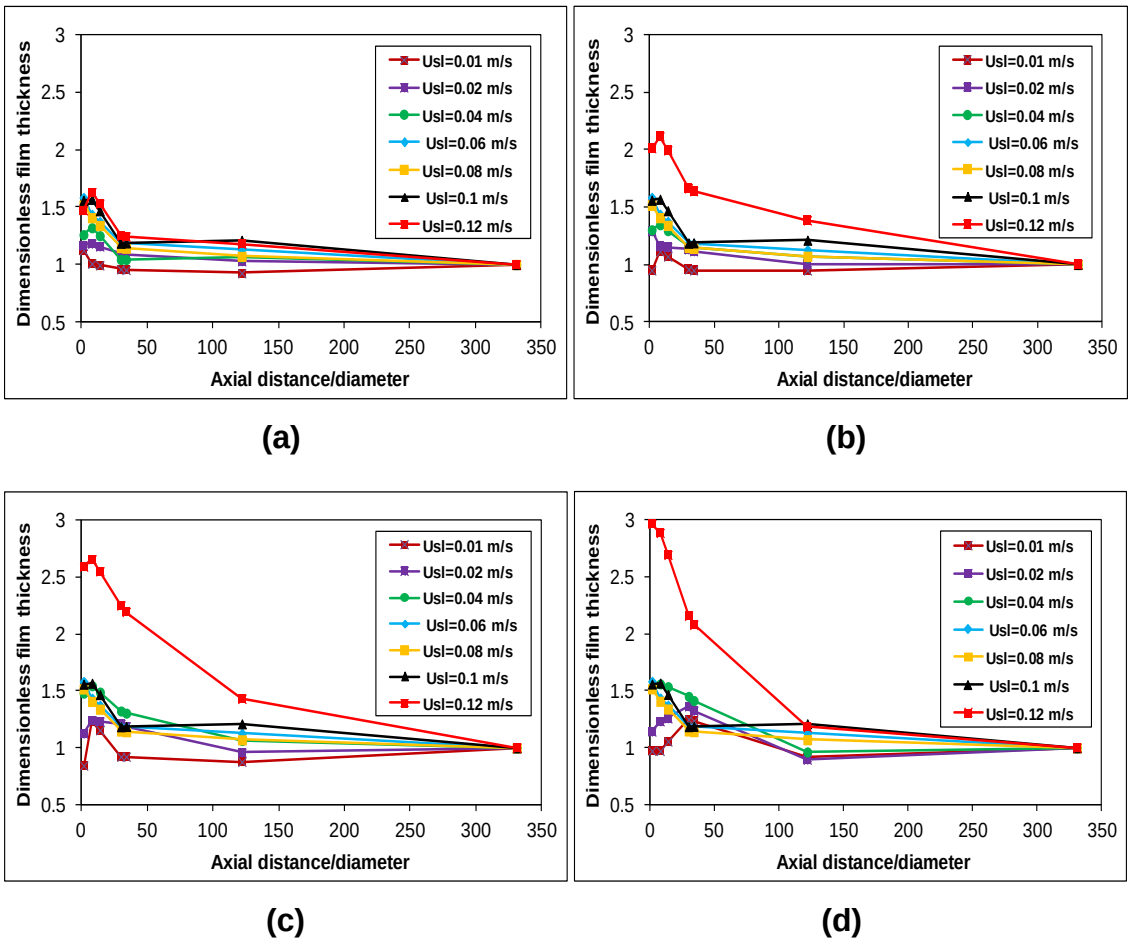

Figure 5-36 Axial development of liquid film thickness reported by Wolf et al. (2001). Air mass flux (a) 71, (b) 97, (c) 124 and (d) 154 kg/m^{2}s at different liquid mass fluxes

5.3.3 Circumferential distribution of the liquid film along the downward flow

Figure 5-37 (a-d) illustrates the circumferential distributions of liquid film along the downward flows for air superficial velocities of 1.44, 6.20, 12.47 and 28.87 m/s, while water superficial velocity is kept fixed at 0.1 m/s.

It was noted from the plots that, the film profile at the middle position is almost identical to that at the bottom position, but is quite different from that at the top position, where the thickest film appears at the 90^o position (corresponding to the outside of the upstream top bend) and the thinnest film at 270^o position (corresponding to the inside of the upstream top bend), when comparing with those at other circumferential positions. This is due to the effect of the centrifugal force of the upstream top bend on the liquid distribution. For the highest air flow rate, which is 28.87 m/s, an asymmetric film profile is observed at the top, middle and bottom positions, suggesting that the centrifugal force effect on the liquid film distribution persists through the whole downward section. It is worth noting that, the circumferential film thickness profile is fairly symmetric at the 0^o-180^o axis. This feature is observed for almost all the flow conditions tested in this study.

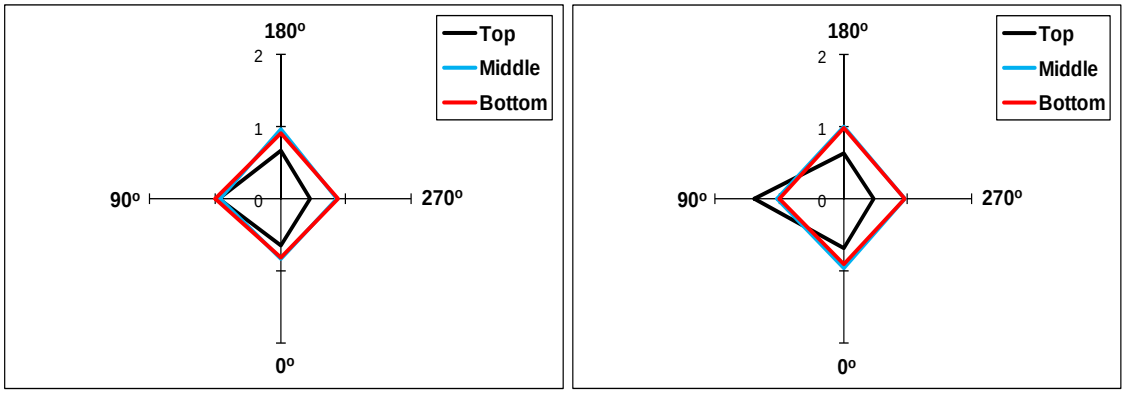

(a) Usg=1.44 m/s **(b) Usg=6.20 m/s**

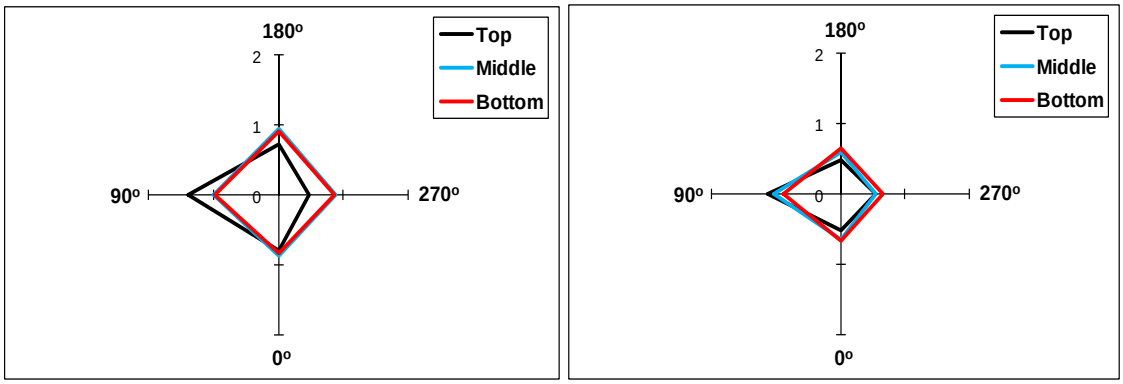

(c) Usg=12.47 m/s **(d) Usg=28.87 m/s**

Figure 5-37 Circumferential profile developments of liquid film in downward section for air superficial velocity of (a) 1.44, (b) 6.20, (c) 12.47 and (d) 28.87 m/s, with constant water superficial velocity of 0.1 m/s. Axis unit in all plots is mm

Figure 5-38 illustrates the circumferential distributions of liquid film at the downward flows for water superficial velocity of 0.3 m/s, with different air superficial velocities. In all cases, the effect of the centrifugal force of the upstream top bend on the circumferential profile of the film is observed at the top position. Also for all cases, the profile related to the middle position shows a similar tendency in comparison to that at the bottom position. The centrifugal force effect of the upstream bend on these lower positions is insignificant for the first three cases, namely for air velocities of 1.39, 6, 11.70 m/s. In addition to the top position, the centrifugal force is observed at the middle and bottom positions for air velocity of 25.12 m/s. It is also observed that, the mean liquid film thickness at the top position is significantly thinner than those at the lower axial positions. However, the liquid film measured at the top position is thicker in 90^{o}

side than those measured in the same side of the middle and bottom positions, for water superficial velocities ranging from 1.39 to 11.70 m/s. This is due to the impact of centrifugal force present in the top bend.

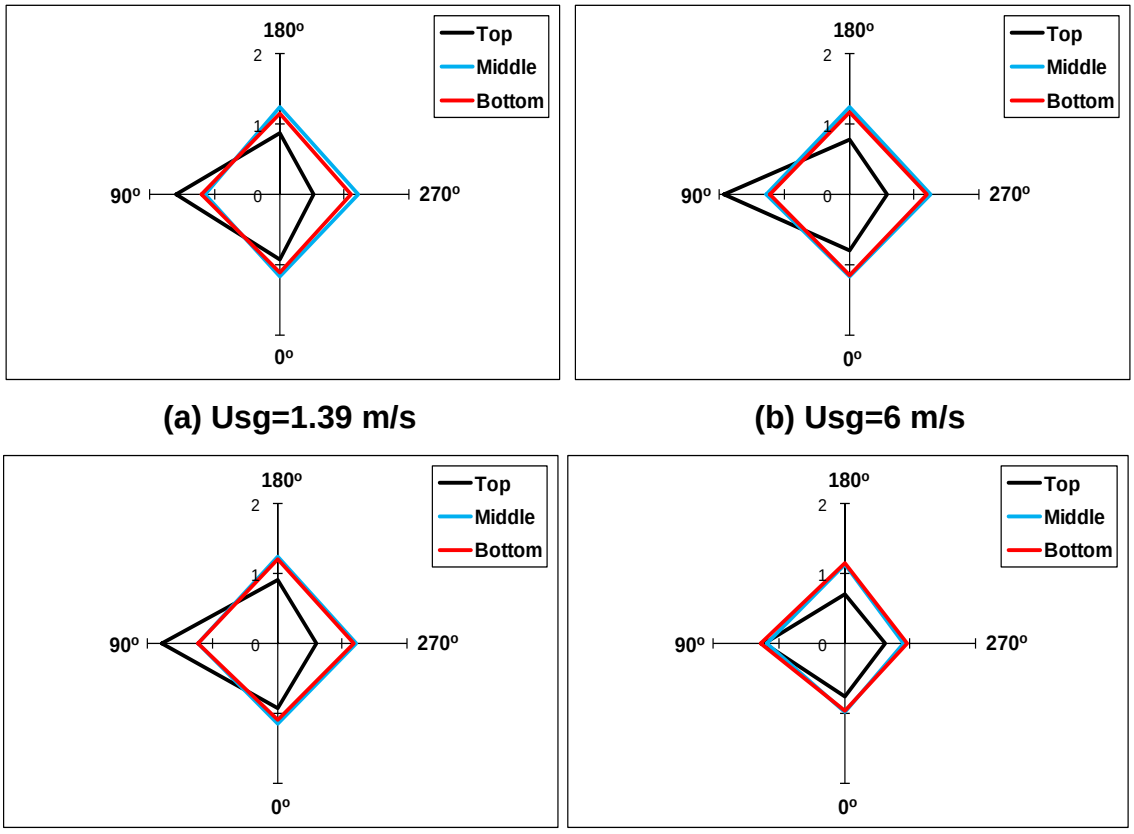

(a) Usg=1.39 m/s **(b) Usg=6 m/s**

(c) Usg=11.70 m/s **(d) Usg=25.12 m/s**

Figure 5-38 Circumferential profile developments of liquid film in the downward section for air superficial velocity of (a) 1.39, (b) 6, (c) 11.70 and (d) 25.12 m/s, with constant water superficial velocity of 0.3 m/s. Axis unit in all plots is mm

Figure 5-39 illustrates the circumferential distributions of liquid film for water superficial velocity of 1 m/s and for air superficial velocities of 9.65, 13.15 and 18.56 m/s. For the three cases, the circumferential profile of the film thickness at the top position shows an extremely high liquid film appearing on the 90^{o} side, while at the 180^{o}, 270^{o} and 0^{o} sides the film thickness is fairly even. Again, striking similarity between film profiles at the middle and bottom positions is observed.

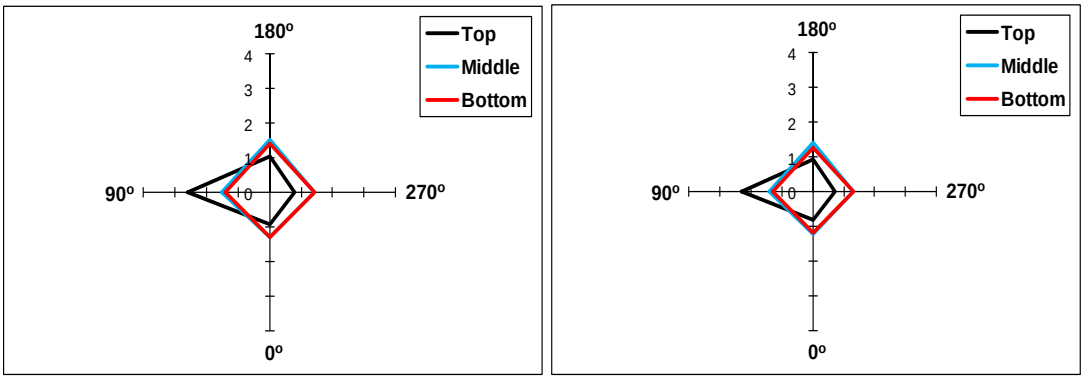

(a) Usg=9.65 m/s **(b) Usg=13.15 m/s**

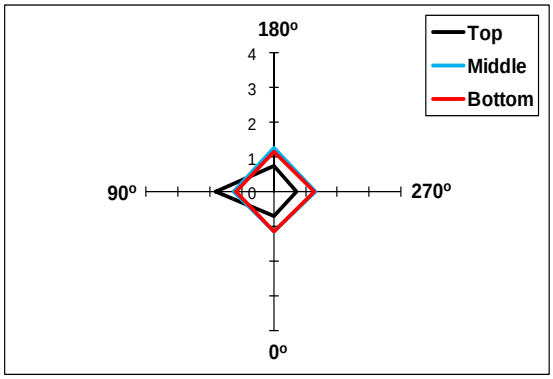

(c) Usg=18.56 m/s

Figure 5-39 Circumferential profile developments of liquid film in the downward section for air superficial velocity of (a) 9.65, (b) 13.15 and (c) 18.56 m/s, with constant water superficial velocity of 1 m/s. Axis unit in all plots is mm

Film thickness data were also interpreted by dividing the standard deviation of circumferential distribution of the liquid film thickness by the mean circumferential film thickness values, and then plotting against the axial position along the downward and upward sections. As mentioned above, the circumferential distribution values are measured by the sensors that are located in each film thickness probe.

Figure 5-40 (a-f) illustrates the variations of average film thickness at 5, 30, 46 pipe diameters from the top bend. The presented results were achieved for a number of air and water superficial velocities, where the annular flow regime is well formed. The plots in Figure 5-40 (a-f) demonstrate the variations of the film thickness at the measuring points. The film thickness at the axial position of 5

pipe diameters is observed to have stronger variations than the other axial positions. This is due to the instability caused by the 180^{o} top bend. The variations of the liquid film are less at the lower measuring point which was at 30 pipe diameters, due to the reduction in bend effect. It can be also seen from the plots that, the flow conditions have a significant effect on the film development. For instance, at low water superficial velocity of 0.1 m/s and air superficial velocity ranging from 1.44 to 18.39 m/s, the film shows a higher variation against the axial distance of 5 pipe diameters than those for higher air velocities of 23.66 and 28.87 m/s. It is also observed that, the film values at 30 and 46 pipe diameters are close to each other, indicating that the film is in a development stage on reaching 30 pipe diameters. It can be seen from Figure 5-40 (a) that, the film has decreased very steeply at lower velocities of air. The film slope is noted to be less at higher air velocities. Similar observations can be made at higher water velocities of 0.2 and 0.3 m/s, as illustrated in Figure 5-40 (b) and (c) respectively. This is not the case for higher water velocities of 0.48, 0.7 and 1 m/s (Figure 5-40 (d-f)), where the film is seen to decrease very rapidly at 5 pipe diameters (close to the inverted U-bend) towards the lower axial positions over all air velocities. A striking similarity is noted between film thickness values measured at 30 and 46 pipe diameters. The reason for this similarity can be explained as that, under these flow conditions, the flow is quite stable when reaches 30 pipe diameters. It can be concluded that, the higher the air flow rates the faster the film development.

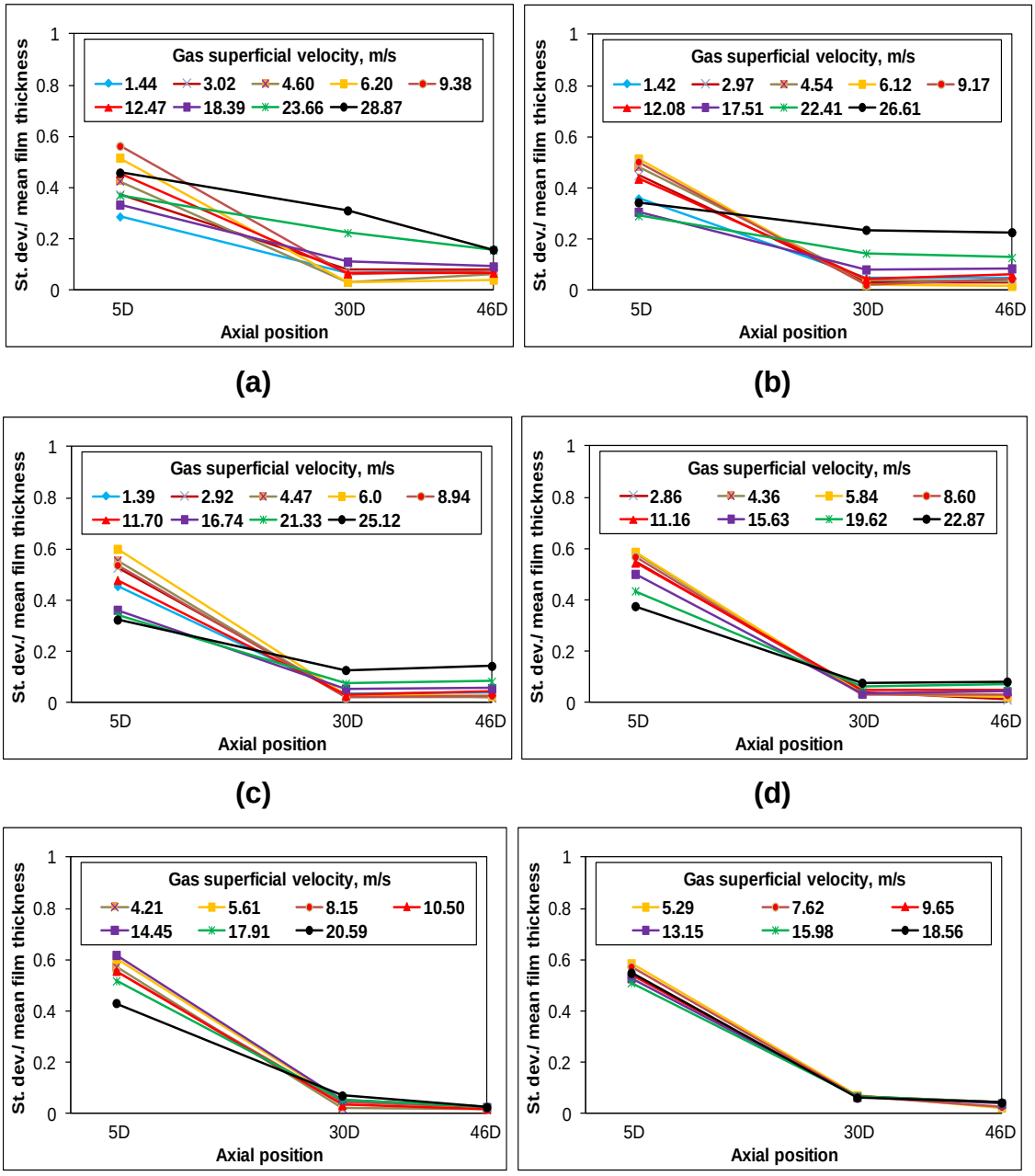

Figure 5-40 Variations of liquid film thickness with the axial distance from the inverted U-bend (along the downward flow) for water superficial velocities of (a) 0.1, (b) 0.2, (c) 0.3, (d) 0.48, (e) 0.7 and (f) 1 m/s, with different air superficial velocities

5.3.4 Circumferential distribution of the liquid film along the upward flow

Figure 5-41 (a-d) shows the circumferential distribution of liquid film for fixed water superficial velocity of 0.1 m/s and air superficial velocities of 12.47, 18.39, 23.66 and 28.87 m/s respectively. From the plots of Figure 5-41 (a), the profiles of film thickness related to the three positions are quite systematically circumferentially uniform and similar to each other. However, the film thickness at the bottom position is a bit thicker than those at the higher positions. This evidence suggests that, under these conditions, the centrifugal force has no obvious effects on the liquid film distributions at all positions. At air superficial velocities of 18.39 and 23.66 and 28.87 m/s, the film profile becomes asymmetric at the bottom. The thickest film appears at the 90^o position (corresponding to the outside of the upstream bottom bend) and the thinnest film appears at the 270^o position (corresponding to the inside of the upstream bottom bend), in comparison with those at other circumferential positions, as illustrated in Figure 5-41 (b-d) respectively. This should be due to the effect of the centrifugal force generated by the upstream bottom bend on the liquid film distribution. For the highest air superficial velocity tested, which is 28.87 m/s, the effect of this force is also noted when the flow reaches the middle section, while it is reduced on entering the top position. It is worth mentioning that, the film thickness profiles are fairly symmetric at the 0^o-180^o axis, for most air velocity ranges tested.

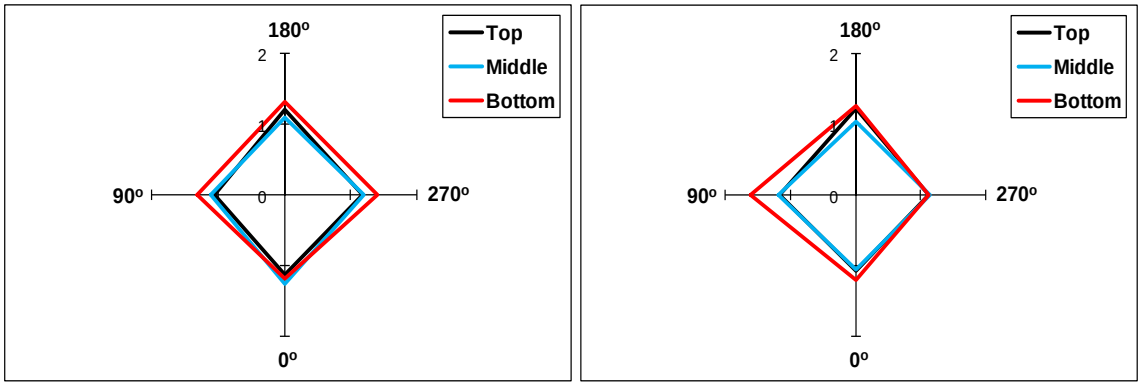

(a) Usg=12.47 m/s **(b) Usg=18.39 m/s**

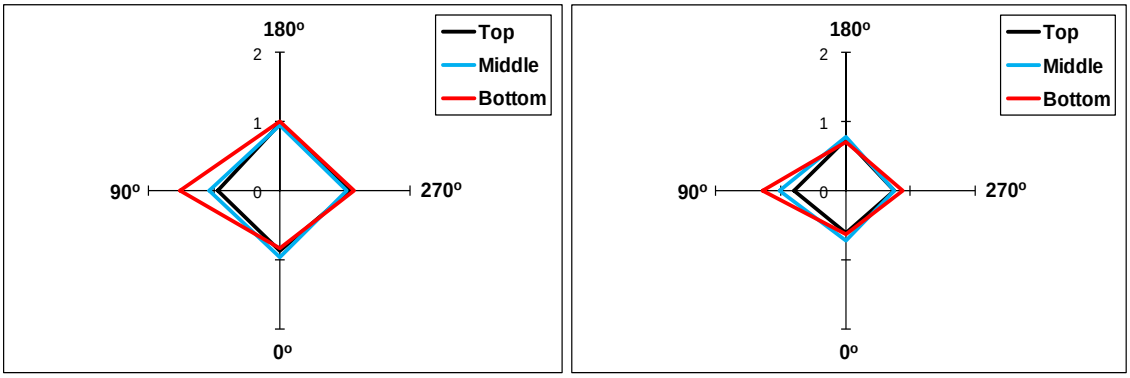

(c) Usg=23.66 m/s **(d) Usg=28.87 m/s**

Figure 5-41 Circumferential profile developments of liquid film in the upward section for air superficial velocity of (a) 12.47, (b) 18.39, (c) 23.66 and (d) 28.87 m/s, with constant water superficial velocity of 0.1 m/s. Axis unit in all plots is mm

Figure 5-42 (a-d) illustrates the circumferential distributions of the liquid film in upward flow for air superficial velocities of 11.16, 15.63, 19.62 and 22.87 m/s respectively, with fixed water superficial velocity of 0.48 m/s. For all cases, the action of the upstream bottom bend is clearly observed at the bottom position (i.e. at 5 pipe diameters), where the film shows asymmetric distribution at this position. It can be seen in all plots that, the film is thicker in the 90^{o} position, due to the impact of the centrifugal force of the upstream bottom bend, as stated above.

Obviously, the mean liquid film thickness at the bottom position is much thicker than those at higher positions, for air superficial velocities of 11.16 and 15.63 m/s, as can be seen in Figure 5-42 (a) and (b) respectively. The liquid film is

circumferentially uniformly distributed at the top and middle positions. Also both the film thickness measured at the top and middle positions is almost identical.

For air velocities of 19.62 and 22.87 m/s, the film thickness at the bottom position is thinner than those at the higher positions, as shown in Figure 5-42 (c) and (d) respectively. Another observation is that, the film thickness at the middle position is a bit thicker than that at the top position for these velocities.

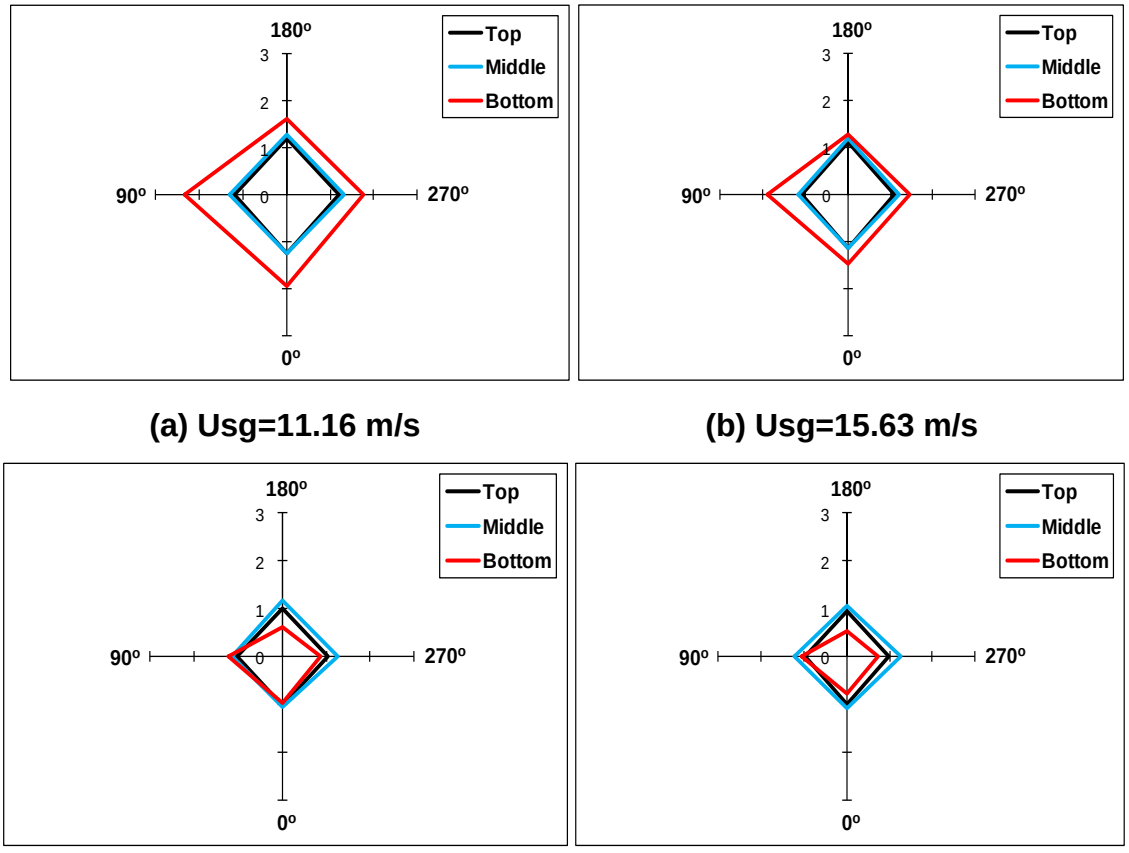

(a) Usg=11.16 m/s **(b) Usg=15.63 m/s**

(c) Usg=19.62 m/s **(d) Usg=22.87 m/s**

Figure 5-42 Circumferential profile developments of liquid film in the upward section for air superficial velocity of (a) 11.16, (b) 15.63, (c) 19.62 and (d) 22.87 m/s, with constant water superficial velocity of 0.48 m/s. Axis unit in all plots is mm

Figure 5-43 (a-d) shows the circumferential distributions of liquid film for air velocities of 9.65, 13.15, 15.98 and 18.56 m/s respectively, while the water velocity is maintained constant at 1 m/s. Obviously, the film thickness is increased in the circumferential positions of 90^{o} (corresponding to the outside of the upstream bottom bend) for all conditions. As mentioned earlier, this is

because of the centrifugal force that acts to push the liquid from inside the bend into its outer curvature. This could lead to an asymmetric liquid film distribution at the bottom position, where the liquid film becomes thicker at the 90^{o} position of the film probe (i.e. the probe located at 5 pipe diameters after the bottom bend). The force effect is reduced when the flow reaches the middle and top positions; consequently the film profile becomes more symmetrically distributed. It is also clear that, for the lower air velocity (Figure 5-43 (a)); the film thickness at the bottom position is considerably thicker than those at the higher positions. The difference between the film thickness at the bottom position and those at higher positions becomes less as the air velocity increases further. For the highest air velocity which is 18.56 m/s (Figure 5-43 (d)), the film thickness profiles show similar tendencies at all positions.

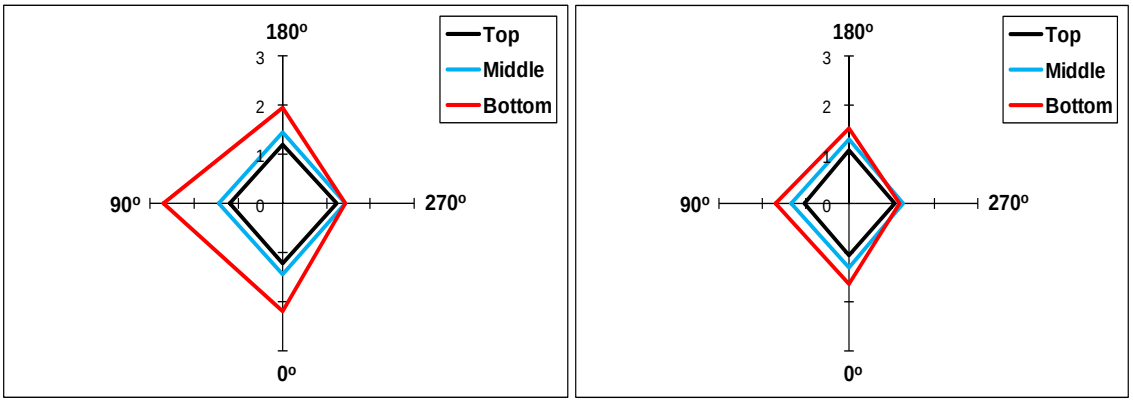

(a) Usg=9.65 m/s **(b) Usg=13.15 m/s**

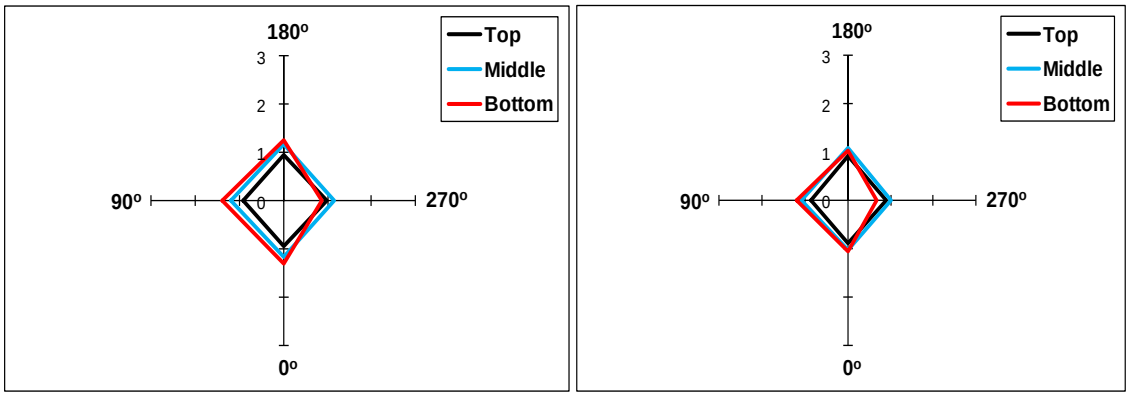

(c) Usg=15.98 m/s **(d) Usg=18.56 m/s**

Figure 5-43 Circumferential profile developments of liquid film in the upward section for air superficial velocity of (a) 9.65, (b) 13.15, (c) 15.98 and (d) 18.56 m/s, with constant water superficial velocity of 1 m/s. Axis unit in all plots is mm

5.4 PDFs, time series and wave identification of liquid film

The probability density functions (PDFs) and corresponding time traces of averaged liquid film can also provide information about the film behaviour in the downward and upward flows. For comparison, in the downward flows there are some differences among the film thicknesses at the top position from those at the lower positions; this could be due to the effect of the centrifugal force of the top bend on the film thickness distributions at the top position, while the effect of this bend at the same velocities of air and water is not distinguishable at the middle and bottom positions.

In an upward flow, with the same conditions of air and water velocities, the PDFs and time traces of liquid film show that the statistical features of the liquid film thickness at the three positions are similar to each other. However, at these flow conditions (relatively low velocities) the film thickness is obviously thicker than that in the downward flow; this evidence suggests that in the upward flow the annular flow can only be obtained at high air superficial velocities. Therefore, more investigations have been carried out at relatively high flow rates in order to obtain annular flow in the upward direction. It can be noted from the time traces of the downward and upward flows that, the roughness in the interface between the air and the water are considerably affected by the variation of the air and water superficial velocities.

5.4.1 PDFs, time series and wave identification of liquid film in the downward flow

Figure 5-44 illustrates the probability density functions (PDFs) and corresponding time traces data of measured film thickness at the (a) top, (b) middle and (c) bottom positions with air superficial velocity of 3.02 m/s and water superficial velocity of 0.1 m/s. It is important mentioning that the top, middle and bottom probes are located in the downward section at 5, 30, 46 pipe diameters, from the top bend respectively.

The liquid film signal at the top position is considerably larger and significantly different from those at the middle and bottom positions, while the characteristics

of the liquid film signals at the middle and bottom positions are quite similar to each other. Large wavelength and amplitude (also known as disturbance waves), can be seen at the top position of the downward section (i.e. at 5 pipe diameters from the top bend). This is because a centrifugal force exists in the top bend that has a substantial effect on the film thickness distributions in the top position of the straight downward pipe. In contrast, this force has no obvious effect on the film thickness distributions in the middle and bottom positions in the same flow direction. In particular, the centrifugal force effect is observed at sensor CT2 located in the same direction as the bend's outer curvature. In addition, the time traces of the downward flow in all plots show that the waves on the liquid film are more regular and coherent with each other at the middle and bottom positions. These waves can be also classified as disturbance waves, which are more evenly distributed. This suggests that, for these flow velocities of gas and liquid the film becomes reasonably stable when reaching the middle and bottom positions.

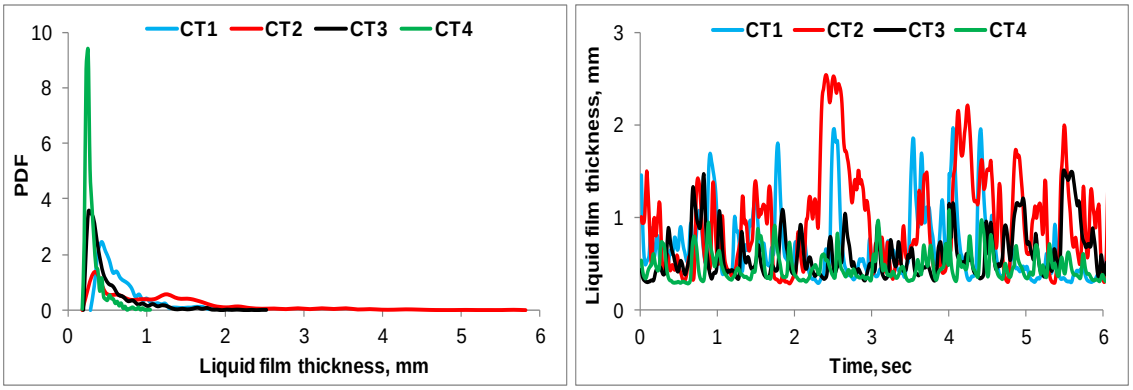

(a) Top position

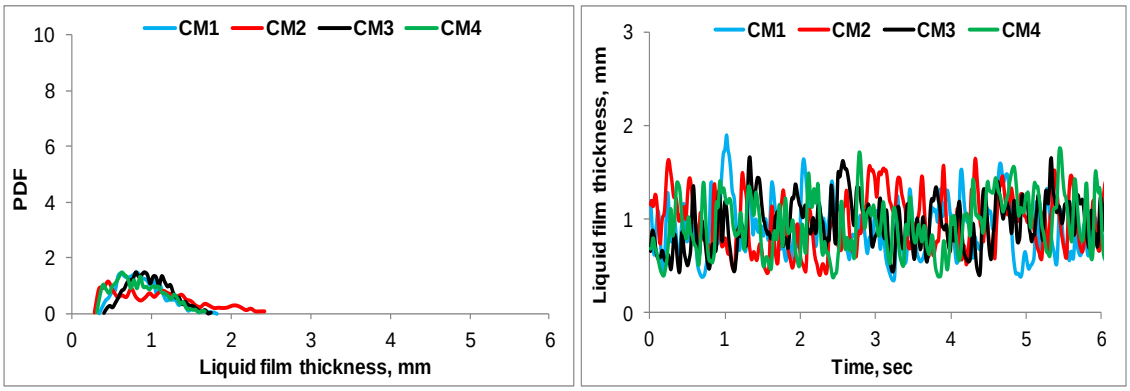

(b) Middle position

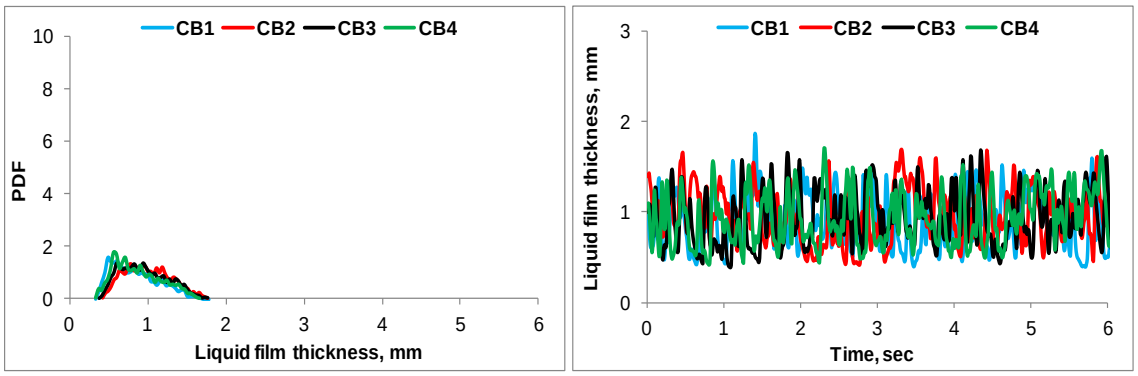

(c) Bottom position

Figure 5-44 PDFs and time traces of liquid film at (a) top, (b) middle and (c) bottom positions of the downward section for air superficial velocity of 3.02 and water superficial velocity of 0.1 m/s; PDFs in the left and time traces in the right

Figure 5-45 (a-c) illustrates the PDF and time traces of the liquid film at top, middle and bottom positions of the downward section (i.e. at 5, 30 and 46 pipe diameters from the top bend respectively), for air and water superficial velocities of 28.87 and 0.1 m/s respectively. For all cases, the PDF and statistical features of the liquid film signal at all positions are extremely different from each other, particularly those measured by sensor CT2 located in the top probe. The dissimilarity can be attributed to the centrifugal force present in the top bend. The force effect was also observed when the flow reached the middle position. At the top probe (Figure 5-45 (a)), the liquid film measured by sensor CT2 is much thicker than that measured by sensors CT1, CT3 and CT4. Similarly, the film thickness measured by CM2 located in the middle probe (Figure 5-45 (b)), is obviously thicker than those measured by CM1, CM3 and CM4. This indicates that, for these conditions the top bend effect can also reach the middle position (i.e. 30 pipe diameters from the bend). The bend effect is reduced, when the flow enters the bottom position (i.e. 46 pipe diameters from the bend). This led to similar characteristics of the film thickness as measured by CB1, CB2, CB3 and CB4. The time traces of the liquid film at the bottom position are observed to be more regular and coherent with each other. While in the top and middle positions the waves appear more irregular and random. The film thickness signal measured by both CT2 and CM2 is characterised by huge waves (classified as disturbance waves). On the other hand, the signals of the film thickness measured by CT1, CT3 and CT4 located in the top film probe are apparent to have smaller wavelength and amplitude. Similarly, the signals of liquid film that measured by the sensors CM1, CM3 and CM4 located in the middle film probe, appear to have lower wavelength and amplitude than that measured by sensor CM2. This is due to the fact that, the upstream bend (top bend) has significant effect on the top and middle position of the downward flow behaviour, although the bend effect is reduced when the flow reaches the bottom section. The bend effect was mainly observed on sensors CT2 and CM2, which are located in the same direction of the bend's outer radius.

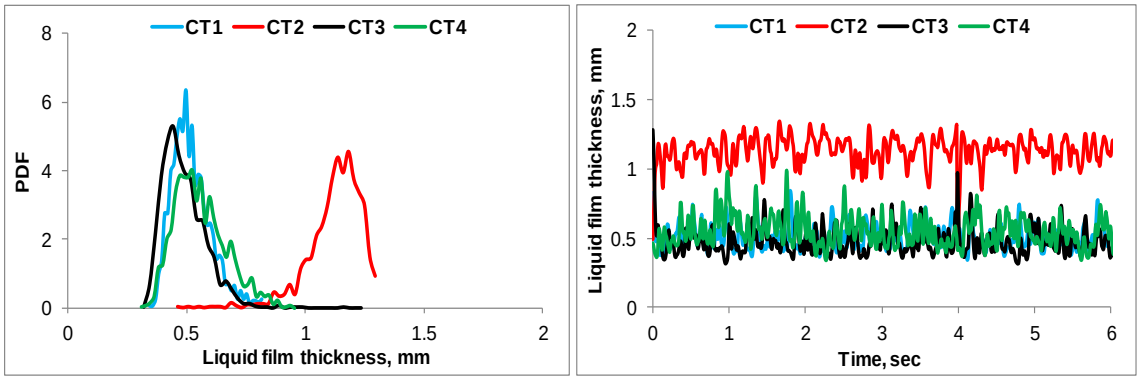

(a) Top position

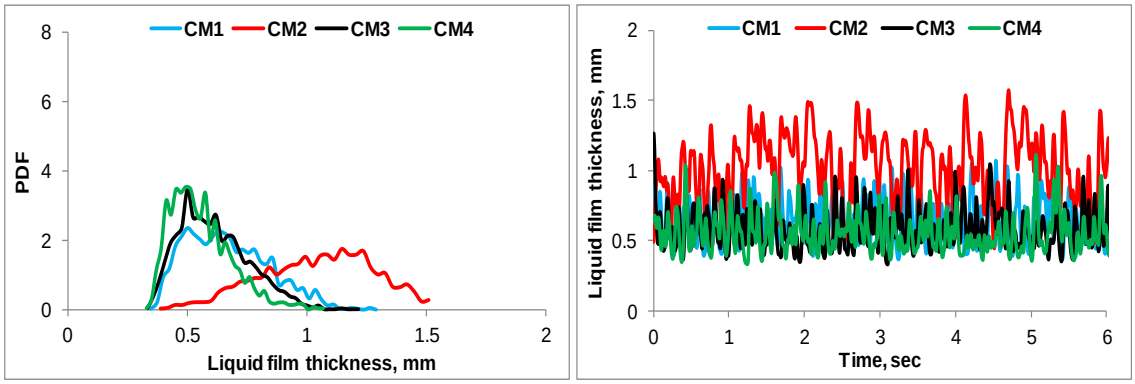

(b) Middle position

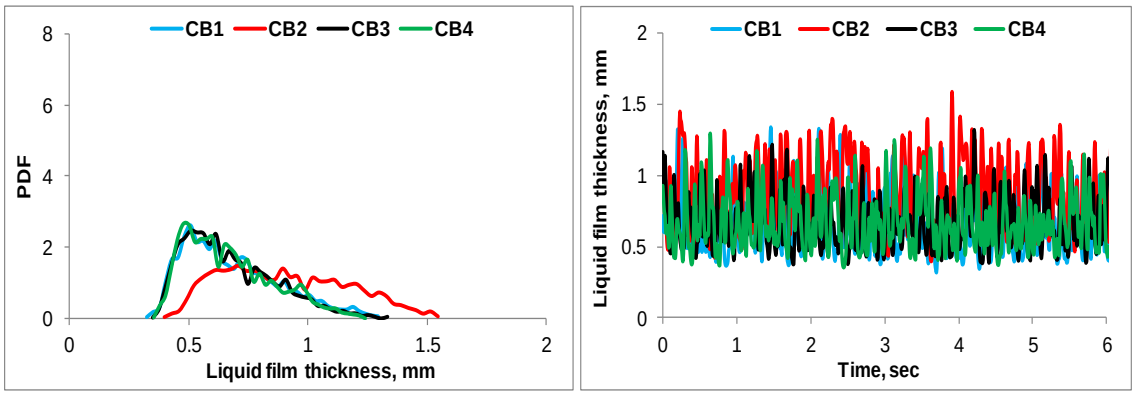

(c) Bottom position

Figure 5-45 PDFs and time traces of liquid film at (a) top, (b) middle and (c) bottom positions of the downward section for air superficial velocity of 28.87 and water superficial velocity of 0.1 m/s; PDFs in the left and time traces in the right

Figures 5-46 and 5-47 show the PDFs and time traces of liquid film at top, middle and bottom positions of the downward flow (i.e. at 5, 30 and 46 pipe diameter from the top bend respectively), for higher water superficial velocity of 1 m/s and air superficial velocities of 2.67 and 18.56 m/s respectively. In both Figures the film thickness signal measured by sensor CT2 of the top probe is very agitated and is characterised by irregular disturbance waves with high peaks. Similarly to the previous flow conditions, the film measured by the top probe also shows different behaviour from those measured by the middle and bottom probes. As stated above, this is due to the effect of the centrifugal force of the top bend on the liquid film located at the CT2 position (i.e. in the same direction as the bend's outer curvature). Striking similarity can be seen between the liquid film measured by the middle and bottom probes, which are at 30 and 46 pipe diameters respectively. This can be attributed to the fact that, the centrifugal force of the top bend did not reach these positions when these conditions were applied. It is worth mentioning that, in Figure 5-46 (a) the time traces data show that, the signal of liquid film thickness measured by CT2 is higher than the permitted range of the probes. The liquid film at the lower (middle and bottom) positions is much thinner than that in the top location which can be accurately measured by the probes. Thus, it can be concluded that the flow is still developing into an annular flow regime after the middle section of the pipe.

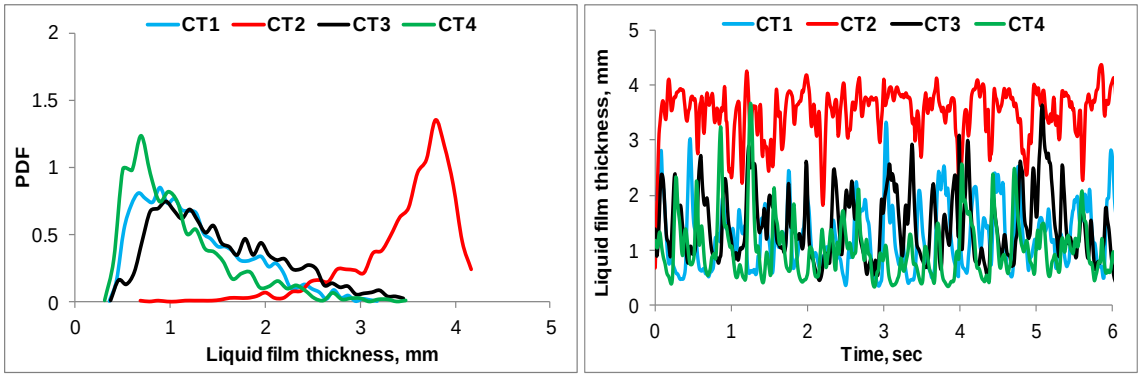

(a) Top position

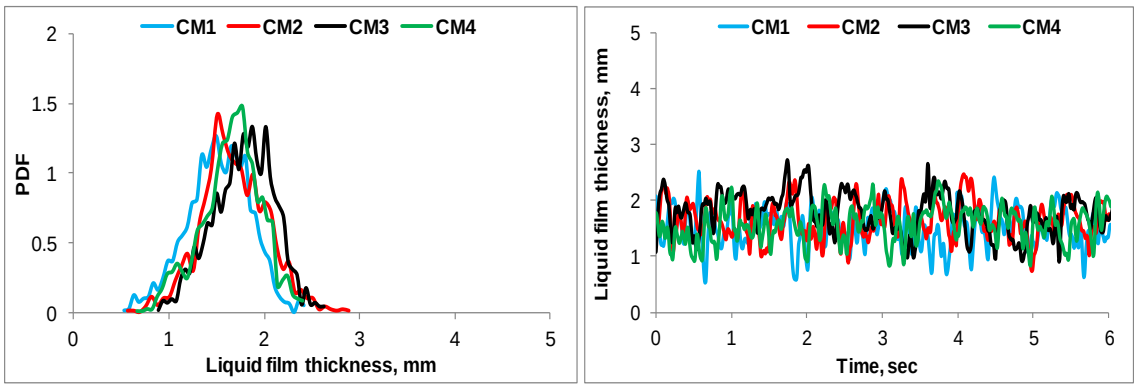

(b) Middle position

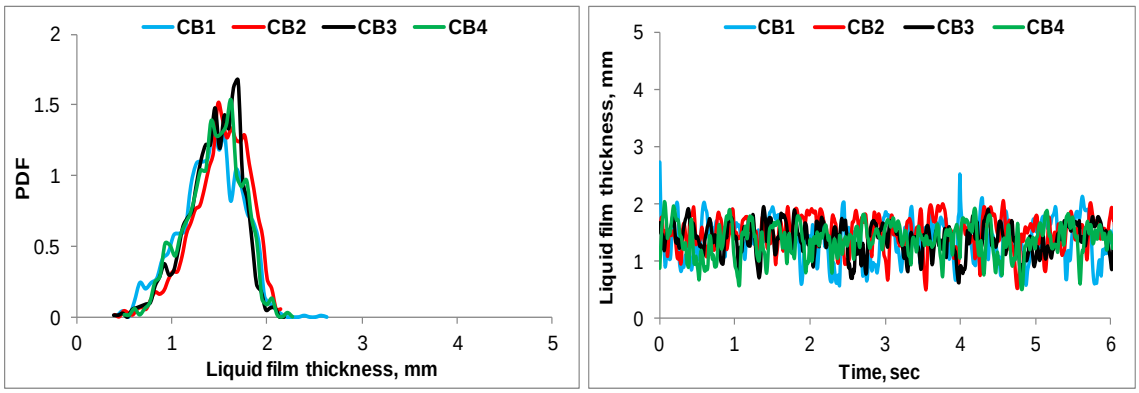

(c) Bottom position

Figure 5-46 PDFs and time traces of liquid film at (a) top, (b) middle and (c) bottom positions of the downward section for air superficial velocity of 2.67 and water superficial velocity of 1 m/s; PDFs in the left and time traces in the right

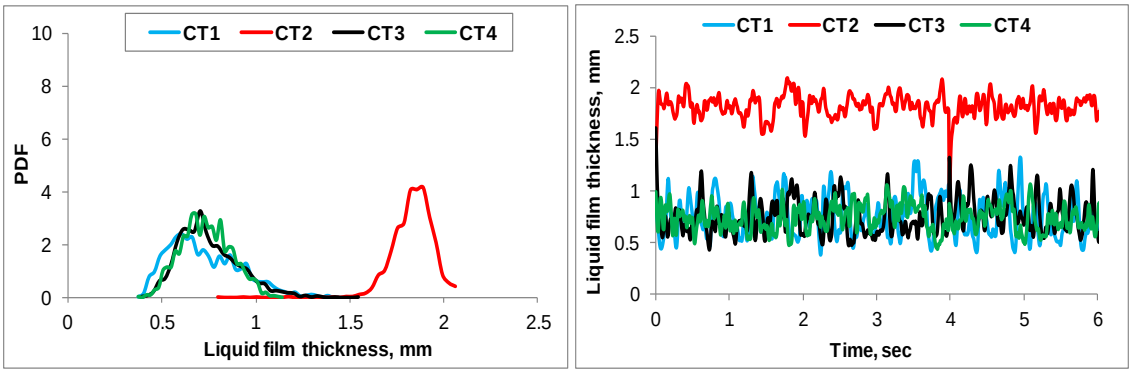

(a) Top position

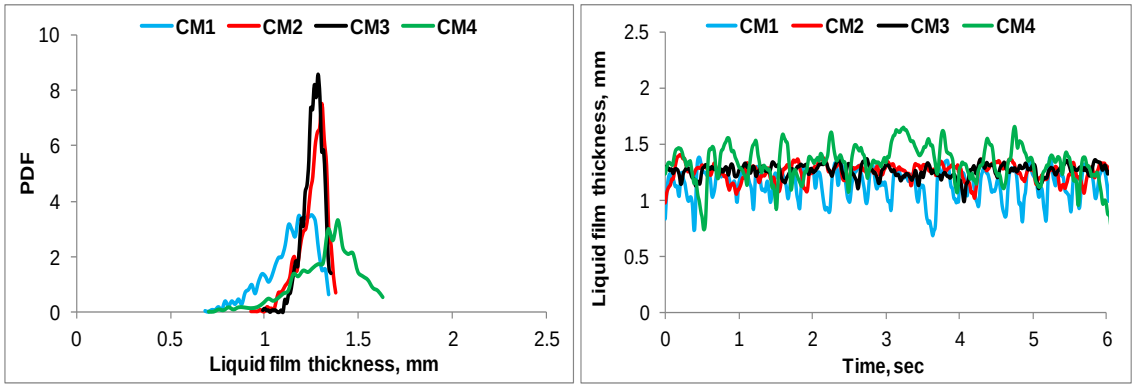

(b) Middle position

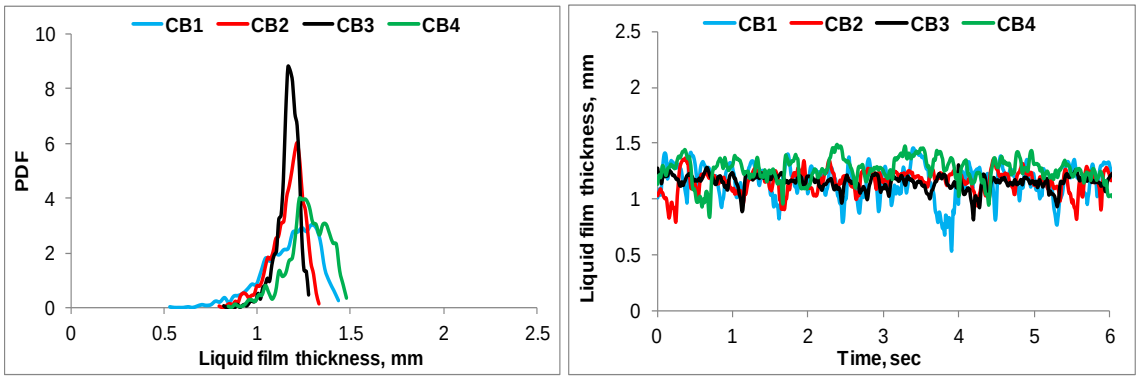

(c) Bottom position

Figure 5-47 PDFs and time traces of liquid film at (a) top, (b) middle and (c) bottom positions of downward section respectively for air superficial velocity of 18.56 and water superficial velocity of 1 m/s; PDFs in the left and time traces in the right

5.4.2 PDFs, time series and wave identification of liquid film in the upward flow

Figures 5-48 and 5-49 show the PDFs and time traces of liquid film measured at the bottom, middle and top positions of the upward section, which are at 5, 28, 47 pipe diameters from the bottom bend respectively. The data was collected for air superficial velocities of 3.02 and 28.87 m/s respectively, while the water superficial velocity was kept constant at 0.1 m/s. At a relative low air flow rate (air superficial velocity of 3.02 m/s), the PDFs, wave amplitude and trends of the liquid film signals at the three positions are extremely similar to each other, as shown in Figure 5-48 (a-c). This suggests that, at these velocities the centrifugal force of the upstream bend (bottom bend) has no distinguishable effects on the characteristics of the liquid film at all positions of the upward flow. It can be noted from the time traces data presented in Figure 5-48 (a-c) that, the wave characteristics of liquid film at the top, middle and bottom positions are very high, which can be classified as disturbance waves. The high peak of the disturbance waves can be attributed to the intermittent flow observed at these conditions. These waves are decreased with increasing gas flow rates, as shown in Figure 5-49 (a-c). This evidence suggests that, by increasing the air flow rate, the film thickness decreases at a fixed water flow rate, due to the fact that the annular flow is dominated by increasing the gas flow rates. It is important mentioning that, the observed waves in Figure 5-49 (a-c) are also disturbance waves having lower peak than those observed in Figure 5-48 (a-c).

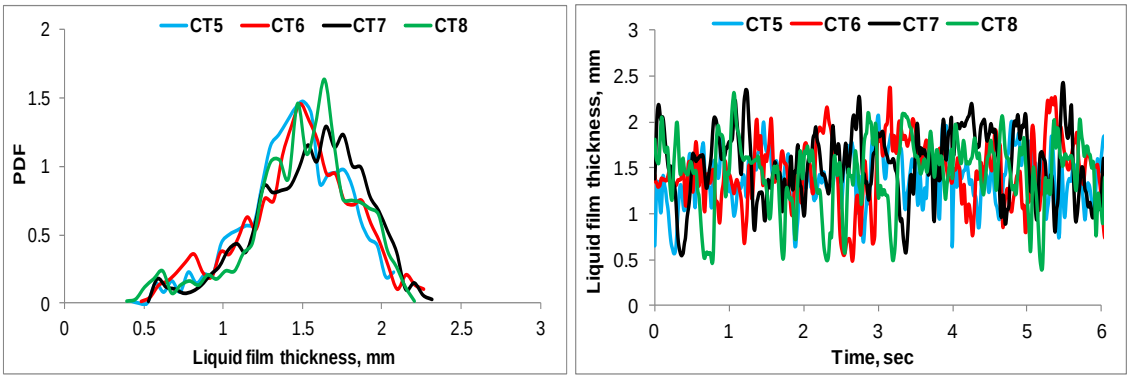

(a) Top position

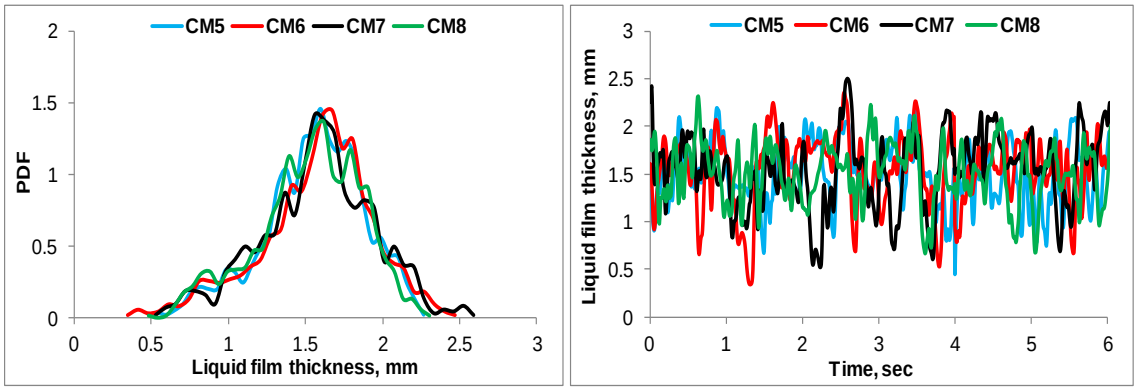

(b) Middle position

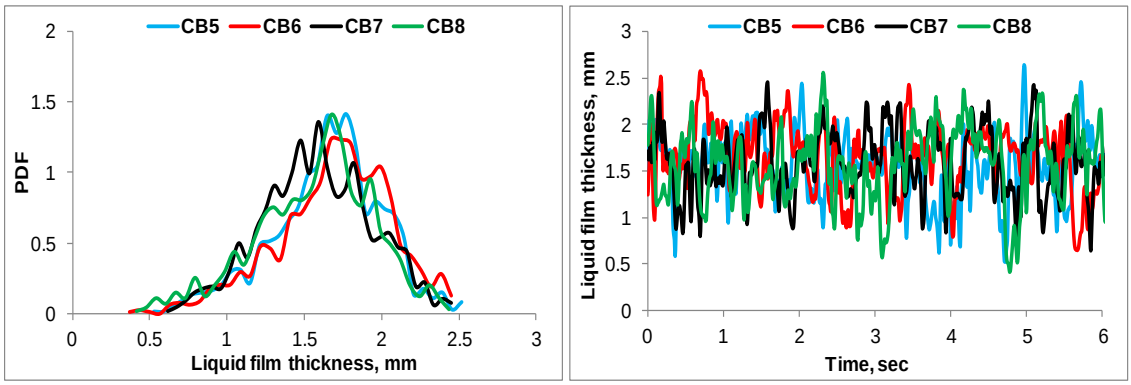

(c) Bottom position

Figure 5-48 PDFs and time traces of liquid film at (a) top, (b) middle and (c) bottom positions of upward section for air superficial velocity of 3.02 and water superficial velocity of 0.1 m/s; PDFs in the left and time traces in the right

It can be seen from Figure 5-49 (c) that, the profile of the liquid film measured by the bottom probe (at 5 pipe diameters from the bottom bend), is notably different from that measured by the middle and top probes, located at 28 and 47 pipe diameters from the bottom bend respectively. This is based on the fact that, the film thickness measured by the bottom probe is affected by the centrifugal force present in the bottom bend. In addition, the liquid film thickness measured by sensor CB6 located in the bottom probe, is observed to be thicker than that measured by sensors CB5, CB7 and CB8 located in the same probe, as presented in Figure 5-49 (c). This observation is attributed to the effect of centrifugal force. Furthermore, the time traces results illustrated in Figure 5-49 (c) clearly show that, the signal of the film thickness measured by CB6 is a bit higher than those measured by CB5, CB7 and CB8.

Less effect of the bend's centrifugal force on the film thickness measured at the middle position (i.e. at 28 pipe diameters), as shown in Figure 5-49 (b). On the other hand, no obvious effect can be identified when the film reaches the top position, which is at 47 pipe diameters (Figure 5-49 (a)). This evidence suggests that, the bend action is reduced as the film is initiated to the higher positions.

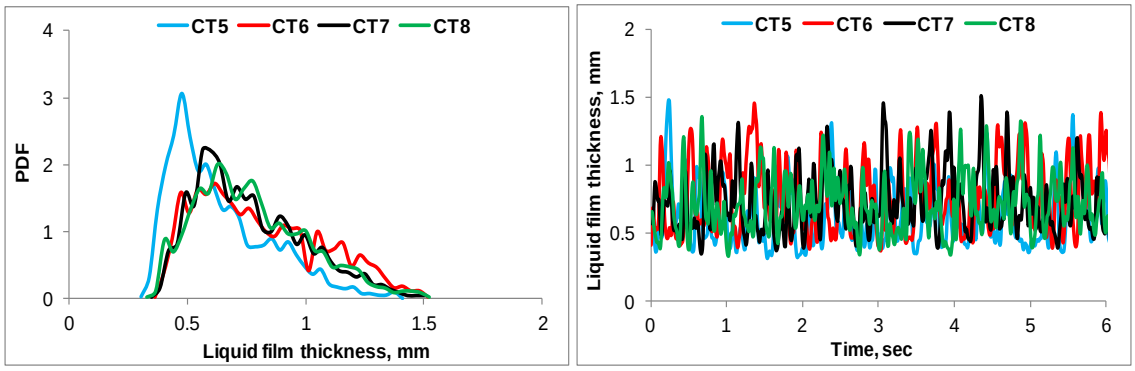

(a) Top position

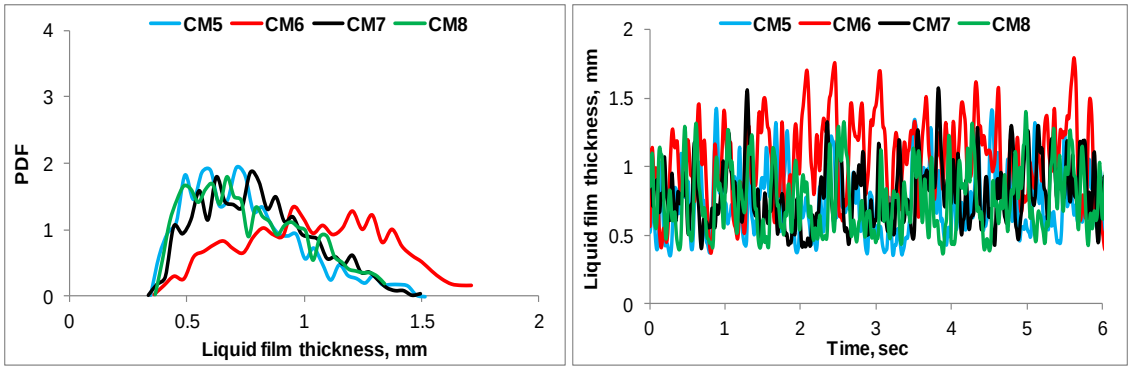

(b) Middle position

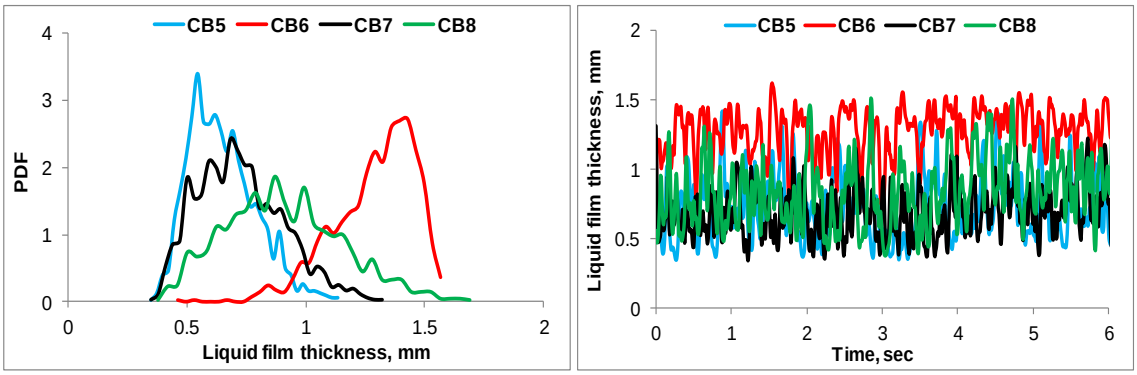

(c) Bottom position

Figure 5-49 PDFs and time traces of liquid film at (a) top, (b) middle and (c) bottom positions of the upward section for air superficial velocity of 28.87and water superficial velocity of 0.1 m/s; PDFs in the left and time traces in the right

Figures 5-50 and 5-51 show the PDFs and time traces of liquid film thickness measured in three positions for air superficial velocity of 2.67 m/s and 18.56 m/s respectively, with water superficial velocity of 1 m/s. In both Figures 5-50 and 5-51, the characteristics of the liquid film signal at the bottom position are more varied than those at the top and middle positions. The profile of PDFs at the bottom position is significantly different from those at the higher (top and middle) positions. Moreover, in both Figures 5-50 and 5-51 the profile of PDFs at the bottom position varied from one location to another circumferentially. This suggests that, the wave structure is related to the circumferential positions. This phenomenon may be caused by the centrifugal force effect of the upstream bend (bottom bend). Furthermore, the plots show that the wave amplitude of the liquid film signal measured by the bottom probe is much larger than those measured by the higher probes, while the characteristic of the liquid film signal at the middle position is quite similar to that at the top position. These evidences suggest that, under these particular upward flow conditions the liquid film becomes reasonably stable after the middle section (i.e. after 28 pipe diameters). The stability of the liquid film may indicate that the flow starts developing on reaching the 28 pipe diameters. This suggestion is supported by the similarity that can be seen between the waves of liquid film at 28 and 47 pipe diameters. In all cases, the disturbance waves are formed continuously and appear to have very high amplitude. It is important to note that, the observed disturbance waves are larger than the permitted range of the film probe for air and water superficial velocities of 2.67 and 1 m/s respectively, as presented in Figure 5-50 (c). This is due to the fact that, the intermittent flow regime is created when these velocities are used. With increasing the air superficial velocity to 18.56 m/s and water superficial velocity is kept constant at 1 m/s, as presented in Figure 5-51 (a-c) , the flow regime became annular flow. As a result, the disturbance waves exhibit relatively lower peaks at all positions.

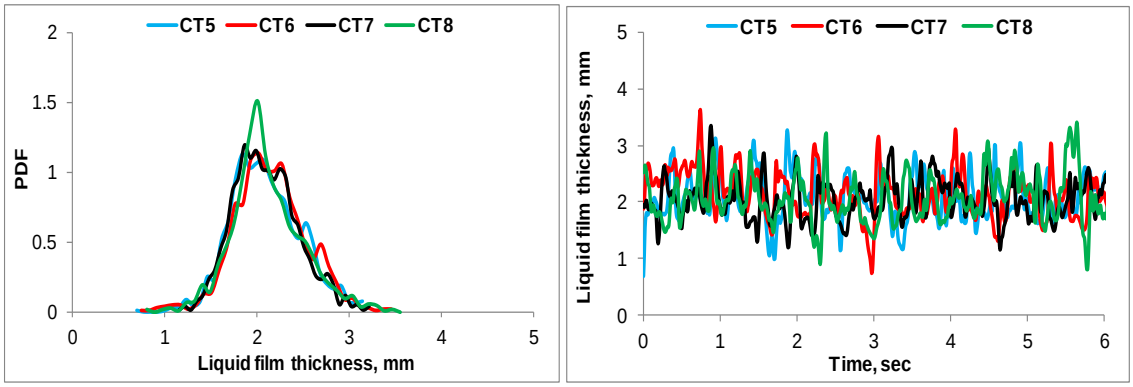

(a) Top position

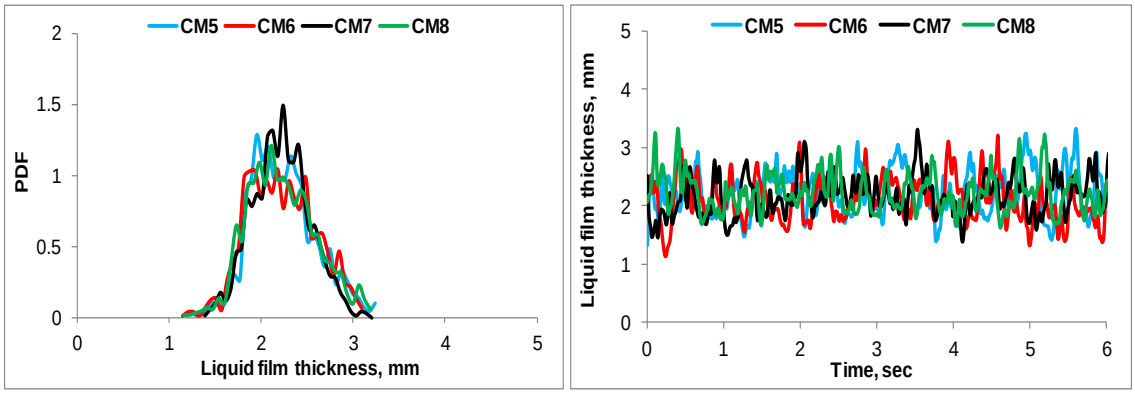

(b) Middle position

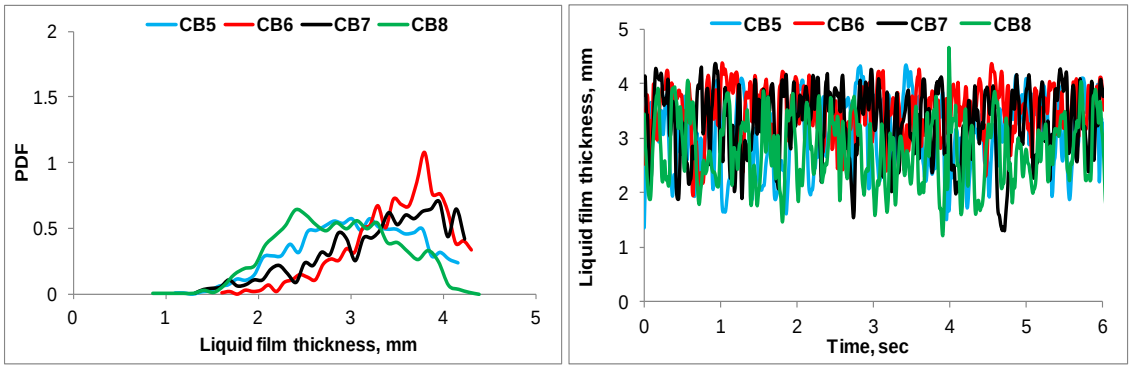

(c) Bottom position

Figure 5-50 PDFs and time traces of liquid film at (a) top, (b) middle and (c) bottom positions of the upward section for air superficial velocity of 2.67 and water superficial velocity of 1 m/s; PDFs in the left and time traces in the right

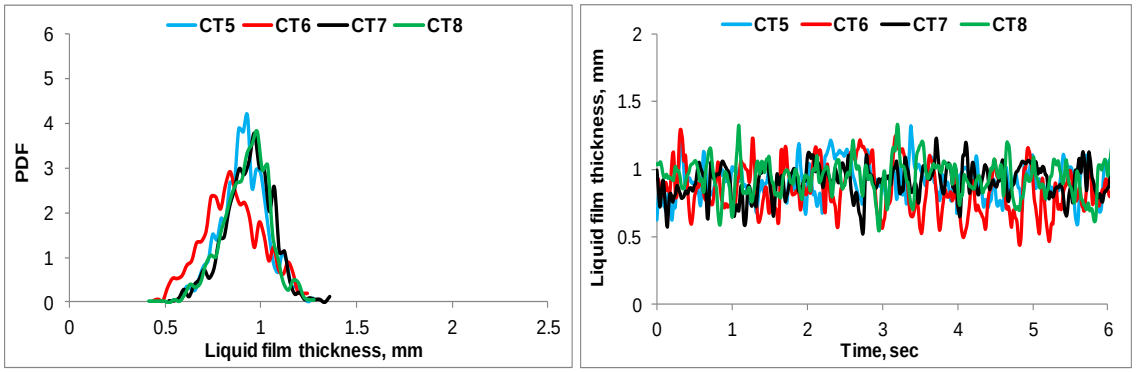

(a) Top position

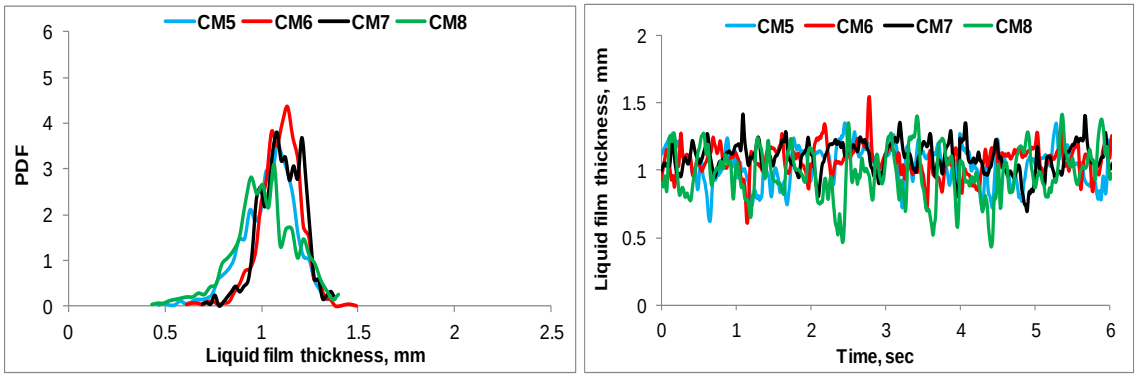

(b) Middle position

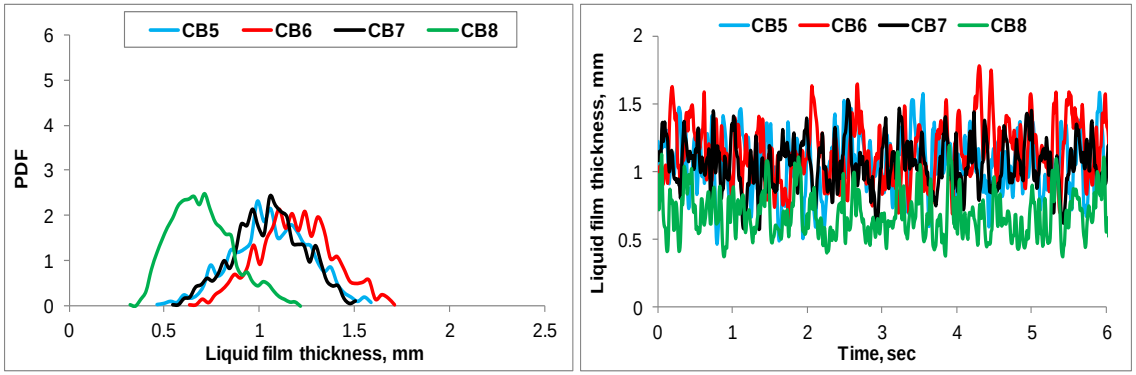

(c) Bottom position

Figure 5-51 PDFs and time traces of liquid film at (a) top, (b) middle and (c) bottom positions of the upward section for air superficial velocity of 18.56 and water superficial velocity of 1 m/s; PDFs in the left and time traces in the right

5.5 Frequency of liquid film thickness

The frequency plots presented in this section was determined using the power spectral density (PSD) function. The methodology represents the distribution of the measured signal and its variation with a range of frequency, which is extracted from direct Fourier transformations of the experimental data. The power spectral distributions were applied to identify the dominant frequency at different positions along downward and upward sections for various flow rates of air and water.

From the examination of a set of flow conditions, the frequency tendencies are obtained. In general, it was observed that the PSD shape located close to the bends (namely at 5 pipe diameters after the top and bottom bends), is significantly different from those located further away from the bends for the same flow rates.

5.5.1 Frequency of liquid film thickness along the downward flow

Figure 5-52 shows the generated PSDs at the top, middle and bottom positions of the downward section for air superficial velocities of 3.02, 12.47 and 28.87 m/s, with constant water superficial velocity of 0.1 m/s.

It can be noted from the plots of Figure 5-52 that, the PSD height appears much larger at the top position, particularly at sensor CT1 located in the same direction of the top bend's outer radius than those at the middle and bottom positions for air and water superficial velocities of 3.02 and 0.1 m/s respectively. This is because of the bend effect on the flow distribution in the adjacent section. Similar tendency of the PSD is found at the middle and bottom positions of the downward section. This can be attributed to the fact that, the effect of the top bend became less as the flow approached to further positions. Another observation is that, under these flow rates of air and water, the PSD shape decreases considerably with increasing the air superficial velocity. For higher air superficial velocity which is 12.47 m/s and at constant water superficial velocity of 0.1 m/s, the PSD shape at the three (top, middle and bottom) positions shows a similar trend. One can conclude that, the bend effect was not distinguishable when these flow rates of air and water are applied. Similar behaviour can be seen for air superficial velocity of 28.87 m/s. Again, this is based on the fact that the bend action becomes less for higher air flow rates.

Position	Usg=3.02 m/s	Usg=12.47 m/s	Usg=28.87 m/s
Top	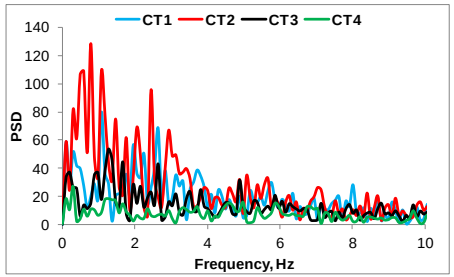	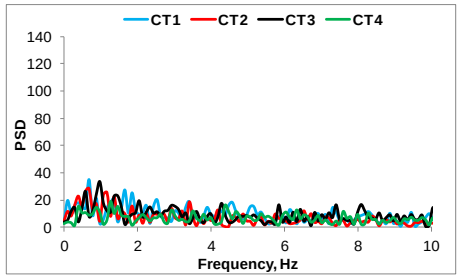	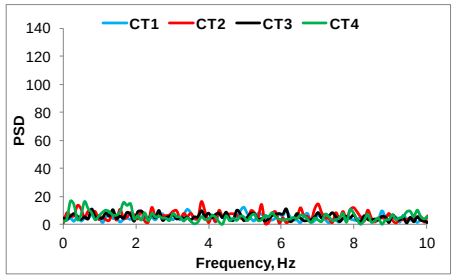
Middle	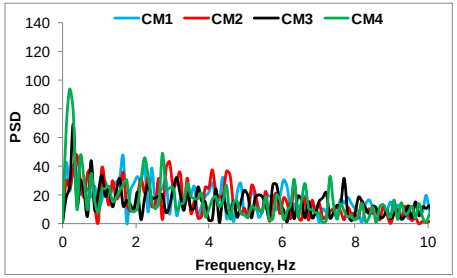	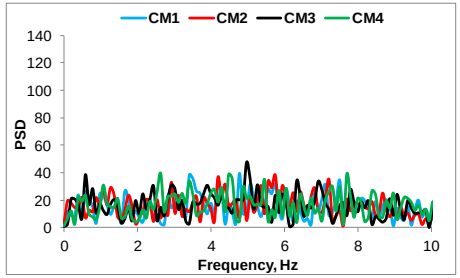	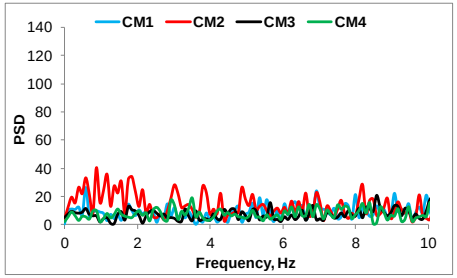
Bottom	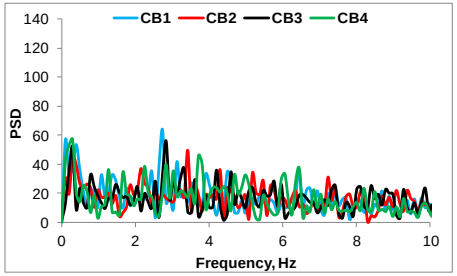	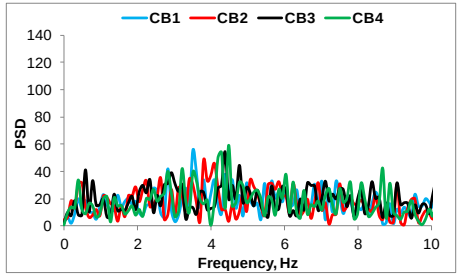	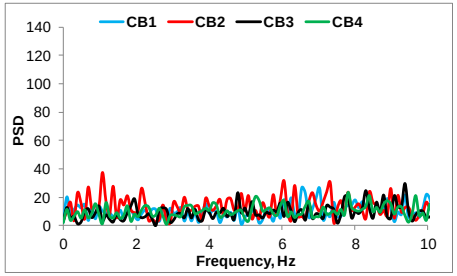

Figure 5-52 Power spectral density (PSD) of liquid film thickness at top, middle and bottom positions of the downward section for different air superficial velocities and water superficial velocity of 0.1 m/s

For air superficial velocity of 2.86 and water superficial velocity of 0.48 m/s, as presented in Figure 5-53, the PSD's signal at the top position still shows different tendency than those at lower positions. The variation of PSD was decreased as the air superficial velocity increased to 11.16 m/s, while the water superficial velocity remains fixed at 0.48 m/s. For all air superficial velocities tested (i.e. 2.86, 11.16 and 22.87 m/s), a striking similarity between the locations of the frequency is observed at the middle and bottom positions. Again, this is due to the reduction of the bend impact as the flow reaches the middle position and that the flow is fully developed. It is worth nothing that, the sensor CT2 located in the top film probe shows a higher PSD at a relatively low frequency value than those located in the other sensors, i.e. CT1, CT3 and CT4. As the air superficial velocity increased to 22.87 m/s and the water superficial velocity is kept constant at 0.48 m/s (Figure 5-53), the PSD plots did not yield any considerable differences at the top, middle and bottom positions. This indicates that, the flow distribution is consistent along the downward section when these velocities are applied and that, the flow becomes less sensitive at highest air flow rates.

Figure 5-54 illustrates the PSDs at the top, middle and bottom positions of the downward section, for a highest water superficial velocity of 1 m/s and air superficial velocities of 2.67, 9.65 and 18.56 m/s. From the plots of the Figure 5-54, it can be seen that the PSD height decreased with increasing the air superficial velocity, having a minimum value at air superficial velocity of 18.56 m/s. Similar to the cases of water superficial velocities of 0.1 and 0.48 m/s, the PSD at the top position (at 5 pipe diameters from the top bend), shows significant differences when compared with those at the middle and bottom positions, i.e. at 30 and 46 pipe diameters respectively. While PSDs shapes at the middle and bottom positions are consistent for all air superficial velocities, which indicates that the bend effect was reduced and the flow started to develop on entering the middle position. For air superficial velocity of 2.86 m/s, higher peak of PSDs is observed at the top position, while those at the middle and bottom positions are similar to each other and characterised by lower peaks. Similar behaviour can be seen when air superficial velocity increased to 9.65 m/s. For a highest air superficial velocity of 18.56 m/s, all PSDs shapes are close to each other.

Position	Usg=2.86 m/s	Usg=11.16 m/s	Usg=22.87 m/s
Top	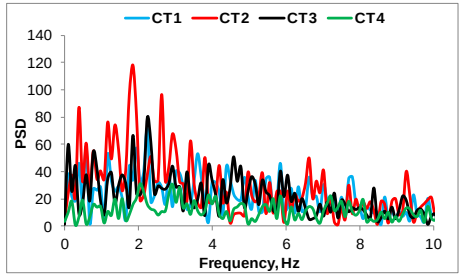	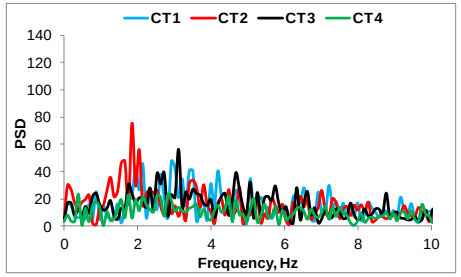	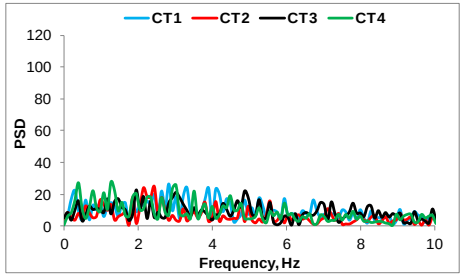
Middle	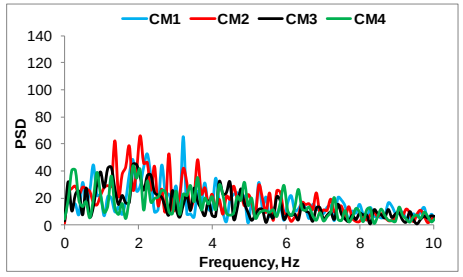	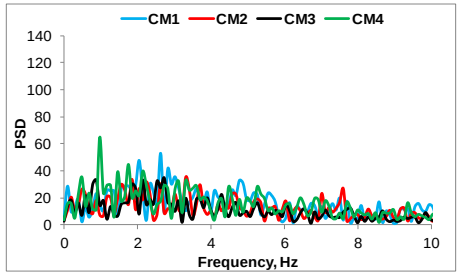	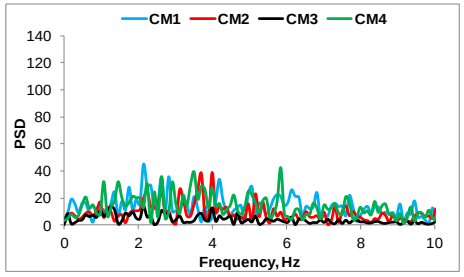
Bottom	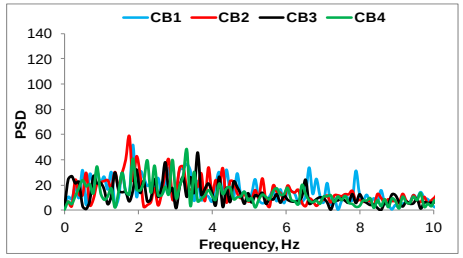	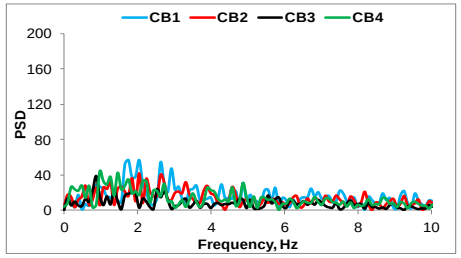	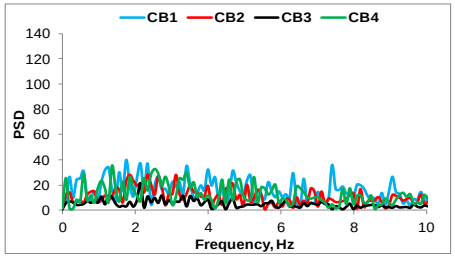

Figure 5-53 Power spectral density (PSD) of liquid film thickness at top, middle and bottom positions of the downward section for different air superficial velocities and water superficial velocity of 0.48 m/s

Position	Usg=2.67 m/s	Usg=9.65 m/s	Usg=18.56 m/s
Top	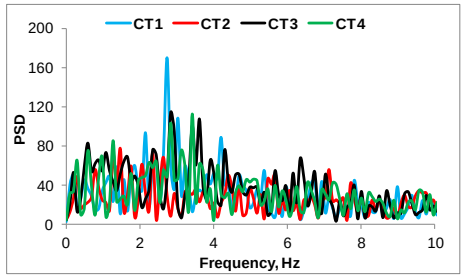	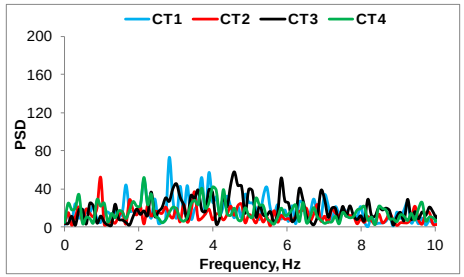	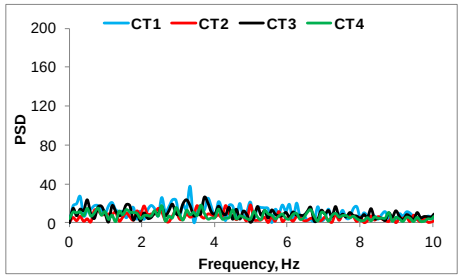
Middle	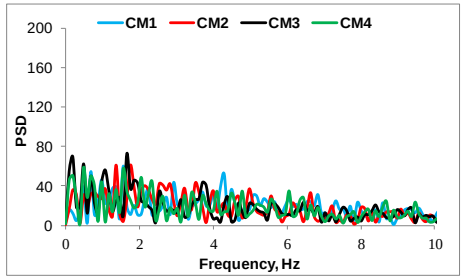	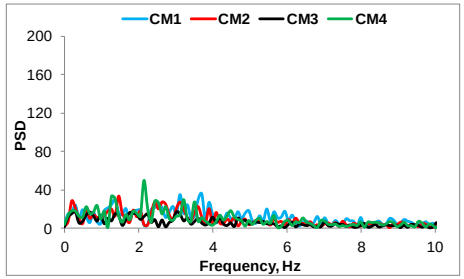	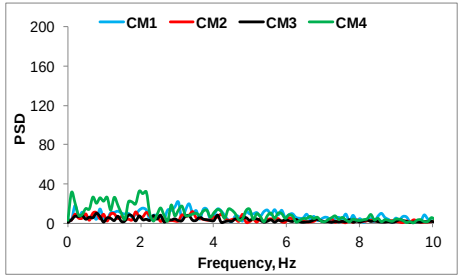
Bottom	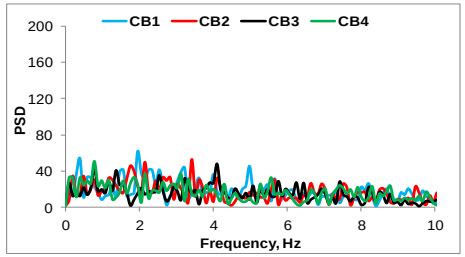	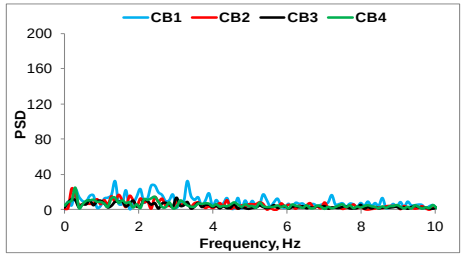	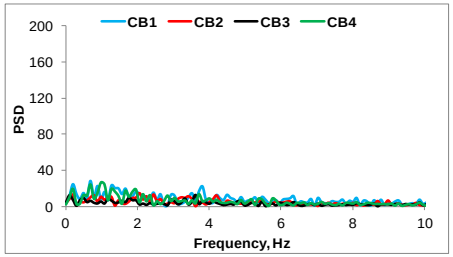

Figure 5-54 Power spectral density (PSD) of liquid film thickness at top, middle and bottom positions of the downward section for different air superficial velocities and water superficial velocity of 1 m/s

5.5.2 Frequency of liquid film thickness along the upward flow

An examination of power spectral density (PSD) of liquid film thickness at different positions of upward section, and for a range of air and water superficial velocities is presented in Figures 5-55, 5-56 and 5-57.

In all plots of Figures 5-55, 5-56 and 5-57, it can be seen that the frequency increases with increasing the water superficial velocity. For example the amplitude of PSDs at 0.1 m/s is much lower than those at 1 m/s, for all air superficial velocities. On the other hand, for a given water superficial velocity, the PSDs amplitude is decreased as air superficial velocity increased further.

Figure 5-55 shows that, the frequency distribution and PSDs shape at the top, middle and bottom positions are consistent, for air superficial velocities of 3.02 and 12.47 m/s. However, for a highest air superficial velocity of 28.87 m/s, the PSDs amplitude and frequencies location at the bottom position are a bit different than those at top and middle positions. The similarity of PSDs and frequencies at air velocities of 3.02 and 12.47 m/s, is based on the fact that the flow regime is the same along the upward section which is intermittent flow, when these velocities were applied, while an annular flow is observed for air superficial velocity of 28.87 m/s. It can be concluded that, the behaviour of the frequency is highly depends on the flow regime, which in turn led to different frequency.

Figure 5-56 illustrates a set of power spectral density (PSD), for water superficial velocity of 0.48 m/s and air superficial velocities of 2.86, 11.16 and 22.87 m/s. In all positions, namely top, middle and bottom positions, the PSD amplitude are decreased as the air velocity increased.
For air superficial velocities of 2.86 and 11.16 m/s, the frequencies behaviour at the bottom position is observed to be different with much larger amplitude of PSDs and different locations of the dominant frequency, when compared with those located at the higher positions. For air superficial velocity of 22.87 m/s, the PSDs at all positions appear similar to each other, as illustrated in Figure 5-56.

Position	Usg=3.02 m/s	Usg=12.47 m/s	Usg=28.87 m/s
Top	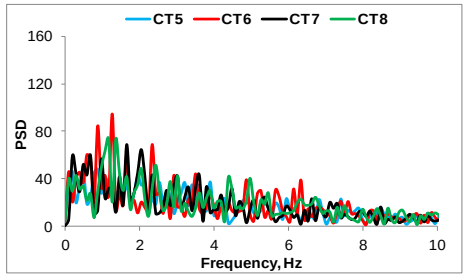	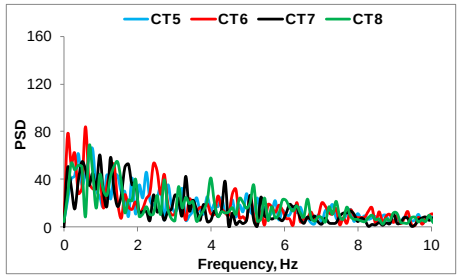	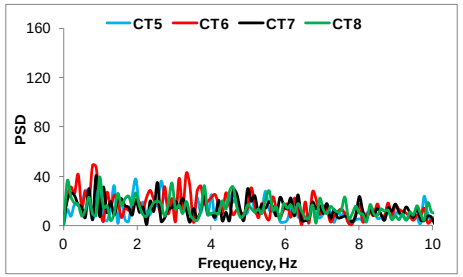
Middle	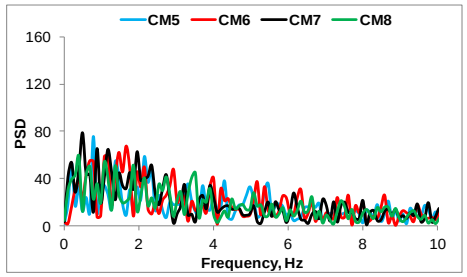	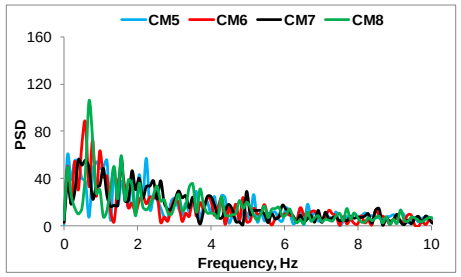	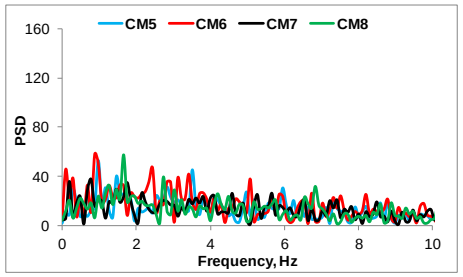
Bottom	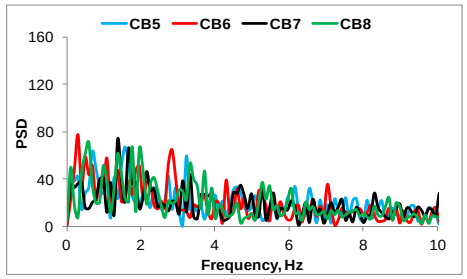	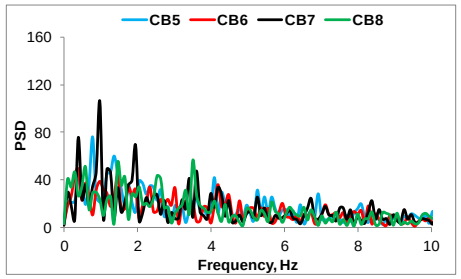	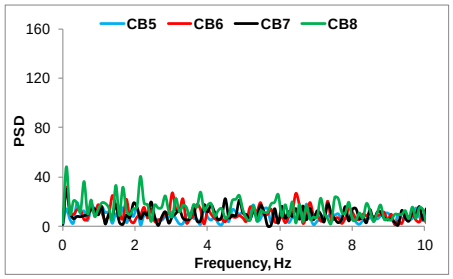

Figure 5-55 Power spectral density (PSD) of liquid film thickness at top, middle and bottom positions of the upward section for different air superficial velocities and water superficial velocity of 0.1 m/s

Position	Usg=2.86 m/s	Usg=11.16 m/s	Usg=22.87 m/s
Top	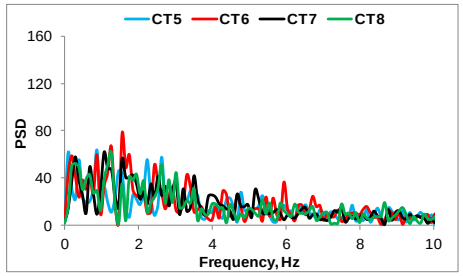	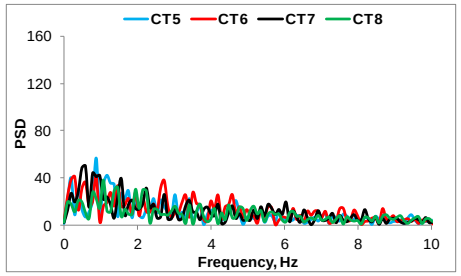	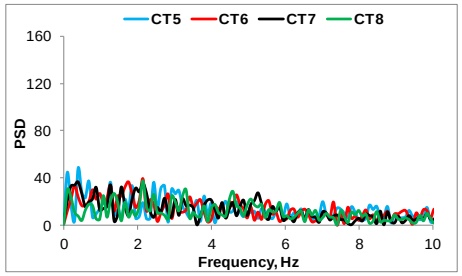
Middle	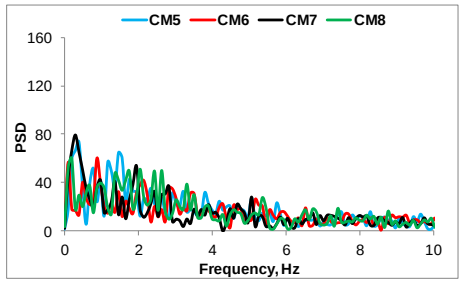	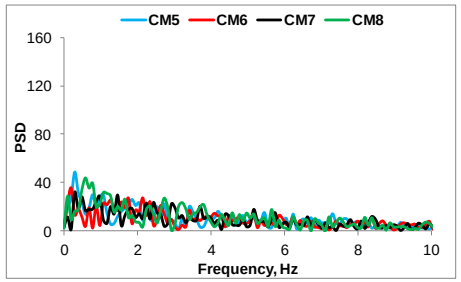	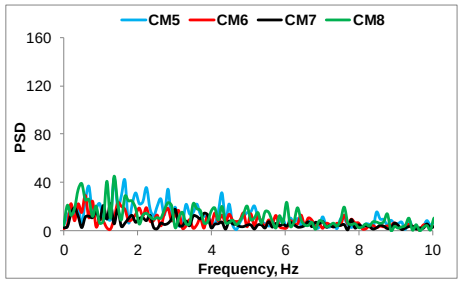
Bottom	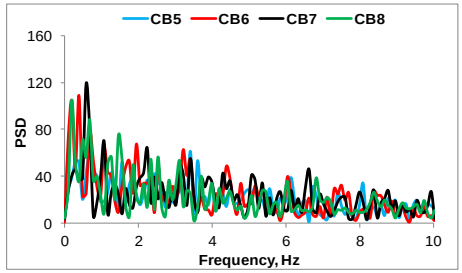	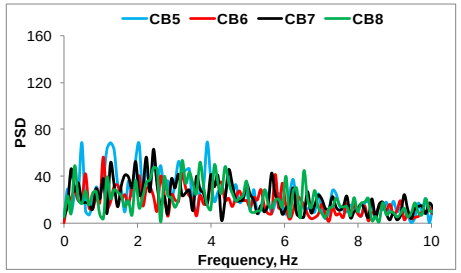	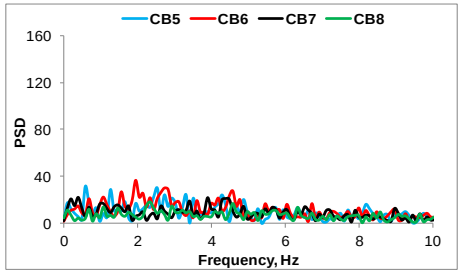

Figure 5-56 Power spectral density (PSD) of liquid film thickness at top, middle and bottom positions of the upward section for different air superficial velocities and water superficial velocity of 0.48 m/s

Figure 5-57 shows how air superficial velocity can affect the frequency distribution. The PSDs are observed to change as air superficial velocity increased to higher values, which in turn led to a relatively low peak of PSDs. It is observed in all plots of Figure 5-57 that, the PSDs are decreased as the air superficial velocity increased. Also, it can be noted that for air superficial velocities of 2.67 and 9.65 m/s and water superficial velocity of 1 m/s, the frequency behaviour at the top and middle positions almost follow the same trend and has similar frequency locations. This is not the case for the PSDs that identified at the bottom position, which are a bit higher than those at the top and middle positions. With increasing the air superficial velocity to 18.56 m/s and the water superficial velocity remains constant at 1 m/s, the PSDs shape is almost identical for all positions along the flow path.

Position	Usg=2.67 m/s	Usg=9.65 m/s	Usg=18.56 m/s
Top	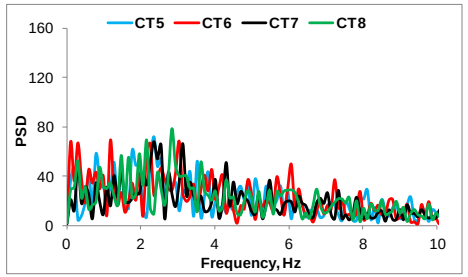	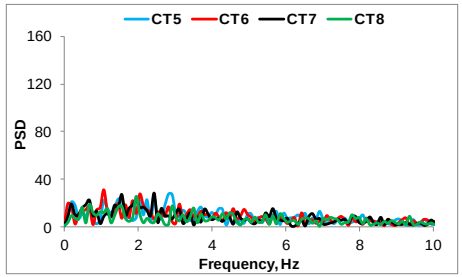	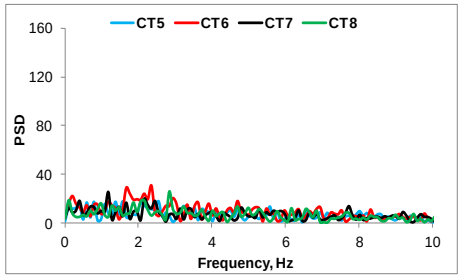
Middle	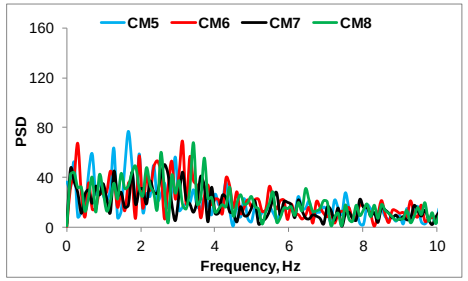	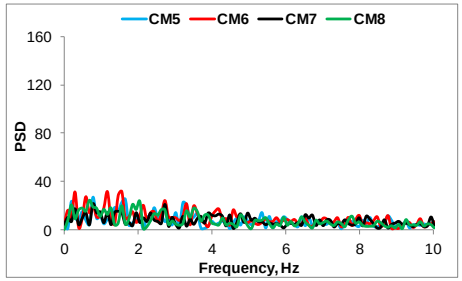	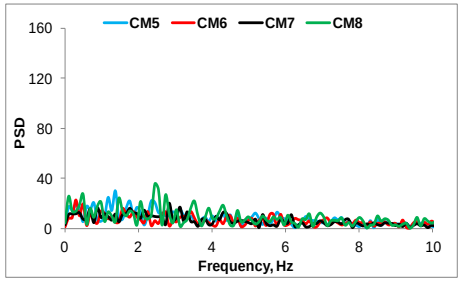
Bottom	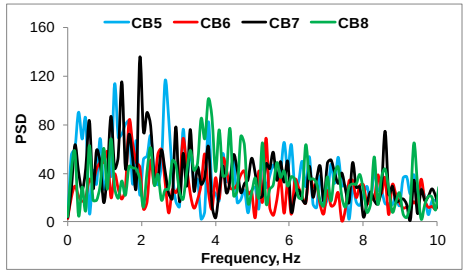	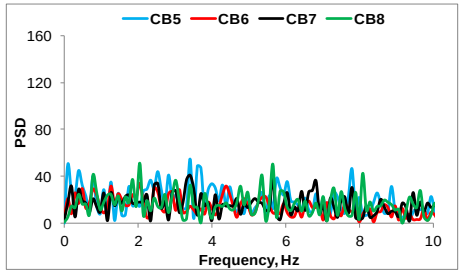	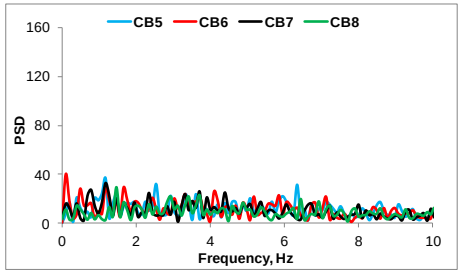

Figure 5-57 Power spectral density (PSD) of liquid film thickness at top, middle and bottom positions of the upward section for different air superficial velocities and water superficial velocity of 1 m/s

5.6 Liquid film velocity and liquid entrainment

In this study, an important aspect is to investigate the liquid film velocity in both downward and upward flows. For a given liquid flow rate and film thickness, the liquid entrainment rate can be obtained using the following equation:

$$E = 1 - \frac{4\,U_f \delta}{U_{sl} D_{tube}} \quad \textbf{(5-1)}$$

Where E, δ, U_f, U_{sl} and D_{tube} are the liquid entrainment rate, measured film thickness, measured film velocity, water superficial velocity and pipe diameter respectively.

5.6.1 Liquid film velocity and liquid entrainment rate in the middle position of the downward section

Figure 5-58 (a) shows the liquid film velocity data obtained in the middle position of the downward section for water superficial velocity ranging from 0.1 to 1 m/s. It is worth mentioning that, the electrolyte injection method was used to obtain the film velocity results. This method is based on injecting the electrolyte into the liquid film in order to increase its conductivity. The transit time between the two sensors in the integrated probe can be determined by the cross correlation method, and then the film velocity can be calculated by dividing the distance between two sensors on the transit time.

It can be seen from Figure 5-58 (a) that, the film velocity increases in a parabolic pattern when increasing the velocity of air, for all water velocities. However, for air superficial velocity higher than 12 m/s, the liquid film velocity is noted to increase moderately or even remain constant.

Figure 5-58 (b) illustrates the liquid entrainment rate in the downward flows for a range of air and water velocities. It can be seen from Figure 5-58 (b) that, the entrainment rate of the liquid droplets gradually decreases when increasing the air velocity until it reaches a minimum value, and then increases for the rest of the air velocities.

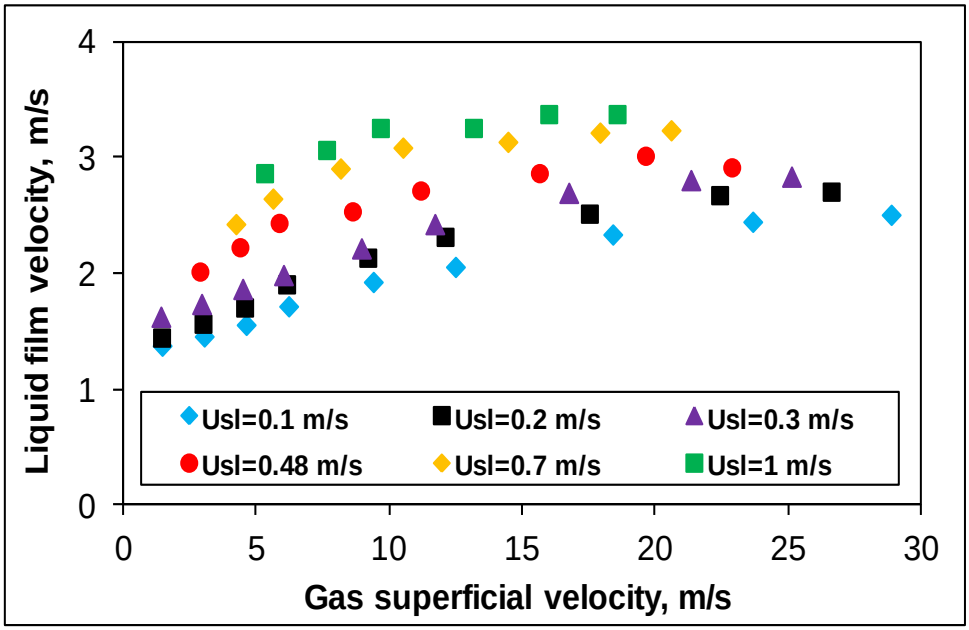

(a)

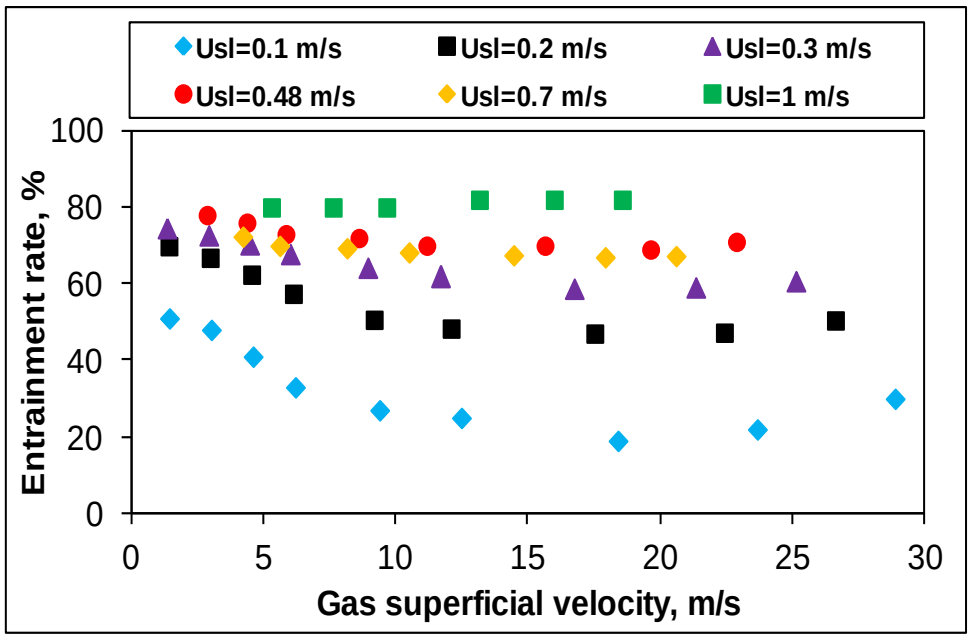

(b)

Figure 5-58 Liquid film velocity measurements (a) and calculated entrainment rate (b) in the middle position of the downward section

5.6.2 Liquid film velocity and liquid entrainment rate in the middle position of the upward section

Liquid film velocity data, illustrated in Figure 5-59 (a), are obtained at the middle position of the upward section. The liquid film velocity and entrainment rate of the liquid droplets is tested for higher air flow rates (i.e. when the annular flow was formed). It is observed from Figure 5-59 (a) that, the film velocity increases steeply for water superficial velocities of 0.7 and 1 m/s. However, it increases moderately for air superficial velocities higher than 15 m/s. On the other hand, for water velocities ranging from 0.1 to 0.48 m/s, it is found that the film velocity increases moderately over all air superficial velocities. This means that the higher the water flow rate, the greater the film velocity for a given air flow rate.

Both the measured liquid film thickness and film velocity are used to calculate the liquid entrainment rate. The droplet entrainment rate is found to be quite stable for water superficial velocities of 0.48, 0.7 and 1 m/s, as illustrated in Figure 5-59 (b). The entrainment rate of droplets shows higher variations against the air superficial velocity when the water superficial velocity ranges from 0.1 to 0.3 m/s.

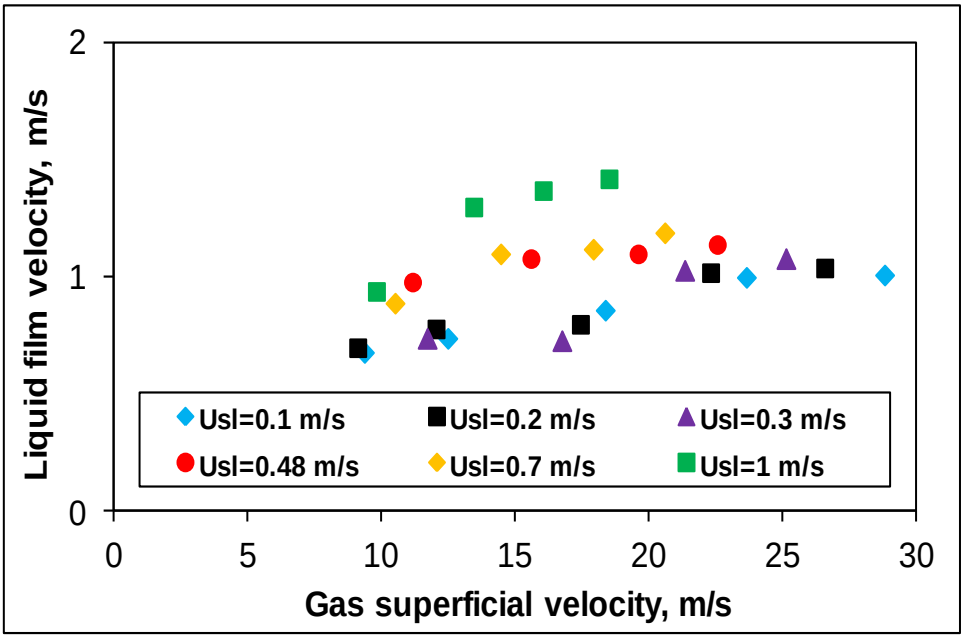

(a)

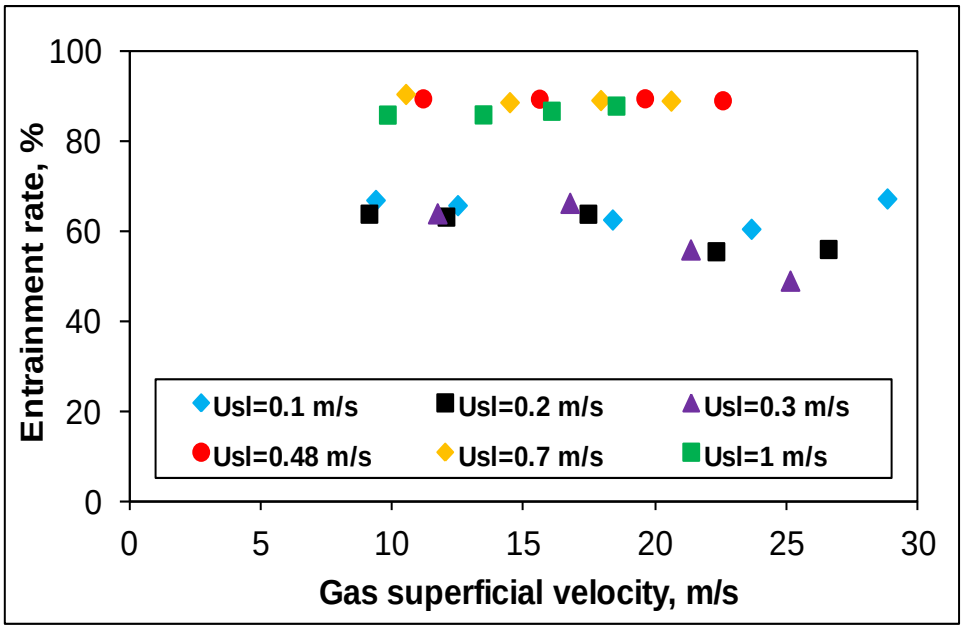

(b)

Figure 5-59 Liquid film velocity measurements (a) and calculated entrainment rate (b) in the middle position of the upward section

5.7 Pressure drop in downward and upward flows

Pressure drop is an essential parameter in the design and operation of several engineering equipment. For instance, the pressure loss in a system is a very important variable for the determination of pumping energy at a particular flow.

It is important to note that, the presented pressure drops data refer to the overall pressure drops in which the hydraulic pressure drop, frictional pressure drop and acceleration pressure drop are included. Measurements of pressure drop are carried out for the downward section of the Serpent rig, by considering the differential pressures of pressure transducers P2 and P3 which are located at the higher and lower positions of the downward section respectively, while those obtained at the upward section are calculated from the differential pressures of pressure transducers P4 and P5. Both sensors are installed at the lower and higher locations of the upward section respectively.

Plots of pressure drops over straight sections against air superficial velocities at different water superficial velocities are illustrated in Figure 5-60 (a) and (b). For the downward flow at different air superficial velocities and for water superficial velocity ranging from 0.07 to 0.48 m/s, the pressure drop is increased slightly as air superficial velocity increases, until it reaches higher values, when it decreases along the rest of the air superficial velocities, as shown in Figure 5-60 (a). This is in contrast to when water superficial velocity ranged from 0.7 to 1.5 m/s. The pressure drop under these velocities is observed to sharply decrease over all air velocities. On the other hand, pressure drop observed at the upward flow is noted to increase when air velocity increases for the water superficial velocity ranging from 0.7 to 1.5 m/s, as presented in Figure 5-60 (b). However, the pressure drop values obtained at water superficial velocities of 0.7 and 1 m/s noted to increase until they reach maximum values at air superficial velocity of about 1 m/s, when they are decreased to minimum values at air superficial velocity of about 5 m/s, then they are increased again for the rest of air superficial velocities. Whilst, for water superficial velocity ranging from 0.07 to 0.48 m/s, the pressure drop is extremely decreased when air superficial velocity is lower than 5 m/s. For air superficial velocities higher than 5 m/s, the pressure drop values are increased until they reach maximum value at the highest air superficial velocity. It can be noted from the curves of the downward and upward pressure drops that there are two main features of these pressure drops. Firstly, the tendency of the pressure drops show a similar behaviour to that observed in the liquid film thickness. The main contribution to this phenomenon can be attributed to the flow transition from intermittent to annular flows. Secondly, each curve of the upward pressure drop

is observed to have a turning point around a particular air superficial velocity. This corresponds to a critical (transition) gas velocity, where a transition from intermittent to annular flow has occurred. It is well accepted that in upward flows, the flow regime transition from intermittent to annular flows does cause the pressure drop curve to turn.

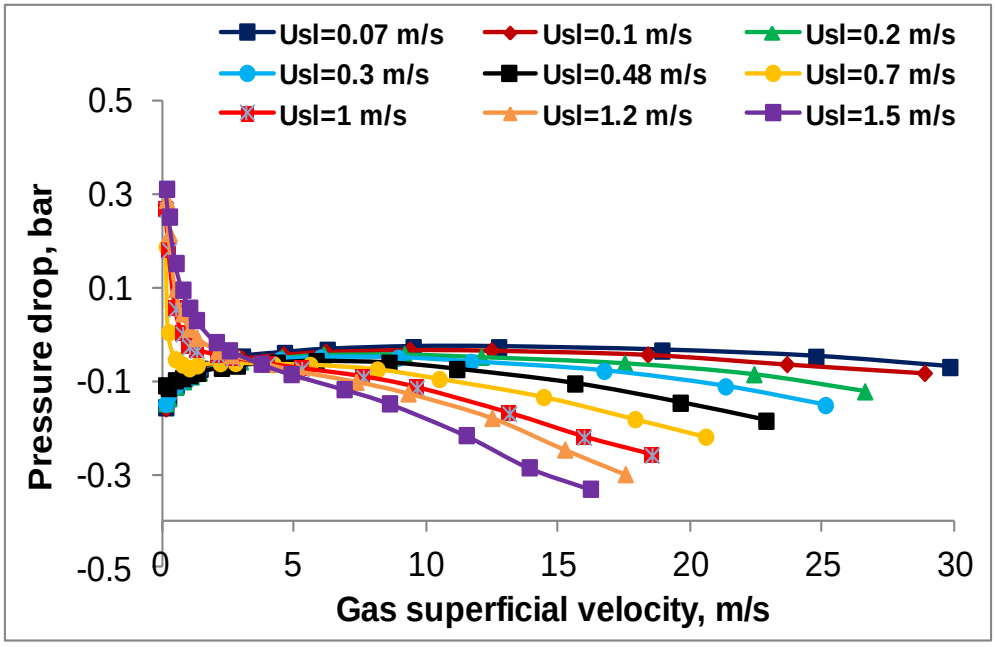

(a) Downward section (DP23)

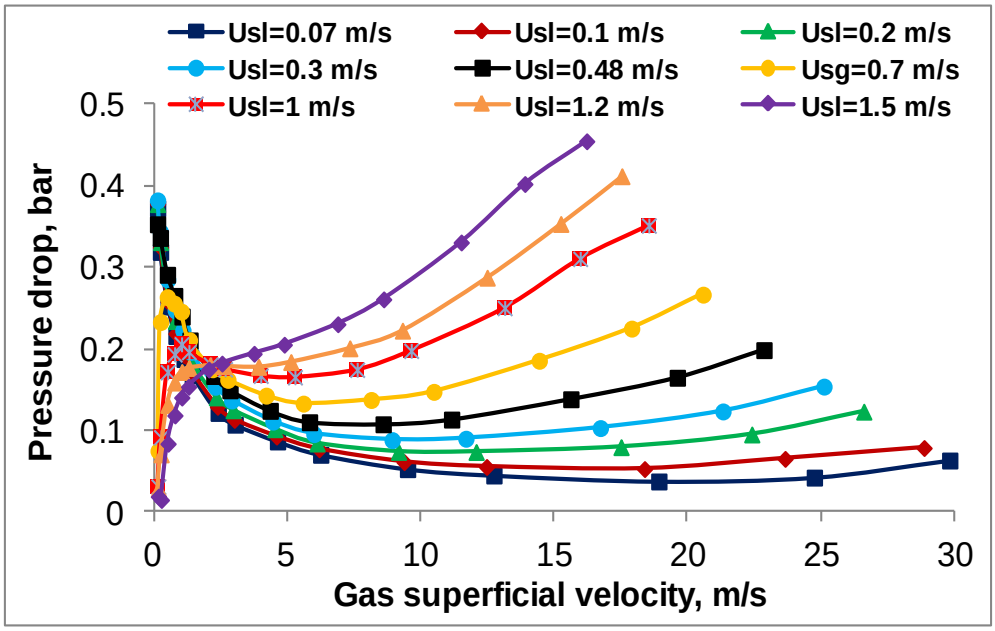

(b) Upward section (DP45)

Figure 5-60 Average pressure drops over straight sections of the Serpent rig

6 Comparisons of the present work against existing experimental work and empirical correlations

The effects of pipe diameter on liquid film behaviour were reported by several studies. However, the majority of them focused on vertical upward and downward pipes with small diameter (smaller than 50 mm) with low flow rates. Studies on the effect of large diameter (particularly larger than 100 mm) with high liquid flow rates on liquid film development are very limited. Therefore, real impacts of large diameter on liquid film thickness in upward and downward vertical flow still need more investigation.

6.1 Comparison of the present work with that of Webb and Hewitt (1975) for downward flow

A comparative study was made with the other resources, in order to gain a deeper understanding about the impacts of the pipe diameter on liquid film behaviour in the downward flow. Webb and Hewitt (1975) carried out experimental studies for two downward vertical pipes with small diameters (i.d. 31.8 and 38.2 mm). It was observed that the air superficial velocity required for establishing the downward vertical annular flow is significantly higher in the case of the current study than that conducted by Webb and Hewitt (1975). This indicates that for the larger diameter, larger air velocity is needed to establish the annular flow regime. Therefore, for a given range of air superficial velocity, the extent of annular flow formation is different for different pipe sizes. More precisely, for a given range of air superficial velocity the larger the pipe diameter the less well established the annular flow. Figure 6-1 shows a plot for the film thickness against the liquid film mass flux (the mass flow rate in one unit of circumferential length of the film, in kg/m s) in downward annular flows for different diameters, i.e. 31.8 mm, 38.2 mm, which was reported by Webb and Hewitt (1975) and for a pipe diameter of 101.6 mm (this study). The air superficial velocity used for the comparison was around 9.0 m/s, and the positions of the measurements were conducted at 30 pipe diameters after the top bend for this study, 19 pipe diameters after the liquid inlet for the 31.8 and 38.2 mm diameter pipes. The film thickness was predicted using an empirical correlation proposed by Henstock and

Hanratty (1976) which is also presented in Figure 6-1. The correlation is based on both liquid and gas Reynolds numbers as follows:

$$\frac{\delta}{D} = \frac{6.59\,F}{(1+1400\,F)^{\frac{1}{2}}} \quad \textbf{(6-1)}$$

$$F = \gamma \left(\frac{\boldsymbol{v_L}}{\boldsymbol{v_G}}\right) \left(\frac{\boldsymbol{\rho_L}}{\boldsymbol{\rho_G}}\right)^{\frac{1}{2}} {Re_G}^{-0.9} \quad \textbf{(6-2)}$$

$$\gamma = [\,(0.707\,Re_L^{0.5})^{2.5} + (0.0379\,Re_L^{0.9})^{2.5}\,]^{0.4} \quad \textbf{(6-3)}$$

Where δ is the film thickness, D the internal diameter, v_G and v_L are the kinematic viscosity of the gas and liquid respectively. For smaller diameter pipes, the Reynolds numbers Re_G and Re_L are based on the gas and liquid superficial velocities respectively.

It appears that, the correlation agrees reasonably well with the data of the small diameter pipe, but it has grossly over-predicted the data obtained from 101.6 mm diameter pipe. As a reference, the results of free falling film thicknesses are calculated using the correlation (6-4) proposed by Karapantsios et al. (1989), which is also presented in Figure 6-1. In this correlation the Reynolds number is also based on liquid film mass flux.

$$\delta = 0.451 \left(\frac{v^2}{g}\right)^{\frac{1}{3}} Re^{0.538} \quad \textbf{(6-4)}$$

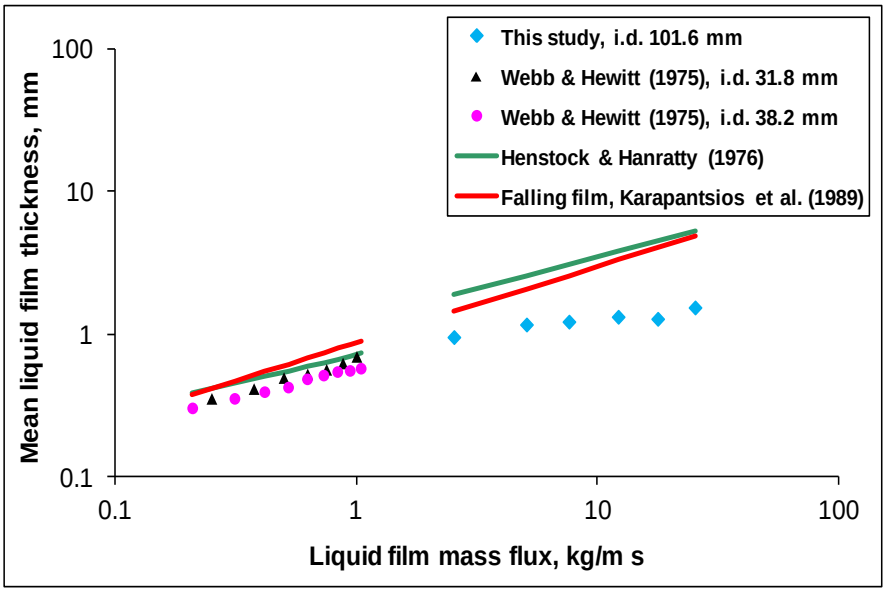

Figure 6-1 Comparison between the film thickness in downward annular flow for different pipe diameters with air superficial velocity of 9 m/s; the position of measurements were conducted at 30 pipe diameters after the top bend for this study (101.6 mm diameter pipe), 19 pipe diameters after the liquid inlet for the 31.8 and 38.2 mm diameter pipes

The following conclusions were drawn from the comparison between the present work and that reported by Webb and Hewitt (1975) for downward flow

- The diameter of the pipe has an appreciable effect on the relationship between the film thickness and liquid film mass flux. It appears that, the film thickness is thinner for larger diameters.
- The correlation proposed by Henstock and Hanratty (1976) is reasonably good for the data sets of the small diameter pipe (i.d. 31.8 mm). However, the correlation has grossly overestimated the liquid film thickness data that was obtained from the large diameter pipe (i.d. 101.6 mm).
- It was identified that the falling film thickness presented the highest values among all achieved results for Webb and Hewitt's (1975) data. The reason is that, with any falling film, the thickness with concurrent air flow is always thinner than that without concurrent air flow. On the other hand, the data of this study show greater values using Henstock and Hanratty's (1976) correlation than the calculated ones using the correlation reported by Karapantsios et al. (1989). According to Laurinat et al. (1984) this was based on the fact that, the Henstock and Hanratty's (1976)

correlation needs to be applied for annular flow with high gas mass flux. A possible reason for the overestimation of liquid film thickness is that, the correlation used the laminar flow assumption, thus the liquid entrained rate was neglected in the downward flows. It is worth noting that, in terms of the liquid film mass flux presented in the correlation, the Reynolds number related to liquid film in both studies is defined as:

$$Re_{LF} = \frac{\Gamma}{\mu} \quad \textbf{(6-5)}$$

Where the liquid film mass flux Γ, ranges from 200 to 1000 from which the film flow regime can be treated as a wavy flow, as stated by Dukler and Bergelin (1952). With this range of Reynolds numbers, disturbance waves could occur on the liquid film surface, and as a result some liquid is likely to be entrained from the film into the gas core.

6.1.1 Modifications of Henstock & Hanratty (1976) and Karapantsios et al. (1989) correlations

In the previous section (i.e. section 6-1), it was noted that the correlations reported by Henstock & Hanratty (1976) and Karapantsios et al. (1989) yielded close prediction to the experimental data reported by Webb & Hewitt (1975), as can be seen in Figure (6-1). On the other hand, those correlations presented significant differences when used for the current experimental data. Therefore, attempts were made to modify Henstock & Hanratty (1976) and Karapantsios et al. (1989) correlations (i.e. correlations (6-1) and (6-4) respectively) by changing their coefficients, to give a closer prediction of the measured liquid film thickness data obtained from the present study. The updated correlations of Henstock & Hanratty (1976) and Karapantsios et al. (1989) are presented below, which are correlations (6-6) and (6-7) respectively.

$$\frac{\delta}{D} = \frac{6.5\,F}{(1+1400\,F)^{0.75}} \qquad \textbf{(6-6)}$$

$$\delta = 0.6\left(\frac{v^2}{g}\right)^{\frac{1}{3}} Re^{0.41} \qquad \textbf{(6-7)}$$

It can be observed from Figure 6-2 that, both correlations yielded a closer prediction for the current experimental data when the new coefficients were applied. However, insignificant deviation can be seen at higher water velocities. This was based on the fact that, the higher the water velocity the thicker the liquid film.

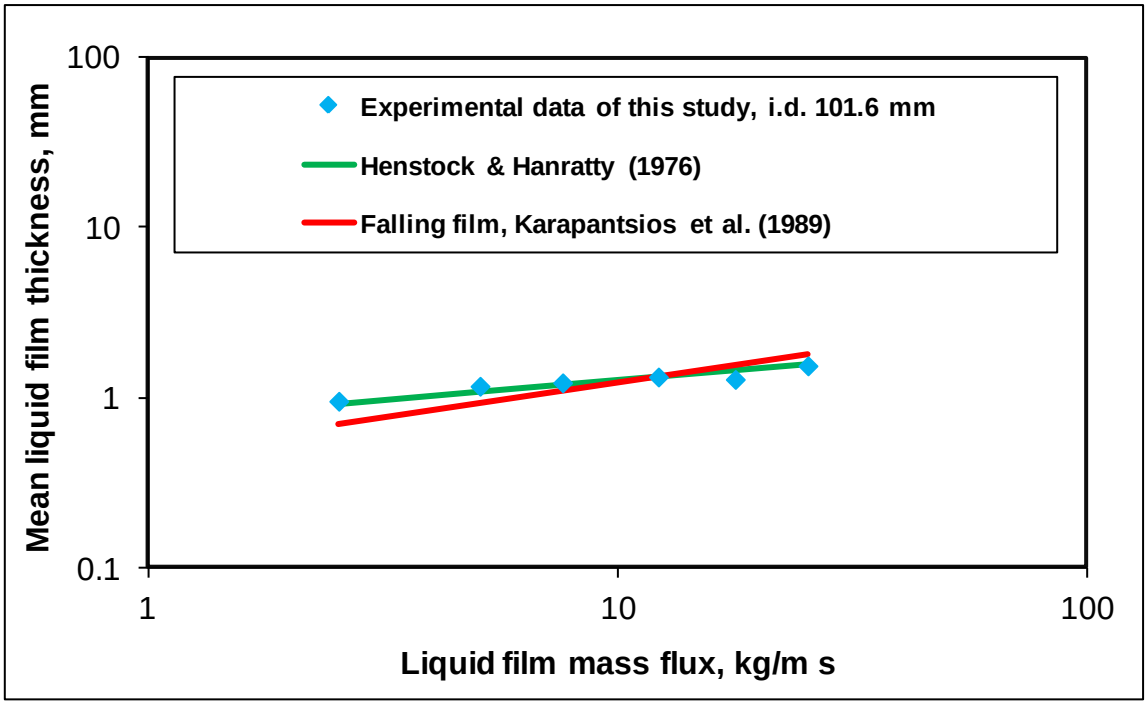

Figure 6-2 Liquid film thickness data obtained from current study in downward flow using the updated correlations of Henstock & Hanratty (1976) and Karapantsios et al. (1989), for different water superficial velocities and air superficial velocity of 9 m/s; the position of measurements is 30 pipe diameters after the top bend

In order to apply Henstock & Hanratty (1976) and Karapantsios et al. (1989) correlations for different diameter, it was necessary to change their constants. The following correlations, i.e. correlations (6-8) and (6-9) are corresponding to the updated correlations of both the Henstock & Hanratty (1976) and Karapantsios et al. (1989) respectively.

$$\frac{\delta}{D} = \frac{7.1\,F}{(1+1400\,F)^{0.73}} \qquad \textbf{(6-8)}$$

$$\delta = 0.45\left(\frac{v^2}{g}\right)^{\frac{1}{3}} Re^{0.45} \qquad \textbf{(6-9)}$$

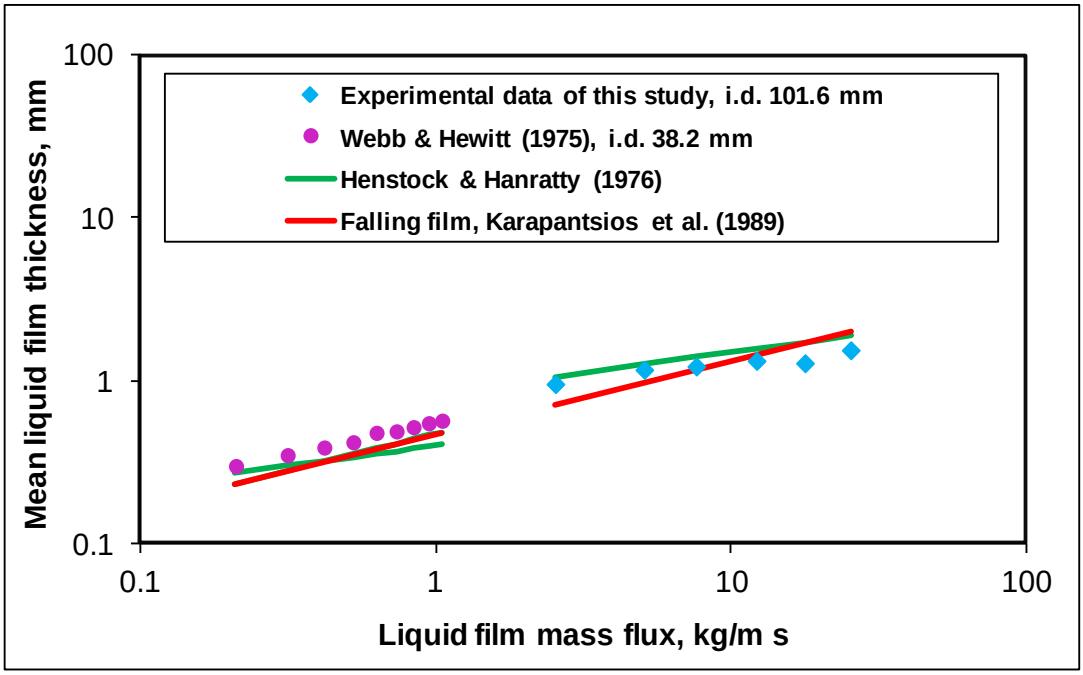

Figure 6-3 Liquid film thickness data for current study and that reported by Webb & Hewitt (1975), in downward flow using the updated correlations of Henstock & Hanratty (1976) and Karapantsios et al. (1989). The position of measurements were 30 pipe diameters after the top bend for current study and 19 pipe diameters after the liquid inlet for Webb & Hewitt (1975) study

It can be seen from Figure 6-3 that, the updated correlations (6-8) and (6-9) gave a reasonable well prediction, for the current experimental data and Webb & Hewitt (1975) data respectively.

In general, it can be noted that the theoretical and experimental data of both studies (i.e. present study and Webb & Hewitt (1975) study) were consistent to each other. Both the predictions and experimental results show that, the liquid film thickness increases as the liquid mass flux increased. This was due to the fact that, the liquid film becomes thicker for the higher water flow rates.

Figure 6-3 illustrated that, the updated correlation of Henstock & Hanratty (1976) presented insignificant deviation at higher film mass flux when it was applied for the present experimental data. Whereas, the updated correlation of Karapantsios et al. (1989) shows a small deviation at lower film mass flux. Figure 6-3 also shows inconsiderable deviation when the updated correlations of Henstock & Hanratty (1976) and Karapantsios et al. (1989) were used for the experimental data reported by Webb & Hewitt (1975). The deviation was a bit increased as the liquid film mass

flux increased further. This can be attributed to the fact that, the higher the liquid flow rate the thicker the liquid film. It was worth mentioning that, the maximum standard deviations for the data of liquid film thickness, using the updated and original correlations of Henstock & Hanratty (1976) were 0.3 and 2.7 mm respectively, for the present study. While, the maximum standard deviations for those using the updated and original correlations of Karapantsios et al. (1989), were 0.3 and 1.7 mm respectively. The maximum standard deviation for the liquid film data using both, the updated and original correlations of Henstock & Hanratty (1976) and Karapantsios et al. (1989), was almost the same for all liquid film thickness data presented by Webb & Hewitt (1975), which was about 0.1 mm. It can be concluded that, the updated correlations, i.e. correlations (6-8) and (6-9) are applicable to some extent for small and large diameter pipes.

6.2 Comparison of the present work with that of Wolf et al. (2001) for upward flow

The pipe diameter effect was also investigated by comparing the results achieved from the upward section of this study with those reported by Wolf et al. (2001), as can be seen in Figure 6-4. They conducted an experimental work using 31.8 mm diameter pipe, while the diameter used in this study was 101.6 mm, as stated before. For both studies, the data were collected at different positions along the vertical upward flow, for fixed water superficial velocity of 0.1 m/s. It is worth mentioning that, for both studies the reported data were for an annular flow regime, where the film thickness is present.

In general, it was found that pipe diameter has a significant effect on the film thickness behaviour. At a gas mass flux of 24.5 m/s, for example, the film thickness in a 101.6 mm diameter pipe is about twice that in the 31.8 mm diameter pipe. Also, the slopes of the curves related to the two pipes in same range of air velocity were appreciably different. The reduction of the film thickness with the increase of gas mass flux in the larger pipe is much faster than that in the smaller pipe. However, the film thickness values for the large diameter pipe were quite stable for the lowest gas mass flux, particularly at 5 and 47 pipe diameters. The main reason behind the significant difference of film thickness can be attributed to the significant difference of

the liquid film fluxes in the two pipes. In annular flow, with a given water superficial velocity, the liquid film flux is proportional to the pipe diameter. Thus, the liquid film flux in the 101.6 mm diameter pipe should be much higher than that in the 31.8 mm diameter pipe for the same air and water superficial velocities. Tentatively, the difference in the slopes of film thickness curves for the two pipes was based on the fact that, the air superficial velocities required to establish the annular flow in the 101.6 mm diameter pipe were much higher than those required to establish the same flow regime in a 31.8 mm diameter pipe. The larger the diameter, the higher the gas velocity required to establish the annular flow. Thus, for a given range of air superficial velocity, the extent of the annular flow formation would be different for different pipe diameters. More precisely, for a given range of air superficial velocity, the larger the pipe diameter, the less well established the annular flow. Usually the film thickness changes are much larger at the onset point of the annular flow than at the well-established point.

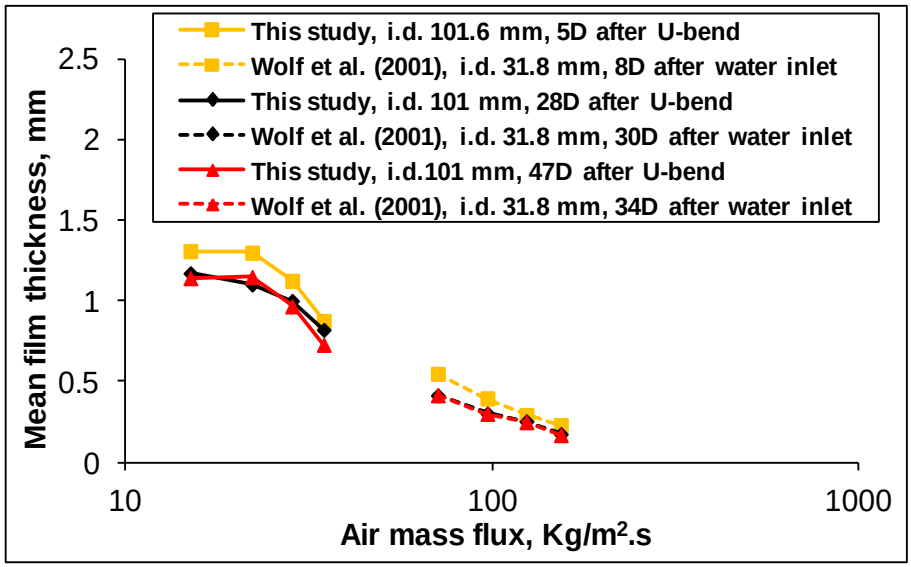

Figure 6-4 Comparison between the upward film thickness obtained from this study and that reported by Wolf et al. (2001). The data were collected at different positions for fixed water superficial velocity of 0.1 m/s

6.3 Comparison of the present work with that of McQuillan et al. (1985) using Alekseev et al.'s (1972) correlation

A considerable number of experimental works, have been carried out to determine the flow regime transition between churn flow and annular flow in different pipe diameters. Most of these studies were for small diameter pipes (< 50 mm). The results for large diameter pipes (> 100 mm) are very scarce. It was noted from the published studies that, there are differences for both the experimental and theoretical results. This evidence was based on the fact that, the identified flow regime transition occurred over quite a large range. It can be suggested that, the lack of a definitive method to identify the onset of flow regime transition, and the occurrence of the transition for a wide range of gas velocities, may contribute to the controversies between the previous studies. However, the obtained data using the flooding method showed that the transition gas velocity (U_{st}) is related to the pipe diameter. This was consistent with the observation made in this study.

It was found from the published materials that, a number of correlations were developed to predict the occurrence of flow regime transition. However, different understandings of the mechanism and definition of the churn/annular transition has led to different results. Alekseev et al. (1972) reported a correlation, which is considered the liquid flow rate, surface tension and pipe diameter. The correlation presented good results for the transition gas velocity in both the 101.6 mm diameter pipe (present study) and 31.8 mm diameter pipe (previous study).

However, although a number of published data related to the upward annular flow have been reported, very few complete data sets related to churn/annular flow transition with detailed information on liquid flow rate were found in published sources.

In this section, two sets of experimental data were used for the comparisons. The first set was from this study (101.6 mm vertical upward diameter pipe), and the second set was collected from McQuillan et al. (1985) who conducted experiments in a 31.8 mm vertical upward diameter pipe. For the data of vertical upward flows obtained from the 101.6 mm diameter pipe, the minimum pressure gradient method

was applied to identify the transition gas velocities. The pressure drop curves were obtained along 4 m of the upward section, as illustrated in Figure 6-5. It is important to mention that, the pressure data presented in Figure 6-5 are corresponding to those located in churn and annular flow regions. The other pressure flow measurements which included all flow regimes were presented in Figure 5-54 (b).

It can be observed from Figure 6-5 that, the curves show good minima for water superficial velocities higher than 0.3 m/s. On the other hand, for water velocities lower than 0.3 m/s, visual observation was considered in order to identify the transition gas velocity (U_{st}) because the minima were not observed until the air velocity reached the highest value, which is 28 m/s.

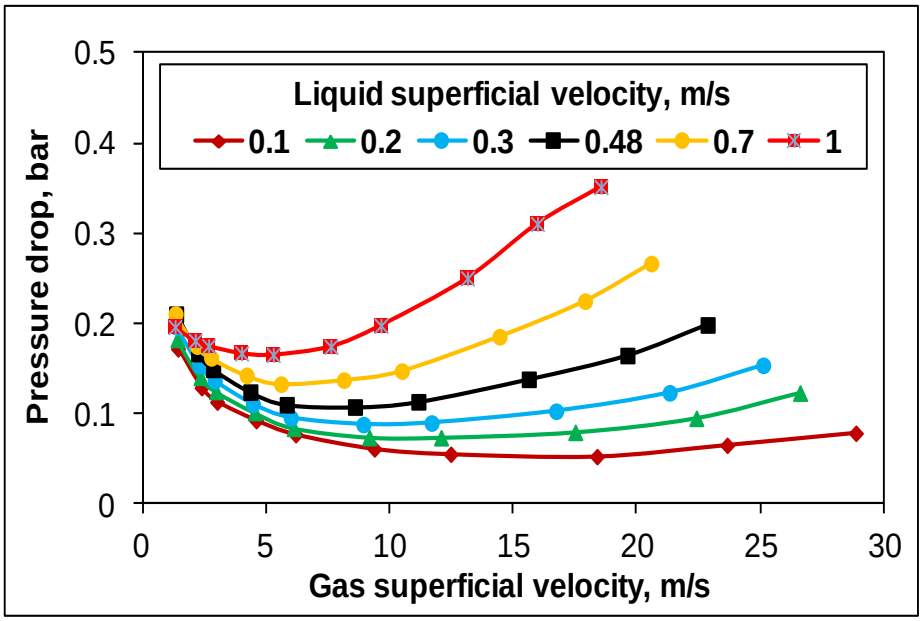

Figure 6-5 Pressure drops along the upward section; the transition air velocity was identified from the minima of each pressure value against the corresponding air velocity

The regime transition data for flows in the 31.8 mm diameter pipe were retrieved from the work reported by McQuillan et al. (1985), as illustrated in Figure 6-6. It is worth mentioning that, there are insignificant errors between the retrieved and original data. McQuillan et al. (1985) identified the air and water superficial velocities when the flooding occurred. Also in Figure 6-6, the comparison was made between the experimental results and those achieved by calculation. The calculated results were obtained using the empirical correlation proposed by Alekseev et al. (1972),

which is correlation (2-11). From the obtained results it was noted that, the correlation of Alekseev et al. predicted both sets of experiments very well. The RMS error of the fitting is less than 3% for the 101.6 mm diameter pipe, for the whole water superficial velocity range and 6% for the 31.8 mm diameter pipe, at water superficial velocity ranging from 0.02 to 0.2 m/s. However, the correlation underestimated the transition gas velocity for the small pipe diameter, at the lowest and highest velocities. The correlation provides good information about the effects of the pipe diameter and water superficial velocity on the transition velocities of churn/annular flows.

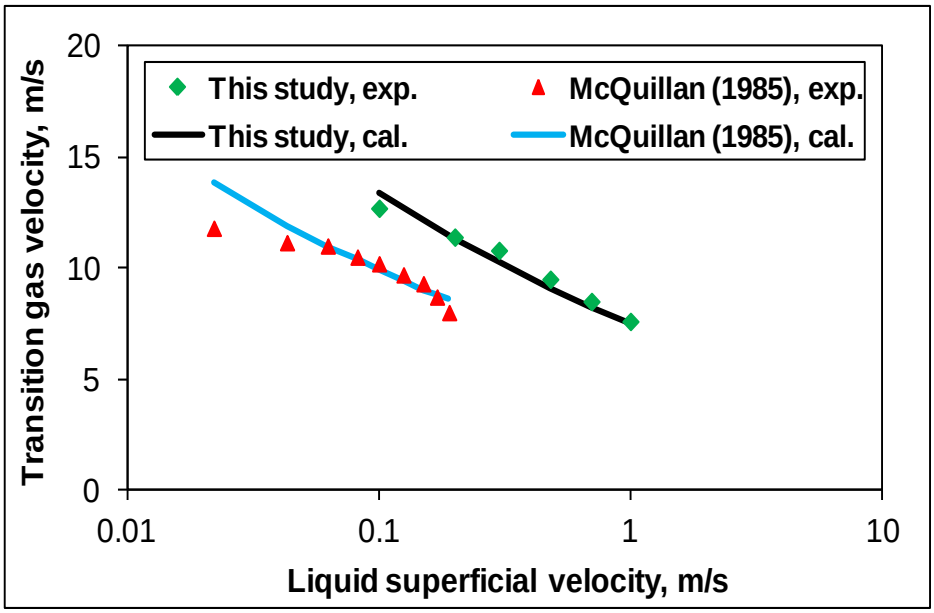

Figure 6-6 Comparison of the present study and that of McQuillan (1985) using equation reported by Alekseev et al. (1972)

6.4 Hewitt and Wallis (1963) criterion for the onset of annular flow

Most of the models for correlating film thickness and interfacial phenomena are based on the assumption that the liquid film is smooth with very small, if any, wave amplitude. They are sometimes called smooth film theories. Hypothetically smooth films are obtained at very high gas superficial velocities far away from the churn-annular transition region. Hewitt and Wallis (1963), who reported a simple criterion (correlation (6-10)) for the onset of annular flow, stated that the transition from churn to annular flow can occur when a modified Froude number (U_g^*) is in the vicinity of 1. The criterion is given by the following form:

$$U_g^* \equiv U_g \sqrt{\frac{\rho_g}{gD_t[\rho_g\alpha+\rho_L(1-\alpha)]}} \gg 1 \qquad \textbf{(6-10)}$$

Where U_g^* is a dimensionless variable (also called a modified Froude number), U_g is the gas velocity, D_t is the pipe diameter, g is the gravitational force, α is the measured void fraction and ρ_g and ρ_L are the gas and liquid density respectively.

It was noted that the dimensionless variable U_g^* progressively exceeds 1, as the gas velocity increased to higher values. Hewitt and Wallis (1963) assumed that all values higher than 1 are located in the annular flow region, while those lower than 1 are located in the non-annular (bubbly and/or intermittent) flow region. It can be seen from the plots of Figure 6-7 (a-c) that, the reported correlation typically agrees with the data obtained from this study.It can be seen that, the points fall in the annular flow region with a number falling along the intermittent-annular transition region. The plots confirm (according to Hewitt & Wallis's (1963) criteria) that the flow conditions are within the annular flow region.

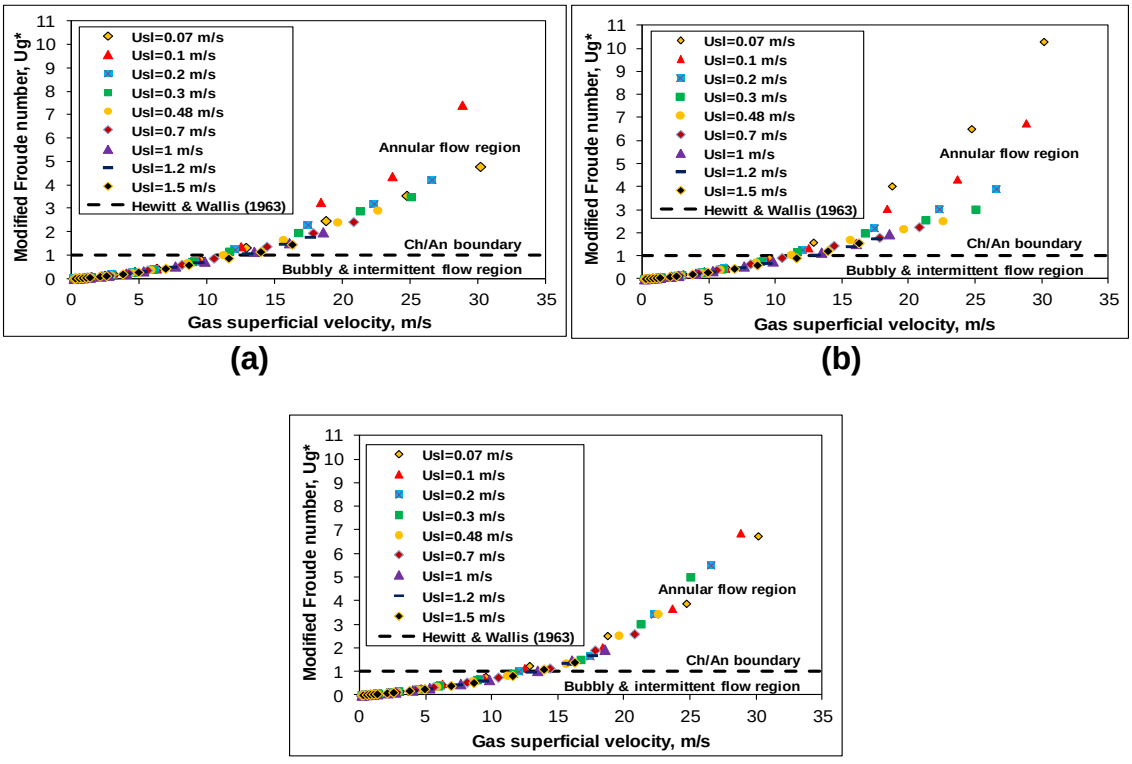

Figure 6-7 Local dimensionless variable U_g^* (modified Froude number) calculated for each water superficial velocity at (a) top, (b) middle and (c) bottom positions of the upward section

6.5 Comparison of the film thickness data obtained from the present study with the existing models

Most of the available models for predicting film thickness are based on the dimensionless film thickness and liquid film Reynolds number in a power law, as expressed in the following form:

$$\delta^{+} = A\, Re_{Lf}^{B} \qquad \textbf{(6-11)}$$

Where A and B are constant. Researchers such as Kosky (1971) reported that A and B are 0.0512 and 0.875 respectively for Re_{Lf}>1000.

Later on, Asali et al. (1985) determined the values of A and B as 0.34 and 0.6 respectively for Re_{Lf}< 1000. Similar values were found in the literature, but these were validated by the various data of different pipe diameters.

Henstock & Hanratty (1976) developed the following model based on available data of air-water fluids in a vertical upward orientation:

$$\delta^{+} = [\left(0.707 Re_{Lf}^{0.5}\right)^{2.5} + \left(0.0379 Re_{Lf}^{0.9}\right)^{2.5}]^{0.4} \qquad \textbf{(6-12)}$$

Where δ^{+} is the dimensionless film thickness and Re_{Lf} is the liquid film Reynolds number.

It is important to mention that, the equation (6-12) has neglected both the entrainment and deposition rates of droplets. However, these may occur at a high flow rate of gas.

Hori et al. (1978) considered the effect of gas flow rates on a vertical upward film thickness, as shown in equation (6-13). Fukano & Furukawa (1998) noted that this equation gives rather poor predictions for small δ/D_t values.

$$\delta/D_t = 0.905\, Re_{GO}^{-1.45} Re_{LO}^{0.90} Fr_{GO}^{0.93} Fr_{LO}^{-0.68} (\mu_L/\mu_w)^{1.06} \qquad \textbf{(6-13)}$$

Where $Fr_{LO} = U_{sl}/\sqrt{gD_t}$, $Re_{GO} = \rho_g U_{sg} D_t/\mu_g$ and μ_L and μ_w are the viscosity of water under experimental conditions and at 20ºC respectively.

Fukano & Furukawa (1998) tested Kosky (1971) and Asali et al.'s (1985) correlations by using the liquid film thickness and entrainment rate data presented by Nishikawa et al. (1967). From the achieved results they stated that, Nishikawa et al.'s data are very useful as they gave a good fit with Kosky and Asali et al.'s models (Figure 6-8).

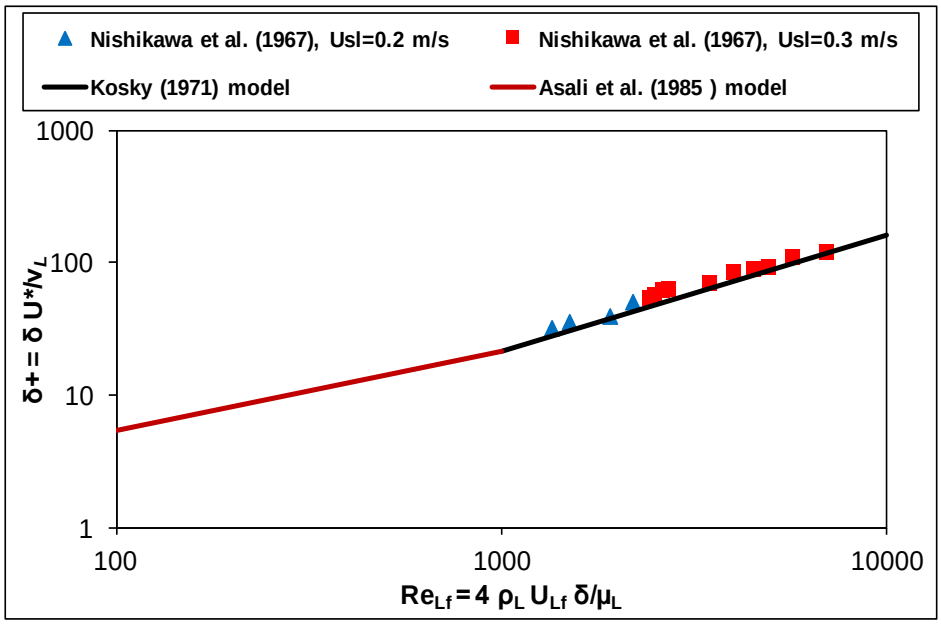

Figure 6-8 Prediction of mean liquid film thickness using Kosky (1971) and Asali et al. (1985) models with Nishikawa et al.'s (1967) data for 25.1 mm diameter pipe

Fukano & Furukawa then estimated the film thickness by developing correlation (6-14). They used air-glycerine and air-water mixtures as working fluids. They claimed the developed correlation to be within 15% of the obtained experimental film thickness data. The correlation is expressed as follows:

$$\delta/D_t = 0.0594 \ \exp\ (-0.34\, Fr_g^{0.25} Re_{Lf}^{0.19} x^{0.6}) \qquad \textbf{(6-14)}$$

Where x is the gas quality (ratio of gas mass flow rate to the total gas and liquid mass flow rates), Fr_g is the gas Froude number which is calculated from:

$$\mathrm{Fr}_g = \frac{U_{sg}}{(gD)^{0.5}} \qquad \textbf{(6-15)}$$

Where g= 9.81 m/s^2 and U_{sg} is the gas superficial velocity and the liquid film Reynolds number is defined by:

$$Re_{Lf} = \frac{U_{Lf} D_t}{\nu_L} \quad \textbf{(6-16)}$$

Where U_{Lf} is the measured liquid film velocity and ν_L is the liquid kinematic viscosity (m^2/s). They then proceeded to estimate the interfacial friction factor and the frictional pressure drop from the film thickness. They noted that, the estimated film thickness using their correlation is different when compared with published work, such as that of Hewitt and Hall-Taylor (1970); Kosky (1971); Henstock and Hanratty (1976); Asali et al. (1985); and Ambrosini et al. (1991), in that the procedure is not iterative but purely correlation.

Table 6-1 summarises some reported correlations for different pipe diameters. As can be seen, the data presented in the table were conducted using small diameter pipes.

Correlation	**Pipe diameter, mm**	**Axial distance, Z/D**	**U_{sg} range, m/s**	**U_{sl} range, m/s**
Henstock & Hanratty (1976)	25.4	200 – 550	10 – 100	0.015 – 0.7
Asali et al. (1985)	23, 42	n/a	n/a	n/a
Hewitt & Govan (1990)	7.72	n/a	n/a	n/a
Ambrosini et al. (1991)	10–42.2	n/a	>25 m/s	0.012 – 0.7
Fukano & Furukawa (1998)	19.2, 26	n/a	10–50	0.04–0.3
Holt et al. (1999)	5–10	180	3.67 – 67	0.04 – 0.14
Omebere-Iyari et al. (2008)	5	400	0.06 – 50	0.03 – 0.65
Kaji & Azzopardi (2010)	19	300	0.87 – 33.9	0.03 – 0.65

Table 6-1 A summary of experimental conditions collected from the literature for air-water upward flow in vertical pipes

6.5.1 Comparison of film thickness data against Kosky's (1971) model

The measured data of liquid film obtained from this study were compared with the model developed by Kosky (1971), as shown in Figure 6-9. It can be seen from Figure 6-9 that, there is a scatter on both sides of the fit line. This was because the model was derived without taking into consideration the liquid entrainment. However, according to this study a large number of entrainments were observed to occur over the range of flow rates. As a result, the thickness of the liquid film attached on the pipe will be decreased significantly. It is worth mentioning that, liquid entrainment can be neglected only when equilibrium occurs (where the droplets are entrained into the gas core and soon back into the pipe wall). Hewitt & Govan (1990) stated that the equilibrium phenomenon can only occur for an adiabatic flow (where the rate of heat transfer is zero) and also when the gas flow rate is high enough. According to Hewitt and Govan the assumption of equilibrium is not present in some units such as those depending on evaporation and condensation processes. The equilibrium in these units will collapse due to the significant evaporation and condensation of the entrained droplets. In this work, the assumption of equilibrium was made due to the fact that the heat transfer did not exist. As a result, the difference between the deposition and entrainment rates was neglected. Therefore, a reason for the scatter can be attributed to the difference between the pipe diameter used in the current study (i.d. =101.6 mm) and the one used in developing the model (i.d. <100 mm).

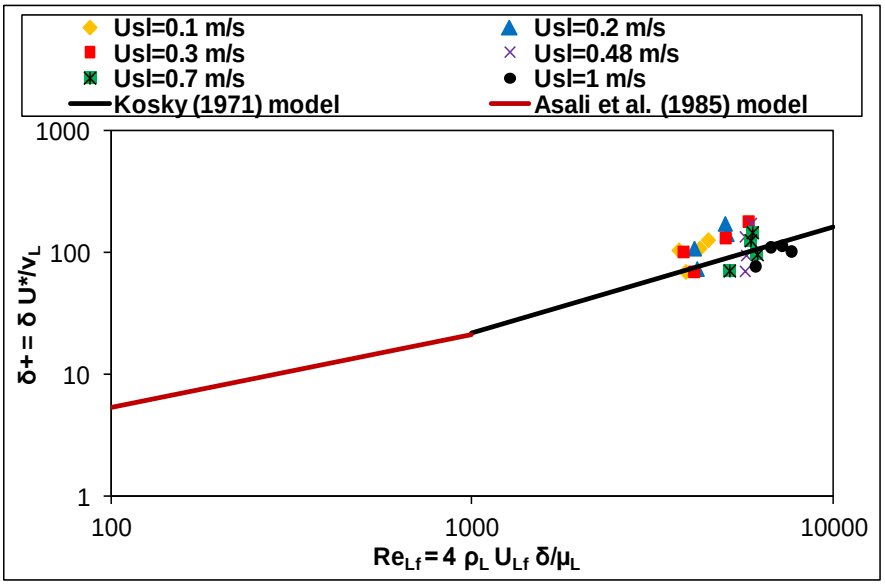

Figure 6-9 Prediction of mean liquid film thickness using Kosky (1971) model and Asali et al. (1985) model with data obtained from this study

By examining entrainment data reported by Asali et al. (1985) who used a small diameter pipe (D_t=22.9 mm) against Kosky's (1971) model, it was found that the data did not fare much better either (developed using D_t=42 mm with the consideration of entrainment), as shown in Figure 6-10. This then lends credence to the suggestion that the effect of the pipe diameter is considerable.

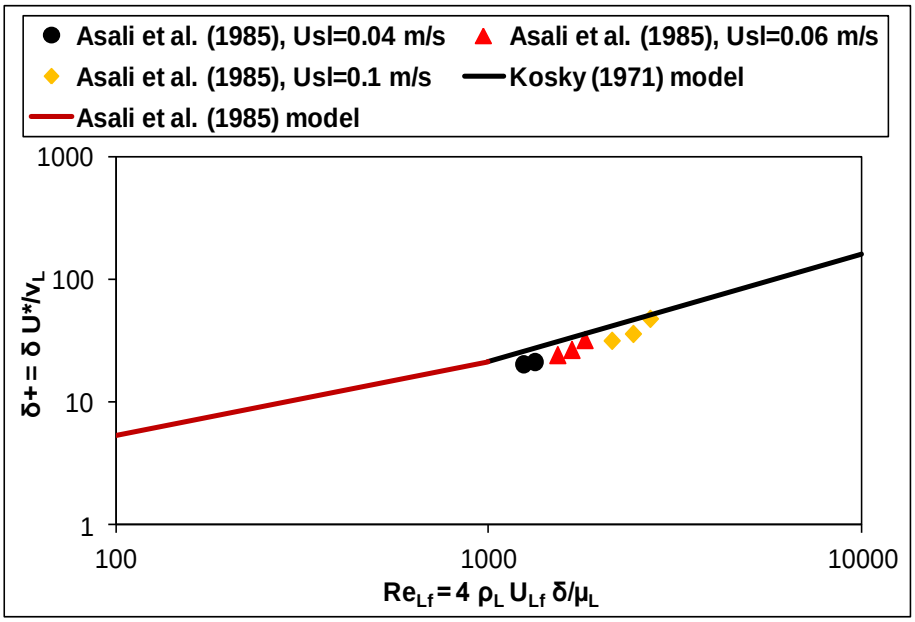

Figure 6-10 Prediction of mean liquid film thickness using Kosky (1971) model with Asali et al. (1985) entrainment data

6.5.2 Comparison of film thickness data against the Henstock & Hanratty (1976), Fukano & Furukawa (1998) and Hori et al. (1979) models

The Henstock & Hanratty (1976) model presented in equation (6-12) was applied to calculate the dimensionless film thickness (δ/D_t) as a function of the liquid film Reynolds number given by: $Re_{Lf} = 4\rho_L U_{Lf}\delta/\mu_L$.

The overall calculated dimensionless film data against measured values are shown in Figure 6-11 (a). It can be seen that, the trend of both the calculated dimensionless film thickness and measured values are generally consistent. However, the prediction was not in complete agreement from point to point. The discrepancy can be attributed to the fact that, the droplet entrainment was not considered in the model. Similarly, Figure 6-11 (b) shows a comparison of dimensionless film thickness (δ/D_t) and that predicted using the model reported by Fukano & Furukawa (1998), which is presented in equation (6-14). It can be seen that, there are good predictions for most of air superficial velocities when water superficial velocity= 0.1 m/s (where the thinner film was identified). On the other hand, increasing the water superficial velocity has led to significantly poor predictions for all air superficial velocities when compared with the experimental data collected from this work (where the film became thicker). A possible reason for the huge difference is that Fukano & Furukawa obtained their data using a pipe with 26 mm i.d. As such, their model does not adequately predict the thick film in large pipe diameters (> 100 mm) such as that used for this study. A similar trend was obtained for the prediction of Hori et al.'s (1979) model, as shown in Figure 6-11 (c). This however, produced far less spread than Fukano & Furukawa's (1998) model. It can be stressed that, there is a need to improve an adequate model in order to predict the thicker films at higher liquid velocities.

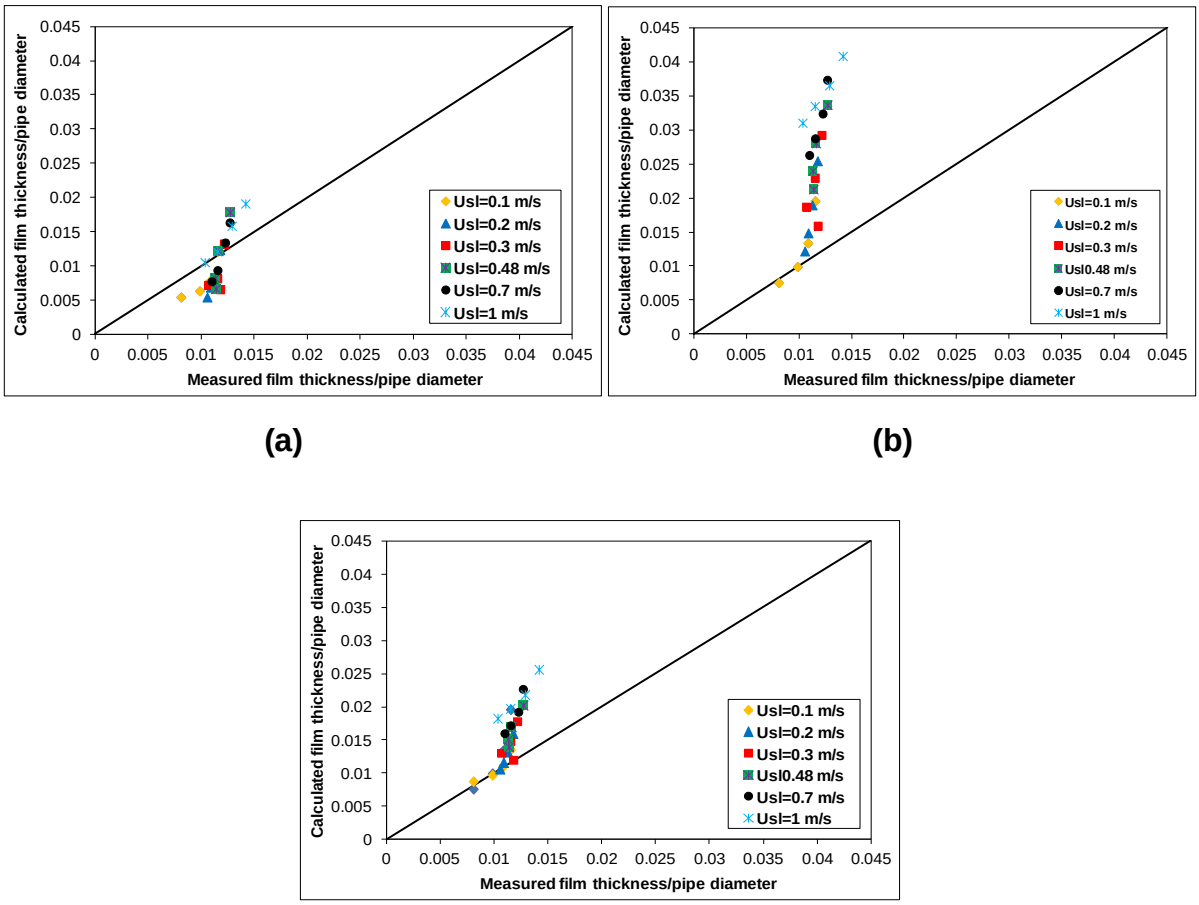

Figure 6-11 Dimensionless film thickness versus that calculated using the (a) Henstock & Hanratty (1976), (b) Fukano & Furukawa (1998) and (c) Hori et al. (1979) models

Figure 6-12 (a-f) presented a comparison between the measured film thickness obtained from this study with models reported by Henstock & Hanratty (1976), Hori et al. (1979) and Fukano & Furukawa (1998). In general, all models follow similar tendencies when compared with the current data. The performance of all models was noted to be better over the range of gas velocities for liquid velocity of 0.1 m/s. However, the Fukano & Furukawa model shows a poor prediction as against the measured data obtained from this study for gas superficial velocity lower than 13 m/s. By increasing the liquid superficial velocity further from 0.2 to 0.48 m/s, the models developed by Henstock & Hanratty (1976) and Hori et al. (1979) still show good agreement with the experimental data obtained from this study. These models presented better performance when compared with Fukano & Furukawa's model over the range of U_{sg} values. This is also because of the strong exponential dependence of film thickness over large U_{sg} ranges, as expressed by Fukano & Furukawa's model. For liquid superficial velocity of 0.7 and 1 m/s, the models of Hori et al. (1979), and Fukano & Furukawa (1998) diverged away to show a significantly poor prediction when compared with the measured data of this study, as shown in Figure 6-12 (e) and (f), while the Henstock & Hanratty model still shows a close prediction with the current data. Thus, it can be concluded that the model developed by Henstock & Hanratty (1976) showed better predictions to the measured data of this study than the other two models.

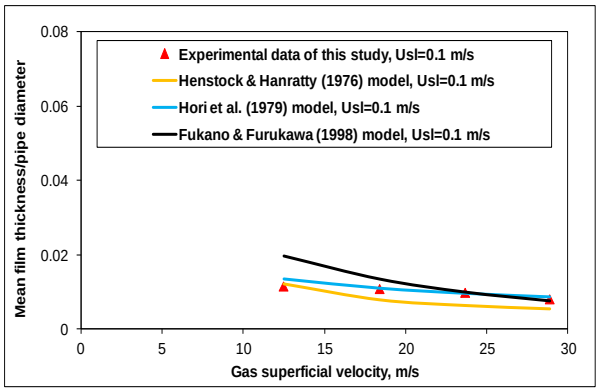

(a) Usl=0.1 m/s

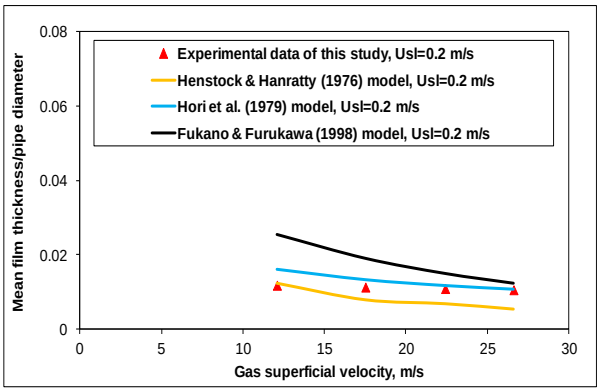

(b) Usl=0.2 m/s

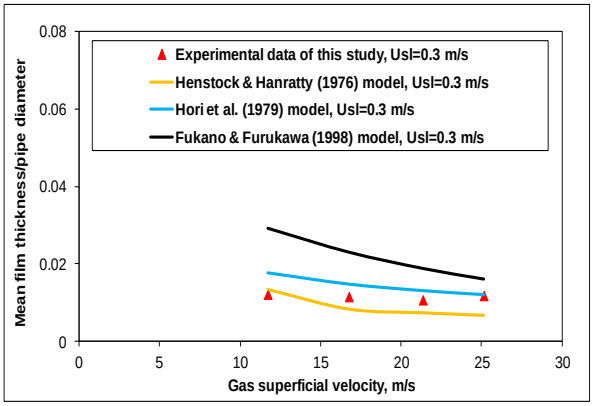

(c) Usl=0.3 m/s

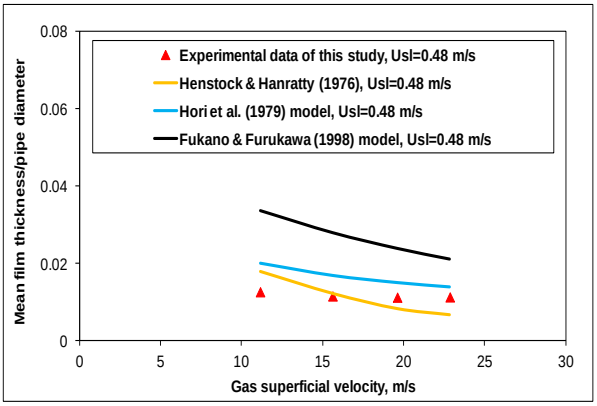

(d) Usl=0.48 m/s

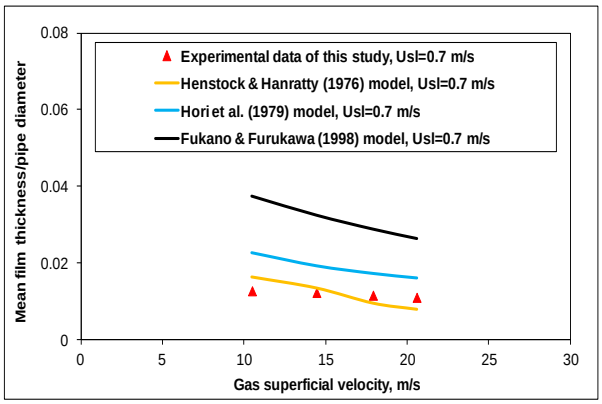

(e) Usl=0.7 m/s

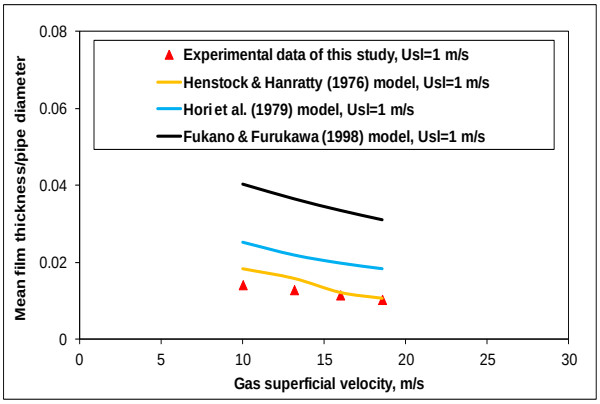

(f) Usl=1 m/s

Figure 6-12 Variations of dimensionless film thickness against gas superficial velocity for a number of liquid superficial velocities using the Henstock & Hanratty (1976), Hori et al. (1979) and Fukano & Furukawa (1998) models

6.5.3 Modifications of Fukano & Furukawa (1998) and Hori et al. (1979) models

A comparison of the measured liquid film thickness data, obtained from the present study and that reported by Wolf et al. (2001) was made with those predicted using the models proposed by Fukano & Furukawa (1998) and Hori et al. (1979). The comparison between the experimental data of the present study and theoretical study demonstrates that, the experimental data were less than the predicted, as illustrated in Figure 6-11 (b) and (c) respectively, for water superficial velocities of 0.3, 0.48, 0.7, 1 m/s. On the other hand, for water superficial velocities of 0.1 and 0.2 m/s, both the measured and calculated liquid film thickness data are close to each other.

Figure 6-12 (a-f) above shows that, the present study was in good agreement with the model developed by Henstock & Hanrraty (1976) over all air superficial velocities. Whilst, the present experimental data did not fit well the model reported by Fukano & Furukawa (1998) and Hori et al. (1979), particularly for high water superficial velocities. However, the model proposed by Hori et al. (1979) presents good agreement with the experimental data of the current study for water superficial velocities of 0.1 and 0.2 m/s, as shown in Figure 6-12 (a) and (b). The model gave poor prediction as the water superficial velocity increased further (Figure 6-12 (c-f)).

Therefore, there was need to modify the models reported by Fukano & Furukawa (1998) and Hori et al. (1979). The models were modified by changing their coefficients in order to give a closer prediction with experimental data of the current study, as shown in correlations (6-17) and (6-18) respectively.

$$\delta/D_t = 0.0196\ \exp\ (-0.18\, Fr_g^{0.2} Re_{Lf}^{0.11} x^{0.22}) \quad \textbf{(6-17)}$$

$$\delta/D_t = 0.67\, Re_{GO}^{-1.48} Re_{LO}^{0.9} Fr_{GO}^{0.98} Fr_{LO}^{-0.8} (\mu_L/\mu_w)^{0.7} \quad \textbf{(6-18)}$$

To verify the applicability of the updated correlations (i.e. correlations (6-17) and (6-18)), the measured liquid film is plotted against the calculated one, as shown in Figure 6-13 (a) and (b). Also, a relationship between the gas superficial velocity and mean liquid film thickness using the developed correlations is presented in Figure 6-

14 (a-f). It can be seen from Figure 6-13 that, the updated correlations can provide reasonably well results for the experimental data obtained from the present study. Similarly, Figure 6-14 presented a closer prediction for the data obtained from the present study and that reported by Wolf et al. (2001), for the whole range of air and water flow rates. It was found that, the maximum standard deviations for the liquid film thickness data were 0.001 and 0.02 mm respectively, when the updated and original correlations of Fukano & Furukawa (1998) were applied for the current study. While, the updated and original correlations of Hori et al. (1979) show that, the maximum standard deviations for the liquid film thickness data were 0.002 and 0.008 mm respectively. For the data presented by Wolf et al. (2001), it was noted that the maximum standard deviations for the liquid film thickness were 0.002 and 0.004 mm, for the updated correlations of Hori et al. (1979) and Fukano & Furukawa (1998) respectively. This indicates that the developed correlations are applicable for both, the small and large diameter pipes.

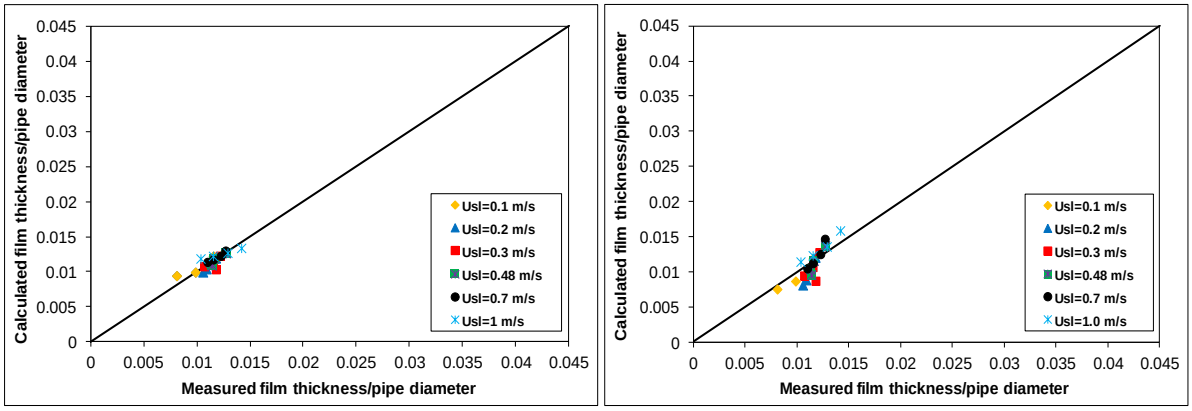

(a) **(b)**

Figure 6-13 Dimensionless film thickness versus that calculated using the modified models (a) Fukano & Furukawa (1998) and (b) Hori et al. (1979)

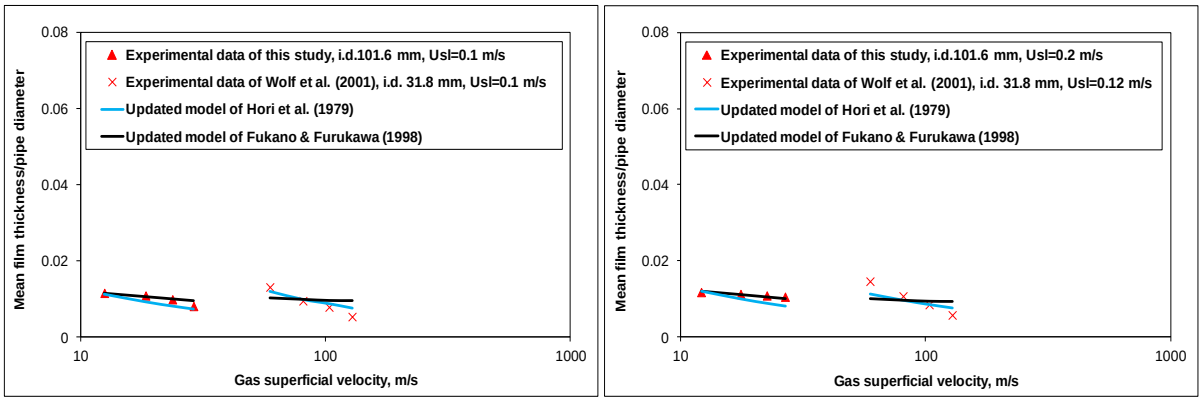

(a)

(b)

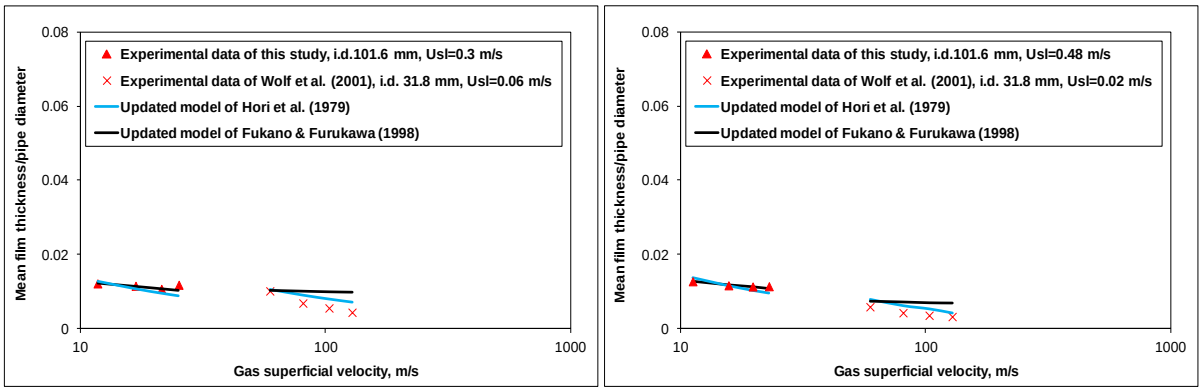

(c)

(d)

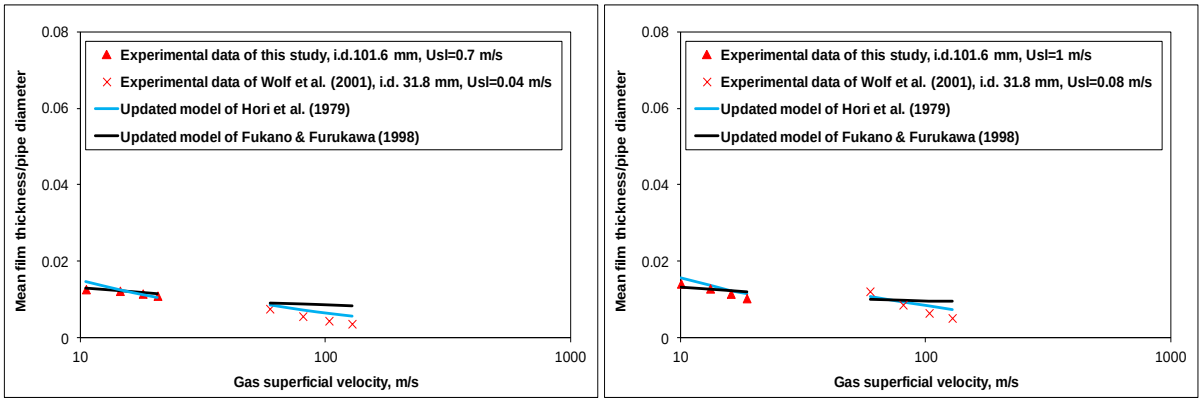

(e)

(f)

Figure 6-14 Data of liquid film thickness against gas superficial velocity, obtained from current study and that reported by Wolf et al. (2001) in upward flow, using the modified models of Hori et al. (1979) and Fukano & Furukawa (1998)

7 Conclusions and recommendations for future work

In this chapter the final conclusions drawn from this study are summarised. Further work is also proposed, to improve and expand the knowledge of two-phase flow behaviour in downward and upward vertical pipes.

7.1 Conclusions from the experimental work of void fraction and film thickness

In this study, WMS and film thickness probes were used to investigate the effects of 180^{o} bends on the behaviours of gas-liquid flows in a vertical serpentine large diameter pipeline, covering the superficial air and water velocities ranging from 0.15 to 30 m/s and from 0.07 to 1.5 m/s respectively. The following conclusions can be drawn from the experimental investigation that was carried out in this study.

7.1.1 Conclusions from the downward flow

- Bubbly, intermittent, and annular flows were observed in the downward pipe. In the bubbly flow regime large cap bubbles occasionally appeared. The flow regime map at the top measuring position (i.e. 5D below the top bend) differs from those at the middle position (i.e. 30D below the top bend) and bottom position (i.e. 46D below the top bend), while the flow regime maps at the middle and bottom positions are fairly similar to each other. An oscillatory feature is observed in the flows with a combination of low air and high water flow rates.
- The flow regime map at the middle position of the downward section was compared with the prediction using a method proposed in Barnea et al. (1982). It was noted that, the boundary between the bubbly and intermittent flows from this study matches the predicted boundary fairly well. However, the prediction significantly overestimates the critical liquid velocity for the transition of intermittent flow to annular flow.
- The cross-sectional phase distributions measured at the top position show a significantly higher void fraction on the half corresponding to the inside of the upstream top bend (i.e. at 270^{o}) than that on the half outside the bend (i.e. at

90^o). This asymmetry was reduced as the flow moved towards the lower axial positions. However, it was also noted that in contrast, the cross-sectional phase distributions were remarkably symmetrical with respect to the 0^o-180^o axis. For most flow conditions tested, the cross section void fraction distribution at the middle and bottom positions are close to each other, which may suggest that the flow has been fairly well developed in the downward section after 30D from the upstream top bend.

- In most downward annular flows tested, the average liquid film at the top axial position was significantly different from those at the lower axial positions. However, the liquid film thicknesses at the middle and bottom positions were remarkably close to each other, which may again suggest that the flow was reasonably developed in the downward section both at and after 30 pipe diameters from the upstream top bend.

- Circumferentially liquid film at the top position was not evenly distributed for all flow rates tested in this study. The thickest film appears at the 90^o position (corresponding to the outside of the upstream top bend) and the thinnest film at the 270^o position (corresponding to the inside of the upstream top bend). However, similarly to the cross-sectional phase distribution, the film's circumferential profile was fairly symmetrical with respect to the 0^o-180^o axis. This suggests that the effect of the upstream top bend on the film and phase distribution in a cross section at the downward section is mainly along the 90^o-270^o direction, due to the effect of the centrifugal force that is produced by the bend. For most flow conditions tested, the liquid film circumferential profiles became fairly even both at and after the middle position. However, when in a combination of low liquid loading and high air velocity, the liquid film circumferential profile is still uneven at an axial position of 46 pipe diameters from the top bend, suggesting that the bend effect persists through the whole downward section.

- By analysing the time traces of the mean liquid film thickness at the top, middle and bottom positions of the downward section showed that, the signals measured by both CT2 located in the top film probe and CM2 located in the middle film probe, are characterised by huge waves (classified as disturbance waves), for high air and low water superficial velocities. On the other hand, the signals of the film thickness measured by sensors CT1, CT3 and CT4 located in the top film probe are apparent to have smaller wavelength and amplitude. Similarly, the signals of liquid film that measured by sensors CM1, CM3 and CM4 located in the middle film probe, appear to have lower wavelength and amplitude than that measured by the sensor CM2. For the other flow velocities (i.e. low air and water superficial velocities and high air and water superficial velocities), it was found that the signals of liquid film measured by middle and bottom probes are similar to each other, while those measured by the top film probe shows different behaviour. This indicates that, the liquid film became stable at the middle and bottom positions; due to reduction of the bend effect when these flow conditions are applied.
- From the examination of a set of flow conditions, the frequency tendencies are obtained. In general, it was observed that the power spectral density (PSD) shape located close to the bend (namely at 5 pipe diameters after the top bend), is significantly different from those located further away from the bend for the same flow rates.

7.1.2 Conclusions from the upward flow

- This study found that, the upstream bottom bend has considerable impacts on the upward flow behaviour. The action of this bend was highly dependent on the air and water superficial velocities. Obviously, the air moves towards the region of the lesser radius of curvature and the water towards the outer zone. Consequently, much water was observed on the outer pipe wall (i.e. in the same direction of the bend’s outer curvature), while dry spots were identified on the other surfaces of the pipe.

- The average void fraction values were observed to increase when increasing the air superficial velocity, at all positions of the upward section. Conversely, they were observed to decrease when increasing the water superficial velocity.
- From the characteristic signature of the probability density function (PDF) data, it can be concluded that both the air and water superficial velocities have an obvious effect on the flow behaviour along the upward orientation, where the flow regime varied over all the velocity ranges tested.
- Different flow regimes were identified at various positions (i.e. 5, 28 and 47 pipe diameters after the upstream bottom bend) of the upward section. In addition to bubbly, intermittent and annular flows, unstable flow was also observed at the three positions of the upward section for particular ranges of air and water flow rates. This is probably due to the vertical serpentine configuration of the pipeline, as observed by Golan and Stenning (1969). In this study it was found that, the lower bend was periodically blocked by the liquid and then blown through by the accumulated air. This certainly an undesirable flow regime in heat exchange facilities as can lead to dryout phenomenon.
- Liquid film development was closely related to both the air and water flow rates. However, the length of the average film thickness development is mainly dominated by the water flow rate; the lower the water flow rate the shorter the length of the film development.
- When water superficial velocity was constant, the average liquid film thickness decreased as the air superficial velocity increased.
- At higher flow rates, it was noted that the 180^{o} upstream bottom bend has a major impact on the circumferential distribution of the liquid film at the bottom position, but has only a minor impact on liquid film distribution at the middle and top positions.
- The large amplitude disturbance (ripple) waves were observed at low air superficial velocity and high water superficial velocity. This is due to the fact that, the intermittent flow is a dominant flow in upward flow when low air and high water flow rates are applied. On the other hand, the annular flow was formed at

high air and low water superficial velocities respectively. Consequently, the identified disturbance waves appear to have relatively small height. The disturbance waves reported in the current study were observed for all flow conditions tested.

- An examination of power spectral density (PSD) of liquid film thickness at different positions of upward section and for a range of air and water superficial velocities shows that, the frequency increases with increasing the water superficial velocity, for all air superficial velocities. On the other hand, for a given water superficial velocity, the PSDs amplitude is decreased as air superficial velocity increased further.

7.2 Conclusions from theoretical studies on liquid film thickness

- It was noted that, most of the models used to predict the film thickness systematically provide poor predictions in regions of low air superficial velocity where the liquid film is thick.
- From a comparison made between this study and available models used to predict the film thickness in the downward and upward flows, it was observed that the models were developed with data obtained from small diameter pipes. However, the data collected from this study were carried out using a large diameter pipe (i.d. = 101.6 mm). The pipe diameter partly responsible for the model deviations. It was found from the previous work that, the two-phase flow behaviour in a small pipe diameter is different from in the large one. This has led to poor prediction of the measured film thickness data when these models were used. Therefore, the reported models were updated to provide a closer prediction for the current experimental data and those found in literature.
- The data presented in this study were obtained at 28 pipe diameters after a U-bend, and the bends partly responsible for the flow behaviour, even on reaching the middle positions (particularly at high air flow rates), so that the flow was not fully developed. As a result, modifications to the Serpent rig were recommended to reduce the aforementioned shortcomings, together with using adequate models that take into consideration the droplet entrainment into the gas core.

7.3 Recommendations for future work

From the achieved results, it was noted that the following recommendations need to be carried out for further experimental studies using the Serpent rig with appropriate modifications:

- The flow behaviour, flow regimes, film thickness and pressure drop, for liquids of viscosity different from water need to be established, possibly using CMC aqueous solutions.
- It was noted that, the entrainment was not considered in the correlations used to calculate the film thickness. The reported correlations such as those of Oliemans et al. (1985) and Hewitt & Govan (1990) were found to be difficult to use, due to their iterative nature. Other correlations, for example those developed by Barbosa et al. (2002), were not iterative but had limited applications. Thus, there is need to develop a correlation that takes into consideration the entrainment, in order to achieve accurate film thickness results.
- The data of entrainment obtained from the upward section of the Serpent rig were collected at distance of 28 pipe diameters from the U-bend. Investigators such as Omebere-Iyari et al. (2008) stated that, the fully developed flow can only occur at (or greater than) 40 pipe diameters. Therefore, the length of both the downward and upward sections of the Serpent rig needs to be extended to a maximum of 2 m (due to space limitations). To ensure a fully developed flow, the integrated film thickness and film velocity probe needs to be placed at the highest position of the upward section rather than the middle position (current position).
- Appropriate injectors, such as the porous sinter injector, need to be placed at the top and bottom positions of the downward and upward sections respectively, so that the liquid film is injected into the walls of the pipe with air introduced at the annulus (Figure 7-1). This can ensure an annular flow to be obtained at the onset stage thereby aiding fully developed flow.

- Wire mesh sensor and film thickness probes could then be placed at different locations along the downward and upward sections in order to investigate the flow behaviour in the new configuration of the Serpent rig.

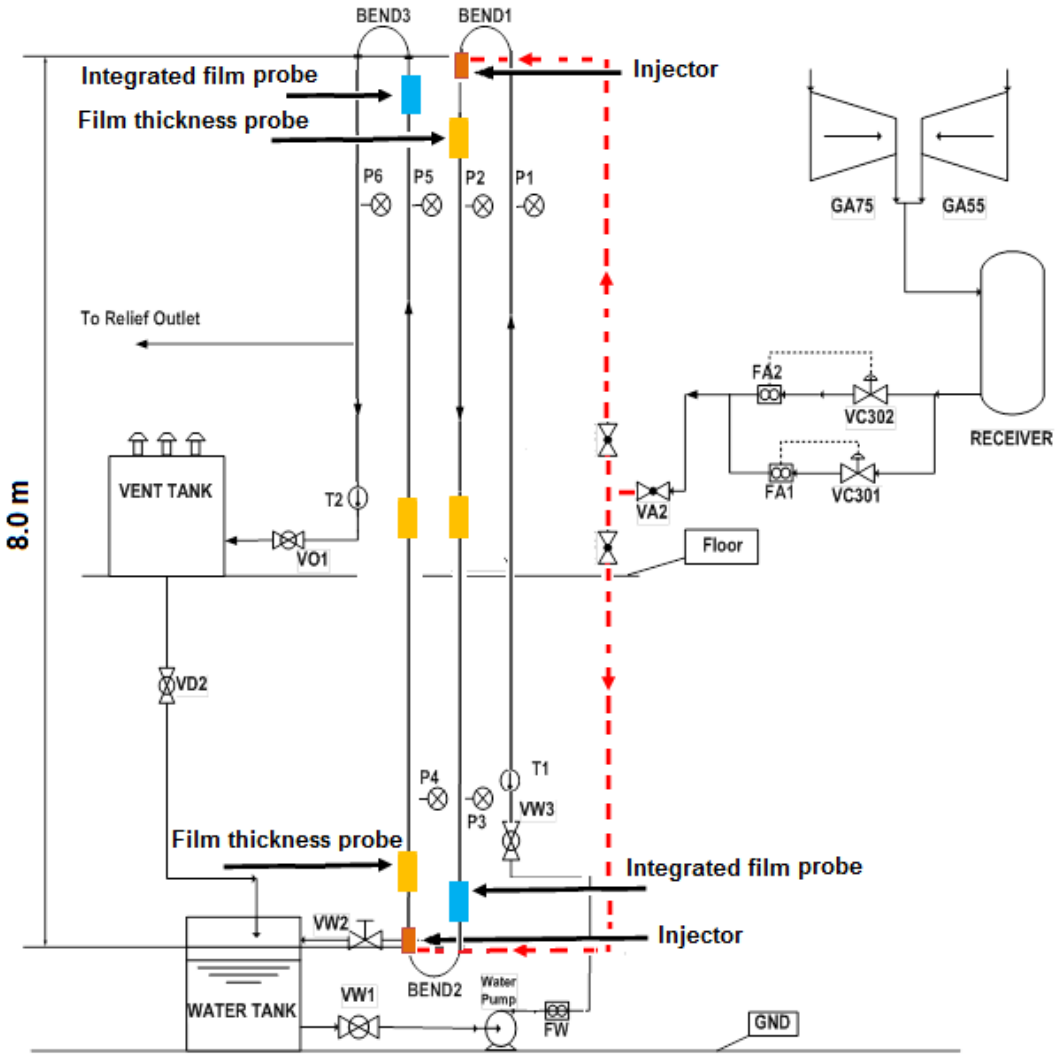

Figure 7-1 Schematic of the Serpent rig with suggested modifications

REFERENCES

Abdullah, A. and Al-Khatab, S. (1994). Experiments on flow characterization in vertical downward two-phase flow. *Experimental Thermal and Fluid Science*, 9, pp. 34-38.

Abdulkadir, M. (2011). Experimental and computational fluid dynamics (CFD) studies of gas-liquid flow in bends. PhD thesis, University of Nottingham, UK.

Abdulkadir, M., Zhao, D., Azzi, A., Lowndes, I. S. and Azzopardi, B.J. (2012). Two-phase air-water flow through a large diameter vertical 180º return bend. *Chemical Engineering Science*, 79, pp. 138-152.

Alekseev, V.P., Poberezkin, A.E. and Gerasimov, P.V. (1972). Determination of flooding rates in regular packing. *Heat Transfer Soviet Res*earch, 4, pp. 159-163.

Ali, S. F., Yeung, H., (2008). Slug dissipation in large diameter horizontal pipeline-vertical riser system. *6th North American Conference on Multiphase Flows Technology*, Banff, Canada.

Alves, G.E. (1954). Co-current liquid-gas flow in a pipeline contractor. *Chemical Engineering Progress*, 50, pp. 449-456.

Ambrosini, W., Andreussi, P. and Azzopardi, B. J. (1991). A physically based correlation for drop size in annular flow. *International Journal of Multiphase Flow*, 17, pp. 497-507.

Anderson, G. H. and Hills, P. D. (1974). Two-phase annular flow in tube bends. *Symposium on Multiphase flow Systems.* University of Strathclyde, Glasgow, paper J1, Published as Institution of Chemical Engineers Symposium, series no. 38.

Ariyadasa, U. (2002). An investigation of film thickness and pressure in upward and downward annular two-phase flow. M.Sc. thesis, Department of Mechanical Engineering, University of Saskatchewan.

Arnold, C.R. and Hewitt, G.F. (1967). Further developments in the photography of two-phase gas- liquid flow. *Journal of Photographic Science*. 15, pp. 97-114.

Asali, J. C., Hanratty, T. J., and Andreussi, P. (1985). Interfacial drag and film height for vertical annular flow. *AIChE Journal*, 31, pp. 895-902.

Azzi, A. and Friedel, L. (2005).Two-phase upward flow 90 degree bend pressure loss model. *Forschung im Ingenieurwesen*, 69, pp. 120-130.

Azzopardi, B. J. (1997). Drops in annular two-phase flow. *International Journal of Multiphase Flow*, 23, pp.1-53.

Azzopardi, B. J. and Whalley, P. B. (1980). Artificial waves in annular two-phase flow. *ASME Winter Annual Meeting, Chicago*, Published in Basic Mechanisms in Two-Phase Flow and Heat-Transfer, pp.1-8.

Azzopardi, B. J., and Wren, E. (2004). What is entrainment in two phase churn flow? *Journal of Multiphase Flow*, 30, pp. 89-103.

Badie, S., Lawrence, C. and Hewitt, G. (2001). Axial viewing studies of horizontal gas-liquid flows with low liquid loading. *International Journal of Multiphase Flow*, 27, pp. 1259-1269.

Balfour, J. D. and Pearce, D. L. (1978). Annular flows in horizontal 180^{o} bends: Measurements of water rate distributions in the film and vapour Core. C.E.R.L., Note no. RD/L/N96/78.

Barbosa, J. R., Jr., Hewitt, G. F., Konig, G. and Richardson, S. M. (2002). Liquid entrainment, droplet concentration and pressure gradient at the onset of annular flow in a vertical pipe. *International Journal of Multiphase Flow*, 28, pp. 943-961.

Barnea, D. (1987). A unified model for predicting flow pattern transitions for the whole range of pipe inclinations. *International Journal of Multiphase flow*, 13, pp. 1-12.

Barnea, D, Shoham, O. and Taitel, Y. (1982). Flow pattern transition for downward inclined two-phase flow: Horizontal to vertical. *Chemical Engineering Science*, 37, pp. 735-740.

Bashforth, W. Q., Fraser, J. B. P., Hutchinson, H. P. and Nedderman, R. M. (1963). Two phase flow in a vertical tube. *Chemical Engineering Sci*ence, 18, pp. 41-46.

Bennett, A. W., Hewitt, G. F., Kearsey, H. A., Keeys, R. K. F. and Lacey, P. N. C. (1965). Flow visualisation studies of boiling at high pressure. *Proceedings of the Institution of Mechanical Eng*ineers, 180 (Part 3C), pp.1-11.

Brown, D. J., Jensen, A. and Whalley, P. B. (1975). Non-equilibrium effects in heated and unheated annular two-phase flow. *ASME*, paper no. 75-WA/HT-7.

Butterworth and Hewitt, G. F. (1977). Flow patterns in two-phase flow and heat transfer, pp. 18-39, Oxford University Press.

Carey, V. P. and Mandrusiak, G. D. (1986). Annular film-flow boiling of liquids in a partially heated, vertical channel with offset strip fins. *International Journal of Heat and MassTransfer*, 29, pp. 927-939.

Cheng, H., Hills, J. H. and Azzopardi, B. J. (1998). A study of the bubble-to-slug transition in vertical gas-liquid flow in columns of different diameter. *International Journal of Multiphase Flow*, 24, pp. 431-452.

Cheng, L., Ribatski, G., and Thome, J. R. (2008). Two-phase flow patterns and flow-pattern maps: Fundamentals and applications. *Applied Mechanics Reviews*, 61, pp.28.

Chong, L. Y., Azzopardi, B. J. and Bate, D.J. (2005). Calculation of conditions at which dryout occurs in the serpentine channels of fired reboilers. *Chemical Engineering Research and Design*, 83, pp. 412-422.

Cousins, L. B. and Hewitt, G.F. (1968). Liquid phase mass transfer in annular two-phase flow: droplet deposition and liquid entrainment. *UKAEA Report AERE-R5657*.

Crawford, T. J. (1983). Analysis of steady state and transient two phase flows in downwardly inclined lines. PhD thesis, Mechanical Engineering, Drexel University.

Da Silva, M. J., Schleicher, E. and Hampel, U. (2007). Capacitance wire-mesh sensor for fast measurement of phase fraction distributions. *Measurement Science and Technology*, 18, pp. 2245-2251.

Da Silva, M. J., Thiele, S., Abdulkareem, L., Azzopardi, B. J. and Hampel, U. (2010). High-resolution gas-oil two-phase flow visualization with a capacitance wire-mesh sensor. *Flow Measurement and Instrumentation*, 21, pp. 191-197.

Dean, W. R. (1927). Note on the motion of fluid in a curved pipe. *Philosophical Magazine Series 7*, 4, pp. 208-223.

Dean, W.R. (1928). The streamline motion of fluid in a curved pipe. *Philosophical Magazine Series 7*, 5, pp. 673-695.

Dong, F., Liu, X., Deng, X., Xu, D. and Xu, L. (2001). Identification of two-phase flow regimes in horizontal, inclined and vertical pipes, *Measurement Science and Technology,* 12, pp. 1069-1075.

Dukler, A. E., Bergelin, O. P. (1952). Characteristics of flow in falling films. *Chemical Engineering Progress*, 48, pp. 557-563.

Eustice, J. (1911). Experiments on stream-line motion in curved pipes. *Proceedings of the Royal Society*, A85, pp. 119-131.

Eustice, J. (1910). Flow of water in curved pipes. *Proceedings of the Royal Society*, A84, pp. 107-118.

Fukano, T. and Furukawa, T. (1998). Prediction of the effects of liquid viscosity on interfacial shear stress and frictional pressure drop in vertical upward gas-liquid annular flow. *International Journal of Multiphase Flow*, 24, pp. 587-603.

Geraci, G., Azzopardi, B. J. and Van Maanen, H. R. E. (2007). Inclination effects on circumferential film distribution in annular gas/liquid flows. *AIChE Journal*, 53, pp. 1144-1150.

Gill, L. E., Hewitt, G. F., Hitchon, J. W. and Lacey, P. M. C. (1963). Sampling probe studies of the gas core in annular two phase flow-1: The effect of length on phase and velocity distribution. *Chemical Engineering Science*, 18, pp. 525-535.

Gill L. E. and Hewitt G. F. (1966). Sampling probe studies of the gas core in annular two phase flow: III, Distribution of velocity and droplet flow rate after injection through axial jet. *AEREM 1202*.

Golan, L. P. (1968). An air-water study of vertical upward and downward two phase flow. PhD thesis, Mechanical Engineering, Leigh University.

Golan, L. P. and Stenning, A. H. (1969). Two-phase vertical flow maps. *Proceedings of the Institution of Mechanical Engineers*, 184, pp. 108-114.

Govan, A. H. (1990). Modelling of vertical annular and dispersed two-phase flows. Ph.D. thesis, Imperial College, London.

Hanratty, T. and Woodmansee, D. (1965). Stability of the interface for a horizontal air-liquid flow gas-liquid wave. *Symposium on Two-Phase Flow, Exeter*, Paper A1.

Hawkes, N. J., Lawrence, C. J. and Hewitt, G. F. (2000). Studies of wispy-annular flow using transient pressure gradient and optical measurements. *International Journal of Multiphase Flow*, 26, pp. 1565-1582.

Hazuku, T., Takamasa, T. and Matsumoto, Y. (2008). Experimental study on axial development of liquid film in vertical upward annular two-phase flow. *International Journal of Multiphase Flow*, 34, pp.111-127.

Henstock, W. H. and Hanratty, T. J. (1976). The interfacial drag and the height of the wall layer in annular flows. *AIChE Journal*, 22, pp. 990-1000.

Hewitt, G. F.and Govan, A. H. (1990). Phenomenological modelling of non-equilibrium flows with phase change. *International Journal of Heat and Mass Transfer*, 33, pp.229-242.

Hewitt, G. F. and Hall-Taylor, N. S. (1970). Annular Two-Phase Flow. Pergamon, Oxford, UK.

Hewitt, G. F. and Jayanti, S. (1993). To churn or not to churn. *International Journal of Multiphase Flow*, 19, pp. 527-529.

Hewitt, G. F. and Roberts, D. N. (1969). Studies of two phase patterns by simultaneous X-ray and flash photography. *UKAEA Report*, AEREM 2159.

Hewitt, G. F. and Wallis, G. B. (1963). Flooding and associated phenomena in falling film in a vertical tube. *Multiphase flow symposium*, Philadelphia, pp. 62-74.

Hewitt, G. F., Lacey, P. M. C. and Nicholls, B. (1965).Transitions in film flow in a vertical tube. University of Exeter, Devon, England, 1, pp. 401-430.

Hills, P. D. (1973). A study of two-phase (gas-liquid) flow in a tube bend. PhD thesis, Imperial College, London.

Hoang, K. and Davis, M. R. (1984). Flow structure and pressure loss for two-phase flow in round bends. *Journal of Fluids Engineering*, 106, pp.30-37.

Holt, A. J., Azzopardi, B. J. and Biddulph, M. W. (1999). Calculation of two-phase pressure drop for vertical upflow in narrow passages by means of a flow pattern specific model. *Chemical Engineering Research and Design*, 77, pp. 7-15.

Hori, K., M. Nakazatomi, K. Nishikawa, and Sekoguchi, K. (1979). On ripple of annular two-phase flow: effect of liquid viscosity on characteristics of wave and interfacial friction factor. *Bulletin of the JSME.*

Imura, H., Kusuda, H. and Funatsu, S. (1977). Flooding velocity in a counter current annular two-phase flow. *Chemical Engineering Science*, pp. 32, and 79-87.

Ishii, M. and Mishima, K. (1989). Droplet entrainment correlation in annular two-phase flow. *International Journal of Heat and Mass Transfer*, 32, pp.1835-1846.

James, P. W., Azzopardi, B.W., Graham, D.I. and Sudlow, C. A. (2000). The effect of a bend on droplet distribution in two-phase flow. *International Conference on Multiphase Flow in Industrial Plants, Bologna*.

Jayanti, S. and Hewitt, G. F. (1992). Prediction of the slug-to-churn flow transition in vertical two-phase flow. *International Journal of Multiphase Flow*, 18, pp. 847-860.

Jayanti, S., Hewitt, G. F., Low, D. E. F. and Hervieu, E. (1993). Observation of flooding in the Taylor bubble of co-current upwards slug flow. *International Journal of Multiphase Flow*, 19, pp. 531-534.

Kaji, R. and Azzopardi, B. J. (2010). The effect of pipe diameter on the structure of gas/liquid flow in vertical pipes. *International Journal of Multiphase Flow*, 36, pp. 303-313.

Karapantsios, T. D., Paras, S. V. and Karabelas, A. J. (1989). Statistical characteristics of free falling films at high Reynolds numbers. *International Journal of Multiphase Flow*, 15, pp. 1-21.

Karimi,G. and Kawaji, M. (2000). Flooding in vertical counter-current annular flow. *Nuclear engineering and design*, 200, pp. 95-105

Kataoka, I. and Ishii, M. (1987). Drift-flux model for large diameter pipe and new correlation for pool void fraction. *International Journal of Heat and Mass Transfer*, 30, pp. 1927-1939.

Kelessidis, V. C. and Dukler, A. (1989). Modelling flow pattern transitions for upward gas-liquid flow in vertical concentric and eccentric annulus. *International Journal of Multiphase Flow*, 15, pp.173-191.

Kosky, P.G. (1971). Thin liquid films under simultaneous shear and gravity forces. *International Journal of Heat and Mass Transfer*, 14, pp.1220-1224.

Lao, L., Antonio, L., Lawrence, C. and Hewitt, G. (2004). Experimental studies of the effects of inlet geometry on the annular flow development at high mass fluxes. 5th *International Conference on Multiphase Flow*, ICMF' 04, paper no. 22, Yokohama, Japan.

Lao, L., Xing, L. and Yeung, H. (2012). Behaviours of elongated bubbles in a large diameter riser, *8th North American Conference on Multiphase Technology*, Banff, Canada, pp.381-392.

Laurinat, J. E., Hanratty, T. J. and Dallman, J. C. (1984). Pressure drop and film height measurements for annular gas-liquid flow. *International Journal of Multiphase Flow*, 10, pp. 341-356.

Liu, T. J. and Bankoff, S. G. (1993). Structure of air–water bubbly flow in a vertical pipe—II. Void fraction bubble velocity and bubble size distribution. *International Journal of Heat and Mass Transfer*, pp. 36, and 1061-72.

MacGillivray, R. and Gabriel, K. S. (2003). A Study of Annular Flow Characteristics in Microgravity and Hypergravity Conditions, Acta Astronautica, 53, pp. 289-297.

Malnes, D. (1966). Slip ratios and fraction factors in the bubble flow region in vertical tubes, Report Institute for Atomenergi, Kjeller Research Establishment.

Maqbool, M. H., Palm, B., and Khodabandeh, R. (2012). Experimental investigation of dryout of propane in uniformly heated single vertical mini-channels. *Experimental Thermal and Fluid Science*, 37, pp. 121-129.

McQuillan, K. W. and Whalley, P. B. (1985). Flow patterns in vertical two-phase flow. *International Journal of Multiphase Flow*, 11, pp. 161-175.

McQuillan, K. W., Whalley, P. B. and Hewitt, G. F. (1985). Flooding in vertical two phase flow. *International Journal of Multiphase Flow*, 11, pp. 741-760.

Namie, S. and Ueda, T. (1973). Droplet transfer in two-phase annular mist flow: Part 2, Predictions of droplet transfer rate. *JSME*, 16, pp. 752-764.

Newitt, D. M., Dombrowski, N. and Knelman, F. H. (1954). Liquid entrainment: I, the mechanism of drop formation from gas or vapour bubbles. *Transactions of the Institution of Chemical Engineers*, 32, pp. 244.

Nguyen, V. T. (1975). Two phase gas-liquid co-current flow. An investigation of hold up, pressure drop and flow pattern in a pipe at various inclinations. PhD thesis, The University of Auckland.

Nicholas, C. R. (1965). A study of vertical flow of air-water mixture. PhD thesis, Chemical Engineering, University of Maryland.

Nicholas P. Cheremisinoff (2000). Handbook of chemical processing equipment, Butterworth-Heinemann, USA.

Nicklin, D. J. and Davidson, J. F. (1962). The onset of instability in two-phase slug flow. Presented at *International Mechanical Engineer Symposium on Two-Phase Flow*, Exeter, Devon.

Nishikawa, K., Sekoguchi, K., Nakasamomi, M., and Kaneuzi, A. (1967). Liquid film flow in upwards two-phase flow. *JSME Semi-International Symposium*. Tokyo, pp. 65-74.

Olerni, C., Jia, J., Wang, M. (2013). Measurement of air distribution and void fraction of an upwards air-water flow using electrical resistance tomography and a wire-mesh sensor. *Measurement Science and Technology*, 24, pp.9.

Oliemans, R. V. A., Pots, B. F. M. and Trompe, N. (1985). Modelling of annular dispersed two-phase flow in vertical pipes. *International Journal of Multiphase Flow*, 12, pp. 711-732.

Omebere-Iyari, N. K., Azzopardi, B. J., Ladam, Y. (2007). The identification of two-phase flow patterns and their transitions in large diameter vertical pipes at elevated pressures. *American Institute of Chemical Engineering Journal*. 53, pp. 2493-2504.

Omebere-Iyari, N. K., Azzopardi, B. J., Lucas, D., Beyer, M. and Prasser, H. M. (2008). Gas/liquid flow in large risers. *International Journal of Multiphase Flow*, 34, pp. 461-476.

Oshinowo, O. (1971). Two phase flow in a vertical tube coil. PhD thesis, Department of Chemical Engineering and Applied Chemistry. Toronto, University of Toronto.

Oshinowo, T. and Charles, M. E. (1974). Vertical two-phase flow–Part 1: Flow pattern correlations. *The Canadian Journal of Chemical Engineering*, 52, pp. 25-35.

Pan, L. and Hanratty, T. J. (2002). Correlation of entrainment for annular flow in vertical pipes. *International Journal of Multiphase Flow*, 28, pp. 363-384.

Paras, G. (1982). Characterization of Downward Two Phase Flow By Neutron Noise Analysis. MSc thesis, Nuclear Engineering, University of Washington.

Peng, D. J., Ahmad, M, Hale, C. P., Matar, O. K., and Hewitt, G. F. (2010). Flow regime transition in large diameter pipes. *7th International Conference on Multiphase Flow, ICMF*, Tampa, Florida, USA, May 30-June 6.

Poulson, B. (1991). Measuring and modelling mass transfer at bends in annular flow two phase flow. *Chemical Engineering Science*, 46, pp. 1069-1082.

Prasser, H. M., Beyer, M., Carl, H., Gregor, S., Lucas, D., Pietruske, H., Schütz, P. and Weiss, F. P, (2007). Evolution of the structure of a gas-liquid two-phase flow in a large vertical pipe. *Nuclear Engineering and Design*, 237, pp.1848-1861.

Pushkina, O. L. and Sorokin, Y. L. (1969). Breakdown of liquid film motion in vertical tubes. *Heat Transfer--Soviet Research*, 1, pp. 56-64.

Richter, H. L. (1981). Flooding in tubes and annuli. *International Journal of Multiphase Flow*, 7, pp. 647-658.

Rooyen, E. V., Agostini, F., Borhani, N. and Thome, J. R. (2012). Boiling on a tube bundle: Part I-flow visualization and onset of dryout. *Heat Transfer Engineering*, 33, pp. 913-929.

Schlegel, J. P., Miwa, S., Chen, S., Hibiki, T. and Ishii, M. (2012). Experimental study of two-phase flow structure in large diameter pipes. *Experimental Thermal and Fluid Science*, 41, pp.12-22.

Sekoguchi, K. and Takeishi, M., (1989). Interfacial structures in upward huge wave flow and annular flow regimes. *International Journal of Multiphase Flow,* 15, pp. 295-305.

Serizawa, A. and Feng, Z. P. (2002). Two-phase fluid flow, in G. F. Hewitt (ed.), Chapter 2.13: Heat transfer and fluid flow in microchannel. *Heat Exchanger Design Handbook,* Begell House, Inc.

Serizawa, A. and Kataoka, I. (1988). *Phase distribution in two-phase flow Transient Phenomena in Multiphase Flow,* Washington, DC: Hemisphere, pp. 179-224.

Smith, T. R, Schlegel, J. P., Hibiki, T. and Ishii, M. (2012). Two-phase flow structure in large diameter pipes. *International Journal of Heat and Fluid Flow*, 33, pp.156-167.

Suzuki, S. and Ueda, T. (1977) Behaviour of liquid films and flooding in counter-current two-phase flow--Part I. Flow in circular tubes. *International Journal of Multiphase Flow*, 3, pp. 517-532.

Taitel, Y., Barnea, D. and Dukler, A. E. (1980). Modelling flow pattern transitions for steady upward gas-liquid flow in vertical tubes. *The AIChE Journal*, 26, pp. 345-354.
Takemura, T., Roko, K. and Shiraha, M. (1986). Dryout characteristics and flow behaviour of gas-water flow through U-shaped and inverted U-shaped bends. *Nuclear Engineering Design*, 95, pp. 365-373.

Usui, K. and Sato, K. (1989). Vertically Downward Two Phase Flow (I) Void Distribution and Average Void Fraction. *Journal of Nuclear Science and Technology*, 26, pp. 670-680.

Usui, K., Aoki, S. and Inoue, A. (1983). Flow behaviour and phase distributions in two phase flow around inverted U-bend. *Journal of Nuclear Science and Technology*, 20, pp. 915-928.

Usui, K., Aoki, S. and Inoue, A. (1980). Flow behaviour and pressure drop of two-phase flow through C-shaped bend in a vertical plane-I: Upward Flow. *Journal of Nuclear Science and Technology*, 17, pp. 875-887.

Vijayan, M., Jayanti, S. and Balakrishnan, A. R. (2001). Effect of tube diameter on flooding. *International Journal of Multiphase Flow*, 27, pp. 797-816.

Wallis, G. B. (1969). One-dimensional two-phase flow. McGraw-Hill, New York.

Wallis, G. B. and Makkenchery, S. (1974). The hanging film phenomenon in vertical annular two-phase flow. *Journal of Fluids Engineering*, 96, pp. 297-298.

Wang, C. C., Chen, I. Y., Lin, Y. T. and Chang, Y. J. (2008). A visual observation of the air-water two-phase flow in small diameter tubes subject to the influence of vertical return bends. *Chemical Engineering Research and Design*, 86, pp. 1223-1235.

Wang, C. C., Chen, I. Y., Yang, Y. W. and Chang, Y. J. (2003). Two-phase flow pattern in small diameter tubes with the presence of horizontal return bend. *International Journal of Heat and Mass Transfer*, 46, pp. 2976-2981.

Wang, C. C., Chen, I. Y., Yang, Y. W. and Hu, R. (2004). Influence of horizontal return bend on the two-phase flow pattern in small diameter tubes. *Experimental Thermal and Fluid Science*, 28, pp. 145-152.

Wang, S. K., Lee, S. J., Jones, O. C. Jr. and Lahey, R.T. Jr. (1987). Turbulence structure and phase distribution measurements in bubbly two-phase flow. *International Journal of Multiphase Flow*, 3, pp. 327-43.

Webb, D.R. and Hewitt, G.F. (1975). Downward co-current annular flow. *International Journal of Multiphase Flow*, 2, pp. 35-49.

Wolf, A. (1995). Film structure of vertical annular flow. PhD thesis, Imperial College, University of London.

Wolf, A., Jayanti, S. and Hewitt, G. F. (2001). Flow development in vertical annular flow. *Chemical Engineering Science*, 56, pp. 3221-3235.

Woodmansee, D. E. and Hanratty, T. J. (1969). Mechanism for the removal of droplets from a liquid surface by a parallel air flow. *Chemical Engineering Science*, 24, pp. 299-307.

Yamazaki, Y. and Yamaguchi, K. (1979). Characteristics of Two Phase Down flow in Tubes: Flow pattern ,void fraction and pressure drop. *Journal of Nuclear Science and Technology,* 16, pp. 245-255.

Yijun, J. and Rezkallah, K. (1993). A study on void fraction in vertical co-current upward and downward two-phase gas-liquid flow - I: Experimental Results. *Chemical Engineering Communication*, 126, pp. 221-243.

APPENDICES

Appendix A Comparison between capacitance and conductive WMS

The reported results in this study showed that, using the capacitance wire mesh sensor (CapWMS) was good technique for providing detailed information about the local distribution of void fraction.

To validate these results it was necessary to compare them with those obtained from another appropriate technique such as conductive wire mesh sensor (CondWMS).

A comparative study between 32 x 32 capacitance and conductive wire mesh sensors was made at the top and bottom positions of each section, i.e. the upward and downward sections of the Serpent rig. The measurements were conducted for air superficial velocities of 0.18, 0.54, 2.56 and 11.52 m/s, while water superficial velocity was kept fixed at 1.5 m/s. These conditions were needed in order to establish various flow regimes. The frequency was recorded at 1,000 Hz over a time period of 60s.

It is noteworthy that, the capacitance wire mesh sensor measurements were based on the difference of permittivity between the two working fluids (i.e. air and water), while the conductive wire mesh sensors were based on the measurements of the local conductivity of the fluids. Data of the time traces of average void fraction and corresponding PDFs, and local void fraction distributions, were used to clarify the differences and/or similarities between both the capacitance and conductive wire mesh sensors.

A.1 Void fraction identification using capacitance and conductive WMS

Figure A-1 (a) and (b) illustrates the mean void fraction against the air superficial velocity, for water superficial velocity of 1.5 m/s. The data plotted in the Figure were collected from the conductive and capacitance wire mesh sensors placed at the bottom position of the downward section and the top position of the upward section. The Figure shows that, the void fractions measured by both techniques have similar tendencies to the air superficial velocities, where they increase systematically when increasing the air superficial velocity.

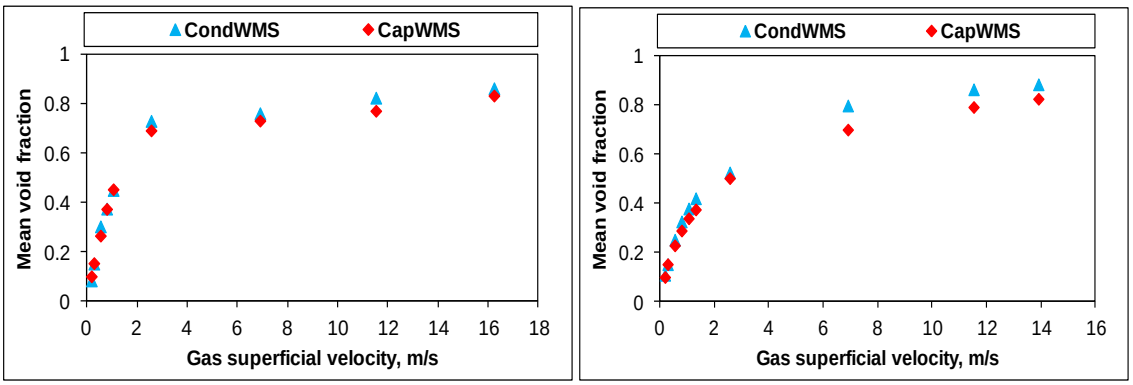

Figure A-1 Variation of mean void fraction against gas superficial velocity for constant liquid superficial velocity of 1.5 m/s, at (a) bottom position of the downward section and (b) top position of the upward section

Figure A-2 (a) and (b) comprises the mean void fraction obtained from CapWMS against that obtained from CondWMS at the bottom and top positions of the downward and upward sections respectively. It can be seen from the plots that, the mean void fraction values obtained from both sensors were close to each other, with linear deviation. However, quite a high discrepancy between the conductive and capacitance WMS was observed for the data obtained from the top position of the upward section. This high discrepancy was attributed to the fact that, the measurements were carried out separately when both techniques were used. The differences were found between -1.66 and 5.32% for the bottom position of the downward section, and between 0 and 9.81% for the top position of the upward section. The negative percentages indicate that, void fraction values measured by

capacitance WMS were greater than those measured by conductive wire mesh sensors; vice versa, the positive percentages mean that the void fraction values measured by conductive WMS have greater values than those measured by capacitance WMS. In general, a good agreement was noted between the two techniques for bubbly flow. On the other hand, the discrepancy increased gradually when intermittent and annular flow regimes were formed.

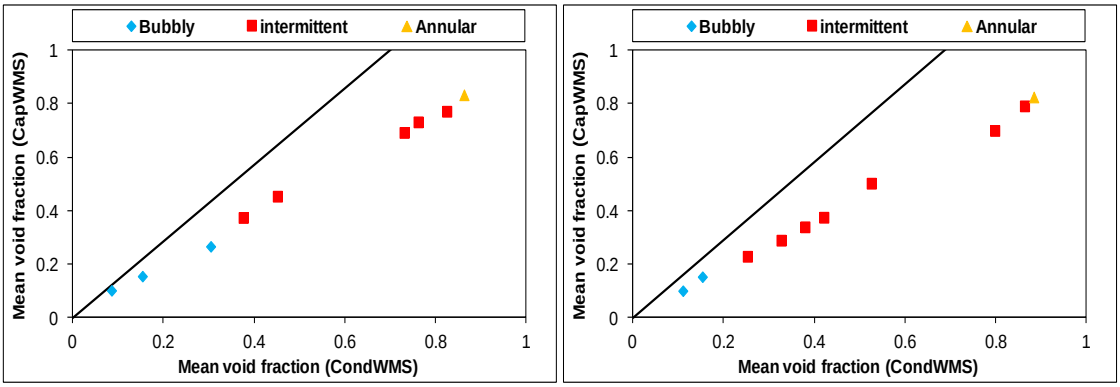

Figure A-2 Comparison of mean void fraction measured by conductive and capacitance WMS at (a) the bottom position of the downward section and (b) the top position of the upward section

A.2 Comparison of local void fraction distribution measured by CondWMS and that measured by CapWMS

Flow regimes were identified using conductive and capacitance wire mesh sensors. Data of time traces of average void fraction and corresponding PDFs were used. The observed flow regimes were obtained for air superficial velocities of 0.18, 0.54, 2.56 and 11.52 m/s, whereas the water superficial velocity maintained a constant 1.5 m/s.

Figure A-3 (a) and (b) presents the results of time traces and corresponding PDFs generated from both sensors at the top and bottom positions of the downward section respectively. Figure A-4 (a) and (b) presents the same data produced from the instruments at the top and bottom positions of the upward section respectively.

From all plots it can be noted that, for each particular position and air superficial velocity the time traces of average void fraction extracted from both the CapWMS and CondWMS were similar. Also, the PDF results obtained from both techniques show similar tendencies. However, the data of CapWMS presented slightly higher

amplitude of PDFs than those of CondWMS for relatively low air superficial velocities of 0.18, 0.54 and 2.56 m/s, where the flow regimes were bubbly and/or intermittent. On the other hand, it was identified that for air superficial velocity of 11.52 m/s, the CondWMS data presented higher PDF values, where the flow was in the intermittent and annular transition region. A similar flow regime was found in both techniques. The measured void fraction using the CapWMS was observed to be lower at the pipe wall than that using CondWMS. This observation suggests that, the CapWMS is unable (or limited) to detect the flow at the pipe wall. The length and character of the PDFs and the void fraction at the top and bottom positions of the downward section were similar for low velocities of air. This similarity was identified even when increasing the air superficial velocity further to higher values. A similar observation was made at the top and bottom positions of the upward section for the same range of air superficial velocity and for water velocity of 1.5 m/s.

The measurements of local void fraction distributions presented in Figures A-3 and A-4 were conducted for various air superficial velocities, while water superficial velocity maintained fixed at 1.5 m/s. The void fraction distributions were made by averaging the void fractions measured at wires numbered 15, 16, 17 and 18 of each crossing point corresponding to the four wires of 32, going from 0^o to 180^o and from 90^o to 270^o over 101.6 mm internal diameter pipe, as shown below in the local void fraction plots. The plots of the local void fraction distributions presented in Figures A-3 and A-4 show that, there is a good agreement between the CapWMS and CondWMS for the greatest range of air superficial velocities. However, in some cases of the top and bottom positions of the downward section there is a significant difference in the instrumentation as the flow reached the wall of the pipe. The CapWMS was noted to provide less information about the local void fractions than the CondWMS. For instance, at air velocity of 11.52 m/s (at the top position of the downward section) it can be noted that, an extreme difference in the instrumentation has been found at the pipe wall. Obviously, the data of local void fraction achieved from CondWMS show a wall peak. This peak was not identified when using the CapWMS. It can be suggested that, the CapWMS is unable (or limited) to measure the void fraction at the pipe wall.

(a) Top position of downward section (Usl=1.5 m/s)			
Usg=0.18 m/s	**Usg=0.54 m/s**	**Usg=2.56 m/s**	**Usg=11.52 m/s**
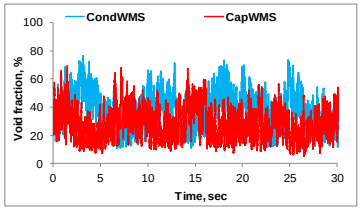	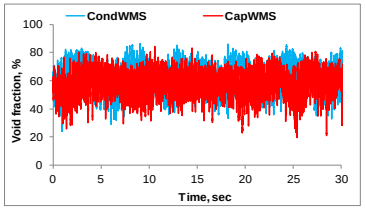	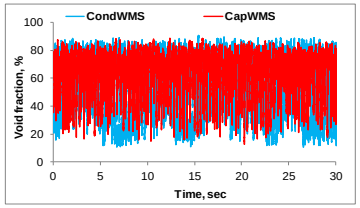	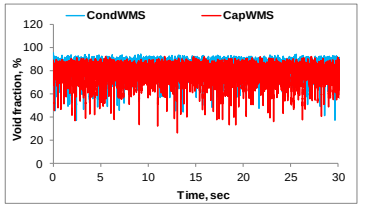
Time traces	**Time traces**	**Time traces**	**Time traces**
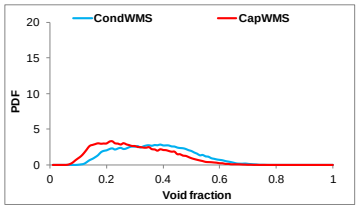	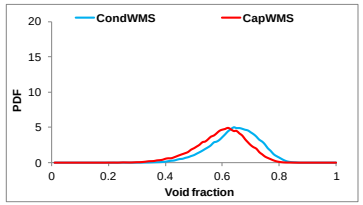	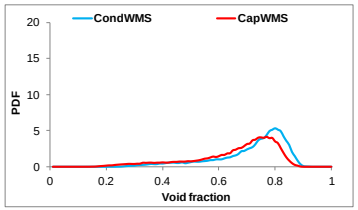	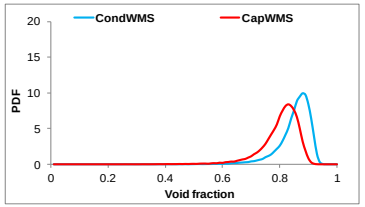
PDFs	**PDFs**	**PDFs**	**PDFs**
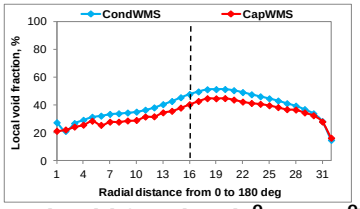	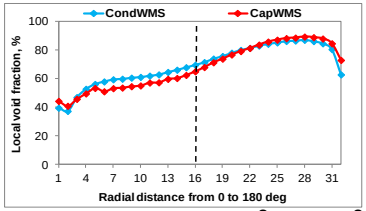	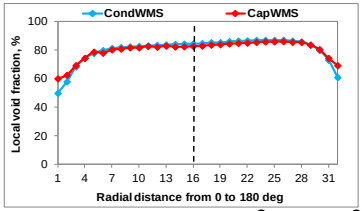	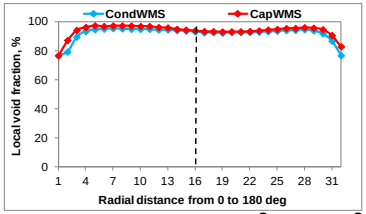
Local void fraction (0^o to 180^o)	**Local void fraction (0^o to 180^o)**	**Local void fraction (0^o to 180^o)**	**Local void fraction (0^o to 180^o)**
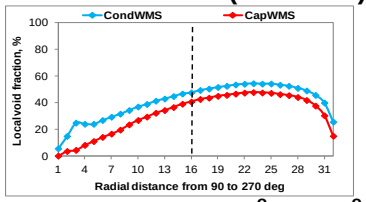	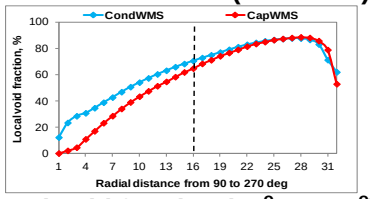	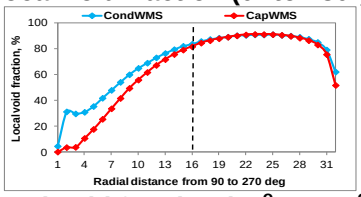	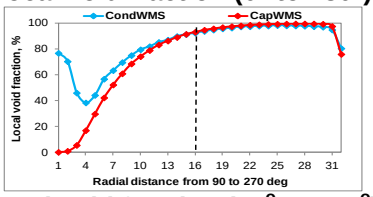
Local void fraction (90^o to 270^o)	**Local void fraction (90^o to 270^o)**	**Local void fraction (90^o to 270^o)**	**Local void fraction (90^o to 270^o)**

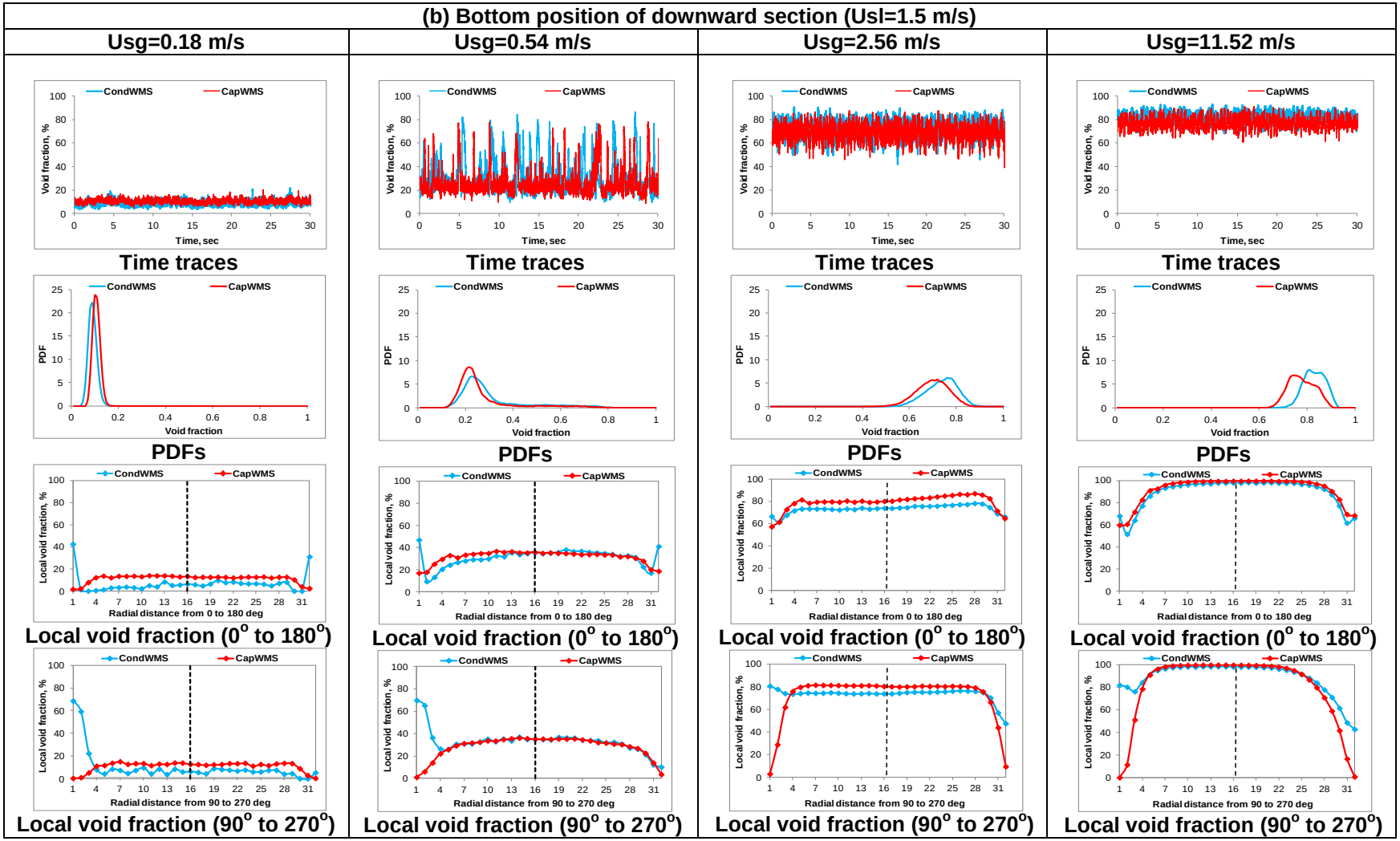

Figure A-3 Void fraction distribution at (a) top and (b) bottom positions of the downward section

(a) Top position of upward section (Usl=1.5 m/s)			
Usg=0.18 m/s	**Usg=0.54 m/s**	**Usg=2.56 m/s**	**Usg=11.52 m/s**
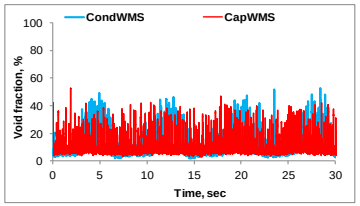	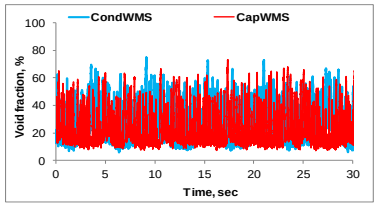	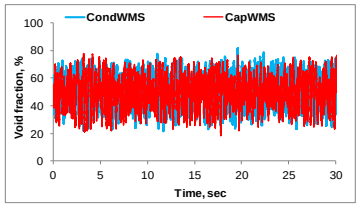	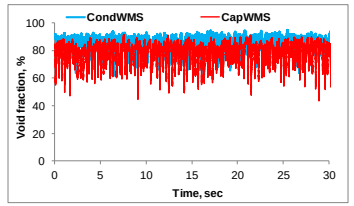
Time traces	**Time traces**	**Time traces**	**Time traces**
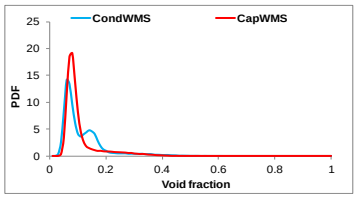	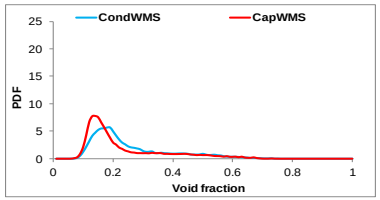	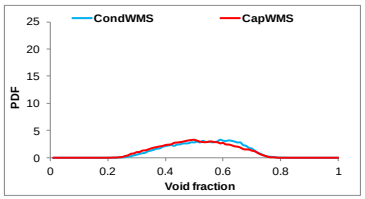	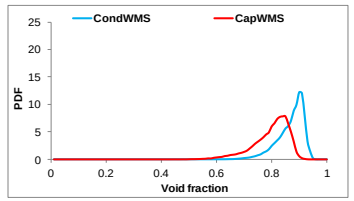
PDFs	**PDFs**	**PDFs**	**PDFs**
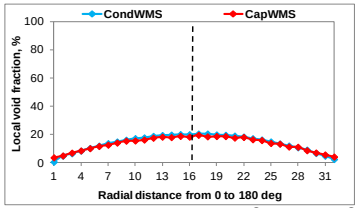	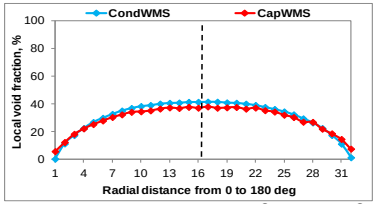	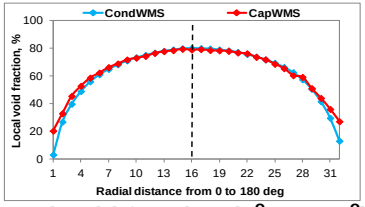	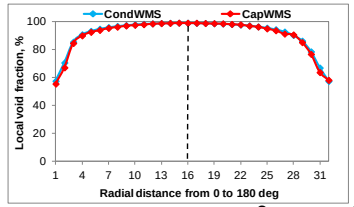
Local void fraction (0^o to 180^o)	**Local void fraction (0^o to 180^o)**	**Local void fraction (0^o to 180^o)**	**Local void fraction (0^o to 180^o)**
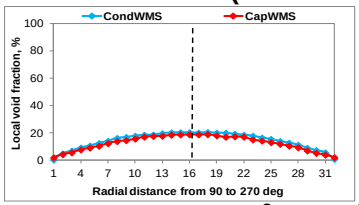	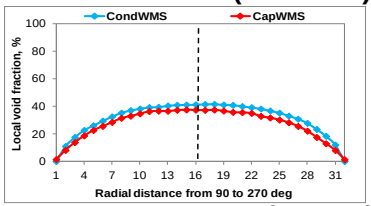	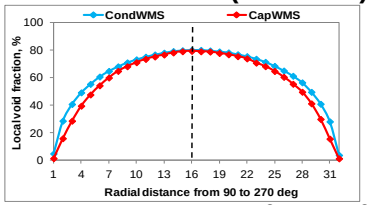	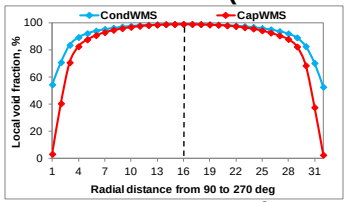
Local void fraction (90^o to 270^o)	**Local void fraction (90^o to 270^o)**	**Local void fraction (90^o to 270^o)**	**Local void fraction (90^o to 270^o)**

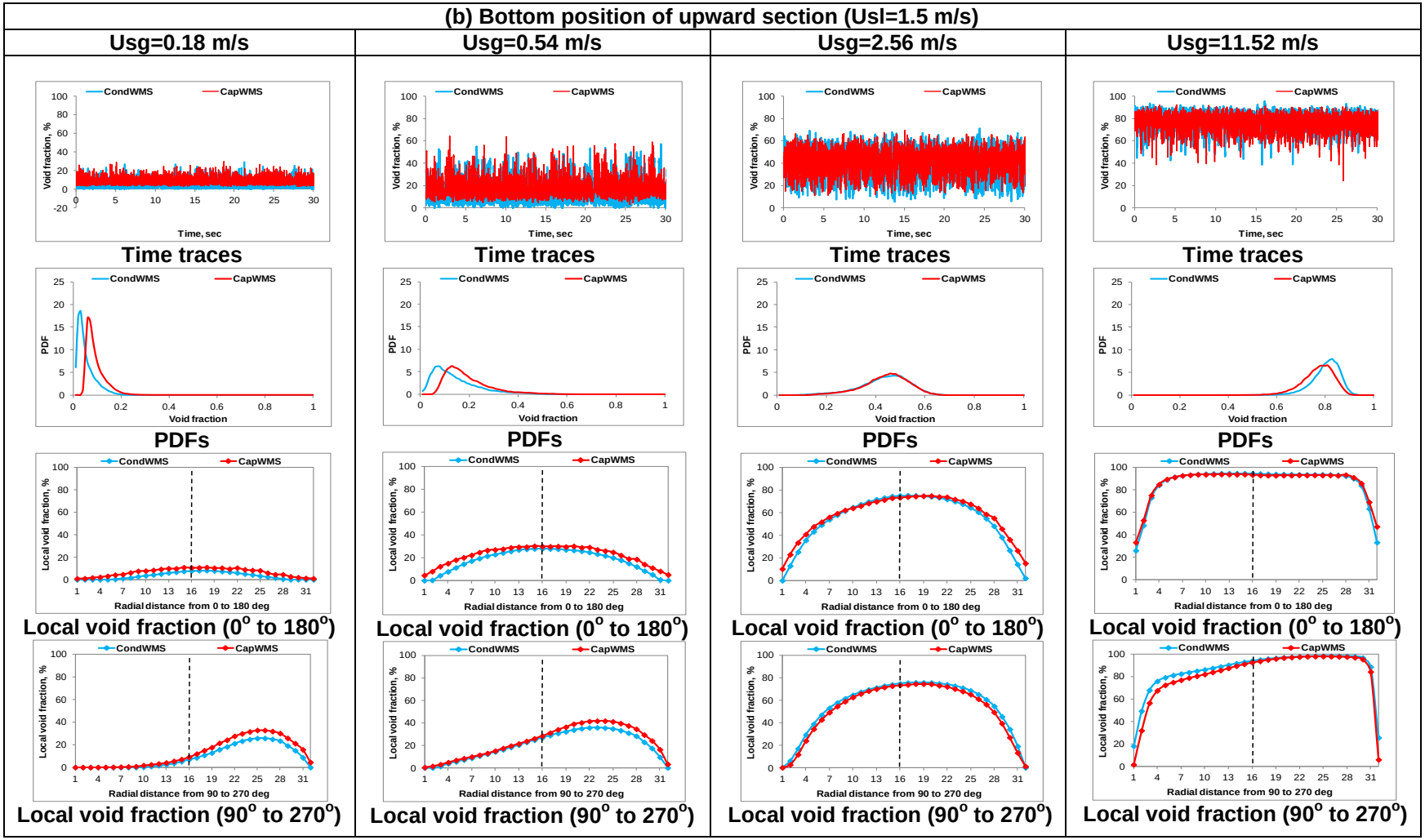

Figure A-4 Void fraction distribution at (a) top and (b) bottom positions of the upward section

A.3 Identification of flow regimes using reconstructed images of WMS

Reconstructed images (the cross-sectional and slice images) of wire mesh sensors were also used as another means to interpret the flow behaviour inside the Serpent rig. As mentioned earlier, the number of cross section images N was used to reconstruct the obtained axial slice images in order to give near reality geometries of phase structures inside the pipe. N is inversely proportional to the mixture velocity, which is expressed as, $N = {f_s L_p}/{U_m}$, where f_s is the recorded frame rate= 1000 fps; L_p is the length of pipe section represented by the axial sliced images, i.e. 1000 mm in this study; and U_m is the mixture velocity for each particular measurement. Figure A-5 presents slice view images of the void fraction's data obtained from the conductive WMS and capacitance WMS installed at the top position of the upward section, for a varying range of air superficial velocity and for water superficial velocity of 1.5 m/s. The red and blue colours depict the gas and liquid phase respectively. It can be seen that there is a good agreement between the images obtained from CondWMS and CapWMS. Both instruments identified similar flow regimes for each particular air superficial velocity.

For simplicity, only the reconstructed images observed at the top location of the upward section were presented. It can be seen from the plots of Figure A-5 that the CondWMS and CapWMS identified the flow regime as a bubbly flow for the air superficial velocity of 0.18 m/s. This is characterised by dispersed small bubbles being evenly distributed across the pipe centre. These bubbles are periodically accompanied by large bubbles. The large bubbles can be classified as spherical cap bubbles, of which the sizes are notably smaller than the pipe diameter. For a higher air superficial velocity of 0.54 m/s, a transition from bubbly to intermittent flow occurred due to the bubbles' coalescence. As the air velocity increased to 1.05 m/s, an intermittent flow was observed accompanied by large bubbles. By increasing the air superficial velocity further, to 2.56 m/s, an intermittent flow was also observed. An

annular flow regime was identified when the air superficial velocity was increased to 11.52 m/s. At this flow condition, a large number of droplets were entrained into the pipe centre.

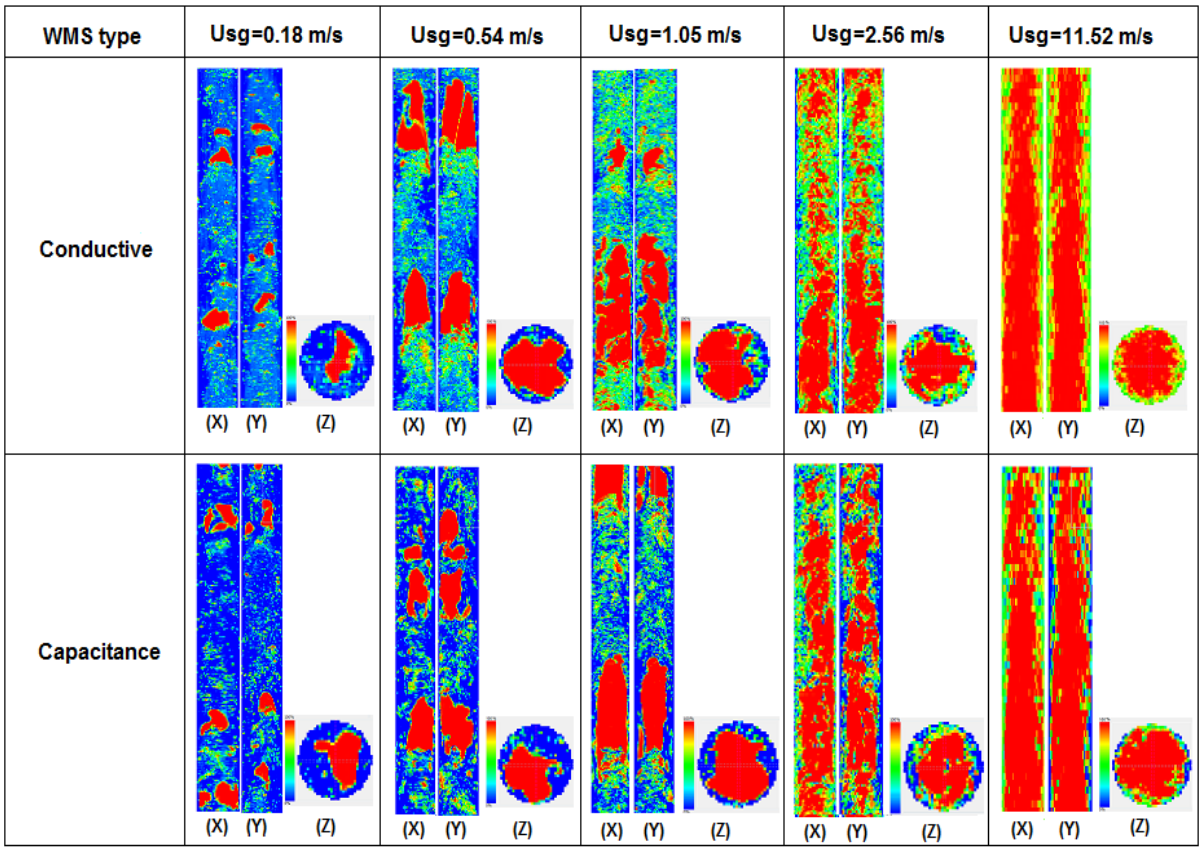

Figure A-5 Reconstructed images obtained from conductive and capacitance WMS at the top location of the upward section for different gas superficial velocities, while liquid superficial velocity was kept constant at 1.5 m/s (X and Y represent the axial slice images, and Z represents the cross section images). For all images the red colour is air and the blue is water

Appendix B Calculation of PDF

In the current study, the probability density function (PDF) methodology was used to identify the flow regimes formed at different positions along the downward and upward flows.

The PDF was generated by counting the number of the measured void fraction data, presented in the form of data bin of a fixed width. Each bin value will then divided by the total number of these data and the width. By this way, the dominant flow regime for particular air and water flow rates, can be determined based on the peak shape and corresponding void fraction values. Some examples of the flow regimes generated from the PDF are illustrated in Figure B-1.

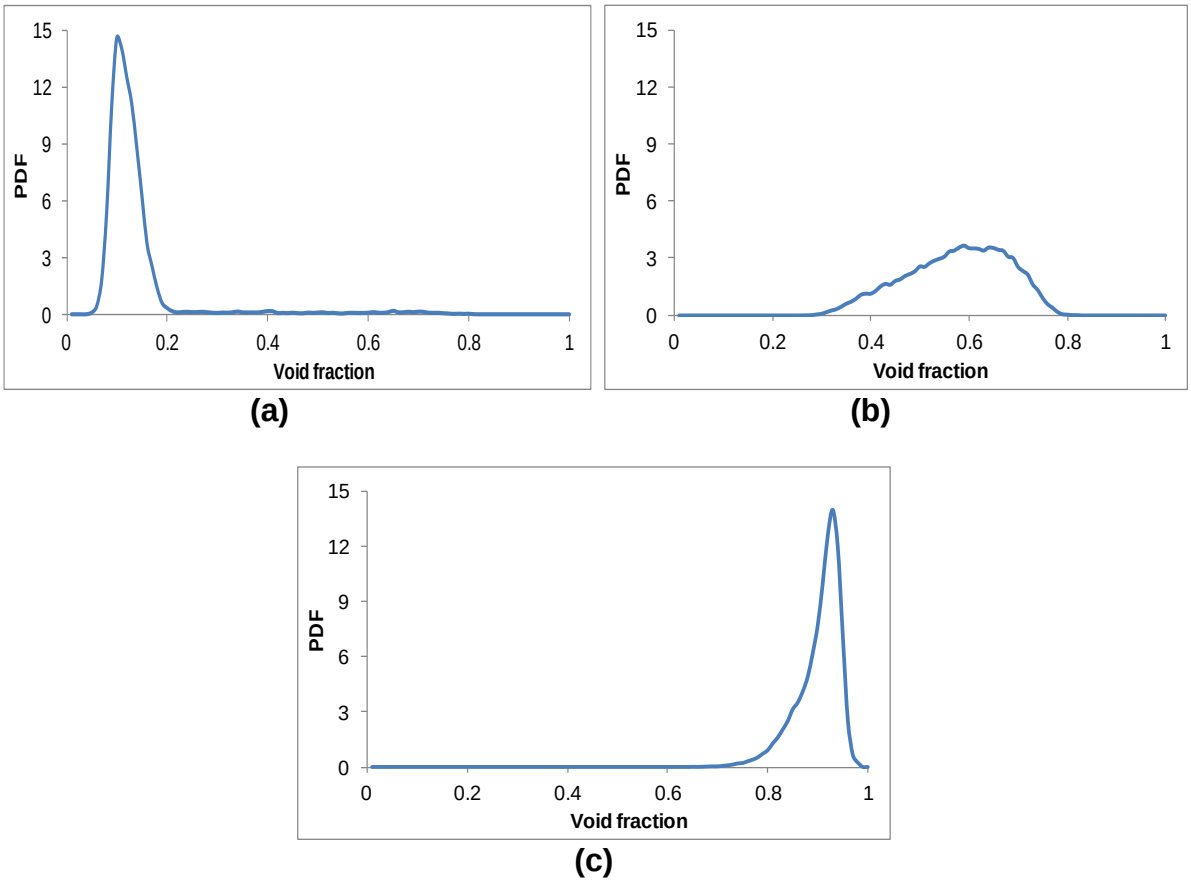

Figure B-1 Examples of flow regimes obtained from probability density function (PDF), (a) bubbly flow, (b) intermittent flow and (c) annular flow

Appendix C Results of gas void fraction

Usl, m/s	0.07	0.1	0.2	0.3	0.48	0.7	1	1.2	1.5
Qg, Sm^3/h	**Gas void fraction, %**								
6	98.15	97.02	93.58	90.49	83.83	68.75	50.79	38.56	29.17
10	97.86	96.99	93.57	90.36	83.80	77.51	58.55	57.93	49.45
20	97.49	96.62	93.25	90.71	84.30	77.83	67.13	62.21	59.17
30	97.66	96.67	93.41	90.67	85.10	78.68	70.07	65.23	59.95
40	97.79	97.02	93.80	91.23	85.66	80.10	71.27	66.09	61.07
50	97.81	97.03	93.86	91.12	86.35	80.83	71.89	66.74	61.31
80	97.77	97.02	93.85	91.27	86.60	81.74	73.52	68.64	63.87
100	97.93	97.04	93.84	91.70	87.36	82.27	74.38	70.20	65.48
150	97.94	97.11	94.34	91.96	87.94	83.34	76.52	72.86	68.53
200	98.02	97.08	94.42	92.21	89.12	84.42	78.17	74.57	71.03
300	98.17	97.47	94.93	92.93	90.22	86.22	80.69	77.51	74.46
400	98.40	97.80	95.65	93.83	90.58	87.68	82.32	79.51	76.73
600	98.59	98.13	96.60	95.19	92.80	89.44	84.52	82.01	79.64
800	98.79	98.42	97.30	95.93	94.07	90.99	85.88	83.82	81.81
1000	99.04	98.66	97.67	96.68	94.74	91.97	87.22	85.79	83.25

Table C-1 Void fraction results at the top position of the downward section

Usl, m/s	0.07	0.1	0.2	0.3	0.48	0.7	1	1.2	1.5
Qg, Sm^3/h	**Gas void fraction, %**								
6	98.50	97.49	94.95	92.44	88.35	32.02	16.80	14.06	11.43
10	98.51	97.31	95.03	93.01	88.16	49.47	36.72	25.27	17.27
20	98.46	97.29	95.17	93.28	88.97	78.13	47.19	39.74	29.92
30	98.55	97.92	95.04	93.30	89.60	83.57	71.03	57.66	41.62
40	98.53	97.50	95.12	93.26	89.85	84.04	74.51	67.77	51.48
50	98.50	97.39	95.08	93.32	90.06	84.25	76.15	72.85	59.19
80	98.44	97.50	95.14	93.43	90.31	84.80	78.50	77.75	69.00
100	98.44	97.54	95.29	93.33	90.41	85.50	79.41	78.80	71.40
150	98.50	97.64	95.39	93.45	90.49	86.04	80.43	78.77	73.39
200	98.52	97.74	95.29	93.79	90.82	86.24	80.77	79.03	74.08
300	98.59	97.92	95.35	93.80	90.67	86.59	81.48	80.28	75.76
400	98.58	97.80	95.81	94.07	91.16	87.16	82.30	81.41	77.36
600	98.82	98.18	96.43	94.67	92.00	88.13	84.33	83.59	80.50
800	99.22	98.75	96.82	95.42	92.35	88.49	85.44	85.04	82.93
1000	99.51	99.16	97.47	95.94	92.51	89.17	86.00	86.24	84.63

Table C-2 Void fraction results at the middle position of the downward section

Usl, m/s	0.07	0.1	0.2	0.3	0.48	0.7	1	1.2	1.5
Qg, Sm^3/h	**Gas void fraction, %**								
6	97.95	96.06	93.41	90.60	86.71	21.86	13.26	12.42	10.22
10	97.78	96.06	93.68	90.56	86.29	52.12	21.71	18.15	15.53
20	97.70	96.10	93.33	90.25	86.90	73.17	47.30	38.34	26.68
30	97.65	95.96	93.94	91.18	87.69	78.25	52.06	47.03	37.48
40	97.24	96.14	93.86	91.37	88.29	81.08	68.81	55.12	45.44
50	97.53	95.94	93.99	90.93	88.37	81.56	71.71	63.44	51.40
80	97.82	95.82	94.03	91.11	88.56	83.02	77.76	71.18	65.50
100	97.90	96.07	93.85	90.97	88.79	83.38	78.71	73.34	69.27
150	98.01	96.31	93.89	90.97	88.61	83.61	79.45	75.04	71.99
200	98.04	96.30	93.96	90.91	88.62	84.01	79.73	75.14	72.50
300	98.12	96.59	94.27	91.21	88.93	84.43	80.12	75.74	73.23
400	98.14	96.79	94.55	91.71	89.23	84.98	80.50	76.77	74.51
600	98.45	97.31	95.42	92.77	89.96	85.81	82.26	80.78	77.21
800	98.93	97.92	96.20	93.88	90.93	87.16	84.21	82.91	80.29
1000	99.26	98.34	96.58	94.36	91.70	87.75	85.10	84.41	83.37

Table C-3 Void fraction results at the bottom position of the downward section

Usl, m/s	0.07	0.1	0.2	0.3	0.48	0.7	1	1.2	1.5
Qg, Sm^3/h	**Gas void fraction, %**								
6	23.83	25.45	22.61	21.13	16.52	13.04	11.96	11.29	10.09
10	35.25	37.82	36.37	34.56	23.88	20.34	17.64	17.01	15.33
20	46.76	45.04	43.58	41.55	35.31	31.53	27.27	26.25	22.97
30	51.72	50.67	47.86	46.51	41.85	36.60	33.56	32.40	28.99
40	54.50	52.96	50.64	50.33	46.24	41.56	38.16	36.92	33.98
50	57.05	55.01	54.62	52.17	49.15	46.02	42.58	42.30	37.57
80	64.43	63.96	60.53	59.20	57.51	55.04	51.59	50.77	46.16
100	67.59	66.61	64.68	62.56	61.56	59.19	56.95	55.24	50.30
150	70.85	70.80	69.75	68.63	67.68	66.10	63.57	62.80	57.47
200	75.63	75.23	75.04	73.97	73.35	71.90	68.89	68.89	63.31
300	82.84	82.68	82.82	82.10	81.56	78.47	75.80	74.65	70.03
400	91.42	90.27	88.90	88.25	85.91	82.67	79.26	78.70	74.21
600	97.41	96.33	93.23	91.43	89.60	87.06	84.08	82.89	79.21
800	98.14	96.61	94.30	93.62	92.24	90.17	86.92	86.73	82.55
1000	99.08	98.31	95.36	93.96	92.98	91.34	89.75	88.43	85.32

Table C-4 Void fraction results at the top position of the upward section

Usl, m/s	0.07	0.1	0.2	0.3	0.48	0.7	1	1.2	1.5
Qg, Sm^3/h	**Gas void fraction, %**								
6	30.48	21.91	16.59	16.58	16.49	13.77	12.53	11.67	10.48
10	40.60	32.14	28.72	25.43	22.09	20.90	17.70	17.32	17.06
20	52.76	42.79	41.59	37.42	32.07	26.96	25.57	25.41	24.46
30	56.89	47.58	46.58	44.06	38.72	35.06	33.59	32.70	31.73
40	61.64	53.47	51.34	48.99	44.90	39.50	38.82	38.59	35.35
50	65.53	56.43	55.06	53.15	49.29	46.73	44.57	42.27	40.65
80	72.69	64.54	63.07	61.90	58.88	57.86	54.93	52.03	49.63
100	74.96	70.02	66.91	65.92	63.12	62.24	59.62	56.57	54.32
150	78.20	74.12	73.02	72.18	71.30	69.86	67.22	64.49	61.71
200	81.63	78.13	77.75	76.84	76.74	75.74	73.21	69.77	66.55
300	87.28	84.10	84.13	83.85	83.68	81.50	77.65	74.62	71.98
400	92.26	89.82	89.31	88.46	86.81	84.53	80.98	78.10	75.53
600	97.52	95.78	92.64	91.64	90.14	88.27	83.90	81.84	80.84
800	98.39	96.54	93.61	91.82	90.37	88.36	86.97	85.38	84.43
1000	99.09	97.94	94.57	91.89	90.51	89.92	89.32	88.07	87.08

Table C-5 Void fraction results at the middle position of the upward section

Usl, m/s	0.07	0.1	0.2	0.3	0.48	0.7	1	1.2	1.5
Qg, Sm^3/h	**Gas void fraction, %**								
6	17.54	17.06	13.93	13.60	13.16	8.65	8.54	8.37	7.82
10	26.06	24.35	18.93	16.80	16.42	12.67	12.60	12.02	11.44
20	33.17	33.51	29.90	25.50	23.01	20.88	20.74	19.52	18.76
30	38.25	39.40	38.07	32.36	30.17	26.17	25.93	25.78	24.29
40	46.17	44.98	42.72	38.89	35.59	31.81	30.52	30.24	28.49
50	49.68	49.14	47.19	44.96	41.07	37.23	35.58	34.22	32.20
80	59.81	58.22	56.50	53.27	49.67	47.26	44.38	42.29	40.41
100	62.64	61.95	60.05	57.54	53.95	52.27	49.38	46.71	43.55
150	69.21	68.08	67.36	64.72	62.68	61.12	58.43	56.16	51.77
200	74.60	80.48	73.76	71.52	70.06	67.97	64.82	62.41	58.41
300	82.46	80.95	79.58	77.84	75.86	73.98	70.43	68.21	64.29
400	87.36	86.09	82.90	81.00	78.98	77.03	73.63	72.53	68.29
600	93.47	90.35	86.78	85.33	84.22	81.07	80.23	79.61	76.42
800	95.26	95.16	95.00	94.16	92.96	89.65	85.99	84.24	80.80
1000	97.72	98.01	97.32	97.12	94.99	92.42	89.19	87.10	83.80

Table C-6 Void fraction results at the bottom position of the upward section

Appendix D Results of liquid film thickness, liquid film velocity and liquid entrainment

Usg, m/s	CT3, mm	CT4, mm	CT1, mm	CT2, mm	Mean, mm	CM3, mm	CM4, mm	CM1, mm	CM2, mm	Mean, mm	CB3, mm	CB4, mm	CB1, mm	CB2, mm	Mean, mm
1.44	0.67	0.46	0.65	0.94	0.68	0.97	0.86	0.84	0.92	0.90	0.91	0.88	0.82	0.99	0.90
3.02	0.59	0.43	0.66	1.03	0.68	0.96	0.82	0.86	0.96	0.90	0.93	0.85	0.82	0.98	0.90
4.60	0.61	0.45	0.67	1.17	0.73	0.98	0.92	0.94	0.98	0.96	0.95	0.93	0.87	1.01	0.94
6.20	0.62	0.47	0.68	1.39	0.79	1.00	0.96	0.96	1.03	0.99	0.98	0.95	0.91	1.00	0.96
9.38	0.69	0.44	0.74	1.54	0.85	0.99	0.89	0.92	1.02	0.96	0.93	0.88	0.85	1.00	0.92
12.47	0.72	0.48	0.80	1.39	0.85	0.95	0.87	0.88	1.00	0.92	0.92	0.86	0.84	0.97	0.90
18.39	0.69	0.70	0.75	1.28	0.86	0.88	0.81	0.80	1.01	0.88	0.90	0.84	0.82	1.01	0.89
23.66	0.59	0.61	0.65	1.18	0.76	0.77	0.68	0.70	1.07	0.81	0.77	0.75	0.73	1.00	0.81
28.87	0.47	0.55	0.52	1.12	0.66	0.60	0.54	0.65	1.03	0.71	0.66	0.66	0.67	0.89	0.72

Table D-1 Liquid film thickness results in the downward section for water superficial velocity of 0.1 m/s

Usg, m/s	CT3, mm	CT4, mm	CT1, mm	CT2, mm	Mean, mm	CM3, mm	CM4, mm	CM1, mm	CM2, mm	Mean, mm	CB3, mm	CB4, mm	CB1, mm	CB2, mm	Mean, mm
1.42	0.78	0.52	0.75	1.22	0.82	1.12	1.06	1.02	1.02	1.06	1.03	1.02	0.94	1.05	1.01
2.97	0.70	0.49	0.75	1.35	0.82	1.12	1.07	1.04	1.07	1.07	1.06	1.01	1.01	1.06	1.04
4.54	0.75	0.52	0.75	1.56	0.94	1.17	1.12	1.06	1.11	1.12	1.09	1.07	1.03	1.12	1.07
6.12	0.73	0.54	0.77	1.68	1.00	1.15	1.14	1.10	1.14	1.13	1.12	1.09	1.08	1.12	1.10
9.17	0.82	0.54	0.91	1.80	1.08	1.20	1.16	1.15	1.18	1.17	1.14	1.10	1.07	1.18	1.12
12.08	0.86	0.56	0.94	1.64	1.04	1.15	1.10	1.09	1.19	1.13	1.13	1.05	1.03	1.17	1.09
17.51	0.81	0.71	0.90	1.36	0.95	1.11	0.99	1.00	1.17	1.07	1.15	1.03	1.03	1.22	1.11
22.41	0.75	0.65	0.81	1.21	0.85	1.06	0.86	0.91	1.17	1.00	1.09	0.94	0.93	1.21	1.04
26.61	0.63	0.56	0.68	1.13	0.75	0.94	0.72	0.83	1.23	0.93	0.98	0.82	0.82	1.29	0.98

Table D-2 Liquid film thickness results in the downward section for water superficial velocity of 0.2 m/s

Usg, m/s	CT3, mm	CT4, mm	CT1, mm	CT2, mm	Mean, mm	CM3, mm	CM4, mm	CM1, mm	CM2, mm	Mean, mm	CB3, mm	CB4, mm	CB1, mm	CB2, mm	Mean, mm
1.39	0.87	0.52	0.93	1.58	0.98	1.25	1.21	1.17	1.15	1.19	1.15	1.10	1.12	1.20	1.14
2.92	0.83	0.52	0.84	1.72	0.98	1.23	1.21	1.14	1.20	1.20	1.17	1.13	1.11	1.16	1.14
4.47	0.80	0.55	0.81	1.79	0.98	1.21	1.23	1.18	1.22	1.21	1.18	1.15	1.15	1.19	1.17
6.00	0.79	0.57	0.80	1.93	1.02	1.24	1.24	1.18	1.27	1.23	1.17	1.19	1.15	1.22	1.18
8.94	0.90	0.60	0.93	1.94	1.09	1.24	1.23	1.19	1.25	1.23	1.18	1.17	1.17	1.24	1.19
11.70	0.90	0.60	0.94	1.78	1.06	1.24	1.22	1.16	1.21	1.21	1.21	1.18	1.10	1.21	1.18
16.74	0.85	0.71	0.88	1.51	0.99	1.22	1.15	1.08	1.21	1.16	1.25	1.22	1.12	1.28	1.22
21.33	0.78	0.68	0.83	1.38	0.92	1.20	1.03	1.05	1.16	1.11	1.23	1.10	1.07	1.27	1.17
25.12	0.71	0.61	0.76	1.21	0.82	1.14	0.90	0.99	1.19	1.05	1.16	0.96	0.96	1.28	1.09

Table D-3 Liquid film thickness results in the downward section for water superficial velocity of 0.3 m/s

Usg, m/s	CT3, mm	CT4, mm	CT1, mm	CT2, mm	Mean, mm	CM3, mm	CM4, mm	CM1, mm	CM2, mm	Mean, mm	CB3, mm	CB4, mm	CB1, mm	CB2, mm	Mean, mm
1.36	1.07	0.60	0.99	1.94	1.15	1.36	1.29	1.28	1.27	1.30	1.24	1.24	1.22	1.29	1.25
2.86	0.92	0.61	0.94	2.01	1.12	1.40	1.31	1.26	1.31	1.32	1.29	1.27	1.26	1.30	1.28
4.36	0.91	0.66	0.89	2.14	1.15	1.36	1.32	1.28	1.39	1.34	1.28	1.30	1.26	1.32	1.29
5.84	0.95	0.71	0.92	2.27	1.21	1.36	1.38	1.27	1.35	1.34	1.26	1.33	1.29	1.31	1.30
8.60	0.97	0.74	0.96	2.28	1.24	1.35	1.34	1.26	1.35	1.33	1.31	1.31	1.24	1.33	1.30
11.16	0.96	0.70	0.97	2.15	1.19	1.38	1.38	1.24	1.33	1.33	1.34	1.36	1.22	1.32	1.31
15.63	0.84	0.67	0.85	1.83	1.05	1.31	1.29	1.20	1.27	1.27	1.30	1.34	1.21	1.28	1.28
19.62	0.78	0.68	0.82	1.60	0.97	1.30	1.28	1.13	1.24	1.24	1.30	1.32	1.13	1.30	1.26
22.87	0.80	0.61	0.77	1.37	0.89	1.29	1.32	1.12	1.17	1.23	1.32	1.33	1.11	1.27	1.26

Table D-4 Liquid film thickness results in the downward section for water superficial velocity of 0.48 m/s

Usg, m/s	CT3, mm	CT4, mm	CT1, mm	CT2, mm	Mean, mm	CM3, mm	CM4, mm	CM1, mm	CM2, mm	Mean, mm	CB3, mm	CB4, mm	CB1, mm	CB2, mm	Mean, mm
1.34	1.00	0.70	1.07	2.23	1.25	1.43	1.46	1.38	1.35	1.40	1.25	1.26	1.27	1.39	1.29
2.78	0.97	0.63	0.91	2.09	1.15	1.40	1.34	1.30	1.31	1.34	1.24	1.20	1.23	1.28	1.24
4.21	0.93	0.65	0.93	2.14	1.16	1.37	1.41	1.35	1.42	1.39	1.31	1.30	1.28	1.32	1.30
5.61	0.90	0.63	0.93	2.20	1.16	1.39	1.40	1.29	1.45	1.38	1.29	1.31	1.27	1.34	1.30
8.15	0.92	0.68	0.96	2.14	1.18	1.26	1.37	1.24	1.27	1.28	1.20	1.26	1.24	1.27	1.24
10.50	0.89	0.66	0.93	2.08	1.14	1.24	1.29	1.20	1.29	1.25	1.19	1.23	1.21	1.25	1.22
14.45	0.85	0.73	0.83	2.24	1.16	1.29	1.24	1.18	1.34	1.26	1.26	1.24	1.21	1.28	1.24
17.91	0.84	0.76	0.80	1.91	1.08	1.27	1.28	1.15	1.30	1.25	1.27	1.28	1.21	1.28	1.26
20.59	0.87	0.70	0.82	1.66	1.02	1.24	1.33	1.12	1.24	1.23	1.25	1.28	1.21	1.25	1.25

Table D-5 Liquid film thickness results in the downward section for water superficial velocity of 0.7 m/s

Usg, m/s	CT3, mm	CT4, mm	CT1, mm	CT2, mm	Mean, mm	CM3, mm	CM4, mm	CM1, mm	CM2, mm	Mean, mm	CB3, mm	CB4, mm	CB1, mm	CB2, mm	Mean, mm
1.32	1.72	1.05	1.37	3.82	1.99	1.83	1.67	1.48	1.79	1.69	1.57	1.51	1.50	1.54	1.53
2.67	1.48	1.01	1.21	3.46	1.79	1.76	1.63	1.49	1.66	1.63	1.42	1.42	1.38	1.49	1.42
4.01	1.27	0.94	1.20	3.26	1.67	1.73	1.62	1.51	1.67	1.63	1.47	1.54	1.48	1.51	1.50
5.29	1.25	0.92	1.10	3.05	1.58	1.72	1.65	1.45	1.67	1.62	1.50	1.43	1.49	1.49	1.48
7.62	1.12	0.91	0.99	2.85	1.47	1.62	1.56	1.40	1.60	1.54	1.46	1.44	1.38	1.45	1.43
9.65	1.04	0.81	0.94	2.60	1.35	1.54	1.44	1.32	1.50	1.45	1.39	1.43	1.29	1.40	1.38
13.15	0.92	0.74	0.82	2.28	1.19	1.40	1.31	1.22	1.39	1.33	1.28	1.31	1.20	1.28	1.27
15.98	0.80	0.73	0.74	2.01	1.07	1.32	1.28	1.14	1.32	1.27	1.20	1.26	1.14	1.22	1.21
18.56	0.74	0.72	0.71	1.82	1.00	1.26	1.32	1.14	1.25	1.24	1.16	1.26	1.17	1.16	1.19

Table D-6 Liquid film thickness results in the downward section for water superficial velocity of 1 m/s

Usg, m/s	CT7, mm	CT8, mm	CT5, mm	CT6, mm	Mean, mm	CM7, mm	CM8, mm	CM5, mm	CM6, mm	Mean, mm	CB7, mm	CB8, mm	CB5, mm	CB6, mm	Mean, mm
1.44	1.76	1.80	1.68	1.79	1.76	1.83	1.89	1.89	1.87	1.87	1.93	1.93	2.26	1.89	2.00
3.02	1.53	1.48	1.43	1.45	1.47	1.54	1.50	1.53	1.54	1.53	1.55	1.54	1.62	1.66	1.59
4.60	1.35	1.40	1.32	1.36	1.36	1.45	1.45	1.48	1.35	1.43	1.48	1.49	1.55	1.53	1.51
6.20	1.22	1.27	1.27	1.30	1.26	1.41	1.40	1.34	1.29	1.36	1.45	1.37	1.41	1.47	1.42
9.38	1.18	1.15	1.21	1.22	1.19	1.22	1.25	1.21	1.26	1.23	1.28	1.27	1.31	1.42	1.32
12.47	1.21	1.17	1.14	1.05	1.14	1.10	1.20	1.27	1.11	1.17	1.32	1.41	1.19	1.32	1.31
18.39	1.22	1.12	1.09	1.17	1.15	1.04	1.13	1.07	1.17	1.10	1.26	1.12	1.21	1.61	1.30
23.66	0.96	1.09	0.88	0.94	0.97	0.95	1.02	0.96	1.07	1.00	1.01	1.14	0.83	1.52	1.13
28.87	0.75	0.76	0.62	0.79	0.73	0.78	0.76	0.73	1.02	0.82	0.71	0.89	0.64	1.27	0.88

Table D-7 Liquid film thickness results in the upward section for water superficial velocity of 0.1 m/s

Usg, m/s	CT7, mm	CT8, mm	CT5, mm	CT6, mm	Mean, mm	CM7, mm	CM8, mm	CM5, mm	CM6, mm	Mean, mm	CB7, mm	CB8, mm	CB5, mm	CB6, mm	Mean, mm
1.42	1.82	1.80	1.78	1.82	1.81	1.87	1.85	1.77	1.94	1.86	1.91	1.95	1.88	1.92	1.91
2.97	1.59	1.48	1.53	1.51	1.53	1.65	1.60	1.58	1.55	1.59	1.66	1.62	1.66	1.65	1.65
4.54	1.41	1.40	1.38	1.37	1.39	1.48	1.45	1.47	1.46	1.46	1.57	1.57	1.58	1.59	1.58
6.12	1.30	1.28	1.32	1.31	1.31	1.37	1.36	1.35	1.37	1.36	1.44	1.41	1.47	1.54	1.46
9.17	1.27	1.21	1.29	1.23	1.25	1.34	1.26	1.30	1.32	1.31	1.42	1.44	1.49	1.58	1.48
12.08	1.20	1.18	1.20	1.23	1.20	1.20	1.21	1.13	1.25	1.20	1.33	1.38	1.42	1.67	1.45
17.51	1.21	1.20	1.01	1.20	1.16	1.19	1.09	1.18	1.12	1.14	1.43	1.35	1.29	1.84	1.48
22.41	1.05	1.15	0.87	1.06	1.03	1.10	1.13	1.09	1.10	1.11	1.18	1.18	0.98	1.52	1.21
26.61	1.08	1.10	0.74	0.92	0.96	1.24	1.11	0.93	1.01	1.07	0.70	0.67	0.72	1.03	0.78

Table D-8 Liquid film thickness results in the upward section for water superficial velocity of 0.2 m/s

Usg, m/s	CT7, mm	CT8, mm	CT5, mm	CT6, mm	Mean, mm	CM7, mm	CM8, mm	CM5, mm	CM6, mm	Mean, mm	CB7, mm	CB8, mm	CB5, mm	CB6, mm	Mean, mm
1.39	2.02	1.94	1.89	1.86	1.93	1.98	1.95	1.95	1.97	1.96	2.08	2.05	2.09	2.09	2.08
2.92	1.60	1.61	1.59	1.58	1.60	1.68	1.67	1.63	1.64	1.66	1.88	1.88	1.86	1.91	1.88
4.47	1.46	1.43	1.37	1.46	1.43	1.52	1.52	1.45	1.56	1.51	1.69	1.65	1.64	1.78	1.69
6.00	1.37	1.34	1.32	1.40	1.36	1.38	1.37	1.36	1.44	1.39	1.61	1.54	1.59	1.79	1.64
8.94	1.27	1.22	1.24	1.27	1.25	1.33	1.24	1.24	1.25	1.27	1.60	1.42	1.63	1.85	1.62
11.70	1.32	1.23	1.17	1.29	1.25	1.22	1.26	1.19	1.27	1.23	1.52	1.45	1.63	1.97	1.64
16.74	1.23	1.14	0.98	1.05	1.10	1.23	1.18	1.14	1.13	1.17	1.41	1.33	1.37	1.93	1.51
21.33	1.05	1.16	0.86	1.08	1.04	1.06	1.10	1.07	1.10	1.09	1.27	1.02	1.05	1.63	1.24
25.12	1.08	1.02	0.72	0.93	0.94	1.07	1.12	1.08	1.12	1.10	0.70	0.59	0.75	0.99	0.76

Table D-9 Liquid film thickness results in the upward section for water superficial velocity of 0.3 m/s

Usg, m/s	CT7, mm	CT8, mm	CT5, mm	CT6, mm	Mean, mm	CM7, mm	CM8, mm	CM5, mm	CM6, mm	Mean, mm	CB7, mm	CB8, mm	CB5, mm	CB6, mm	Mean, mm
1.36	2.12	1.93	1.90	1.99	1.99	2.06	2.22	1.92	2.07	2.07	2.47	2.43	2.45	2.40	2.44
2.86	1.65	1.62	1.60	1.63	1.63	1.71	1.80	1.68	1.72	1.73	2.19	2.26	2.23	2.28	2.24
4.36	1.50	1.45	1.50	1.51	1.49	1.58	1.56	1.56	1.58	1.57	1.89	2.11	2.06	2.14	2.05
5.84	1.40	1.38	1.34	1.34	1.37	1.50	1.51	1.51	1.50	1.50	1.75	1.92	1.94	2.19	1.95
8.60	1.30	1.32	1.27	1.30	1.30	1.40	1.39	1.38	1.36	1.38	1.65	1.83	2.01	2.25	1.93
11.16	1.20	1.21	1.24	1.19	1.21	1.28	1.33	1.26	1.31	1.29	1.61	1.76	1.95	2.33	1.91
15.63	1.11	1.10	1.14	1.09	1.11	1.21	1.22	1.14	1.16	1.18	1.27	1.46	1.47	1.88	1.52
19.62	1.01	1.05	1.03	1.03	1.03	1.16	1.26	1.05	1.13	1.15	0.62	0.88	0.97	1.21	0.92
22.87	0.95	0.98	0.99	0.97	0.97	1.07	1.27	1.08	1.21	1.16	0.54	0.75	0.77	1.04	0.77

Table D-10 Liquid film thickness results in the upward section for water superficial velocity of 0.48 m/s

Usg, m/s	CT7, mm	CT8, mm	CT5, mm	CT6, mm	Mean, mm	CM7, mm	CM8, mm	CM5, mm	CM6, mm	Mean, mm	CB7, mm	CB8, mm	CB5, mm	CB6, mm	Mean, mm
1.34	2.19	2.11	2.13	2.22	2.16	2.22	2.18	2.25	2.27	2.23	2.60	2.38	2.46	2.61	2.51
2.78	1.62	1.64	1.60	1.61	1.62	1.73	1.69	1.74	1.70	1.71	2.12	1.98	2.03	2.19	2.08
4.21	1.46	1.44	1.38	1.44	1.43	1.61	1.55	1.57	1.57	1.57	2.02	1.80	1.90	2.17	1.97
5.61	1.34	1.33	1.24	1.31	1.30	1.42	1.43	1.43	1.45	1.43	1.86	1.58	1.79	2.08	1.83
8.15	1.21	1.19	1.18	1.20	1.20	1.34	1.35	1.33	1.36	1.34	1.75	1.35	1.69	2.16	1.74
10.50	1.11	1.10	1.11	1.13	1.11	1.29	1.28	1.25	1.33	1.29	1.66	1.33	1.60	2.20	1.70
14.45	1.08	1.07	1.09	1.11	1.09	1.29	1.20	1.22	1.26	1.25	1.55	1.26	1.47	2.14	1.61
17.91	0.99	1.02	0.97	0.99	0.99	1.21	1.13	1.19	1.17	1.17	1.25	0.98	1.16	1.78	1.29
20.59	0.93	0.96	0.87	0.91	0.92	1.15	1.06	1.11	1.14	1.12	1.02	0.66	0.99	1.36	1.00

Table D-11 Liquid film thickness results in the upward section for water superficial velocity of 0.7 m/s

Usg, m/s	CT7, mm	CT8, mm	CT5, mm	CT6, mm	Mean, mm	CM7, mm	CM8, mm	CM5, mm	CM6, mm	Mean, mm	CB7, mm	CB8, mm	CB5, mm	CB6, mm	Mean, mm
1.32	3.04	3.17	3.01	3.10	3.08	3.13	3.05	3.03	3.15	3.09	4.03	3.76	3.81	4.09	3.87
2.67	2.07	2.07	2.06	2.11	2.08	2.19	2.20	2.22	2.19	2.20	3.30	2.80	3.01	3.48	3.03
4.01	1.77	1.76	1.74	1.72	1.75	1.91	1.92	1.91	1.95	1.92	2.78	2.18	2.58	3.19	2.51
5.29	1.53	1.54	1.48	1.50	1.51	1.72	1.69	1.70	1.72	1.71	2.37	1.86	2.49	2.92	2.24
7.62	1.33	1.36	1.32	1.30	1.33	1.55	1.52	1.57	1.52	1.54	2.04	1.63	2.40	2.83	2.02
9.65	1.20	1.24	1.23	1.18	1.21	1.46	1.43	1.44	1.43	1.44	1.96	1.44	2.20	2.69	1.87
13.15	1.08	1.08	1.05	1.02	1.06	1.32	1.27	1.32	1.33	1.31	1.52	1.18	1.63	1.70	1.45
15.98	0.96	0.99	0.95	0.91	0.95	1.17	1.15	1.17	1.19	1.17	1.24	0.88	1.30	1.37	1.14
18.56	0.92	0.91	0.90	0.84	0.89	1.09	1.00	1.02	1.08	1.05	1.04	0.68	1.05	1.18	0.92

Table D-12 Liquid film thickness results in the upward section for water superficial velocity of 1 m/s

Film thickness, mm	Usg, m/s	Film velocity, m/s	Entrainment rate, %
0.90	1.44	1.38	51
0.90	3.02	1.46	48
0.96	4.60	1.56	41
0.99	6.20	1.72	33
0.96	9.38	1.93	27
0.92	12.47	2.06	25
0.88	18.39	2.34	19
0.81	23.66	2.45	22
0.71	28.87	2.51	30

Table D-13 Liquid film velocity and entrainment results in the downward section for water superficial velocity of 0.1 m/s

Film thickness, mm	Usg, m/s	Film velocity, m/s	Entrainment rate, %
1.06	1.42	1.45	70
1.07	2.97	1.57	67
1.12	4.54	1.71	62
1.13	6.12	1.91	57
1.17	9.18	2.14	51
1.13	12.08	2.32	48
1.07	17.51	2.52	47
1.00	22.41	2.68	47
0.93	26.61	2.71	50

Table D-14 Liquid film velocity and entrainment results in the downward section for water superficial velocity of 0.2 m/s

Film thickness, mm	Usg, m/s	Film velocity, m/s	Entrainment rate, %
1.19	1.39	1.63	74
1.20	2.92	1.74	73
1.21	4.47	1.87	70
1.23	6.00	1.99	68
1.23	8.94	2.22	64
1.21	11.70	2.43	62
1.16	16.74	2.70	59
1.11	21.33	2.81	59
1.05	25.12	2.84	61

Table D-15 Liquid film velocity and entrainment results in the downward section for water superficial velocity of 0.3 m/s

Film thickness, mm	Usg, m/s	Film velocity, m/s	Entrainment rate, %
1.32	2.86	2.02	78
1.34	4.36	2.23	76
1.34	5.84	2.44	73
1.33	8.60	2.54	72
1.33	11.16	2.72	70
1.27	15.63	2.87	70
1.24	19.62	3.02	69
1.23	22.87	2.92	71

Table D-16 Liquid film velocity and entrainment results in the downward section for water superficial velocity of 0.48 m/s

Film thickness, mm	Usg, m/s	Film velocity, m/s	Entrainment rate, %
1.39	4.21	2.43	72
1.38	5.61	2.65	70
1.28	8.15	2.91	69
1.25	10.50	3.09	68
1.26	14.45	3.14	67
1.25	17.91	3.22	67
1.23	20.59	3.24	67

Table D-17 Liquid film velocity and entrainment results in the downward section for water superficial velocity of 0.7 m/s

Film thickness, mm	Usg, m/s	Film velocity, m/s	Entrainment rate, %
1.62	5.29	2.87	80
1.54	7.62	3.07	80
1.45	9.65	3.26	80
1.33	13.15	3.26	82
1.27	15.98	3.38	82
1.24	18.56	3.38	82

Table D-18 Liquid film velocity and entrainment results in the downward section for water superficial velocity of 1 m/s

Film thickness, mm	Usg, m/s	Film velocity, m/s	Entrainment rate, %
1.23	9.35	0.68	67
1.17	12.47	0.74	66
1.10	18.36	0.86	63
1.00	23.64	1.00	61
0.82	28.81	1.01	67

Table D-19 Liquid film velocity and entrainment results in the upward section for water superficial velocity of 0.1 m/s

Film thickness, mm	Usg, m/s	Film velocity, m/s	Entrainment rate, %
1.31	9.10	0.70	64
1.20	12.03	0.78	63
1.14	17.43	0.80	64
1.11	22.30	1.02	56
1.07	26.57	1.04	56

Table D-20 Liquid film velocity and entrainment results in the upward section for water superficial velocity of 0.2 m/s

Film thickness, mm	Usg, m/s	Film velocity, m/s	Entrainment rate, %
1.23	11.70	0.74	64
1.17	16.74	0.73	66
1.09	21.33	1.03	56
1.20	25.12	1.08	49

Table D-21 Liquid film velocity and entrainment results in the upward section for water superficial velocity of 0.3 m/s

Film thickness, mm	Usg, m/s	Film velocity, m/s	Entrainment rate, %
1.29	11.15	0.98	90
1.18	15.58	1.08	90
1.15	19.59	1.10	90
1.16	22.55	1.14	89

Table D-22 Liquid film velocity and entrainment results in the upward section for water superficial velocity of 0.48 m/s

Film thickness, mm	Usg, m/s	Film velocity, m/s	Entrainment rate, %
1.29	10.50	0.89	91
1.25	14.45	1.10	89
1.17	17.91	1.12	89
1.12	20.59	1.19	89

Table D-23 Liquid film velocity and entrainment results in the upward section for water superficial velocity of 0.7 m/s

Film thickness, mm	Usg, m/s	Film velocity, m/s	Entrainment rate, %
1.44	9.80	0.94	86
1.31	13.44	1.30	86
1.17	16.04	1.37	87
1.05	18.50	1.42	88

Table D-24 Liquid film velocity and entrainment results in the upward section for water superficial velocity of 1 m/s

Appendix E Results of pressure

Qg, Sm^3/h	Ptest, barg	Ptest+1, bar	Qg, m^3/h	Usg, m/s	P1, barg	P2, barg	P3, barg	P4, barg	P5, barg	P6, barg	T1, C	T2, C
6	0.42	1.42	4.22	0.14	0.46	0.40	0.56	0.44	0.07	0.01	15.90	15.41
10	0.36	1.36	7.37	0.25	0.40	0.34	0.48	0.37	0.05	0.01	15.90	15.40
20	0.27	1.27	15.74	0.54	0.30	0.26	0.37	0.28	0.03	0.01	15.95	15.40
30	0.23	1.23	24.32	0.83	0.26	0.22	0.32	0.24	0.03	0.01	16.01	15.39
40	0.20	1.20	33.23	1.14	0.23	0.20	0.28	0.21	0.02	0.01	16.00	15.35
50	0.19	1.19	42.17	1.45	0.21	0.18	0.26	0.19	0.02	0.01	16.01	15.30
80	0.13	1.13	70.49	2.42	0.16	0.14	0.19	0.13	0.01	0.01	16.02	15.17
100	0.12	1.12	89.00	3.05	0.14	0.13	0.17	0.12	0.01	0.01	16.01	15.13
150	0.11	1.11	135.34	4.64	0.12	0.11	0.15	0.10	0.02	0.01	15.97	14.92
200	0.10	1.10	182.57	6.26	0.11	0.10	0.14	0.09	0.02	0.01	15.89	14.67
300	0.08	1.08	277.49	9.51	0.09	0.09	0.12	0.07	0.02	0.01	15.76	14.17
400	0.08	1.08	371.90	12.75	0.08	0.09	0.11	0.07	0.02	0.02	15.49	13.58
600	0.09	1.09	552.23	18.93	0.09	0.09	0.13	0.08	0.04	0.04	15.16	12.72
800	0.11	1.11	722.27	24.76	0.11	0.11	0.16	0.10	0.06	0.06	14.77	11.98
1000	0.15	1.15	870.29	29.83	0.15	0.14	0.21	0.15	0.09	0.08	14.20	11.47

Table E-1 Pressure results for water superficial velocity of 0.07 m/s

Qg, Sm^3/h	Ptest, barg	Ptest+1, bar	Qg, m^3/h	Usg, m/s	P1, barg	P2, barg	P3, barg	P4, barg	P5, barg	P6, barg	T1, C	T2, C
6	0.43	1.43	4.19	0.14	0.48	0.41	0.57	0.45	0.08	0.01	12.72	12.11
10	0.36	1.36	7.38	0.25	0.39	0.34	0.47	0.37	0.05	0.01	12.74	12.17
20	0.28	1.28	15.69	0.54	0.31	0.26	0.37	0.29	0.03	0.01	12.84	12.21
30	0.24	1.24	24.23	0.83	0.27	0.23	0.33	0.25	0.03	0.01	12.84	12.23
40	0.21	1.21	33.02	1.13	0.24	0.21	0.29	0.22	0.02	0.01	12.89	12.23
50	0.19	1.19	41.87	1.44	0.22	0.19	0.27	0.20	0.03	0.01	12.96	12.23
80	0.15	1.15	69.65	2.39	0.17	0.15	0.21	0.15	0.02	0.01	12.97	12.23
100	0.14	1.14	88.09	3.02	0.15	0.14	0.19	0.13	0.02	0.01	12.99	12.23
150	0.12	1.12	134.15	4.60	0.13	0.12	0.17	0.11	0.02	0.01	13.01	12.15
200	0.11	1.11	180.79	6.20	0.12	0.11	0.15	0.10	0.02	0.01	12.98	12.04
300	0.10	1.10	273.71	9.38	0.11	0.10	0.14	0.09	0.03	0.02	12.84	11.70
400	0.10	1.10	363.87	12.47	0.11	0.11	0.14	0.09	0.03	0.03	12.72	11.38
600	0.12	1.12	536.57	18.39	0.13	0.12	0.17	0.11	0.06	0.05	12.51	10.89
800	0.16	1.16	690.21	23.66	0.16	0.16	0.22	0.16	0.10	0.08	12.27	10.34
1000	0.19	1.19	842.19	28.87	0.19	0.18	0.26	0.20	0.12	0.10	12.11	9.97

Table E-2 Pressure results for water superficial velocity of 0.1 m/s

Qg, Sm^3/h	Ptest, barg	Ptest+1, bar	Qg, m^3/h	Usg, m/s	P1, barg	P2, barg	P3, barg	P4, barg	P5, barg	P6, barg	T1, C	T2, C
6	0.42	1.42	4.22	0.14	0.46	0.41	0.56	0.44	0.06	0.00	15.14	14.65
10	0.35	1.35	7.38	0.25	0.39	0.34	0.48	0.37	0.04	0.00	15.28	14.79
20	0.29	1.29	15.53	0.53	0.32	0.28	0.39	0.30	0.03	0.00	15.40	14.89
30	0.26	1.26	23.81	0.82	0.29	0.25	0.35	0.27	0.03	0.01	15.48	14.92
40	0.23	1.23	32.39	1.11	0.26	0.23	0.32	0.24	0.03	0.01	15.53	15.02
50	0.21	1.21	41.28	1.42	0.24	0.21	0.29	0.21	0.03	0.01	15.65	15.05
80	0.17	1.17	68.51	2.35	0.19	0.17	0.23	0.17	0.03	0.01	15.71	15.12
100	0.15	1.15	86.77	2.97	0.17	0.16	0.21	0.15	0.02	0.01	15.77	15.15
150	0.13	1.13	132.45	4.54	0.15	0.14	0.19	0.13	0.03	0.01	15.77	15.05
200	0.12	1.12	178.54	6.12	0.13	0.13	0.17	0.11	0.03	0.02	15.69	14.95
300	0.12	1.12	267.64	9.17	0.13	0.13	0.17	0.11	0.04	0.03	15.63	14.75
400	0.13	1.13	352.49	12.08	0.15	0.14	0.19	0.13	0.06	0.05	15.42	14.46
600	0.17	1.17	510.92	17.51	0.18	0.18	0.24	0.17	0.09	0.08	15.10	13.92
800	0.22	1.22	653.84	22.41	0.23	0.22	0.30	0.23	0.14	0.11	14.68	13.33
1000	0.29	1.29	776.29	26.61	0.30	0.27	0.39	0.31	0.19	0.16	14.20	12.84

Table E-3 Pressure results for water superficial velocity of 0.2 m/s

Qg, Sm^3/h	Ptest, barg	Ptest+1, bar	Qg, m^3/h	Usg, m/s	P1, barg	P2, barg	P3, barg	P4, barg	P5, barg	P6, barg	T1, C	T2, C
6	0.44	1.44	4.17	0.14	0.48	0.43	0.58	0.45	0.07	0.00	16.87	16.38
10	0.38	1.38	7.23	0.25	0.42	0.38	0.51	0.39	0.05	0.00	16.88	16.44
20	0.31	1.31	15.21	0.52	0.35	0.31	0.42	0.32	0.03	0.00	16.96	16.45
30	0.28	1.28	23.53	0.81	0.31	0.27	0.37	0.28	0.03	0.01	16.99	16.47
40	0.26	1.26	31.86	1.09	0.29	0.25	0.34	0.26	0.03	0.01	16.99	16.44
50	0.23	1.23	40.54	1.39	0.26	0.23	0.32	0.23	0.04	0.01	16.99	16.41
80	0.19	1.19	67.22	2.30	0.21	0.19	0.26	0.19	0.03	0.01	16.99	16.38
100	0.17	1.17	85.22	2.92	0.19	0.18	0.24	0.17	0.03	0.01	16.88	16.33
150	0.15	1.15	130.31	4.47	0.17	0.16	0.21	0.15	0.03	0.02	16.87	16.25
200	0.14	1.14	175.11	6.00	0.16	0.15	0.20	0.14	0.04	0.02	16.75	16.05
300	0.15	1.15	260.66	8.94	0.16	0.16	0.21	0.15	0.06	0.04	16.63	15.84
400	0.17	1.17	341.25	11.70	0.18	0.18	0.23	0.17	0.08	0.06	16.26	15.39
600	0.23	1.23	488.27	16.74	0.24	0.23	0.31	0.23	0.13	0.10	15.71	14.67
800	0.29	1.29	622.31	21.33	0.30	0.27	0.38	0.30	0.18	0.15	15.07	13.91
1000	0.36	1.36	732.76	25.12	0.38	0.34	0.49	0.39	0.24	0.20	14.41	13.21

Table E-4 Pressure results for water superficial velocity of 0.3 m/s

Qg, Sm^3/h	Ptest, barg	Ptest+1, bar	Qg, m^3/h	Usg, m/s	P1, barg	P2, barg	P3, barg	P4, barg	P5, barg	P6, barg	T1, C	T2, C
6	0.44	1.44	4.18	0.14	0.47	0.45	0.55	0.43	0.08	-0.01	14.30	13.82
10	0.38	1.38	7.23	0.25	0.42	0.39	0.50	0.38	0.04	-0.01	14.59	14.15
20	0.34	1.34	14.98	0.51	0.37	0.34	0.44	0.33	0.04	0.00	14.80	14.33
30	0.31	1.31	22.84	0.78	0.35	0.32	0.41	0.31	0.05	0.01	15.15	14.67
40	0.29	1.29	30.95	1.06	0.32	0.29	0.38	0.29	0.05	0.01	15.29	14.80
50	0.26	1.26	39.67	1.36	0.29	0.26	0.35	0.26	0.05	0.01	15.52	15.00
80	0.22	1.22	65.72	2.25	0.24	0.22	0.29	0.21	0.05	0.01	15.66	15.16
100	0.20	1.20	83.37	2.86	0.22	0.20	0.27	0.19	0.04	0.02	15.87	15.31
150	0.18	1.18	127.31	4.36	0.20	0.18	0.24	0.17	0.05	0.02	15.97	15.41
200	0.17	1.17	170.31	5.84	0.19	0.18	0.24	0.17	0.06	0.04	16.03	15.47
300	0.20	1.20	250.82	8.60	0.21	0.20	0.26	0.19	0.08	0.06	16.04	15.41
400	0.23	1.23	325.65	11.16	0.24	0.23	0.30	0.23	0.11	0.09	15.96	15.28
600	0.32	1.32	456.02	15.63	0.33	0.31	0.41	0.32	0.18	0.15	15.65	14.87
800	0.40	1.40	572.48	19.62	0.42	0.38	0.52	0.42	0.25	0.22	15.24	14.39
1000	0.50	1.50	667.15	22.87	0.52	0.46	0.65	0.54	0.34	0.29	14.67	13.81

Table E-5 Pressure results for water superficial velocity of 0.48 m/s

Qg, Sm^3/h	Ptest, barg	Ptest+1, bar	Qg, m^3/h	Usg, m/s	P1, barg	P2, barg	P3, barg	P4, barg	P5, barg	P6, barg	T1, C	T2, C
6	0.25	1.25	4.80	0.16	0.41	0.40	0.22	0.09	0.02	-0.05	23.82	23.39
10	0.34	1.34	7.45	0.26	0.42	0.41	0.40	0.28	0.05	-0.02	23.94	23.52
20	0.35	1.35	14.86	0.51	0.40	0.37	0.43	0.32	0.05	0.00	24.03	23.60
30	0.34	1.34	22.44	0.77	0.38	0.36	0.42	0.32	0.06	0.01	24.08	23.70
40	0.32	1.32	30.20	1.04	0.36	0.34	0.41	0.31	0.06	0.02	24.18	23.71
50	0.28	1.28	38.99	1.34	0.32	0.30	0.36	0.27	0.06	0.01	24.20	23.80
80	0.25	1.25	64.22	2.20	0.27	0.26	0.32	0.23	0.06	0.02	24.20	23.80
100	0.23	1.23	81.04	2.78	0.26	0.25	0.31	0.22	0.06	0.02	24.19	23.71
150	0.22	1.22	122.89	4.21	0.24	0.23	0.29	0.21	0.07	0.04	24.07	23.59
200	0.22	1.22	163.54	5.61	0.24	0.23	0.30	0.22	0.08	0.05	23.90	23.35
300	0.26	1.26	237.70	8.15	0.28	0.27	0.34	0.26	0.12	0.09	23.61	22.99
400	0.31	1.31	306.17	10.50	0.32	0.30	0.40	0.31	0.16	0.13	23.11	22.41
600	0.42	1.42	421.47	14.45	0.44	0.41	0.54	0.44	0.25	0.21	22.05	21.25
800	0.53	1.53	522.49	17.91	0.55	0.50	0.68	0.57	0.34	0.29	18.64	17.86
1000	0.67	1.67	600.58	20.59	0.70	0.61	0.83	0.72	0.45	0.38	17.69	16.91

Table E-6 Pressure results for water superficial velocity of 0.7 m/s

Qg, Sm^3/h	Ptest, barg	Ptest+1, bar	Qg, m^3/h	Usg, m/s	P1, barg	P2, barg	P3, barg	P4, barg	P5, barg	P6, barg	T1, C	T2, C
6	0.20	1.20	5.02	0.17	0.37	0.38	0.11	0.01	-0.02	-0.08	15.98	15.43
10	0.26	1.26	7.96	0.27	0.40	0.40	0.22	0.11	0.02	-0.05	16.38	15.87
20	0.32	1.32	15.20	0.52	0.41	0.40	0.34	0.23	0.06	0.00	16.87	16.36
30	0.31	1.31	22.84	0.78	0.38	0.37	0.37	0.26	0.07	0.00	17.18	16.64
40	0.32	1.32	30.39	1.04	0.37	0.36	0.38	0.28	0.07	0.01	17.56	17.01
50	0.30	1.30	38.46	1.32	0.35	0.33	0.37	0.27	0.07	0.02	17.84	17.32
80	0.28	1.28	62.28	2.13	0.32	0.31	0.35	0.26	0.08	0.03	18.11	17.60
100	0.28	1.28	78.03	2.67	0.31	0.30	0.35	0.26	0.09	0.04	18.42	17.85
150	0.28	1.28	116.97	4.01	0.30	0.30	0.36	0.27	0.10	0.06	18.68	18.09
200	0.30	1.30	154.37	5.29	0.31	0.30	0.38	0.29	0.12	0.08	18.82	18.22
300	0.35	1.35	222.43	7.62	0.36	0.35	0.44	0.35	0.17	0.13	18.82	18.21
400	0.42	1.42	281.49	9.65	0.44	0.41	0.53	0.43	0.23	0.18	18.65	17.97
600	0.56	1.56	383.68	13.15	0.58	0.53	0.70	0.59	0.34	0.28	18.26	17.53
800	0.72	1.72	466.26	15.98	0.74	0.66	0.88	0.77	0.46	0.38	17.60	16.81
1000	0.85	1.85	541.30	18.56	0.88	0.78	1.04	0.92	0.56	0.48	17.16	16.33

Table E-7 Pressure results for water superficial velocity of 1 m/s

Qg, Sm^3/h	Ptest, barg	Ptest+1, bar	Qg, m^3/h	Usg, m/s	P1, barg	P2, barg	P3, barg	P4, barg	P5, barg	P6, barg	T1, C	T2, C
6	0.18	1.18	5.10	0.17	0.36	0.36	0.08	-0.01	-0.04	-0.08	15.17	14.64
10	0.24	1.24	8.06	0.28	0.39	0.40	0.18	0.08	0.01	-0.06	15.80	15.27
20	0.29	1.29	15.44	0.53	0.41	0.40	0.30	0.19	0.06	-0.01	16.26	15.73
30	0.30	1.30	23.01	0.79	0.39	0.38	0.34	0.23	0.07	0.00	16.74	16.17
40	0.30	1.30	30.70	1.05	0.37	0.36	0.35	0.24	0.07	0.01	17.10	16.53
50	0.30	1.30	38.45	1.32	0.36	0.35	0.36	0.25	0.07	0.02	17.54	16.99
80	0.30	1.30	61.53	2.11	0.34	0.33	0.37	0.27	0.09	0.04	17.85	17.32
100	0.30	1.30	76.83	2.63	0.33	0.33	0.37	0.28	0.10	0.05	18.20	17.62
150	0.31	1.31	114.56	3.93	0.33	0.33	0.39	0.29	0.11	0.07	18.37	17.84
200	0.33	1.33	149.91	5.14	0.35	0.34	0.42	0.33	0.14	0.09	18.63	18.06
300	0.40	1.40	214.31	7.35	0.42	0.40	0.50	0.40	0.20	0.14	18.69	18.04
400	0.47	1.47	271.90	9.32	0.49	0.46	0.59	0.48	0.26	0.20	18.46	17.84
600	0.65	1.65	364.54	12.50	0.66	0.61	0.79	0.68	0.39	0.31	18.09	17.37
800	0.80	1.80	444.98	15.25	0.82	0.74	0.98	0.86	0.51	0.41	17.45	16.67
1000	0.95	1.95	511.82	17.55	0.98	0.87	1.17	1.04	0.63	0.52	16.92	16.11

Table E-8 Pressure results for water superficial velocity of 1.2 m/s

Qg, Sm^3/h	Ptest, barg	Ptest+1, bar	Qg, m^3/h	Usg, m/s	P1, barg	P2, barg	P3, barg	P4, barg	P5, barg	P6, barg	T1, C	T2, C
6	0.17	1.17	5.14	0.18	0.36	0.36	0.05	-0.03	-0.05	-0.10	18.73	18.24
10	0.21	1.21	8.29	0.28	0.39	0.39	0.14	0.02	0.00	-0.08	19.64	19.17
20	0.28	1.28	15.65	0.54	0.42	0.41	0.26	0.14	0.06	-0.02	20.89	20.42
30	0.30	1.30	23.14	0.79	0.41	0.40	0.31	0.19	0.07	0.00	21.70	21.23
40	0.31	1.31	30.64	1.05	0.40	0.39	0.33	0.22	0.08	0.01	22.51	22.05
50	0.31	1.31	38.10	1.31	0.39	0.38	0.35	0.24	0.09	0.03	23.27	22.82
80	0.33	1.33	60.11	2.06	0.38	0.37	0.39	0.29	0.11	0.05	24.00	23.55
100	0.34	1.34	74.56	2.56	0.38	0.38	0.41	0.31	0.13	0.07	24.66	24.21
150	0.37	1.37	109.67	3.76	0.39	0.39	0.45	0.35	0.15	0.10	25.17	24.71
200	0.40	1.40	142.71	4.89	0.42	0.41	0.50	0.39	0.19	0.13	25.66	25.18
300	0.49	1.49	201.25	6.90	0.51	0.49	0.61	0.49	0.26	0.20	25.90	25.37
400	0.59	1.59	251.37	8.62	0.61	0.58	0.72	0.61	0.34	0.26	25.79	25.20
600	0.78	1.78	336.15	11.52	0.81	0.74	0.96	0.83	0.50	0.40	25.44	24.78
800	0.97	1.97	405.70	13.91	1.00	0.90	1.18	1.05	0.64	0.53	24.75	24.01
1000	1.11	2.11	473.34	16.23	1.14	1.02	1.35	1.21	0.75	0.63	23.84	23.04

Table E-9 Pressure results for water superficial velocity of 1.5 m/s

Appendix F Publications

- Almabrok A., Lao L. and Yeung H. (2013). Effect of 180^{o} bends on gas/liquid flows in vertical upward and downward pipes. *Computational Methods in Multiphase Flow*, 79, ISSN 1743-3533.

- Almabrok A., Lao L. and Yeung H. (2013). Effect of 180^{o} bends on gas/liquid flows in vertical upward and downward pipes. Presentation presented at *Joint Programme on Transient and Complex Multiphase Flows and Flow Assurance*, Imperial College, London, UK, Meeting on 25 and 26 March.

- Almabrok A., Lao L. and Yeung H. (2010). Two-phase flow in upward and downward pipes. A poster presented at *the Third Academic Symposium of Libyan Students-Universities of UK*, Sheffield Hallam University, Sheffield, UK, 26 Jun.

- Almabrok A., Lao L. and Yeung H. Gas/liquid flow behaviours in a downward section of large diameter vertical serpentine pipes. (In preparation).

- Almabrok A., Lao L. and Yeung H. Gas/liquid flow behaviours in upward section of large diameter vertical serpentine pipes. (In preparation).